Link Acquisition and Optimization for Intersatellite Laser Interferometry

Von der QUEST-Leibniz-Forschungsschule
der Gottfried Wilhelm Leibniz Universität Hannover
zur Erlangung des Grades

DOKTOR DER NATURWISSENSCHAFTEN
– Dr. rer. nat. –

genehmigte Dissertation von

M.Sc. Alexander Koch

2020

In der vorliegenden Arbeit wurden gegenüber der am 19.12.2019 bei der QUEST-Leibniz-Forschungsschule eingereichten Version einige Tippfehler korrigiert. Vereinzelt wurden Textstellen und Abbildungen im Sinne eines besseren Verständnisses leicht überarbeitet.

Abstract

The topic of this thesis is the initial link acquisition process for intersatellite laser interferometers. Furthermore, a technique was studied that can be applied to enhance the signal to noise ratio of the established laser link. This work was carried out in the context of the Gravity Recovery And Climate Experiment Follow-On (GRACE-FO), Next Generation Gravity Field Mission (NGGM) and Laser Interferometer Space Antenna (LISA) satellite missions. Link acquisition is one of the most critical steps during the commissioning phase of an intersatellite laser interferometer. It is required to calibrate unknown pointing offsets of the laser beams that are caused by manufacturing and alignment tolerances of the instrument, structural distortions of the spacecraft (S/C) due to temperature changes and the different gravity levels on ground and in orbit, as well as insufficient knowledge about the attitude of the S/C. Furthermore, the frequencies of the lasers on the different S/C have to be matched to within the bandwidth of the opto-electronics readout chain. This thesis is split into two parts. The first part focuses on the Laser Ranging Interferometer (LRI) on-board the GRACE-FO mission, while the second part is dedicated to future missions: LISA and NGGM, a possible successor to GRACE-FO. In the first part, laboratory tests that verified the robustness of the GRACE-FO link acquisition procedure are presented. These tests were carried out using a realistic mock-up LRI and a proper experimental test bed that allowed for the introduction of MHz Doppler frequency shifts, pW received (RX) laser powers and flat-top RX beams. Also shown in this part are analysis results of the actual in-orbit link acquisition process that was carried out in June 2018. Unambiguous laser beam pointing offsets below $\pm 1\,\mathrm{mrad}$ and a frequency offset, also in the expected range, were obtained. Small alignment errors of the LRI's triple mirror assemblies (TMAs) were studied by analyzing in-orbit data. A trade-off study is presented which shows how these errors can be optimally compensated by introducing dedicated beam pointing offsets.

In the second part of this thesis, the design, construction and characterization of an experimental test bed that simulates the intersatellite laser link of LRI-like instrument is presented. The test bed faithfully recreates the RX laser power as function of the transmitted beam pointing angles with an error below $10\,\%$, even for fast spatial scans of the TX beam. Furthermore, dedicated acquisition sensors were studied in the context of LISA and NGGM. A position sensitive photodetector (PSPD) and an indium gallium arsenide (InGaAs) camera with 256×320 pixels were investigated. The PSPD required a minimum laser power of $\sim 10\,\mathrm{nW}$. The ratio of the achieved resolution, in terms of beamwalk on the sensor, to the sensor size was $0.2\,\%$. Tests of the InGaAs camera were carried out with a laser power of $1\,\mathrm{pW}$. The achieved resolution in relation to the sensor size was $0.065\,\%$. Hence, both sensors fulfill the preliminary NGGM requirements, but only the InGaAs sensor satisfies all considered LISA requirements.

Keywords: laser interferometry, GRACE Follow-On, space instrumentation

Contents

List of Figures

List of Tables

Acronyms

AC	alternating current
ADC	analog to digital converter
AEI	Albert Einstein Institute
AGC	automatic gain control
ANU	Australian National University
AOCS	attitude and orbit control system
AOM	acousto-optic modulator
API	application programming interface
ASD	amplitude spectral density
BPF	bandpass filter
BPM	bad pixel map
CAD	computer aided design
CAE	co-alignment error
CAS	constellation acquisition sensor
CCD	charge-coupled device
CFRP	carbon fiber reinforced polymer
CHAMP	CHAllenging Minisatellite Payload
CLTF	closed-loop transfer function
CMOS	complementary metal-oxide-semiconductor
C/N$_0$	carrier-to-noise density
CoM	center of mass
CP	compensation plate
DAC	digital-to-analog converter
DAQ	data acquisition
DC	direct current
DDS	direct digital synthesizer
DLR	Deutsches Zentrum für Luft- und Raumfahrt
DMA	direct memory access
DoF	degree of freedom
dPLL	digital phase locked-loop
DPS	differential power sensing
DWS	differential wavefront sensing
EOAM	elecotro-optical amplitude modulator
ESA	European Space Agency
FC	fiber collimator
FET	field effect transistor
FFT	fast Fourier transform
FG	frame grabber
FIFO	first in first out
FMA	frequency modulation and power attenuation
FoM	figure of merit
FoV	field of view

FPA	focal plane array
FPGA	field-programmable gate array
FPN	fixed pattern noise
FSM	fast steering mirror
GBWP	gain bandwidth product
GOCE	Gravity Field and Steady-State Ocean Circulation Explorer
GPS	Global Positioning System
GRACE	Gravity Recovery And Climate Experiment
GRACE-FO	Gravity Recovery And Climate Experiment Follow-On
GUI	graphical user interface
GW	gravitational wave
IABG	Industrieanlagen-Betriebsgesellschaft mbH
IC	integrated circuit
ICN	input-referred current noise
InGaAs	indium gallium arsenide
JPL	Jet Propulsion Laboratory
KAGRA	Kamioka Gravitational Wave Detector
KBR	K/Ka band ranging instrument
LIGO	Laser Interferometer Gravitational-Wave Observatory
LISA	Laser Interferometer Space Antenna
LISO	Linear Simulation and Optimization of Analog Electronic Circuits
LLS	laser link simulator
LO	local oscillator
LOF	LRI optical frame
LOS	line of sight
LRI	Laser Ranging Interferometer
LRP	Laser Ranging Processor
LUT	look-up table
µC	microcontroller
NGGM	Next Generation Gravity Field Mission
NPRO	non-planar ring oscillator
NSF	noise shape function
NUC	non-uniformity correction
OB	optical bench
OGSE	optical ground support equipment
OLTF	open-loop transfer function
OPA	operational amplifier
PD	photodiode
PER	polarization extinction ratio
PHPR	pinhole photoreceiver
PM	phasemeter
PR	photoreceiver
PSD	power spectral density
PSPD	position sensitive photodetector
PSS	Position Sensing Subsystem
QE	quantum efficiency
QPD	quadrant photodiode
QPR	quadrant photoreceiver
RF	radio frequency
RIN	relative intensity noise
rms	root mean square

ROI	range of interest
ROIC	readout integrated circuit
RX	received
S/C	spacecraft
SNR	signal to noise ratio
SoC	system on chip
SST	satellite-to-satellite tracking
STI	SpaceTech GmbH
TBD	to be defined
TIA	transimpedance amplifier
TMA	triple mirror assembly
TRL	technical readiness level
TRP	thermal reference point
TTL	tilt-to-(path)length
TX	transmitted
UGF	unity gain frequency
VI	virtual instrument
VOA	voltage-controlled attenuator
WFE	wave front error

Chapter 1

Introduction

On Tuesday, May 22nd, 2018 the two Gravity Recovery And Climate Experiment Follow-On (GRACE-FO) spacecraft (S/C) were successfully launched from the Vandenbeg Airforce Base in the state of California, USA. It was a shared launch with five Iridium Next satellites [1], on-board of a SpaceX Falcon-9 launch vehicle. After approximately three weeks in orbit, during which routine checks of the whole S/C were done, the Laser Ranging Interferometer (LRI) was enabled on June 13th. A procedure, that is referred to as initial laser link acquisition, was carried out. As a consequence, the LRI laser link could be established and the first intersatellite laser interferometer began its operation.

The main topic of this thesis is the the link acquisition mode, as well as the optimization of the signal to noise ratio (SNR) of the laser link of space-based laser interferometers. This work was carried out in the context of three satellite missions: GRACE-FO, Next Generation Gravity Field Mission (NGGM), a possible successor to GRACE-FO and the Laser Interferometer Space Antenna (LISA). A brief overview of these missions is given in the following paragraphs. This introduction is then concluded by an overview of the structure of this thesis.

1.1 Satellite geodesy missions

Geodesy is the science of the measurement and mapping of the Earth's surface [2]. A prominent example of a geodetic field of interest is Earth's gravity. It can be described by an equipotential surface, that is referred to as a *geoid*. If the Earth were completely covered by water and in the absence of winds and tides, the water surface would resemble the shape of a geoid. One example of a geoid is illustrated in Fig. 1.1. Its shape results from the inhomogeneous distribution of mass within and on the surface of the Earth. Thereby, the height differences , shown in Fig. 1.1, are drawn exaggerated. While Earth's gravity is mostly static, the motion of continental plates, earthquakes and the movement of water on or beneath the Earth's surface cause temporal variations of this field. In the context of climate change, especially the redistribution of water is of highest interest to all of mankind. Instead of performing numerous local measurements of the gravity
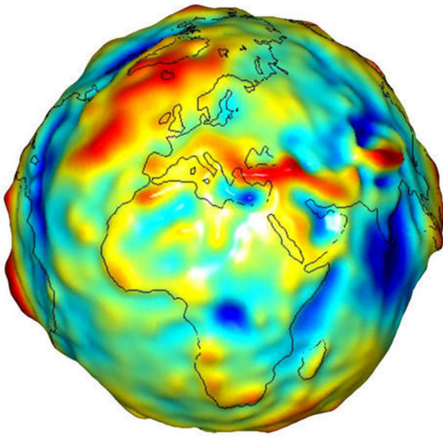
Figure 1.1: Illustration of an equipotential surface of the Earth's gravity field, also referred to as a geoid [5]
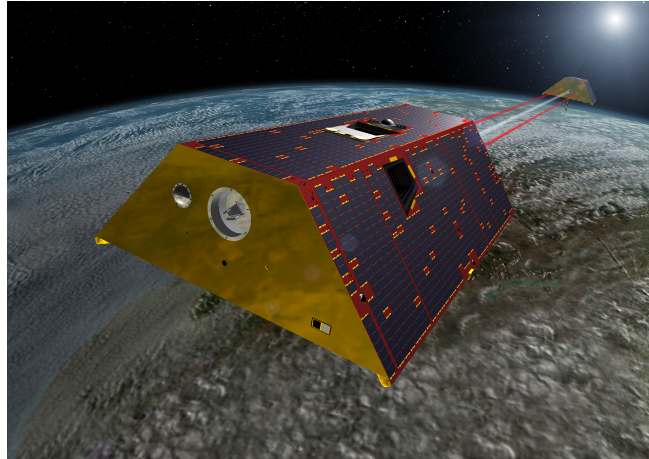
Figure 1.2: Artist's impression of the two GRACE-FO S/C in orbit around the Earth [6]

field, Earth-observation satellites represent a highly appropriate tool, to perform such measurements on a global scale.

Information on the gravity field can be obtained by probing the forces that act on satellites or test masses that are in free fall around the Earth. Various mutations of this concept have already been applied for satellite missions. The CHAllenging Minisatellite Payload (CHAMP) mission, that was operational in the years 2000–2010, mapped Earth's gravity field by means of high-low satellite-to-satellite tracking (SST) [3]. In this scheme, the position and velocity of a S/C in a low-Earth orbit is tracked with the help of Global Positioning System (GPS) satellites that are considered to be in a "high" orbit, hence the name. Thereby, the CHAMP S/C was in an almost circular, polar orbit with an initial altitude of about 450 km [3]. The S/C orbit was tracked with an accuracy of a few cm [2]. An accelerometer, located in the S/C center of mass (CoM), was used to measure non-gravitational forces, e.g. atmospheric drag, solar radiation pressure, and pressure caused by the Earth's albedo as well as by thrust. The gravity field was then obtained by analyzing the orbit data, while taking into account these disturbing influences. As a result, the geoid height could be determined with an accuracy of about 1 cm and a spatial resolution of ~1000 km [4].

Another mission that was developed to probe Earth's gravity field, was the Gravity Field and Steady-State Ocean Circulation Explorer (GOCE) mission [7]. Due to the high atmospheric drag at the nearly polar orbit's low altitude of only ~250 km, the mission life time was limited to the years 2009–2013. However, this low orbit allowed for mapping of the geoid with an unprecedented spatial resolution of less than 100 km and an accuracy of about 1 cm [8]. Similar to CHAMP, a high-low SST scheme was used to accurately determine the S/C orbit. Additionally, three pairs of accelerometers were located inside the S/C, arranged symmetrically around the S/C CoM. This allowed for a three-dimensional

measurement of the gravity gradient with a precision of $10^{-12}\,\mathrm{ms}^{-2}/\sqrt{\mathrm{Hz}}$ [9]. By designing the satellite totally symmetric and by operating the S/C in a drag-free mode, non-gravitational forces were minimized [2].

The first mission that provided high resolution measurements of the Earth's time-variable gravity field was the joint US/German Gravity Recovery And Climate Experiment (GRACE) mission [10]. The two GRACE S/C were operational from 2002 until 2017, more than tripling their design mission time of five years. They flew in a nearly polar orbit of initially 500 km altitude. In contrast to CHAMP and GOCE, GRACE used a K/Ka band ranging instrument to measure changes of the intersatellite distance with µm precision [11]. The nominal S/C separation was 170 km–270 km. The orbits of the S/C were again tracked via GPS and the non-gravitational forces were measured with the help of accelerometers. The geoid height could be resolved with an unprecedented accuracy below the mm level and with a spatial resolution of a few hundred km [4, 2]. This allowed for the first, continuous global measurement of the temporal variations of the gravity field. Up to this day, more than 2000 scientific papers were published that used GRACE data [12]. Among these were high impact publications that reported on accelerated ice mass loss in Greenland, the continuous drought in California's central valley, groundwater depletion in Pakistan and various other phenomena, related but not limited to hydrology [13, 14, 15, 16]. Due to age-related battery issues, the mission ended with the re-entry of the first GRACE S/C on December 24th, 2017.

Due to the immense success of GRACE and to ensure data continuity it was decided to prepare a quick follow-on mission. Consequently, the GRACE-FO mission was launched on May 22nd, 2018 (see Fig. 1.2). The initial orbit altitude was again ∼450 km and the S/C are separated by 220 km±50 km. As was the case for GRACE, the chosen orbit ensures that monthly updates of the global gravity field are produced. The same US/German partnership, as well as a high heritage approach ensured a smooth implementation of the mission. A few changes were made, for example the addition of a third star tracker camera per S/C to improve the attitude and orbit control system (AOCS) [17]. However, one major update stands out: the addition of the Laser Ranging Interferometer (LRI) as a technology demonstrator for a laser-based intersatellite ranging instrument [18, 19, 20]. The LRI is also a joint US/German project, led by the Albert Einstein Institute (AEI) in Germany and the Jet Propulsion Laboratory (JPL) in the US. The LRI has a ranging noise requirement of $80\,\mathrm{nm}/\sqrt{\mathrm{Hz}}$ in the frequency range of 2 mHz–0.1 Hz [18]. Analysis of the first ranging data has revealed a noise floor below $1\,\mathrm{nm}/\sqrt{\mathrm{Hz}}$ for frequencies above 0.1 Hz [19]. The K/Ka band ranging instrument is a rebuild of the GRACE mission [17]. Hence, a comparable resolution in the µm range is expected. However, the expected impact of the low noise of the LRI on the geodetic results is limited [21]. The reason for this is that the retrieval of the gravity signal is currently still dominated by accelerometer noise, ocean tide and non-tidal mass variation errors. The obtained GRACE-FO ranging data has been made publicly available in the summer of 2019 and the first scientific publications that use LRI data are presently expected.

A potential successor to the GRACE-FO mission is Next Generation Gravity Field Mission (NGGM). This is the outcome of the e^{2}motion study [22] that had the goal of developing a mission concept that enables long term, high precision measurements of the time variable gravity field. A requirement of 1 mm monthly geoid height error with a spatial resolution of ~150 km was defined as input to the study. The proposed mission concept foresees two pairs of S/C in an initial altitude of ~400 km. One pair is proposed to be on a polar and one on a 70° inclined orbit. This configuration is referred to as a Bender pair orbit, and is anticipated to yield a higher resolution of the range measurement and a more isotropic noise distribution [23]. A S/C separation of 100 km is foreseen. Again, accelerometers will be used to determine the non-gravitational forces. Partial compensation of the atmospheric drag were found to be required under certain conditions, to keep the accelerometers within their operating bandwidth. The chosen orbits ensure that at least monthly updates of the gravity field can be produced. An LRI-like instrument is planned to completely replace the microwave ranging instrument. The intended accuracy for measurements of intersatellite distance variations is ~25 nm/$\sqrt{Hz}$ in the frequency range of 0.1 mHz–0.1 Hz. The interested reader is referred to the e^{2}motion study report for further information on the mission and instrument design: [22].

1.2   The Laser Interferometer Space Antenna – LISA

On September 14th, 2015 the two Laser Interferometer Gravitational-Wave Observatory (LIGO) observatories detected the first gravitational wave (GW), referred to as *GW150914* [24]. It was generated by a black hole binary merger, which was estimated to have occurred 410 MPc, or $1.337 \cdot 10^9$ light years, away from Earth. As a consequence, the 2017 Nobel Prize was awarded to Rainer Weiss, Barry C. Barish and Kip S. Thorne for: "Decisive contributions to the LIGO detector and the observation of gravitational waves" [25]. Up to this day, various other GW detections have been reported [26]. Currently, in total four GW observatories are operational [27, 28, 29]. It is expected that the Japanese Kamioka Gravitational Wave Detector (KAGRA) detector joins the network shortly [30]. Additional plans to augment the network in the near future with a LIGO detector in India exist [31].

Albert Einstein's General Theory of Relativity predicts that GWs stretch and compress spacetime [32, 33, 34]. Hence, they affect the separation of otherwise undisturbed test masses. That is why all GW detectors share the same concept of precisely tracking the interferometer arm lengths. This is done by means of homodyne interferometry in Michelson-like laser interferometers [35]. Homodyne interferometry describes a scheme in which the output of a single laser is split along two interferometer arms, reflected at test masses and then recombined on a beamsplitter. The resulting beat note signal contains information about length variations of the two arms. However, the ground-based detectors are only sensitive to GWs in a frequency range of about 10 Hz–10 kHz [36]. This is due to gravity gradient and seismic noise, as well as length limitations of the detector arms [37]. By designing a GW observatory in space, far away from Earth, these limitations
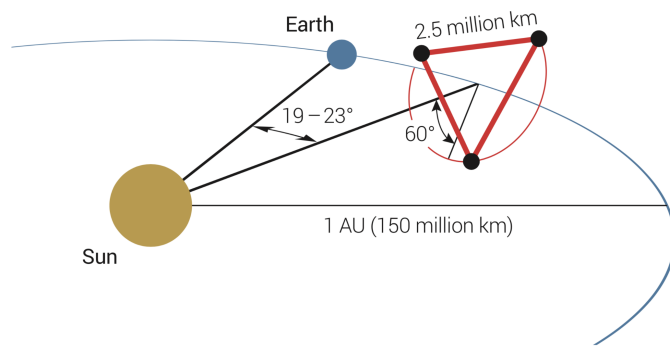
Figure 1.3: Schematic drawing of the LISA constellation in the shape of an equilateral triangle and its orbit around the sun [38]

can be circumvented. The LISA mission will accomplish this. The three LISA S/C will form an equilateral triangle, with each S/C on an individual orbit around the sun. The constellation will trail the Earth at an angle of about 20°, see Fig. 1.3. With its freely floating test masses and its $\sim 2.5 \cdot 10^6$ km long interferometer arms, it will be sensitive to GWs in a frequency range of about 0.1 mHz to 1 Hz [38]. Thereby, LISA uses the same basic measurement principle of the ground-based detectors, of precise determination of distance changes between test masses. However, LISA will use heterodyne interferometry. This scheme describes the interference of optical signals with different frequencies. In the case of LISA, the S/C dynamics cause Doppler shifts of the laser beams, which lead to beat note signals in the low MHz range. While LISA has some technological overlap with the ground-based detectors, a variety of technologies has to be developed to enable a laser interferometer in the harsh environment of free space. Therefore, the LISA Pathfinder mission was designed, in order to show the functionality of key LISA technology on a single S/C [39]. LISA Pathfinder was launched on December 3rd, 2015 and turned out to be a tremendous success. The readiness of key LISA technology could be shown, like drag-free control of the S/C with micronewton thrusters that enabled having two free-floating test masses in one S/C with sub-femto g/$\sqrt{\text{Hz}}$ acceleration noise [40, 41, 42]. Other crucial concepts, like the handling of test mass cubes could be shown. LISA Pathfinder represents a major step in the development of LISA technology that has been ongoing for decades. The long-standing development of the LISA mission reached a climax in 2017, when it was selected by the European Space Agency (ESA) as its third large class mission, L3, with a currently foreseen launch date in 2034 [43]. The development and implementation of LISA technology continues, as the LISA project is currently in its Phase A. The work that is described in this thesis contributes to this undertaking.

1.3   Thesis structure

This thesis is split into two parts. The first part shows analysis of on-ground and in-orbit measurements in the context of the LRI on-board GRACE-FO. In the second part, technology development for future gravity missions, such as LISA and NGGM, is presented. Throughout this thesis, focus was laid on the respective laser interferometer's link acquisition mode. In **Chapter 2** an overview of key components of the LRI is given. The

need for an elaborate laser link acquisition mode is motivated and the chosen procedure is presented.

Chapter 3 then gives an overview of on-ground tests of the LRI's laser link acquisition mode. A realistic mock-up LRI and test equipment, that was originally designed for later testing of the LRI flight hardware, were used here.

The first part of this thesis is concluded by **Chapter 4**. Here, analysis of the as-run initial acquisition mode of the LRI is presented. From this analysis, pointing offset angles for each S/C were estimated that describe the misalignment of the LRI with respect to the line of sight (LOS). Identifying these angles was crucial before the laser link could be established. In the second part of this chapter, a trade-off analysis is presented that had the goal of optimizing the LRI ranging SNR by introducing small laser beam pointing offsets to compensate structural deficiencies of the LRI's triple mirror assemblies (TMAs).

Chapter 5 presents an experimental test bed that allows for end-to-end tests of intersatellite laser interferometers. Again, the focus was laid on enabling tests of the laser link acquisition mode of the respective instrument. Testing this mode is especially demanding, as spatial scans of the laser beams with frequencies $\sim$100 Hz are required for certain mission scenarios, e.g. GRACE-FO.

Different sensor types are investigated as possible dedicated acquisition sensors for LISA and NGGM in **Chapter 6**. In the LISA context, these sensors are referred to as *constellation acquisition sensor* (CAS). This chapter is concluded by a comparison of the analyzed sensors with each other as well as with alternative solutions.

Finally, in **Chapter 7** the presented results are summarized and a brief outlook towards future investigations is given.

Part I

Link acquisition and optimization for the GRACE Follow-On Laser Ranging Interferometer

Chapter 2

The GRACE Follow-On Laser Ranging Interferometer

In the first part of this chapter the Laser Ranging Interferometer (LRI) on-board of the GRACE-FO S/C is described. The LRI is a complex instrument, whose properties and functional principles have already been explained in detail in numerous other publications (e.g. [18, 44, 45, 46, 47] and many others). Therefore, this thesis only focuses on those properties of the LRI that are crucial for the understanding of its so-called *initial acquisition* mode. This operating mode is run at the beginning of the mission in the commissioning phase of the instrument and serves the purpose of finding angular offsets between the reference frames of the LRI sub-units on the two S/C. Furthermore, the set-points that determine the laser frequency on the two S/C are adapted as part of this procedure. This is necessary for numerous reasons which will be explained in the Sec. 2.2, where also a detailed description of the initial acquisition procedure is presented.

2.1 The Laser Ranging Interferometer

The LRI is an off-axis laser interferometer developed to track relative intersatellite distance changes between the two GRACE-FO S/C. Similar to the overall GRACE-FO project, the LRI was developed by a joint US/German team. The LRI team is made up of members of the JPL in the USA and the AEI in Germany. Partners from industry (SpaceTech GmbH (STI), Airbus Defense & Space, Cassidian Optronics GmbH) as well as the Deutsches Zentrum für Luft- und Raumfahrt (DLR) have been involved in the development, construction and operation of the LRI.

The LRI is a technology demonstrator that operates in parallel with GRACE-FO's main ranging instrument, the K/Ka band ranging instrument (KBR). Both instruments measure the same observable, variations of the intersatellite distance. The targeted resolution of the LRI in terms of ranging noise was $80\,\mathrm{nm}/\sqrt{\mathrm{Hz}}$ in a frequency range of $2\,\mathrm{mHz}$–$0.1\,\mathrm{Hz}$, approximately two orders of magnitude below the achieved noise performance of the KBR on the GRACE mission of a few $\mathrm{\mu m}/\sqrt{\mathrm{Hz}}$ [18, 10, 11]. Figure 2.1 shows a spectral

Figure 2.1: The figure shows the amplitude spectral density (ASD) of the LRI one-way ranging signal. The ranging noise requirement of $80\,\text{nm}/\sqrt{\text{Hz}}\times\text{NSF}$ is also shown. NSF stands for *noise shape function* and describes the relaxation of the requirement towards lower frequencies.
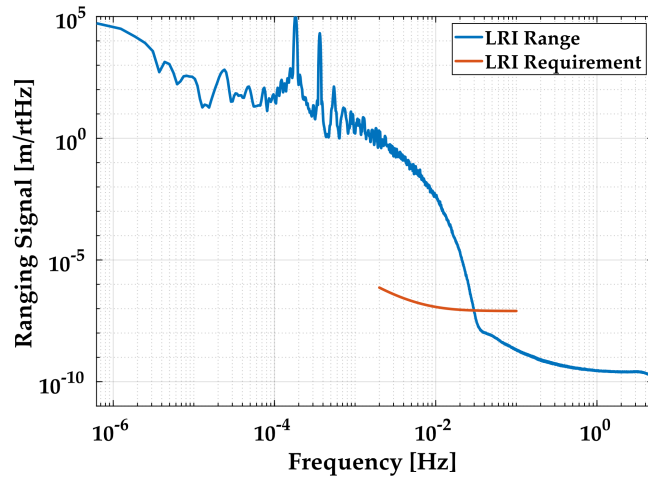
density plot of the measured LRI half-roundtrip range. The noise floor of the LRI range can currently not be evaluated for frequencies below about 40 mHz as the gravity signal is dominating the ranging signal in this frequency range. However, for frequencies above this value, the achieved noise level matches the laser frequency noise,. which is based on predictions from on-ground measurements. For frequencies above about 0.1 Hz, the obtained ranging noise is below $1\,\text{nm}/\sqrt{\text{Hz}}$.

The LRI performs its measurement of the intersatellite range in a so-called transponder scheme (see e.g. [44]). This requires that one S/C is operated as the *master*, where the signal of interest, the intersatellite range, is obtained from the interferometric signal, while the other S/C is set to the *transponder* (sometimes also called *slave*) role. This S/C only serves the purpose of enabling the above-mentioned measurement on the master S/C by transmitting light back to the master S/C. While the LRI hardware on both S/C is identical, these roles define how the LRI sub-units on each S/C are used. This provides redundancy for some components, as each role requires slightly different hardware and software functions. The roles can be swapped if required. This was done a few times during the commissioning phase of the instrument in order to properly calibrate all LRI sub-units.

2.1.1   Architecture of the LRI

The LRI is a heterodyne interferometer whose sub-units are split between the two GRACE-FO S/C, see Fig. 2.2. Each S/C carries an optical bench (OB), a so-called triple mirror assembly (TMA) which routes the laser beam around obstacles on the S/C that do not belong to the LRI, such as the KBR and cold gas tanks. Moreover, a laser, a cavity which is used on the master S/C as a frequency reference for the laser and a Laser Ranging Processor (LRP), which is the central processing unit of the LRI [48, 49], are present.

On the master S/C the LRP locks the local laser to the Fabry-Perot cavity using a Pound-Drever-Hall locking scheme [50]. This ensures a stability of the laser frequency below
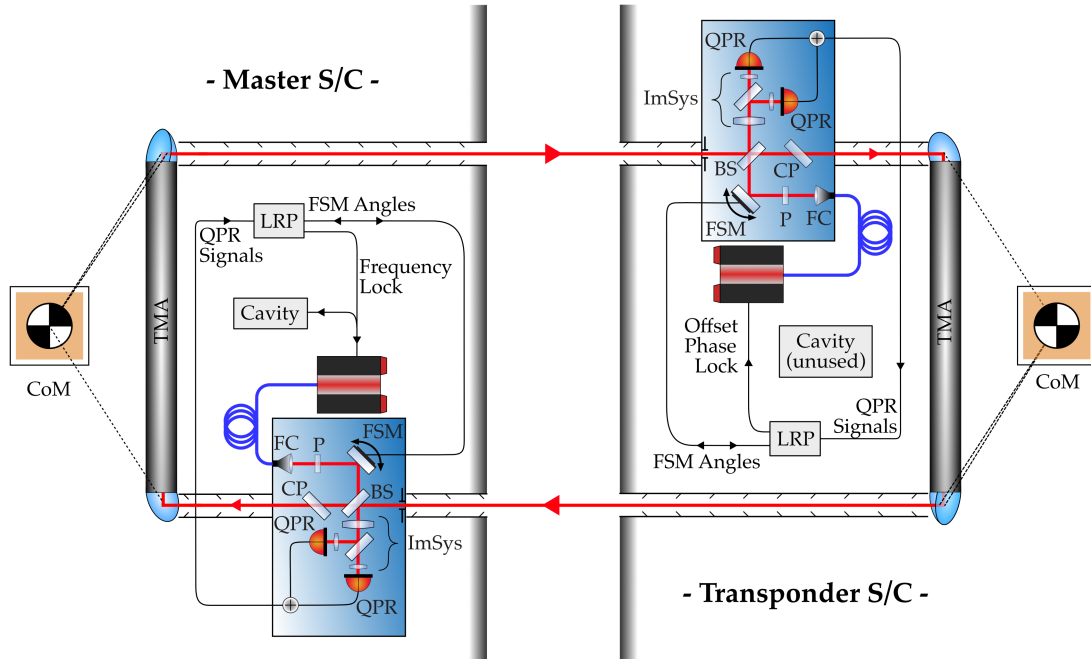
Figure 2.2: Schematic drawing of the LRI. CoM: Center of Mass, TMA: Triple Mirror Assembly, LRP: Laser Ranging Processor, FSM: Fast Steering Mirror, FC: Fiber Collimator, P: Polarizer, BS: Beamsplitter, CP: Compensation Plate, ImSys: Imaging System, QPR: Quadrant Photoreceiver.

$30\,\mathrm{Hz}/\sqrt{\mathrm{Hz}}$ in the required measurement frequency range of 2 mHz–0.1 Hz [18, 51, 49]. The laser is a non-planar ring oscillator (NPRO) with a wavelength of $\lambda = 1064\,\mathrm{nm}$, manufactured by Tesat Spacecom GmbH. The output power is adjustable between 20 mW and 30 mW [49]. The LRP's most important function is to track the phase of an interferometric signal. Due to the S/C dynamics, these signals have frequencies in the low MHz range. The LRP digitizes them with the help of analog to digital converters (ADCs) and then tracks the signals with so-called digital phase locked-loops (dPLLs). A dPLL is a closed-loop controller which adjusts the phase of a digitally created signal to match the phase of the input signal, enabled by the so-called I/Q-demodulation (see e.g. [52]). Here, these are the MHz beat note signals. Thereby, the I-part of the signal is proportional to the amplitude of the input signal and the Q-part is its quadrature component, which should be zero if the dPLL has infinite gain and bandwidth. Therefore, the digital replica is exactly $90°$ out of phase with respect to the input signal being tracked. The phase information of the interferometer signal is henceforth available in the digital domain where it can be stored and processed. As the tracking of an interferometric phase is the key function of devices like the LRP, they are usually also referred to as *phasemeters*.

As these terms will be used throughout this thesis, the distinction between local oscillator (LO), transmitted (TX) and received (RX) beams should be made clear. The term LO is used in the context of heterodyne interferometers, like the LRI, to describe a local reference beam whose phase is stable with respect to the interferometer.

The RX beam is the beam that is received by a S/C which is then interfered with the LO on a beamsplitter. Especially in the presence of a weak RX laser beam a higher power

LO is helpful, as the resulting amplitude of the interference signal is scaled by the square root of the optical power levels of both input beams. The superposition of the light fields contains the sum and the difference of the two input beams' frequencies. However, as the frequency of a laser beam with $\lambda = 1064\,\text{nm}$ is $f \approx 280\,\text{THz}$, the sum of the frequencies is not observable by the opto-electronic components. Thus, only the difference frequency is measured, which is referred to as the *beat note* signal. As the phase of the LO can be considered constant, the phase of this beat note signal yields information on the phase of the RX beam. The part of the LO that is reflected off the beamsplitter, is henceforth referred to as the TX beam. The TX beam leaves the OB after passing through a compensation plate (CP). This is made from the same material as the recombination beamsplitter and suppresses to first order coupling of rotations of the S/C into the interferometric phase, caused by the beamsplitter. This dependency is referred to as *tilt-to-(path)length* (TTL) coupling [18]. The TMA then redirects it in the direction of the distant S/C.

On its way from the master to the transponder S/C, the laser light experiences a one-way Doppler frequency shift due to the relative motion of the S/C. The transponder offset phase-locks its local laser to the RX beam and sends it back to the master S/C. This active transponder scheme is necessary as the laser power at the transponder S/C is already in the pW to nW range and is, hence, too low to be passively reflected back to the master S/C. Neglecting second-order corrections, the one-way Doppler shift can be approximated by

$$f_D \approx -\frac{v_{rel}}{\lambda}, \tag{2.1}$$

with v_{rel} being the relative velocity of the S/C along the line of sight (LOS). Thereby, the LOS is defined by connecting the center of mass (CoM) of the two S/C by a straight line. As was already mentioned, the transponder S/C now phase-locks its local laser to the received beam with an offset f_o. Making the reasonable assumption that the dPLL on the transponder S/C has a high enough gain to properly follow the frequency of the RX beam, the transponder laser frequency is thus:

$$f_t = f_m + f_D + f_o \tag{2.2}$$

with the stabilized master frequency f_m. The beat note frequency on the transponder S/C is therefore simply:

$$\begin{aligned} f_{b,t} &= |f_t - f_{RX,t}| \\ &= |(f_m + f_D + f_o) - (f_m + f_D)| \\ &= f_o. \end{aligned} \tag{2.3}$$

As the relative acceleration of the two S/C is comparably low, one can approximate that the frequency of the RX beam on the master S/C experiences the same Doppler shift twice.

The frequency of the RX beam on the master S/C can thus be expressed as:

$$
\begin{aligned}
f_{RX,m} &= f_{TX,t} + f_D \\
&= (f_{TX,m} + f_D + f_o) + f_D \\
&= f_{TX,m} + f_o + 2f_D,
\end{aligned}
\tag{2.4}
$$

with $f_{TX,t/m}$ the frequency of the TX beams. As the TX and LO beam of each S/C have the same frequency, one can omit the different abbreviations and simply refer to the *master frequency* $f_m = f_{TX,m} = f_{LO,m}$ (and of course vice versa $f_t = f_{TX,t} = f_{LO,t}$ for the transponder). The beat note frequency on the master S/C, where the LO and the RX beam are interfered, thus becomes

$$
\begin{aligned}
f_{b,m} &= |f_m - f_{RX,m}| \\
&= |f_m - (2f_D + f_m + f_o)| \\
&= 2f_D + f_o.
\end{aligned}
\tag{2.5}
$$

Thus, the intersatellite range can be derived from the phase of the beat note between LO and RX beams on the master S/C alone. As was already mentioned, the need for an *active* transponder S/C is only given because the laser power that would be sent back to the master S/C by a *passive retroreflector* would be too low to be detectable. Another benefit of the chosen architecture with two identical S/C is the redundancy that this scheme offers. Additionally, the frequency offset of the transponder dPLL allows for the distinction of a motion of the S/C towards and apart from each other, without the need to keep track of zero crossings of the beat note phase. An offset frequency of the dPLL on the transponder S/C of $f_o = 10\,\text{MHz}$ was chosen. As was already mentioned, typical maximum relative velocities of the GRACE-FO S/C are on the order of $\pm 0.5\,\text{m/s}$. Hence, from using Eqs. (2.1)–(2.3) it follows that the one-way Doppler shifts are $f_D \approx \pm 0.5\,\text{MHz}$ and the beat note frequency on the master S/C therefore ranges from about 9.5 MHz to 10.5 MHz.

2.1.1.1 The optical benches

On each optical bench (OB) the local oscillator (LO) is generated by a monolithic fiber collimator (FC) (see Fig. 2.2). To ensure a clean polarization state, it is filtered with a polarizer. The RX beam is clipped at an aperture on the OB with 8 mm diameter. The two beams are then interfered on a recombination beamsplitter. The interferometric phase of the resulting beat note signal is read out by a pair of two hot redundant quadrant photoreceivers (QPRs). A system of two lenses is used to simultaneously image the RX aperture and the pivot point of the fast steering mirror (FSM) onto the active sensor area of the QPRs. This is possible because the FSM and the aperture have the same distance with respect to the recombination beamsplitter and thus also the imaging system. Hereby, diffraction of the RX beam, which is clipped on the circular aperture, as well as beamwalk
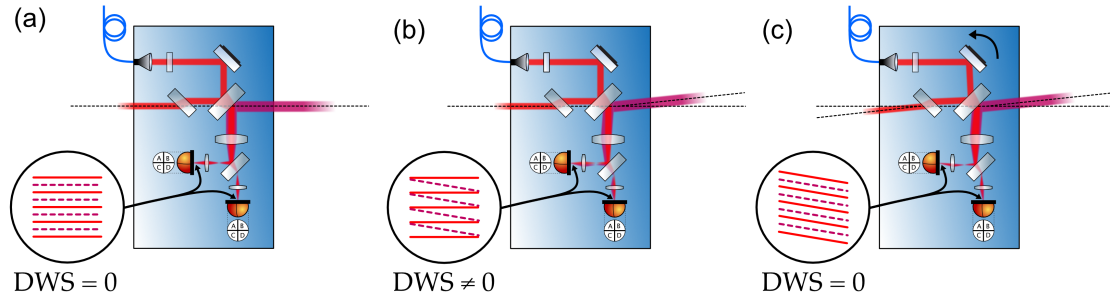
Figure 2.3: Illustration of the functionality of the DWS control loop. The inlay circles show the current relative tilt of the wavefronts. (a) LO and RX beams are aligned – zero DWS signal, (b) The RX beam is tilted which leads to a relative tilt of the wavefronts and a non-zero DWS signal, (c) The DWS signal was zeroed by tilting the LO beam with the FSM.

of the laser beams on the QPRs are suppressed. At the same time, the imaging system enhances the angle of incidence of the laser beams and reduces the beam diameters to the diameter of the QPR of about 1 mm. A hot redundant pair of QPRs is used because their functionality is of course of highest criticality to the success of the LRI. The imaging system is therefore extended by a second output port by splitting the beam within the imaging system with an additional beamsplitter and adding a second lens in front of the redundant QPR.

Within this thesis, the term *photodiode* (PD) is used to describe a semiconductor device that converts light into a proportional electrical current, based on the internal photoelectric effect [53]. A *quadrant photodiode* (QPD) is a PD with four equally sized segments that are separated by a small gap. For a QPD with 1 mm diameter, typical gap widths are on the order of a few ten μm (e.g. [54]). The photocurrent that is produced by a PD, is amplified and converted into a voltage by a *transimpedance amplifier* (TIA). The combination of a PD, or QPD, and a TIA is referred to as *photoreceiver* (PR), or *quadrant photoreceiver* (QPR).

The average phase of the four segments of a QPR yields the longitudinal path length signal of the beat note. However, also the relative tilt of the phasefronts of the beams that impinge on the QPR is of interest. This is encoded in a combination of differences of the QPR phases. This technique is called differential wavefront sensing (DWS) [55], It is used in the LRI to determine the relative tilt of the LO and the RX beams. A DWS control loop, which runs on the LRP, ensures that the tilt between these two beams is minimized during normal operations of the LRI. This is required to keep the laser beams of the two S/C aligned at all times. Figure 2.3 shows the functional principle of this DWS control loop. If local and received beams are aligned, the DWS signal is zero (sub-figure (a)). If then a small misalignment between RX beam and LO occurs, e.g. due to S/C attitude jitter, their wavefronts will not be parallel anymore which results in a nonzero DWS signal (sub-figure (b)). This signal is processed by the LRP, which then commands the FSM, which controls the angle of the LO such that the wavefronts of the beams are aligned (sub-figure (c)). Now both, LO and RX beam, are aligned again and share a relative angle with respect to the nominal FSM orientation, which compensates the S/C attitude. On ground it was shown that a residual misalignment between LO and RX beams on the order of $\pm 10\,\mu\mathrm{rad}$,

with a stability of $10\,\mu\text{rad}/\sqrt{\text{Hz}}$ in the GRACE-FO measurement frequency band could be achieved [47, 56].

The recombination beamsplitters introduce angle of incidence dependent, longitudinal phase shifts of laser beams that pass through them. In order to partially compensate this effect, CPs were implemented on each OB (see Fig. 2.2)

As was derived in the previous section, the beat note signals have frequencies around 10 MHz. The QPRs and all subsequent electronics must thus be designed for this frequency range. The QPRs used on the OBs are made from indium gallium arsenide (InGaAs). For laser radiation with a wavelength of $\lambda = 1064\,\text{nm}$, this material provides a high conversion of photons to electrons. This property is called *responsivity* and is $\rho_{PD} \approx 0.7\,\text{A/W}$ for InGaAs [57]. The photocurrents are amplified and converted to voltages by so-called TIAs. In the case of the LRI the TIAs split the photocurrents into their DC and AC components and amplify the signals with custom amplifier stages. The AC component of these amplifiers shows a passband of 4–16 MHz.

Laser beam properties

As the LOs are well approximated by Gaussian beams, a few parameters will be introduced to describe the properties of these laser beams. The divergence of a Gaussian laser beam is given by [58]:

$$\theta = \frac{\lambda}{\pi w_0} \tag{2.6}$$

with w_0 the waist radius of the beam and λ its wavelength. The beam spot radius at a distance z from the waist position is given by [58]:

$$w(z) = w_0 \sqrt{1 + \left(\frac{z}{z_0}\right)^2}, \tag{2.7}$$

with z_0 being the Rayleigh range of the beam [58]:

$$z_0 = \frac{\pi w_0^2}{\lambda}. \tag{2.8}$$

The radius of curvature of the wavefronts as a function of the distance to the waist position is given by [58]:

$$R(z) = z \left(1 + \left(\frac{z_0}{z}\right)^2\right) \approx z \quad (\text{for } z \gg z_0). \tag{2.9}$$

The intensity distribution of a laser beam that propagates along the z-direction, expressed as a function of the radial distance r from the center axis of the beam, is described by [59]:

$$I(r,z) = |E(r,z)|^2 = I_0 \left(\frac{w_0}{w(z)}\right)^2 \exp\left(\frac{-2r^2}{w(z)^2}\right) \tag{2.10}$$

with I_0 the maximum intensity of the beam at $r = z = 0$. The power of a laser beam within

an aperture of radius r_{ap}, that is centered around the central axis of the beam, is obtained
by integrating Eq. (2.10) over a circle of radius r_{ap}, resulting in:

$$P_{\mathrm{ap}} = \frac{1}{2} I_0 \pi w_0^2 \left[1 - \exp \left(\frac{-2r_{\mathrm{ap}}^2}{w^2(z)} \right) \right]. \tag{2.11}$$

It was assumed that the aperture is oriented perpendicularly to the optical axis and is
placed at the longitudinal position z. The constant terms can be summarized to express
the total optical power of the beam:

$$P_0 = \frac{1}{2} I_0 \pi w_0^2. \tag{2.12}$$

For $w(z) \gg r$, the dependency of the intensity distribution from Eq. (2.10) on r can be
neglected. The power of a laser beam within a circle of radius R, whose center is located
at z and $r = 0$, can then be approximated as:

$$P(r,z) \approx \pi R^2 \cdot I(r,z). \tag{2.13}$$

Using Eq. (2.10) and Eq. (2.12), the approximation $w(z) \approx \theta z$, and expressing the radial
distance to the center axis of the beam, r, by two angles, α and β, as $r = \sqrt{\alpha^2 + \beta^2} \cdot z$, the
beam power within a circle of radius R can be expressed as:

$$P_R (\alpha, \beta) \approx \frac{2P_0}{\pi z^2 \theta^2} \exp \left(\frac{-2 \left(\alpha^2 + \beta^2 \right)}{\theta^2} \right) \pi R^2. \tag{2.14}$$

It can be shown that for $\alpha = \beta = 0$, $R = r_{ap} \ll w(z)$ and by expressing Eq. (2.11) by its
Taylor series, Eq. (2.11) and Eq. (2.14) coincide.

In the case of the LRI, the LO beams can be well approximated by Gaussian laser beams
with a waist radius of $w_0 \approx 2.5\,\mathrm{mm}$ that is located on or close to the respective OB.
Their Rayleigh range is thus $z_0 \approx 18.5\,\mathrm{m}$. The optical power of the LOs at the beginning
of the mission is about $P_{LO} = 25\,\mathrm{mW}$. The beamsplitter on the OB has a reflectivity
of $R = 90\,\%$. If ideal coatings of the remaining components in the optical path of the
LO/TX beam are assumed, the optical power of the TX beam leaving the satellite becomes
$P_{TX} = 0.9 \cdot P_{LO} = 22.5\,\mathrm{mW}$.

The approximation made in Eq (2.9) holds for the LRI as the S/C separation ranges
between 170 km and 270 km which is much greater than the Rayleigh range of the LO
beams. The RX beams can therefore be described to good approximation as having
spherical wavefronts with a radius of curvature of $R(z) \approx z = 170 \ldots 270\,\mathrm{km}$ with the
center of the curvature located inside or at least close to the transmitting S/C. Depending
on the intersatellite distance, the Gaussian beam radii range between $\sim$20 m and $\sim$35 m.

Using Eq. (2.11), the corresponding maximum power received by a S/C can be calculated.
The obtained values range between $P_{RX} \approx 1.4\,\mathrm{nW}$ and 500 pW, with an aperture radius of

$r_{ap} = 4\,\text{mm}$ and for $z = 170\,\text{km}$ and $z = 270\,\text{km}$, respectively. The divergence of the TX laser beam roughly corresponds to the LRI field of view (FoV). Using Eq. (2.6), it follows as:

$$\theta \approx 135\,\mu\text{rad}. \tag{2.15}$$

Derivation of the carrier-to-noise density (C/N$_0$)

A figure of merit to describe signal strengths, which is often used in satellite-related applications, is the carrier-to-noise density (C/N$_0$). It is often expressed in units of dBHz and is defined by the ratio of the squared root mean square (rms) heterodyne amplitude to the noise spectral density. Hereby, the noise must be evaluated within a small range around the Fourier frequency at which the amplitude was measured. This definition of the C/N$_0$ can be very helpful in judging the performance of a phase measurement system, such as the LRP, as the inverse of the C/N$_0$ directly provides the phase readout noise. For the one-way ranging signal of the LRI this property was shown in Fig. 2.1. The dominant additive noise sources are briefly explained in the following paragraphs. First, all noise terms are expressed for the individual segments of the QPR. Later, they are properly summed up to give an expression for the whole PR.

For all the calculations that are presented in the next paragraphs, the noise terms are treated as white noise in the frequency range of interest of approximately 4–16 MHz. Laser intensity noise falls with a slope of $1/f$. However, this is only dominating in the kHz and low MHz range. For frequencies above 3 or 4 MHz, laser intensity noise can be considered as white. The electronic noise of the QPR increases towards higher frequencies, but also this is only dominant above a few dozen MHz [45, 60]. Shot noise can in fact be considered frequency independent [61].

The **electronic noise of a PR** is the noise in absence of a beat note at the PR output in units of $\text{V}/\sqrt{\text{Hz}}$. Using the PR transfer function and the TIA gain, it is often expressed as input-referred current noise (ICN) in units of $\text{A}/\sqrt{\text{Hz}}$. The power spectral density (PSD) of this noise term is then obtained by squaring the ICN:

$$\tilde{S}_{e,s}^2 = \text{ICN}^2. \qquad [\text{A}^2\,\text{Hz}^{-1}] \tag{2.16}$$

The **shot noise**, however, is proportional to the square-root of the optical power on the QPR [62]:

$$\tilde{S}_{s,s}^2 = 2\,q_e\,\rho\,(P_{\text{LO,s}} + P_{\text{RX,s}}) \approx 2\,q_e\,\rho\,P_{\text{LO,s}}. \qquad [\text{A}^2\,\text{Hz}^{-1}] \tag{2.17}$$

Here, q_e is the elementary charge and ρ is the responsivity of the PD. Since $P_{\text{RX,s}}$, the RX power on one segment, is many orders of magnitude lower than $P_{\text{LO,s}}$, the LO power per segment, it can be neglected for the calculation of the shot noise.

The last noise term is the **relative intensity noise (RIN)** of the laser. As the name suggests, this property is referred to the applied optical power of the laser. The PSD of this noise

expression is:

$$\tilde{S}_{i,s}^2 = \left(\rho \left(P_{\text{LO,s}} + P_{\text{RX,s}} \right) \text{RIN} \right)^2 \approx \left(\rho \, P_{\text{LO,s}} \, \text{RIN} \right)^2. \quad [\text{A}^2\,\text{Hz}^{-1}] \quad (2.18)$$

As done before, the comparatively low RX power can be neglected.

The overall noise of the QPR is obtained when one takes into account that the RIN is correlated between the segments, while the other two noise sources are not. For N segments, the coherent sum of the noise sources is described by the following expression:

$$\tilde{n}_{cs}^2 = N(\tilde{S}_{e,s}^2 + \tilde{S}_{s,s}^2) + N^2 \tilde{S}_{i,s}^2. \quad [\text{A}^2\,\text{Hz}^{-1}] \quad (2.19)$$

The peak amplitude of the interferometric signal is called heterodyne amplitude. It is defined as [46]:

$$A_{\text{c}} = \rho \, G \left(f_b \right) \sqrt{P_{\text{LO}} P_{\text{RX}} \eta}. \quad [\text{A}] \quad (2.20)$$

$G(f_b)$ is the gain of the TIA at the beat note frequency f_b. η is the heterodyne efficiency, a value between 0 and 1 which describes the overlap of the LO and RX beams. It is defined as the normalized overlap integral of the two interfered electromagnetic fields. More details about the calculation of η in the context of GRACE-FO can be found in [46].

In the tests described in this document, all signals are recorded in units of digital counts. Taking into account the ADC bit depth and the TIA gain, the heterodyne amplitude can be converted from digital counts to units of ampere. The C/N_0 s then defined by the ratio of the squared rms heterodyne amplitude to the coherent sum of the noise PSD [46]:

$$C/N_0 = 10 \cdot \log_{10} \left(\frac{A_{\text{c}}^2/2}{\tilde{n}_{cs}^2} \right). \quad [\text{dB Hz}] \quad (2.21)$$

2.1.1.2   The Triple Mirror Assembly

After the TX beam leaves the OB, a so-called triple mirror assembly (TMA) directs it to the distant S/C. As the name suggests the TMA consists of three perpendicular mirrors which form a retroreflector [63]. In particular they form a *virtual* retroreflector. This attribute accounts for the fact that only those parts of the mirrors that actually reflect the beam are physically present. Thus, the intersection point of the three mirror surfaces, the so-called TMA vertex, is *virtual*. Under rotations around the vertex, ideal retroreflectors have three important properties that are useful for the LRI:

  I The lateral beam separation of incoming and outgoing beam remains constant.
 II The round-trip path length is preserved. This is twice the distance between the vertex and an arbitrary reference plane.
III Incoming and outgoing laser beams are anti-parallel.

In the case of GRACE-FO a lateral beam offset of 60 cm is required in order to route the beam around components on the S/C such as the KBR antenna and cold gas tanks.

The preservation of the round-trip path length is another benefit of the TMA that is of high importance to the LRI. It implies that by placing the TMA virtex in the CoM of the S/C, the LRI directly measures the range between the two CoM of the S/C. The KBR in contrast has a rather long level arm of more than 1 m which requires thorough calibration [64, 65].

The TMA property **III** in combination with the DWS control loop ensures that the TX laser beams always hit the distant S/C. This is because the DWS control loop ensures that the LO beam stays aligned to the RX beam, even under rotations of the S/C. The special architecture of the OB then makes sure that the TX beam that leaves an OB is also parallel to the RX beam. The TX beam then hits the TMA and its above-mentioned property **III** ensures that the angle of the outgoing TX laser beam is anti-parallel to the in-going beam which means that it is aligned with the RX beam.

All this is valid for an ideal TMA. However, as the TMA is subject to manufacturing tolerances and other effects, it will inevitably show small deviations from these properties. In Sec. 4.2 a detailed analysis of a specific TMA imperfection, the so-called co-alignment error (CAE), is presented. Additionally, a trade-off study is shown which had the goal of minimizing the effect of the CAE.

2.2   The initial laser link acquisition procedure

After enabling the LRI, the intersatellite laser link needs to be established. Fabrication tolerances of the LRI sub-units and tolerances during their integration into the S/C structure, violent vibrations during launch, the transition from 1 g to 0 g and settling effects cause an unknown offset angle between the LRI reference frame and the LOS. Thereby, the LOS is defined by a straight line that connects the CoM of the two S/C. Additionally, the S/C attitude, which is measured by star trackers, is only known with a finite accuracy. All these contributions exceed the required pointing accuracy of the LRI of better than 135 µrad with respect to the LOS. This maximum misalignment angle is defined by the smallest possible optical power level that is still detectable by the LRI.

The LRI needs to carry out spatial calibration scans, in order to identify these unknown offset angles. This initial laser link acquisition, or simply *initial acquisition*, procedure is a simultaneous scan of five degree of freedom (DoF): Two laser beam angles per S/C and the frequency of the laser on the transponder S/C. The spatial scans are required to find the misalignment of the S/C with respect to the LOS. The additional frequency scan is needed because the laser frequencies of the master and transponder S/C must match to within the QPR bandwidth. As it will be shown in this section, all these DoF must be within narrow ranges of their required values *at the same time* at least once during these scans in order to obtain interferometric signals on both S/C.

To illustrate this, the AC photocurrent of a single segment of a QPR is presented [46]:

$$i_s^{AC}(t) \propto \rho_{PD} \cdot \sqrt{P_{LO,s} \cdot P_{RX,s}(\alpha_{TX}, \beta_{TX}) \cdot \eta_s(\alpha_{LO}, \beta_{LO}, \alpha_{RX}, \beta_{RX})} \cdot \cos(w_b t + \phi_s). \quad (2.22)$$

For simplicity, this approximation neglects all DC components as well as overall scaling factors. $P_{LO,s}$ and $P_{RX,s}$ describe the LO and RX power per segment, ρ_{PD} is the PD's responsivity, $w_b = 2\pi f_b$ is the angular heterodyne beat note frequency and ϕ_s is the phase of the segment. η_s is the heterodyne efficiency that was already introduced in Eq. (2.20). As is denoted above, for a given scenario, e.g. the GRACE-FO mission with a Gaussian beam with fixed waist size as LO and a clipped top-hat beam as RX beam, η_s is a function of the relative LO and RX beam angles. It is maximized for $(\alpha_{LO}, \beta_{LO}) = (\alpha_{RX}, \beta_{RX})$. As described in Sec. 2.1.1.1, the RX beams have spherical wavefronts. Thus, the RX beam angle corresponds to the relative tilt of the local S/C with respect to the LOS. Therefore, without loss of generality it can be stated that η_s is maximized if the LO angles compensate the misalignment of the local S/C with respect to the LOS.

From Eq. (2.22) it directly becomes clear that both OBs detect signals simultaneously, once both FSMs have compensated the local misalignments to the LOS. If a signal is detected, the LOs must have been aligned to the respective RX beam, which means that both TX beams are automatically aligned to the LOS (see Sec. 2.1.1.2). Of course a signal is only detectable if also the beat note frequency was within the QPR bandwidth. That is why the initial acquisition procedure does not require any communication between the S/C. The FSM angles and the transponder laser frequency set-point must only be recorded on both S/C as soon as an interferometric signal is detected. These recorded values are the searched for offsets. For this depiction it was assumed that the TMAs are ideal. Non-ideal TMA properties lead to the already mentioned angular offsets between RX and TX beams that will be addressed in Sec. 4.2.

The next section provides more details on the spatial scans that are performed by the transponder and the master S/C. Thereafter the frequency scan on the transponder is explained as well as the chosen order, or hierarchy, of the scans. A brief overview of the processing of the interferometric signal is given before this chapter is concluded by an overview of the sequence of events during initial laser link acquisition.

2.2.1   Spatial scans

Figure 2.4 illustrates the spatial part of the initial acquisition scans. As was already explained, several effects lead to an unknown angular offset of the estimated LOS and the true value. Thereby, the estimation errors are too large in order for the LRI to obtain an interferometric signal. The linear sum of all uncertainties yields a total value that is just below 3 mrad [66]. Thus, the spatial scans in the initial acquisition phase have amplitudes of 3 mrad [67]. Both S/C center the FSM scans around best estimates of the LOS, which are determined via GPS data and orbit information.
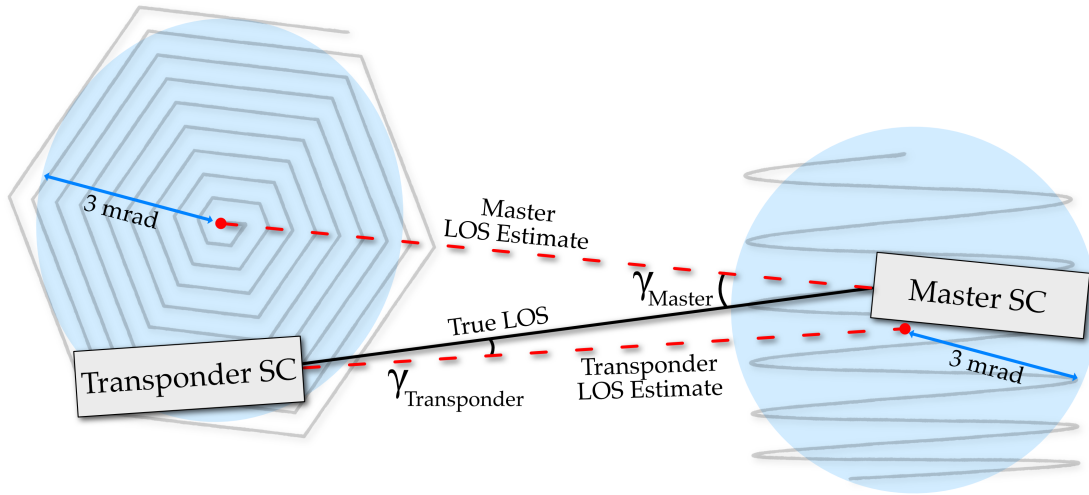
Figure 2.4: Schematic drawing of the spatial component of the initial acquisition scan for GRACE-FO. The true LOS is defined by connecting the two S/Cs' CoM with a straight line. Each S/C produces a LOS estimate, which is based on GPS data and orbit information. The FSM scans are centered around these axes.

The FSM on the master S/C scans the LO along a hexagonal pattern with an amplitude of $A_H = 3$ mrad (see the left panel of Fig. 2.5). The distance between adjacent scan lines, the *grid spacing*, was set to 200 µrad so that the maximum distance from the scan track to the true LOS, the *grid error*, does not exceed 100 µrad. This value was derived by evaluating the allowable minimal SNR of a possible detection (cf. [46, 66]). The transponder S/C commands its FSM to scan a Lissajous pattern with the same $A_L = 3$ mrad amplitude. In contrast to the discrete hexagonal scan steps that the master follows, this is a continuous pattern which is generated by sinusoidal oscillations of both FSM axes (see the right panel in Fig. 2.5). The FSM motion should be considered quasi-continuous, as the angles are stored as discrete steps in digital look-up tables (LUTs). However, the separation of the scan steps is much finer than for the hexagonal scan. The yaw axis is scanned with $f_{L,f} = 100$ Hz while the pitch axis scans at $f_{L,s} \approx 1.8$ Hz. The corresponding grid error is also 100 µrad.

2.2.2 Frequency scan

The LRP on the transponder S/C scans the frequency of the local laser while the master laser is locked to its cavity. The frequency offset between the master and the transponder is mainly caused by temperature effects on the laser and the cavity. A scan range of 360 MHz was chosen based on ground calibrations and expected in-orbit variations. The slope of this linear scan is $\frac{df}{dt} \approx 11$ kHz/s.
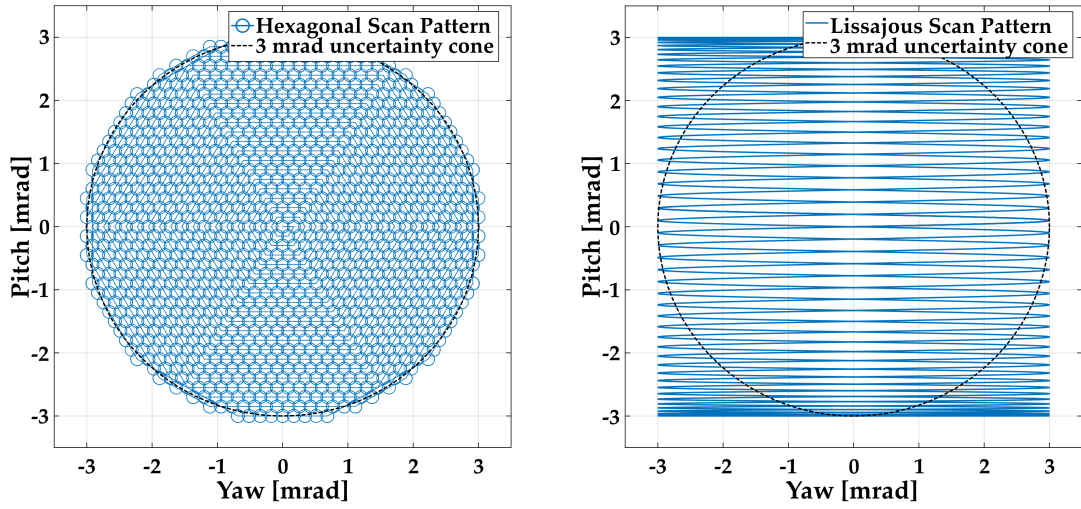
Figure 2.5: The figures show the discrete hexagonal scan pattern (left) and the Lissajous pattern with $f_{\text{L,s}} \approx 1.8\,\text{Hz}$ and $f_{\text{L,f}} = 100\,\text{Hz}$ (right).

2.2.3   Hierarchy of the scans

As was already mentioned, it is crucial that all five DoF match to within certain acceptable ranges at the same time. Therefore, a special hierarchy of nested scans was developed which ensures that this condition is met at least once during the whole procedure. Figure 2.6 shows the order of the scans. The frequency scan on the transponder S/C is a simple linear ramp with a slope of approximately $11\,\text{kHz/s}$. Each frequency point is only covered once. It is this scan that determines the total time required for the initial acquisition procedure of $360\,\text{MHz}/11\,\text{kHz/s} \approx 9\,\text{hrs}$. The frequency scan can be considered the outermost scan in the nested scanning procedure.

The slope of the frequency scan was chosen such that the resulting beat note frequency remains in band of the QPRs for one complete spatial scan of the master S/C. The scan on the master S/C is a discrete hexagonal scan with 1200 scan steps, each of which is held for $T_{\text{H,i}} = 0.56\,\text{s}$. Thus, the total scan time of this scan amounts to $T_{\text{H,tot}} = 1200 \cdot 0.56\,\text{s} \approx 11\,\text{min}$. Hence, the hexagonal pattern is repeated $9 \cdot 60\,\text{min}/11\,\text{min} \approx 49$ times.

The scan on the transponder S/C was derived by demanding that one complete transponder scan is finished within one scan step of the master. Therefore, the frequency of the slow axis of the Lissajous scan was chosen such that $T_{\text{L,s}} = T_{\text{H,i}}$. Thus, $f_{\text{L,s}} \approx 1.8\,\text{Hz}$. The frequency of the fast axis was defined as $f_{\text{L,f}} = 100\,\text{Hz}$ by making a compromise between the power dissipation of the FSM, execution speed of the scan and update rate of the readout of the interferometric signal.

With this hierarchy of the scans it is ensured that the frequency difference between beginning and end of one master scan is within the QPR bandwidth of 4–16 MHz: $11\,\text{min} \cdot 11\,\text{kHz/s} \approx 7.3\,\text{MHz}$. This, together with the fact that one complete Lissajous
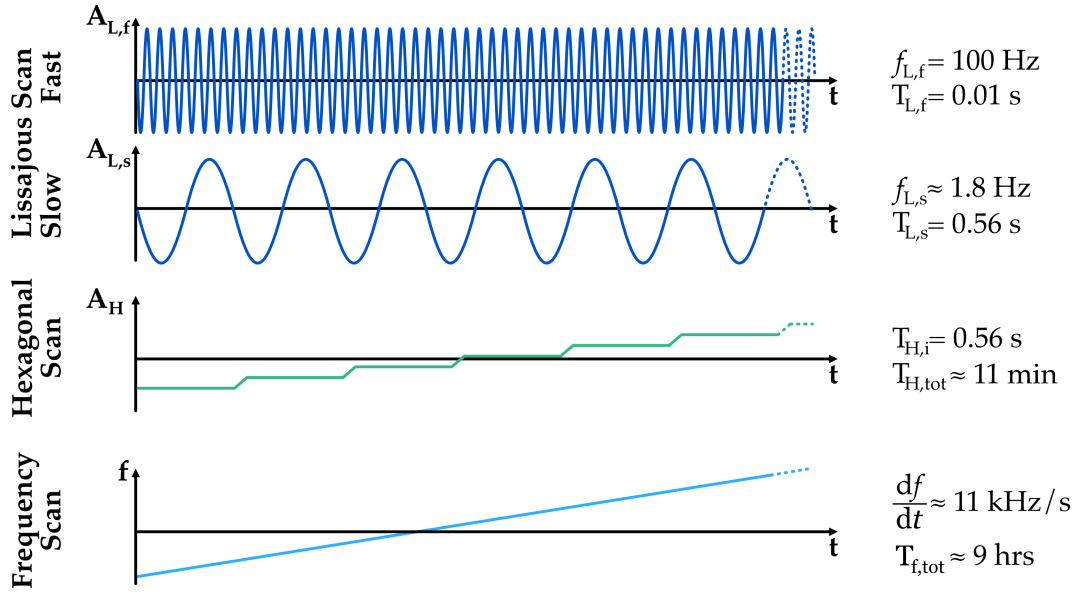
Figure 2.6: The figure shows an overview of the hierarchy of the different scans together with their key parameters. The shown scan steps and frequencies are not drawn to scale.

scan is performed for each hexagonal scan step, ensures that the interferometers on both GRACE-FO S/C at least once during the $\sim 9\,\mathrm{h}$ scan each detect a signal.

2.2.4 FFT readout of the interferometric signal

While the spatial and frequency scans are performed, each LRP continuously calculates an fast Fourier transform (FFT) of the interferometric signal. The sampling rate is $f_s = 39\,\mathrm{MHz}$ and the FFT length is 4096 points. The FFT algorithm evaluates the so-called *coherent sum* of all QPR channels. As was mentioned before, each OB hosts two hot redundant QPRs. That means that two corresponding segments are added in the analog regime before they are forwarded to the LRP. The sum of each pair of segments is referred to as a *QPR channel*.

The coherent sum of these channels is obtained by adding the complex amplitudes, thus taking into account their phase. In contrast to this, for the calculation of the incoherent sum the phases are not considered (see Sec. 4.2.1.2). Both methods have advantages and disadvantages. The coherent sum was chosen for the evaluation during initial acquisition because it shows a higher amplitude at the center of the distribution which is generated if two interfered wavefronts are tilted with respect to each other. Additionally, the coherent sum drops faster than the incoherent sum for relative beam tilts. This allows for better localization of the center of the distribution. More details on this matter in the context of GRACE-FO can be found in [46].

2.2.5 Initial acquisition sequence of events

The initial acquisition scans are scheduled from ground. At a defined starting time, the S/C synchronously start the spatial and frequency scans. While these scans are executed the LRPs continuously calculate FFTs of the interferometric signals. For the majority of the scanning time, no signals are present. If, however, the laser beam angles and the transponder laser frequency are within the optimal range, a beat note signal emerges. If the amplitude of this signal is above a defined threshold, the FFT frequency and amplitude at the peak, both FSM angles, the transponder laser frequency and a time-tag are stored by the LRP. After the complete parameter space was scanned, which takes about 9 hrs, these data sets are sent to Earth where they are then manually processed. Estimates of the offset angles and frequency are then calculated in post-processing and uploaded to the S/C. As the uncertainties of the angles and the frequency have small components which can vary with time (e.g. temperature dependent effects), the S/C then perform a set of autonomous scans, which are very similar to the initial acquisition scans, but with much smaller parameter space.

This operating mode is the so-called *re-acquisition* state. Due to the much reduced parameter space, e.g. the amplitude of the spatial scans is reduced by a factor of 10 to 300 µrad, this process nominally takes only a few seconds. If, however, special conditions occur, e.g. blinding of the LRI by the sun, the re-acquisition state could also last for longer time spans. The re-acquisition state machine is defined such that the LRI tries to automatically lock the DWS and dPLL loops as soon as an interferometric signal is found above a certain threshold. If no lock can be acquired, the instrument continues the scans in the re-acquisition mode. This is the default state to which the instrument transitions if any interruptions of the interferometric link occur.

If all control loops are successfully locked and the phase of the interferometric signal is tracked the instrument is in the so-called *science mode*.

Chapter 3

Simulations and experimental demonstration of LRI laser link acquisition

This chapter gives an overview of previous work on the topic of laser link acquisition for the GRACE-FO Laser Ranging Interferometer (LRI). In Sec. 3.1 simulations of the initial acquisition procedure in the LRI context as well as its first experimental demonstrations are presented. This work was done in the development phase of the LRI and had the goal of identifying promising initial acquisition procedures and validating these with laboratory experiments. Section 3.2 then presents a detailed description of tests of the final initial acquisition procedure that were carried out within this PhD project. The experimental setup made use of realistic replicas of LRI sub-units and a complex setup to simulate the intersatellite laser link. The obtained results confirmed the simulations and the previous experiments, which are explained in the first section of this chapter and provided valuable insights to the LRI project team.

3.1 Previous work on LRI laser link acquisition

During his PhD work, that he carried out at the AEI, Christoph Mahrdt developed the underlying concepts of the initial and re-acquisition algorithms that were later used by the GRACE-FO LRI [46]. Behind the RX apertures on the OBs, the RX laser beams are well approximated by top-hat laser beams. Such beams cannot realistically be described by Gaussian intensity distributions. In order to better simulate the RX beam properties (mainly the mentioned distribution of the intensity), C. Mahrdt developed a *mode-expansion method*. This technique is used to decompose an laser beam (e.g. a Gaussian laser beam or a fiber mode) into higher order Laguerre-Gaussian or Hermite-Gaussian modes [68, 69]. Propagating these decomposed modes to the distant S/C and tracing them through the interferometer provides much more realistic results than the usage of simple Gaussian laser beams. He then used a detailed numerical simulation of the LRI to design suitable spatial and frequency scanning laws for the initial and re-acquisition modes of the LRI. His

proposed scanning laws were eventually adapted by the LRI project team. The procedures that C. Mahrdt helped to define were explained in Sec. 2.2.

In parallel with C. Mahrdt, Danielle Wuchenich at the Australian National University (ANU) also derived scanning laws for the initial and re-acquisition modes of the LRI [70, 71]. Furthermore, she designed an experimental test bed that was eventually used to validate the acquisition schemes developed by her and C. Mahrdt. The obtained results at the time confirmed and supported the simulations of the laser link acquisition modes. However, the experimental setup used at ANU was not yet optimal in various aspects. Mainly the distribution of the RX laser power as a function of beam tilts was not recreated properly and no top-hat beams were used as RX laser beams, which affects the heterodyne efficiency. These and a few other properties were optimized in the experimental setups used at the AEI (see the next section and Chapter 5).

In parallel with the two above-mentioned studies, also Filippo Ales at the DLR in Bremen, Germany and at Airbus Defence & Space in Friedrichshafen, Germany developed and compared different spatial scanning algorithms for the LRI, LISA and future geodesy missions [72, 73, 74]. He came to the same conclusion as Mahrdt and Wuchenich that Lissajous and spiral patterns, e.g. the hexagonal pattern, are best suited for the LRI. Similar patterns, e.g. a constant tangential velocity spiral, might be beneficial for certain, slightly different mission and instrument parameters. He was the first to study random scanning patterns in the context of the LRI. He came to the conclusion that these are worthwhile investigating further for NGGM if no dedicated acquisition sensor is used there. The benefit of such patterns is that they do not need a strict hierarchy of the scans and that they are robust to initialization delays. If, however, a dedicated acquisition sensor is used, these benefits vanish.

3.2 Experimental demonstration of the LRI laser link acquisition procedure

In this section experimental investigations of the initial laser link acquisition procedure for the GRACE-FO LRI are presented. The experiments were carried out with the help of a mock-up LRI designed and built specifically for these tests. An experimental setup that was jointly developed by the AEI and the DLR Institute of Space Systems in Bremen was used to simulate the intersatellite laser link [75, 76, 77, 78]. The latter was developed for end-to-end system testing of the LRI during and after its integration into the S/C. As it relies on the use of optical fibers to guide the laser light from one S/C to the other and is part of the optical ground support equipment (OGSE) for GRACE-FO, it is simply referred to as *Fiber OGSE*.

The goal of the tests described here was twofold: the functionality of the Fiber OGSE had to be shown, which is, however, merely interesting from an engineering point of

view. This aspect is therefore not discussed in detail in this thesis. More important for the overall project was the goal of experimentally verifying the functionality of the acquisition procedure under more realistic conditions and updated parameters, compared to previous experiments detailed in [70, 71].

The Fiber OGSE was developed jointly by the author of this thesis and the DLR Institute of Space Systems in Bremen, Germany. The development was formally led by DLR. That and the fact that details about the Fiber OGSE are provided in [75, 76, 77, 78] is the reason why it is only explained briefly in this chapter. The interested reader is pointed to the afore-mentioned publications. Additionally, in Chapter 5 of this thesis, a detailed description of a very similar experimental setup, the laser link simulator (LLS), developed solely by the author of this thesis is given. Many ideas that had influence on the design and functionality of the Fiber OGSE were also applied in the LLS.

The majority of the content that is presented in this section has been published in a technical note [79] and in a research article in the journal Optics Express [67]. Details on the Fiber OGSE were published in a different article in Applied Optics [77]. As the author of this thesis co-authored [77] and is the first author of [67], necessary citations are provided where applicable to distinguish the content of these two publications.

This section is structured as follows: First, the Fiber OGSE is introduced, then the design and construction of the mock-up LRI is explained and finally, the obtained test results are presented.

3.2.1   The experimental laser link setup

A detailed schematic drawing of the experimental setup is shown in Fig. 3.1. The Fiber OGSE is shown between the two mock-up S/C highlighted in blue. The Fiber OGSE was designed to enable end-to-end testing of the LRI on the two GRACE-FO S/C. By using an all-fiber design it was guaranteed that end-to-end tests could be performed with the S/C being separated by up to 40 m.

The Fiber OGSE was designed to recreate the laser link between the two GRACE-FO satellites for on-ground testing purposes. Due to the dynamics of the corresponding interferometric signals, the most challenging operating mode of the LRI that can be tested is the initial acquisition mode. The Fiber OGSE was designed to enable such tests by providing the following functionalities: simulate the power drop of the RX beams as a function of the TX beam angles, simulate S/C attitude jitter, introduce static initial offset angles between the two S/Cs, simulate Doppler shifts and generate top-hat laser beams at the receiving apertures. The implementation of these functionalities is explained in the following paragraphs. The Fiber OGSE as a whole can be split into three parts: a TX OGSE, a RX OGSE and the frequency modulation and power attenuation (FMA) OGSE (cf. Fig. 3.1).
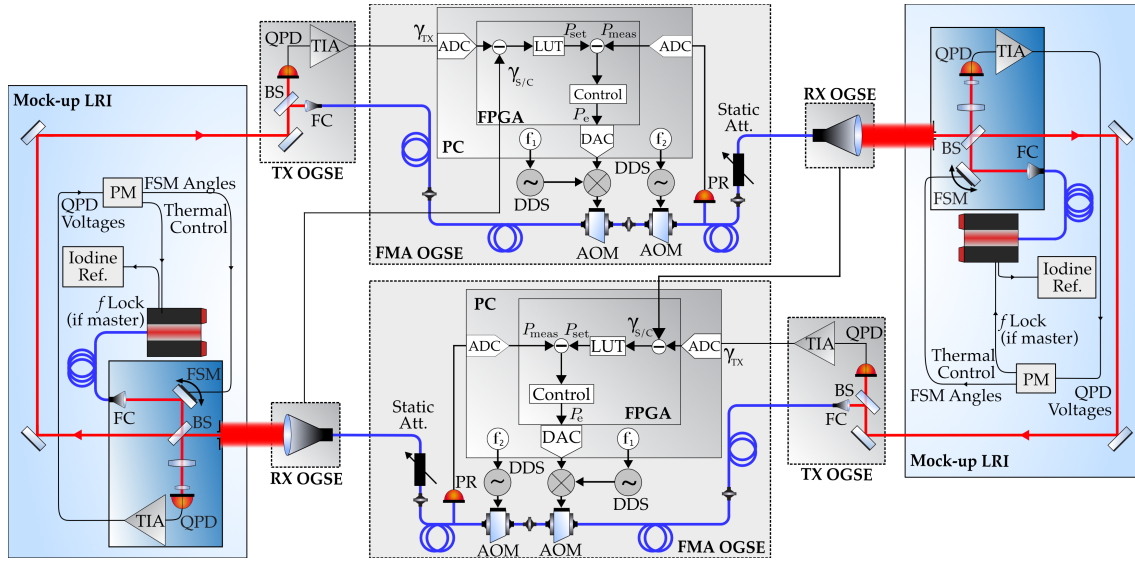
Figure 3.1: The figure shows the experimental setup: two mock-up LRIs (highlighted in blue), each containing one optical bench (OB), phasemeter (PM) and a laser. The master laser is frequency stabilized to an iodine reference whereas the transponder laser is free running. The Fiber OGSE (grey, between the LRI) simulates the 220 km link between the S/C. It can be split into a TX and RX part as well as a frequency modulation and power attenuation (FMA) part. See [77] for details. ADC: analog-to-digital converter. BS: beam-splitter. FC: fiber collimator. DDS: direct digital synthesizer. FPGA: field programmable gate array. LUT: look-up table. DAC: digital-to-analog converter. AOM: acousto-optical modulator.

The two angles of the TX beam leaving one S/C, α_{TX} and β_{TX}, are measured with the help of a calibrated QPR and the differential power sensing (DPS) method. A small fraction of the TX light is split off for this purpose. The DPS method combines the DC voltages of the QPR segments to obtain information on the position of the impinging beam. A preceding calibration of tilt to beam position allows for the calculation of the corresponding TX laser beam angle. This must not be confused with the concept of DWS where the phases of AC voltages are combined to obtain information on the relative tilt angle between two wavefronts (see Sec. 2.1.1.1). As the TX beams nominally show a rotational symmetry around the optical axis, often only the TX beam half-cone angle γ_{TX} is analyzed:

$$\gamma_{TX} = \sqrt{\alpha_{TX}^2 + \beta_{TX}^2} \qquad (3.1)$$

The main part of the TX light from the S/C is launched into an optical fiber with the help of a fiber collimator specifically chosen to have a large acceptance angle, for more details see [77]. Doppler shifts, which occur due to the relative velocity of the two SC, are imprinted onto the laser light by means of two acousto-optic modulators (AOMs). The used AOMs introduce nominal frequency shifts of $-75\,\mathrm{MHz}$ and $+85\,\mathrm{MHz}$, respectively.

The power level sent to the other S/C is attenuated as a function of the TX beam angle, γ_{TX}, to match the predicted value for a given S/C separation. The attenuation is applied by a static optical fiber attenuator in conjunction with a closed-loop system that measures the power that is sent to the other S/C and corrects it by modulating the radio frequency (RF)
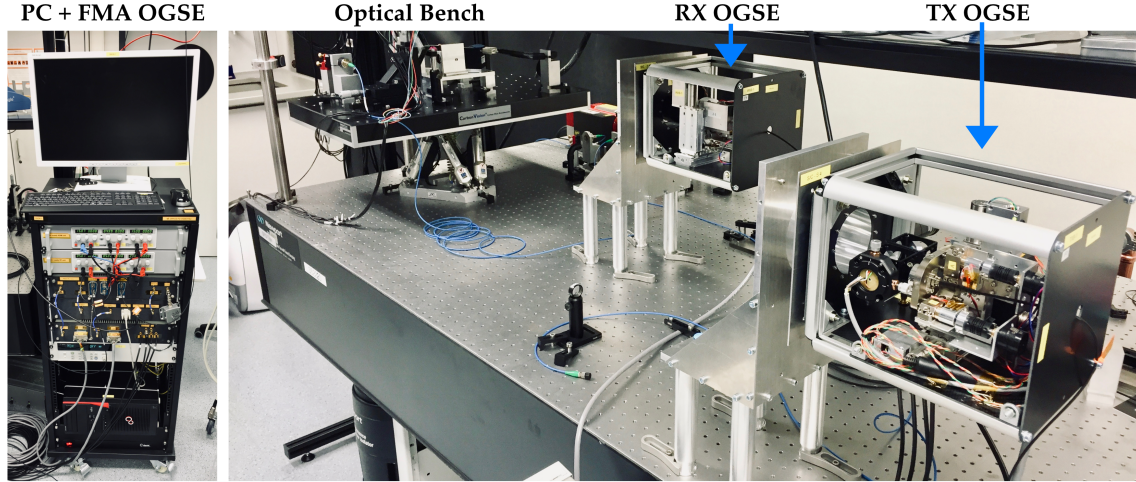
Figure 3.2: Photographs of the experimental setup. The left image shows a rack with a PC and the frequency modulation and power attenuation (FMA) OGSE. The image on the right shows the experimental setup on an optical table. On the left is the OB with the RX aperture facing towards the RX OGSE. On the right, the TX OGSE is shown. Both OGSE boxes are attached to S/C interface simulators.

power driving the AOMs. Using Eq. (2.14), the set-point for the designed power output at the receiving S/C can be expressed as:

$$
P_{\text{RX}} = 2P_{\text{TX}} \frac{r_{\text{ap}}^2}{w_{\text{RX}}^2} \exp\left[\frac{-2\ell^2 \left(\left(\alpha_{\text{TX}} - \alpha_{\text{TX}}^0\right)^2 + \left(\beta_{\text{TX}} - \beta_{\text{TX}}^0\right)^2 \right)}{w_{\text{RX}}^2} \right] \tag{3.2}
$$

with the following values for GRACE-FO: $P_{\text{TX}} \approx 18\,\text{mW}$, $r_{\text{ap}} = 4\,\text{mm}$ the radius of the aperture in the OB, γ_{TX}^0 the half-cone LOS misalignment angle, $w_{\text{RX}} \approx 30\,\text{m}$ the spot radius of the beam when reaching the far SC in free space after $\ell \approx 220\,\text{km}$.

P_{RX} according to Eq. (3.2) is stored digitally in a LUT within a field-programmable gate array (FPGA). An FPGA is an integrated circuit (IC) whose internal logic can be adapted such that the device can serve as a (near) real-time processing unit. Here a closed-loop controller is implemented on said FPGA. γ_{TX} is digitized by an ADC and serves as input to the LUT. The LUT output is the set-point for the controller (see P_{set} in Fig. 3.1). The measured optical power at the output of the controller of the Fiber OGSE, P_{meas}, is also digitized and serves as actual value for the controller. The difference of the two yields the error signal which is driven to zero by the controller (see P_{e} in Fig. 3.1). The control loop has a closed-loop bandwidth of $\sim$50 kHz and accurately reproduces the power drop in the RX beam even when the fast Lissajous scan is present [77].

The simulated RX beam is produced by a large fiber collimator, which creates a Gaussian beam with a waist radius of $w_0 \simeq 16\,\text{mm}$. The intensity of this beam drops by $\sim$10 % towards the edge of the 8 mm diameter aperture [77]. By tilting RX and TX OGSE by the same angle, a tilt of the S/C with respect to the LOS is simulated. In Eq. (3.2) this angle's components α_{TX}^0 and β_{TX}^0 are used. These tilts are introduced by means of motorized stages. The maximum P_{RX} is only transmitted to the other S/C if the local S/C adjusts the tilt of
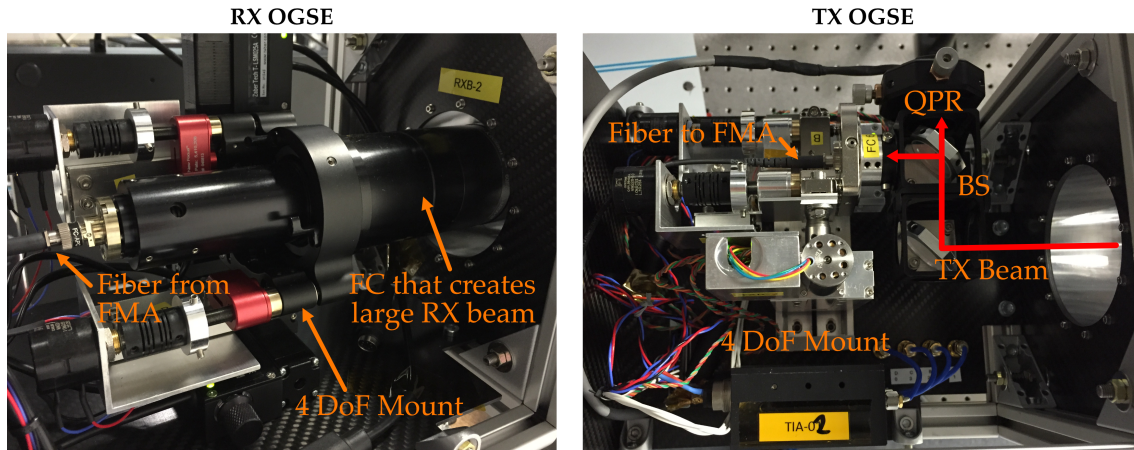
Figure 3.3: The figure shows close-up images of the RX and TX OGSE units. The RX OGSE generates a large top-hat laser beam that serves as RX beam to the LRI. The TX OGSE accepts the LRI's TX beam, measures its angle with the help of a QPR and guides it towards the FMA OGSE. Both OGSEs have motorized mounts that can be used to simulate a tilt of the local S/C.

the TX beam such that the S/C misalignment with respect to the LOS is compensated.

As can be observed in Fig. 3.1 all introduced components are present twice to realize the two laser links between the two mock-up LRIs. Figure 3.2 shows two photographs of the experimental setup in the laboratory. Once again, only half of the setup is shown, the same setup as visible in the pictures was set up a second time on a different optical table. Figure 3.3 shows close-up photographs of the RX and TX OGSEs.

3.2.2 The mock-up LRI

The only parts of the LRI needed for these tests were two lasers, two phasemeters (PMs) and two optical benches (OBs). A TMA was not required. In the following sections, the design and the construction of the components that make up the mock-up LRI are explained.

3.2.2.1 Design and construction of mock-up optical benches

The layout of the LRI optical benches (OBs) was applied for the design of the breadboard OB models that were used for these tests, see Sec. 2.1.1.1. Obviously, the properties of the flight models could not be copied completely, but it could be ensured that key optical properties match: The RX beam must be clipped by a circular aperture of 8 mm diameter, LO and RX beams must be interfered on a recombination beamsplitter, it must be possible to steer the LO in two DoF (pitch and yaw) and beamwalk of the laser beams on the QPR must be suppressed with the help of an imaging system. For the foreseen tests in this test campaign it was not necessary to have a redundant pair of QPRs. Therefore, the redundancy beamsplitter, the second output port of the imaging system and the second
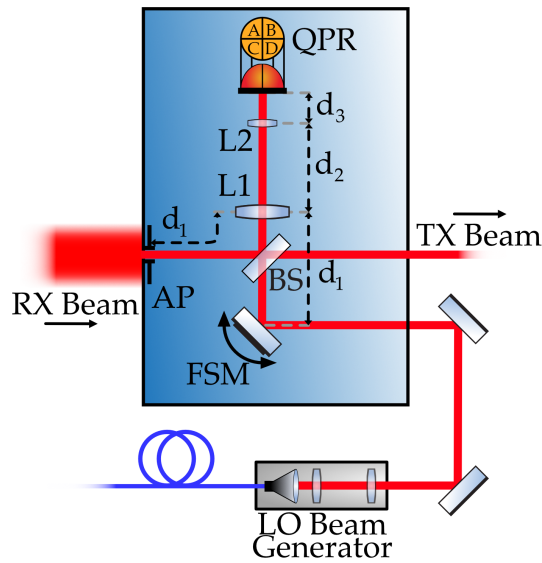
Figure 3.4: The figure shows a schematic drawing of the OB as it was designed for the tests described in this chapter. Additionally, the distances of FSM and aperture to the first lens L1 d_1, the distance between the two lenses d_2 and the distance between L2 and the QPR d_3 are shown. These values were defined by the IfoCAD simulation.

QPR were omitted. Additionally, the CP could also be left out, because no measurements of the optical path length were foreseen.

The optics were custom made and specified to have the same parameters as were used for the flight models. Therefore, all optics were coated such that the required properties were valid for p-polarized light at a wavelength of 1064 nm. The "p" here denotes that the polarization vector of the laser beams is *parallel* to the baseplate of the OB. The beamsplitters and lenses were custom made with the following specifications: The recombination beamsplitters (35 x 45 x 7 mm ±0.25 mm) have a reflectivity and transmission of $R/T = 90\%/10\% \pm 1\%$ for 1064 nm on the surface that faces the FSM and the aperture and an anti-reflective coating on the backside. Thus, they reflect 90 % of the RX beam power to the QPR and transmit 10 % of the strong LO power to the QPR. They are made from BK7 and have a wedge angle of 900 μrad ±100 μrad to prevent ghost beams from disturbing the measurements.

The lens parameters were also taken over from the flight models: L1, which is the lens closer to the recombination beamsplitter (see Fig. 3.4), and L2 are both plano-convex. L1 has a diameter of 20 mm, a center thickness of 4.2 mm and a radius of curvature on the convexly curved side of 30.23 mm. L2 has a diameter of 5 mm, a center thickness of 3 mm and a radius of curvature of 3.58 mm. Both are made from BK7 and have anti-reflective coatings. As the lenses will be separated by the sum of their focal lengths, taking into account the principal points and the respective back and front focal distance of the lenses, the magnification factor of the resulting imaging system becomes $m \simeq 8$. That means the output beam diameters will be scaled down by a factor of m and laser beam tilt angles will be enhanced by a factor of m. The magnification ensures that the RX beam, which has a diameter of 8 mm, is properly imaged onto the QPR of 1 mm diameter. Furthermore, the resolution of the DWS readout that can be achieved with the implemented system benefits from the enhanced angles.

The fast steering mirror (FSM) (model *FSM-300* from Newport) is a voice coil actuated

1" mirror that provides two-axes steering with sub-microradian resolution and a total mechanical angular range of ± 26 mrad. The FSMs are controlled via dedicated controllers which are also provided by Newport. The mirror has a high reflectivity coating for 1064 nm and its plane of rotation lies 12.2 mm behind the center of the mirror surface. This offset must be taken into account for the later design of the optical system. Details about the FSM control bandwidth are provided in the next section.

The LO fiber collimator was designed and built by Daniel Schütze [47]. The Gaussian beam sizes of the laser beams were determined to $w_{0,\text{LO1}} \simeq 2.7$ mm and $w_{0,\text{LO2}} \simeq 2.8$ mm, respectively for the two OBs.

The software IfoCAD, which has been developed at the AEI, was used to design a complete optical model of the OB. IfoCAD is a powerful tool which can for example be used to optimize the positions of various optical components in such a model, like beamsplitters and lenses, if a certain figure of merit (FoM) is defined. The exact positions of all optical components of the OB breadboard model were determined with the help of this tool. Furthermore, IfoCAD was used to calculate the expected laser beam properties behind L1 and L2 which were used for the alignment of these two lenses, see below.

Before the OBs were built according to the IfoCAD simulation, a computer aided design (CAD) model was developed. According to these two models, the OBs were then built completely in-house at the AEI. The OBs are made out of aluminum. The corresponding coefficient of thermal expansion was deemed sufficient, because the OBs were not intended to enable measurements of the optical path length stability in the picometer or even nanometer range. According to the IfoCAD model, the positions of the components were fixed in the CAD model. The OB was not designed monolithically. Instead, each component has its own mount that is then later attached to a common baseplate. Register pins on the baseplate were implemented in order to place each mount placed according to the CAD model. The mounts could then be pressed against the pins and be fixed with a screw from the bottom of the baseplate. All mounts were designed such that the items that they are supposed to hold can easily be attached and detached from the mount. Additionally, the lens mounts were designed such that the lenses themselves could be moved inside their mounts along the optical axis to later allow the alignment of the imaging system. They are then fixed with retaining rings.

After all the mechanical components were manufactured and cleaned, the optics were paired with their mounts and were then attached to the baseplate according to the CAD model. However, the lenses were not yet put into the lens mounts, but instead disks with apertures of about 1 mm diameter were placed in them. These holes now served as reference for the optical axis of the instrument. With the help of a charge-coupled device (CCD) camera (*WinCam LCM-D* from DataRay Inc.), the LO and RX beams were aligned to this optical axis. The beams were aligned one after the other in an iterative process during which the beams were translated and rotated to finally match the OB's optical axis. After performing a rather coarse alignment, a beat note on a large, single
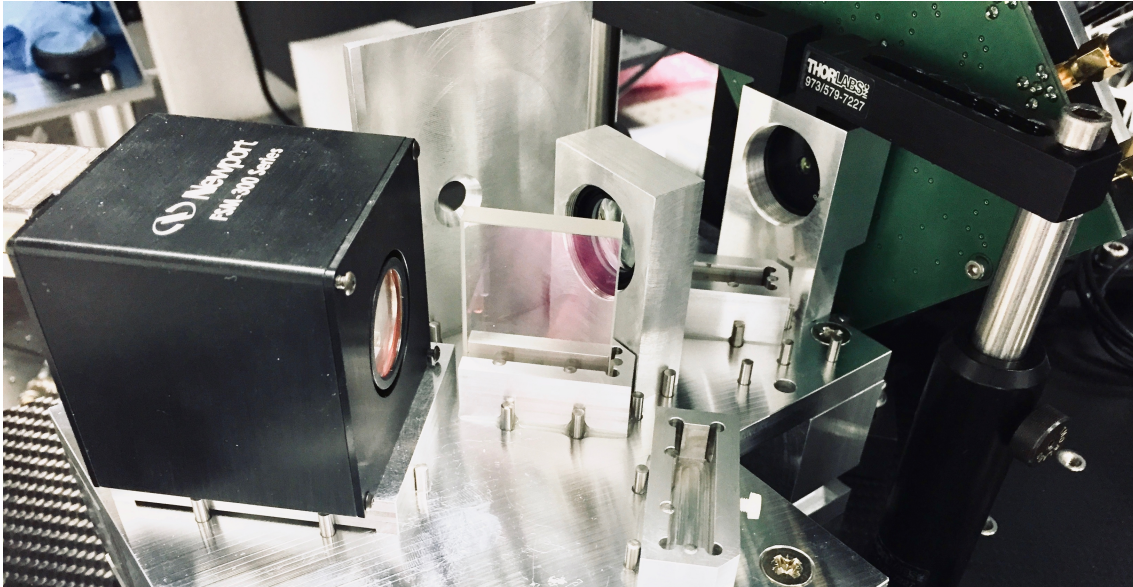
Figure 3.5: The figure shows a photograph of one of the two built OBs. These were specifically designed and constructed for the tests described in this chapter. The black cube on the left is the FSM-300 from Newport, in the center of the image, the recombination beamsplitter, the aperture and L1 can be seen. L2, and behind it the QPR, can be seen in the right half of the image. A mount for a CP is attached to the baseplate but was not equipped with an optic as the function of the CP is not needed for these tests. The same is true for the mount of the redundancy beamsplitter between L1 and L2.

element PR could already be observed. This PR was then used temporarily to maximize the beat note amplitude which implicates that the beams were aligned as well as possible. The aperture disks were then replaced with the lenses. The imaging system was aligned with the help of the expected beam profiles, simulated with IfoCAD, which were observed again with the WinCam camera.

Finally, the QPR was placed behind L2. See Sec. 3.2.2.3 for more details on the used QPR. A signal generator was used to command the FSM to perform slow oscillations which results in beamwalk of the LO on the QPR. By translating the QPR along the optical axis of the interferometer this beamwalk was then minimized. Thus, the lens system was imaging the FSM rotation plane onto the QPR. The design of the OB then ensures that also the aperture plane is imaged onto the QPR. As a result, the alignment of the OB was completed.

For each OB the readout of the optical phases, the control of the two mechanical axes of the FSM as well as the control of the transponder laser frequency (where required) was realized with the help of PMs developed exclusively for this purpose [80]. The PMs employ the same methods as the ones on-board GRACE-FO. For the initial acquisition tests the PMs continuously calculate FFTs with a length of 4096 points at a sampling rate of 40 MHz, just like it is done by the LRP on the LRI [49]. The FFT length was optimized with respect to the expected duration of a detected flash during initial acquisition, which is a result of the fast component of the Lissajous scan (see Fig. 2.5). The amplitudes and frequencies of the FFTs were sent to a computer where they were stored at a frequency
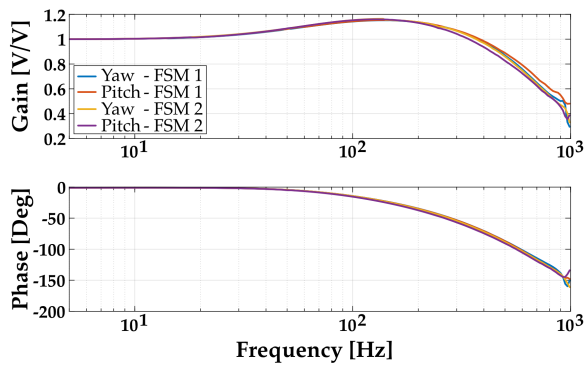
Figure 3.6: Bode plot of the normalized transfer functions of both FSMs used in the mockup LRI.
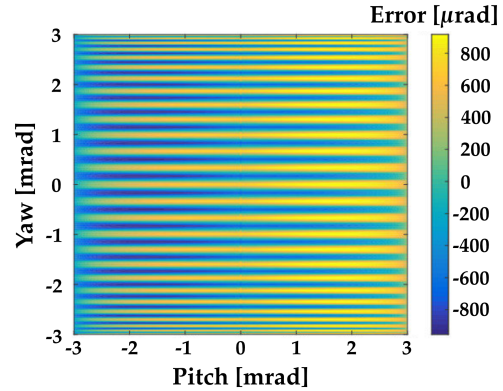
Figure 3.7: Simulation result of the error between the commanded and actual yaw and pitch angles when a Lissajous scan is conducted [67]. $f_{\text{yaw}} = 100\,\text{Hz}$, $f_{\text{pitch}} = 1.79\,\text{Hz}$, $A = 3\,\text{mrad}$

resolution of $40\,\text{MHz}/4096 \simeq 10\,\text{kHz}$ when short measurements were taken. For complete initial acquisition tests that included frequency scans, the data size was reduced by storing only the points that correspond to the 100 highest FFT amplitudes.

The laser on the master S/C was simulated by an Nd:YAG NPRO laser whose frequency was stabilized to an iodine hyperfine structure line (Prometheus from Innolight) while the transponder laser was a free-running Nd:YAG NPRO (Mephisto from Innolight).

3.2.2.2 Calibration of the fast steering mirror

As was explained in Sec. 2.2, one of the goals of the initial acquisition procedure is to find correct beam pointing offsets on both S/C, by performing angular scans with the fast steering mirrors (FSMs). When each FSM compensates for the local S/C misalignment angle, the afore-mentioned properties of the TMAs (see Sec. 2.1.1.2), as well as the unique architecture of the LRI ensure that both TX beams are well aligned. Only then the FFTs, that are calculated on both S/C, exhibit a signal above the noise level, assuming the lasers' frequencies are within the QPR bandwidth of roughly $25\,\text{MHz}$ (see Sec. 3.2.2.3). The FSM angles then correspond to the misalignment angles of the S/C with respect to the LOS. Factors of 2 and $\sqrt{2}$, for the conversion of mechanical to optical beam tilts in the yaw and pitch axes, must be taken into account.

Consequently, the FSM position at the occurrence of an FFT peak needs to be known. In the LRI this is accomplished by monitoring the position of the mirror using a high-speed sensor, which is referred to as Position Sensing Subsystem (PSS). However, in this test setup, only the commanding signals were recorded. In order to assess the frequency response of the FSMs, their transfer functions were measured. This was done with the help of a network analyzer, whose output signal was used to actuate the FSM under test. The driving signal was conditioned such that the FSM was commanded to carry out

Table 3.1: Summary of the parameters of a pole-zero model that was used to fit the transfer function of the FSM-300 from Newport.

Axis		f_z [Hz]	f_{p_1} [Hz]	f_{p_2} [Hz]	f_{p_3} (c.c.) [Hz]	Q_{p_k}
FSM 1	Yaw	58.7	72.6	552.1	1003	0.67
	Pitch	59.8	74.6	470.5	966.7	0.82
FSM 2	Yaw	57.3	71.4	523.2	983.6	0.68
	Pitch	59.4	75.8	418.7	990.3	0.78

a sinusoidal motion of a few mrad amplitude. The FSM's internal sensor was used as representation of the response of the FSM. The left panel in Fig. 3.6 shows the obtained, normalized transfer functions of both FSMs. Gain peaking and phase delay can be observed for frequencies above ~20 Hz.

A pole-zero model was fitted to the measured transfer functions. A model with one zero and three poles, one of which was a complex conjugate pair of poles, turned out to fit the data well:

$$H(f) = \frac{z(f)}{p_1(f) \cdot p_2(f) \cdot p_{3,cc}(f)} . \tag{3.3}$$

Where the zero $z(f)$ and poles $p_k(f)$ are described in the following manner:

$$z(f) = 1 + \frac{if}{f_z} \tag{3.4}$$

$$p_k(f) = 1 + \frac{if}{f_{p_k}} \tag{3.5}$$

$$p_{k,cc}(f) = 1 + \frac{if}{f_{p_k} Q_{p_k}} - \frac{f^2}{f_{p_k}^2} . \tag{3.6}$$

Eq. (3.6) describes a pair of complex conjugate poles. i is the imaginary unit, f the Fourier frequency, f_z / f_p the frequency at which the zero / pole is located and Q_k is the Q factor. It should be noted that the used fit model does not imply a physical meaning about the internal workings of the FSM. It is merely a model that properly well describes the available data. Table 3.1 summarizes the model parameters for each FSM axis. Using this model, the gain overshoot, G, and the delay, ϕ, of the FSMs at a frequency of 100 Hz were determined. These parameters are summarized in Table 3.2.

Table 3.2: Gain and phase correction factors determined by the transfer functions at a frequency of 100 Hz.

Axis		Gain [V/V]	Phase [deg]
FSM 1	Yaw	1.14	-13.9
	Pitch	1.14	-13.9
FSM 2	Yaw	1.15	-14.1
	Pitch	1.15	-15.0
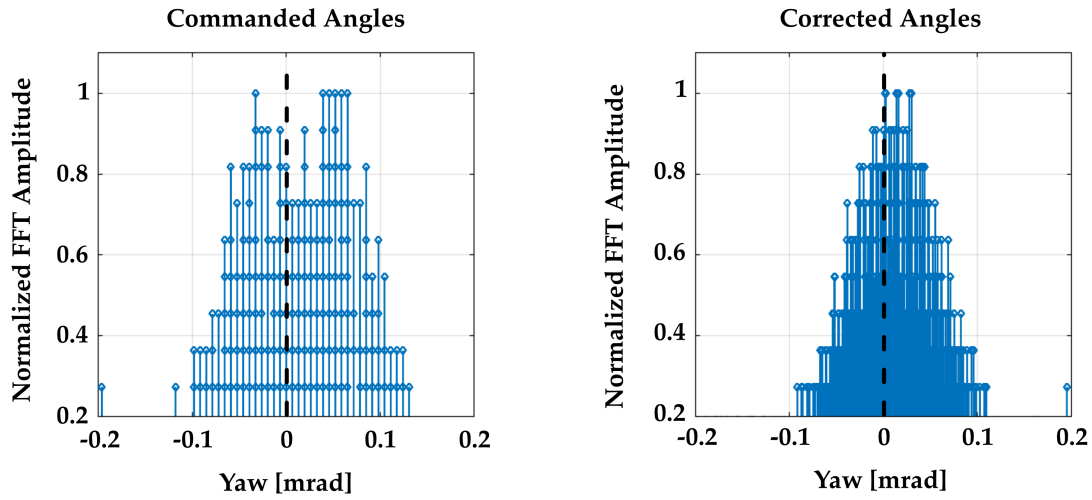
Figure 3.8: The plots show a representative measurement of the recorded, normalized FFT amplitude as a function of the commanded (left) and the corrected (right) FSM angles. The angles were corrected by the FSM gain and phase delay. As can be seen, the uncorrected data shows two peaks while one unambiguous peak is visible in the corrected data. The expected peak position at an angle of 0 mrad is indicated by the dashed, black line.

Figure 3.7 shows a simulation of the difference between a commanded Lissajous scan pattern and the expected motion of the mirrors. Scanning frequencies of $f_{\text{yaw}} = 100\,\text{Hz}$ and $f_{\text{pitch}} = 100/56 \approx 1.79\,\text{Hz}$ and an amplitude of $A = 3\,\text{mrad}$ were simulated. As can be obtained from the plot, the error is within $\pm 800\,\mu\text{rad}$, which is unacceptable. The deviation between commanded and realized angles is due to the large delay of the FSM and the gain overshoot at the yaw scanning frequency of 100 Hz. For comparison it should be noted that the spatial scanning amplitudes in the re-acquisition mode of the LRI are only 300 µrad, as described in Sec. 2.2.5.

Therefore, the obtained parameters for the gain overshoot, G, and the delay, ϕ from Tab. 3.2 were used to correct the commanded angles, such that the actually performed scanning angles could be estimated. As the deficiency of the FSM was only dominating the fast yaw axis of the scans, the pitch angles were not corrected. The used model is:

$$\alpha_{\text{corr}} = A \cdot G \cdot \sin(2\pi f_\alpha t + \phi), \tag{3.7}$$

where A is the commanded amplitude and $f_\alpha = 100\,\text{Hz}$ the frequency of the fast axis (yaw) in the Lissajous scan. G and ϕ are the gain and phase at $f_\alpha = 100\,\text{Hz}$ that are listed in Tab. 3.2.

The left graph in Fig. 3.8 shows the FFT amplitude that was measured with the test setup as a function of the FSM yaw angle, while the FSM performed a Lissajous scan. The setup was aligned such that the maximum FFT amplitude was expected at an angle of 0 mrad, indicated by a dashed line. A clear double-peak structure is visible. This was caused by the delay between commanded and realized angle that was introduced by the FSM. In the right panel of Fig. 3.8, the FFT peaks are shown as a function of the yaw angle that was
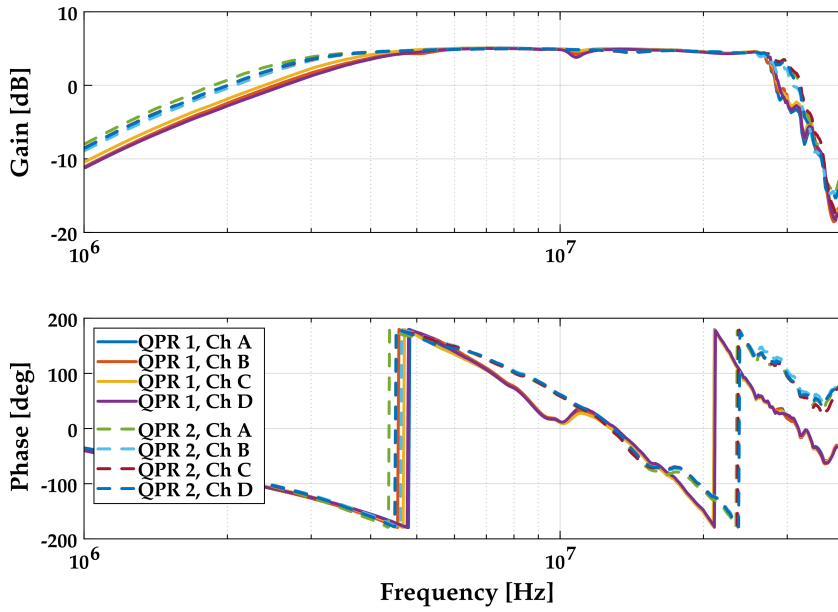
Figure 3.9: The figure shows bode plots of all segments of the two quadrant photoreceiver (QPR) transfer functions.

corrected by applying Eq. (3.7) and the values from Tab. 3.2. It can clearly be seen how the double-peak structure has vanished and now one central FFT peak is visible.

3.2.2.3   Characterization of the quadrant photoreceiver noise

The mock-up LRI OBs utilized quadrant photoreceivers (QPRs), that were initially designed by B. Sheard at AEI as prototypes for the GRACE-FO LRI. The 1 mm diameter photodiodes are made from InGaAs (Hamamatsu G6849-01) which show a responsivity for 1064 nm of $\rho \simeq 0.7\,\text{A/W}$ [81]. The TIAs provide separate amplifier stages for the DC and the AC paths. The latter offers a passband bandwidth of about 5–25 MHz (see Fig. 3.9).

Following the description given in Sec. 2.1.1.1, the coherent sum of all noise contributions of the QPRs is calculated. First, the noise of a single QPR segment is calculated and then the coherent sum for the QPR as a whole is presented.

The **electronic noise of a QPR segment** was obtained by performing a dark measurement and calculating the ASD of the gathered time-series data. This data was then referred back to the input of the QPR by dividing it by the TIA gain and the normalized gain of the QPR transfer function, which is illustrated in Fig. 3.9. The worst case value of all segments, evaluated at a frequency of 10 MHz was:

$$\text{ICN} = 9.8\,\text{pA}/\sqrt{\text{Hz}}. \tag{3.8}$$

It should be noted that the values of the remaining segments were very close to the presented value. According to Eq. (2.16) the PSD of this noise term is obtained by squaring this expression: $\tilde{S}_{e,s}^2 = \text{ICN}^2$.

For comparison, the requirement for the QPRs on GRACE-FO at a frequency of 16 MHz, as well as the measured ICN of the flight models are provided [81]:

$$\text{ICN}_{\text{GFO}}^{\text{req}} = 5\,\text{pA}/\sqrt{\text{Hz}} \tag{3.9}$$

$$\text{ICN}_{\text{GFO}}^{\text{meas}} = 3.5\,\text{pA}/\sqrt{\text{Hz}}. \tag{3.10}$$

Following Eq. (2.17), the **shot noise** of a single segment is calculated by $\tilde{S}_{s,s}^2 = 2\,q_e\,\rho P_{\text{LO,s}}$. With the elementary charge $q_e \simeq 1.602 \cdot 10^{-19}\,\text{C}$ and the responsivity of the InGaAs QPR, $\rho \simeq 0.7\,\text{A}/\text{W}$ [81]. $P_{\text{LO,s}}$ is the local oscillator power on one segment. For these tests, the total LO power was $P_{\text{LO}} = 20\,\text{mW}$. Due to the 90/10 beamsplitter on the OB, the power per segment was $P_{\text{LO,s}} = {}^{0.1 \cdot P_{\text{LO}}}/4 = 500\,\mu\text{W}$.

According to the datasheet of the used laser (Mephisto from Coherent Inc.), the **relative intensity noise (RIN)** at a frequency of 10 MHz is RIN $\approx 3 \cdot 10^{-8}/\sqrt{\text{Hz}}$ [82]. Following Eq. (2.18) the noise spectral density of this term is then described by $\tilde{S}_{i,s}^2 = (\rho\,P_{\text{LO,s}}\text{RIN})^2$.

Considering that only the RIN is correlated between all the segments, the total noise of the QPR is described by the coherent sum of the noise sources from all four segments:

$$\tilde{n}_{cs}^2 = N(\tilde{S}_{e,s}^2 + \tilde{S}_{s,s}^2) + N^2 \tilde{S}_{i,s}^2. \tag{3.11}$$

Using the values that were listed above, the noise PSD becomes:

$$\tilde{n}_{cs}^2 = 2.6 \cdot 10^{-21}\,\text{A}^2/\text{Hz} \tag{3.12}$$

which corresponds to a noise amplitude spectral density of:

$$\tilde{n}_{cs} = 51\,\text{pA}/\sqrt{\text{Hz}}. \tag{3.13}$$

With the help of Eq. (2.21) and the noise PSD given in Eq. (3.12), all detections that are described in the next section were expressed as C/N_0 in units of dBHz.

3.2.3 Tests of the initial acquisition procedure

In a test campaign that was conducted with members of the DLR Bremen numerous test runs, each with an increasing level of complexity, were carried out. First, tests with only one laser whose light was distributed to both OBs were carried out. Thus, allowing to skip the frequency scan on the transponder side. This reduces the complexity of the experimental setup and the time required for each scan. These tests are described in Sec. 3.2.3.1. Complete tests with two independent laser sources including spatial and frequency scans are described in the subsequent section.

3.2.3.1 Tests with a single laser
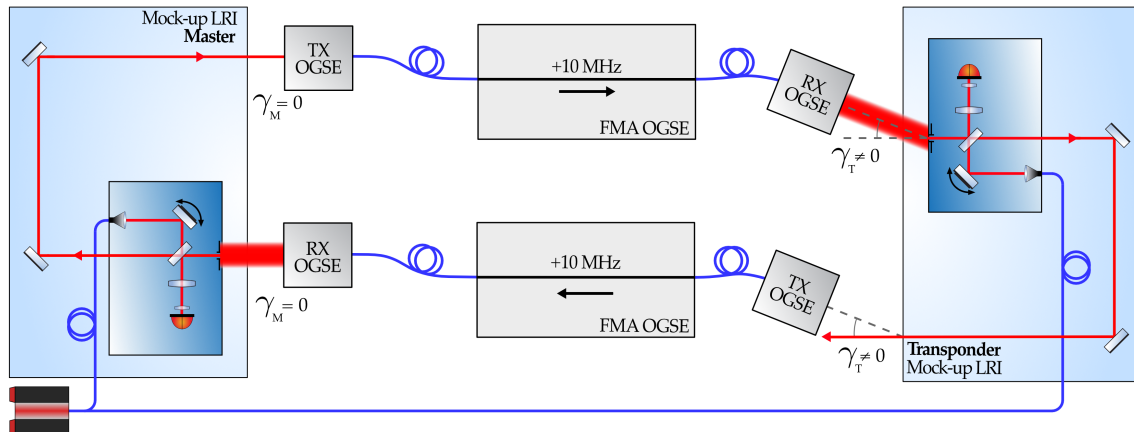
Figure 3.10: Simplified schematic overview of the setup that was used for the initial acquisition scans with a single laser. Here, only the transponder side was manually misaligned by γ_T. In the shown situation, a flash is detected if the misalignment of the transponder mock-up LRI is corrected by its FSM by an amount equal to γ_T and when the FSM on the master OB points to $\gamma_M = 0$. γ_T is shown highly exaggerated.

A simplified drawing of the setup for the tests with a single laser is shown in Fig. 3.10. The angular offsets between the optical axes of the OBs and the LOS were realized by misaligning the RX and TX OGSE with respect to the OBs *by the same angle*. In Fig. 3.10, the OGSEs are only tilted on the transponder side, which simulates a misalignment of the transponder OB with respect to the LOS.

Such tilts were realized by rotating the RX OGSE by a small angle with an accuracy of ~50 µrad, using its motorized stages (see Fig. 3.3). The LO was temporarily disabled. The power of the RX beam was manually enhanced. The TX OGSE was then aligned to the RX beam, which passed through the OB. The QPR on the TX OGSE was used for a coarse alignment. This was then optimized by maximizing the power that coupled into the fiber on the TX OGSE. After the alignment, the powers of the RX and LO beams were restored to their nominal values.

The goals of these tests were, first, to detect the flashes and, second, to measure the introduced bias angles. The FSM on the master OB thereby carried out a hexagonal scan and the FSM on the transponder OB a Lissajous scan. Different scan amplitudes and corresponding grid errors were used. The frequencies matched the GRACE-FO parameters (cf. Fig. 2.6). Thus, the master FSM scanned a hexagonal pattern with an update rate of $T_{hex} = 0.56$ s and the transponder FSM carried out a scan with $f_{yaw} = 100$ Hz and $f_{pitch} = 1.8$ Hz. First, a scan amplitude on both OBs of 3 mrad, which corresponds to a grid error of 140 µrad, was used. The GRACE-FO parameter for the amplitude is also 3 mrad. However, the grid error on GRACE-FO is 100 µrad [66]. The difference was caused by the chosen implementation of the scan pattern. For a second set of scans, the scan amplitude was reduced to 1.5 mrad. This caused the grid error to change to 70 µrad on the transponder side. On the master OB, the grid error was not affected. All provided FSM

angles have been corrected by the FSM gain and delay, as was presented in Sec. 3.2.2.2.

In space, the master and transponder OB only detect a signal when each FSM has compensated its own OB misalignment with respect to the LOS. Thereby, the LOS is defined by a straight line that connects the two CoM. For these experiments, the LOS is simulated by the alignment of the RX and TX OGSEs with respect to the respective OB. The frequency difference between the two LOs were introduced by the AOMs and were kept fixed at 10 MHz. This is a simplification, which causes the heterodyne beat note signal to have a fixed frequency of 10 MHz. For the real LRI this frequency is not static and depends on the introduced Doppler shifts.

The maximum RX power level was set to 80 pW per segment. This corresponds to a total RX power incident on the complete QPR of 320 pW. In the LRI nominal conditions the lowest received power is on the order of ∼500 pW, for a S/C separation of $z = 270$ km. For these tests, the local oscillator power, P_{LO}, was 20 mW, very similar to the LRI.
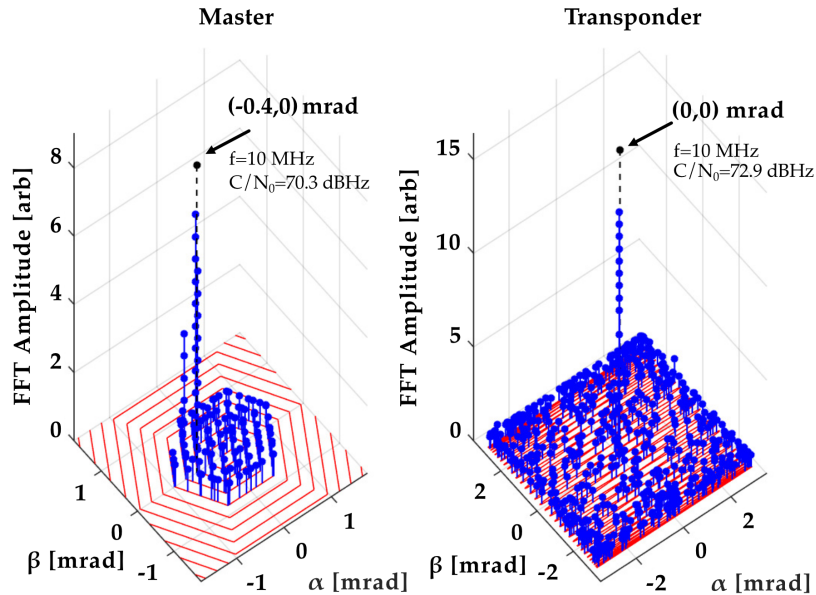
Figure 3.11: Representative example of a detection during one of the measurement runs [67]. The FFT amplitudes of the master (left) and transponder (right) scans are plotted as a function of the FSM angles. Both flashes occurred at a heterodyne frequency of 10 MHz and with a C/N_0s of the order of 70 dBHz. The pre-set LOS offsets were $(\alpha_M^0, \beta_M^0) = (-0.5, 0)$ mrad for the master and $(\alpha_T^0, \beta_T^0) = (0, 0)$ mrad for the transponder. The flashes were obtained at $(\alpha_M, \beta_M) = (-0.4, 0.2)$ mrad and $(\alpha_T, \beta_T) = (0, 0)$ mrad.

Figure 3.11 shows an example of detections made during these experiments. The detections (flashes) with maximum amplitudes happened at a frequency of 10 MHz and $C/N_0 \simeq 70$ dBHz. The flashes occured at FSM angles of $(\alpha_M, \beta_M) = (-0.4, 0.2)$ mrad and $(\alpha_T, \beta_T) = (0, 0)$ mrad. These angles are indicated by black, dashed lines in Fig. 3.11. The simulated OB misalignments, which correspond to the manually introduced misalignments of the OGSEs, were $(\alpha_M^0, \beta_M^0) = (-0.5, 0)$ mrad and $(\alpha_T^0, \beta_T^0) = (0, 0)$ mrad. These values are considered to be in good agreement, if the grid error of the scans of 140 µrad is accounted for.
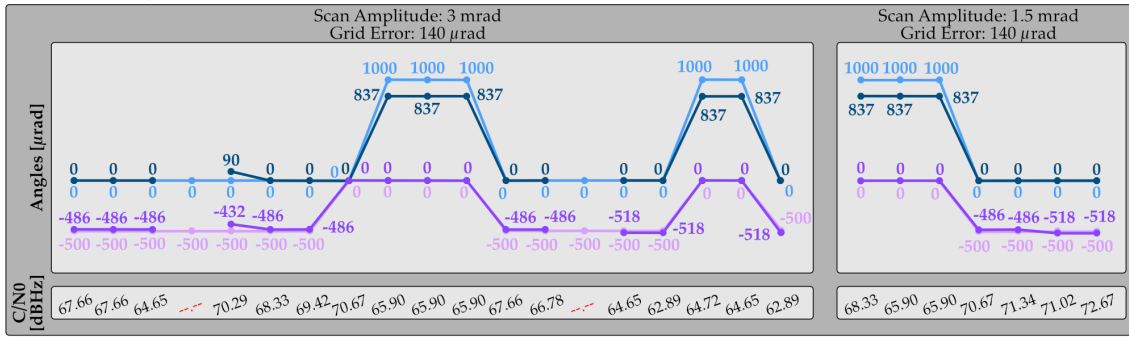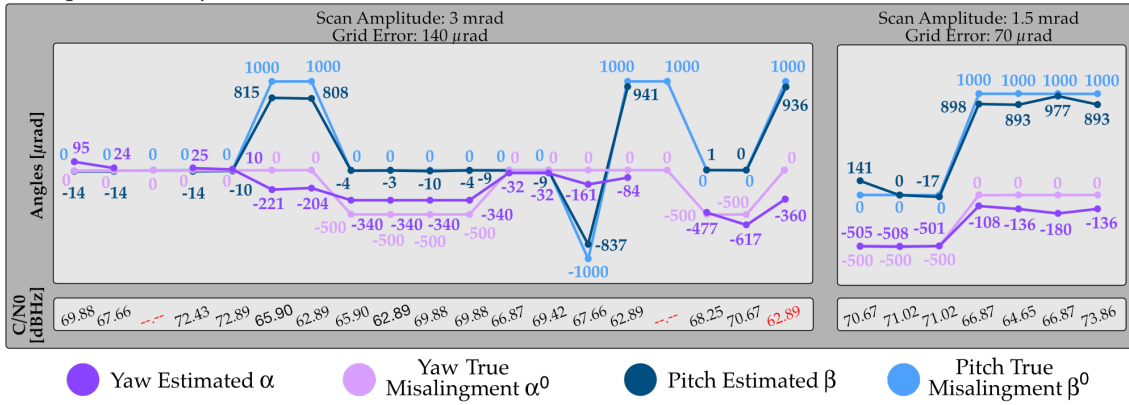
Figure 3.12: Summary of the scans with two OBs and one laser [67]. Only the spatial scans were executed. Top panel: master OB (hexagonal scan). Bottom: transponder OB (Lissajous scan). The colored numbers along the course of the curves indicate the angles in μrad. The C/N_0 values for each of the runs are also shown in units of dBHz below the respective plots. The C/N_0s of unsuccessful scans are marked in red. If no flash was recorded, a C/N_0 of –.– is provided.

While Fig. 3.11 only shows the obtained result of a single scan run, Figure 3.12 gives an overview of all the obtained results. In total, 27 test runs were carried out. The yaw and pitch angles at which the detection occurred are plotted together with the introduced ("true") misalignments. Scans were declared successful, when both OBs showed clear detections and when the half-cone angle of the misalignment with respect to the LOS was estimated with an error of less than 300 μrad, i.e.,

$$\gamma_{\mathrm{err}} = \sqrt{\left(\alpha_{\mathrm{M/T}} - \alpha_{\mathrm{M/T}}^0\right)^2 + \left(\beta_{\mathrm{M/T}} - \beta_{\mathrm{M/T}}^0\right)^2} \leq 300\,\mu\mathrm{rad} \qquad (3.14)$$

where $\alpha_{\mathrm{M/T}}$ and $\beta_{\mathrm{M/T}}$ denote the corrected FSM angles in the yaw or pitch axis of either the transponder (T) or the master (M). The 300 μrad threshold corresponds to the range of the re-acquisition scans, which are carried out by the real LRI in orbit after the initial acquisition procedure. These scans are foreseen to autonomously lead the LRI into the science mode (see Sec. 2.2.5).

Two unsuccessful runs occurred at the master OB (hexagonal scan) due to no flash detection. On the transponder OB (Lissajous scan) three errors occurred, two of them due to no flash detection and one for having an error slightly larger than 300 μrad: 360 μrad.
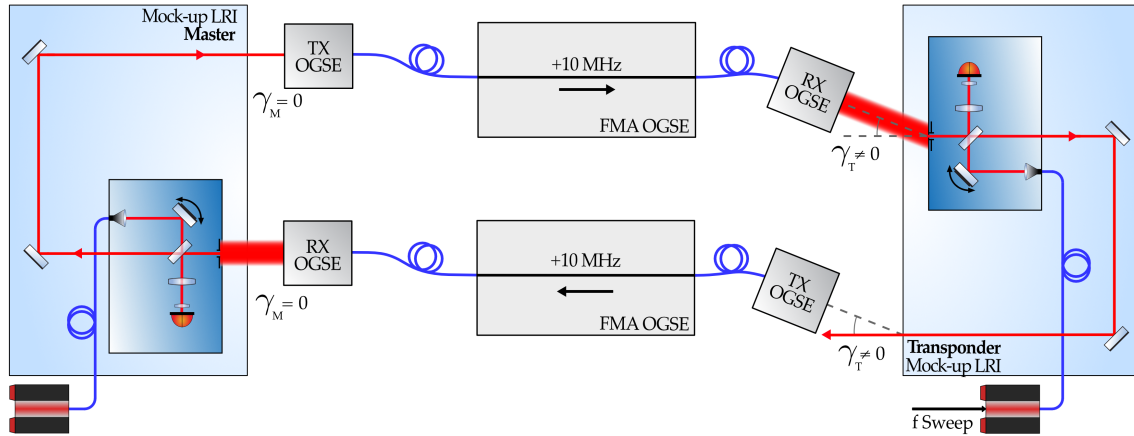
Figure 3.13: Simplified schematic drawing of the setup used for the tests of the initial acquisition procedure with two independent lasers. This setup allows for a full initial acquisition test, i.e. including spatial and frequency scans. Here, only a misalignment of the transponder by γ_T was introduced. In the shown situation, a flash is detected when the misalignment of the transponder mock-up LRI is corrected by its FSM by an amount equal to γ_T, when the FSM on the master OB points to $\gamma_M = 0$ and when the heterodyne frequencies are within the QPRs bandwidths on both sides. γ_T is shown highly exaggerated.

All unsuccessful runs occurred with grid errors of 140 μrad, instead of the LRI value of ∼100 μrad. The fact of using a rather large grid error and low received power led to signals closer to the C/N_0 limit and thus, in some cases they became indistinguishable from the noise. For the successful runs, the half-cone errors were between about 20 μrad and 160 μrad for the slow hexagonal scan and between 0 μrad and 220 μrad for the fast Lissajous one. These errors are a combination of grid error, uncertainty in the introduced LOS misalignments and FSM transfer function correction. For the last seven test runs, the scanning amplitudes were reduced to 1.5 mrad. The corresponding grid error of the Lissajous scan was reduced to 70 μrad. This was done to find out, if higher C/N_0s can be achieved by this. As can be seen in the right part of Fig. 3.12, this assumption was confirmed. Overall most of the runs were successful and delivered acceptable estimates of the LOS misalignments.

3.2.3.2 Tests with two independent lasers

The initial acquisition procedure tests including two independent laser sources with frequency and spatial scans were carried out using the configuration shown in Fig. 3.13. The laser on the master OB was stabilized to an iodine hyperfine line reference that mimicked the optical cavity in the LRI master S/C. The laser on the transponder OB was free-running. The Doppler frequency was kept fixed at $f_D = 10\,\text{MHz}$, which is above the expected values for the LRI. The 10 MHz were defined by the difference of the nominal operating frequencies of the two AOMs (-75 MHz and +85 MHz) that were used in series to generate the Doppler shifts (see Fig. 3.1). Nevertheless, this does not affect the validity of the experiments presented here.
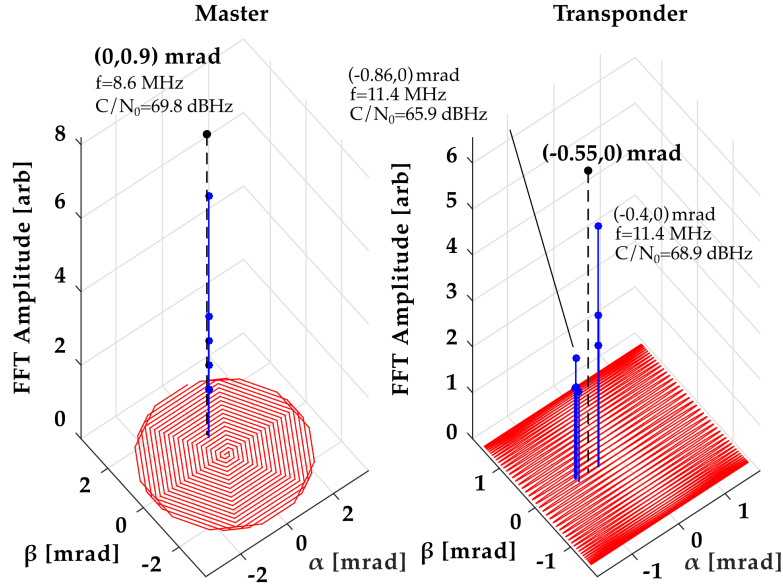
Figure 3.14: One example of a spatial scan result when using two independent lasers, but without frequency scan [67]. The lasers were manually set to be within the QPR bandwidth at the start of the spatial scan. The master laser was locked to an iodine frequency standard, while the transponder laser was left free running. The true LOS values were: $\left(\alpha_M^0, \beta_{,M}^0\right) = (0,1)$ mrad and $\left(\alpha_T^0, \beta_T^0\right) = (-0.5,0)$ mrad. The best estimate of the LOS, derived by calculating the weighted mean of the flashes were: $(\alpha_M, \beta_M) = (0,0.9)$ mrad and $(\alpha_T, \beta_T) = (-0.55,0)$ mrad. These values are marked by a black dashed line.

The maximum received power for perfect alignment was again set to 80 pW per segment. The amplitudes of the hexagonal and Lissajous scans were set to 1.5 mrad. The scanning frequencies for the Lissajous scan were adapted to $f_{yaw} = 100$ Hz and $f_{pitch} = 2.08$ Hz. This caused the grid error of the Lissajous scan to change to 50 µrad, which is slightly smaller than the LRI value. The grid error of the hexagonal scan was adapted to match the LRI value of 100 µrad.

The first tests consisted of an angular scan while the two lasers frequencies where manually kept within the QPR bandwidth, i.e. no actual frequency scan was carried out. These tests were equivalent to the ones described in Sec. 3.2.3.1 but using two independent lasers, of which one was drifting and, thus, affecting the heterodyne frequencies. For all test runs that were carried out with two lasers the LOS misalignments were set to:

$$\left(\alpha_M^0, \beta_M^0\right) \quad = \quad (0,1) \text{ mrad} \tag{3.15}$$

$$\left(\alpha_T^0, \beta_T^0\right) \quad = \quad (-0.5,0) \text{ mrad.} \tag{3.16}$$

A representative measurement result is shown in Fig. 3.14. For this test only 100 datapoints. that showed the highest FFT amplitudes, were stored. Still, most of them were simply noise and were also discarded in post-processing. The ones shown in Fig. 3.14 were kept since their amplitudes were clearly above the noise levels. Numerous flashes are visible in Fig. 3.14 with maximum C/N_0 values around 69 dBHz. The best estimate of
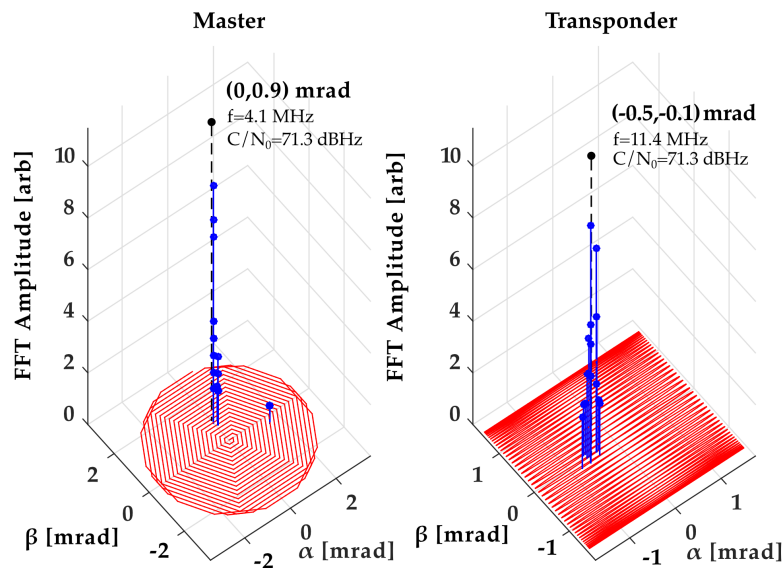
Figure 3.15: Results of a test run that included a frequency and spatial scans [67]. The maximum optical power was set to 135 pW per segment. Lasers were about 35 MHz apart at the beginning of the scan. The master laser was locked to the iodine frequency standard reference, while the transponder performed a frequency scan at a rate of 12.5 kHz/s. The best estimate of the misalignment angles that were calculated as the weighted mean of the flash positions were: $(\alpha_M, \beta_M) = (0, 0.9)$ mrad and $(\alpha_T, \beta_T) = (-0.6, -0.1)$ mrad. These angles are marked by black, dashed lines.

the misalignment angles was obtained by calculating the weighted mean FSM position of all flashes while taking into account the C/N_0 at the peaks. The weighted mean angles are indicated in Fig. 3.14 by black, dashed lines. As a result, the obtained positions of the flashes were $(\alpha_M, \beta_M) = (0, 0.9)$ mrad and $(\alpha_T, \beta_T) = (-0.55, 0)$ mrad. These values must be compared with the introduced misalignment angles from Eqs. (3.15) and (3.16). Within the uncertainties provided by the grid error and the correction of the fast Lissajous scan, the found FSM angles agreed well with the introduced misalignment angles.

An actual frequency scan was finally introduced to put to test the complete initial acquisition procedure. The remaining scan parameters amplitude, frequency and grid error were kept the same. The lasers' frequencies were initially separated by about 35 MHz. The transponder laser frequency was scanned at an average rate of 12.5 kHz/s. Considering the QPR bandwidth of ~25 MHz (cf. Fig. 3.9) and some margin, the scans were stopped after about $^{70\,\text{MHz}}/_{12.5\,\text{kHz/s}} \approx 90$ min. Unfortunately, none of the scans that were carried out in this manner led to detections. Therefore, the maximum RX power was increased from 80 pW to 135 pW per segment, i.e. 540 pW for the whole QPR. This value was closer to the expected maximum RX laser power for the LRI of about ~500 pW, for a S/C separation of 270 km.

The result of a scan that was executed with this increased power is shown in Fig. 3.15. The obtained angles at which the flashes occurred, were $(\alpha_M, \beta_M) = (0, 0.9)$ mrad and

Master (Hexagonal Scan)
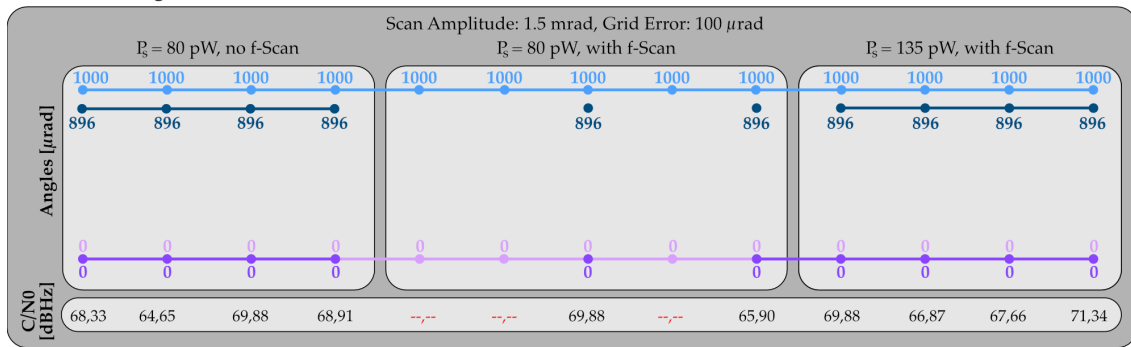
Transponder (Lissajous Scan)
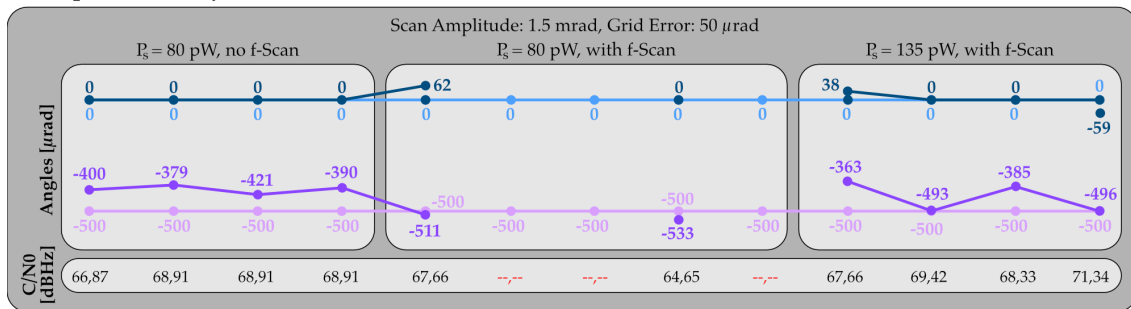
Figure 3.16: Summary of the scans that included spatial scans and frequency scanning on the transponder side. Top panel: master OB (hexagonal scan). Bottom: transponder OB (Lissajous scan). The colored numbers along the course of the curves indicate the angles at which flashes occurred in µrad. The C/N_0 values for each of the scan runs are also shown, in units of dBHz, below the respective plots. If no flash was recorded, a C/N_0 of –.– is provided.

$(\alpha_T, \beta_T) = (-0.6, -0.1)$ mrad. Again, these must be compared to the pre-set misalignment angles, shown in Eqs. (3.15) and (3.16). Taking into account the grid error and the uncertainties of the FSM angle correction algorithm, it can be stated that the estimated LOS misalignments agreed well with the pre-set values.

Figure 3.16 summarizes the results that were obtained during all the tests with spatial scans on the two OBs and frequency scanning of the transponder laser. Again, the obtained and introduced ("true") angles in yaw and pitch are plotted. The corresponding C/N_0s of the detections are plotted below the angles. As can be obtained from the figure, five of all 13 performed scans were unsuccessful. All these failures occurred when the frequency was scanned and when the maximum optical power per segment remained at 80 pW. An increase of the maximum RX power to 135 pW per segment yielded successful scan results. This indicates that the noise of the used QPRs was too high compared to the low RX power levels (cf. Eqs. (3.12) and (3.13)).

3.3 Summary

The results presented in this chapter represented a further step in the experimental verification of the initial acquisition procedure for the GRACE-FO LRI. The presented tests included conditions that were not considered in previous experiments [70, 71]. These included realistic RX power levels as a function of TX beam misalignments, use of top-hat RX beams and the presence of MHz Doppler frequency shifts. In addition, the specifically designed OBs, including the QPRs and FSMs, the phasemeters and lasers served as proper mock-ups of the LRI. The measurement data was obtained and stored in a similar way as it happens in the real LRI.

Different configurations and spatial scan parameters have been tested. By performing a correction of the FSM data during the Lissajous scans, as was detailed in Sec. 3.2.2.2, unambiguous detections could be made and the estimated LOS offsets were found to be in good agreement with the expected values. This was the case despite the maximum received power being set slightly lower than the expected in flight power for a majority of the test runs. Only in the final set of tests, during which also the transponder laser frequency was scanned, the RX laser power had to be increased because no detections could be recorded. This increase immediately led to unambiguous detections. Thereby, the optical power level was still at the lower range of values that were expected for the LRI.

Overall, the results obtained in this test campaign validated the robustness of the initial acquisition procedure. At the time when they were conducted, the experiments provided valuable insights for the whole GRACE-FO LRI team in the process of preparing for the in-orbit calibration phase of the instrument.

As was mentioned earlier, the test campaign was also foreseen to prove the functionality of the Fiber OGSE. With the successful results that were detailed above, also this purpose could be accomplished. As a result, nothing stood in the way of the Fiber OGSE being used as valuable test equipment for the development of the LRI on board of the GRACE-FO S/C. Figure 3.17 shows a photograph of a cleanroom at STI near Immenstaad, Germany, with all the LRI sub-units mounted to optical tables during testing of the instrument. The figure also shows the Fiber OGSE as it is attached to interface simulators on the same optical tables (see the red boxes). Figure 3.18 shows the Fiber OGSE attached to the S/C in a cleanroom at Airbus Defence & Space in Friedrichshafen. The Fiber OGSE accompanied the LRI from testing on sub-system level at STI, throughout the instrument integration into the S/C at Airbus Defense & Space, to system level testing at IABG facilities near Munich, Germany, to the final tests at SpaceX cleanrooms on the Vandenberg Airforce Base, California, USA just before the launch of GRACE-FO on May 22nd, 2018.
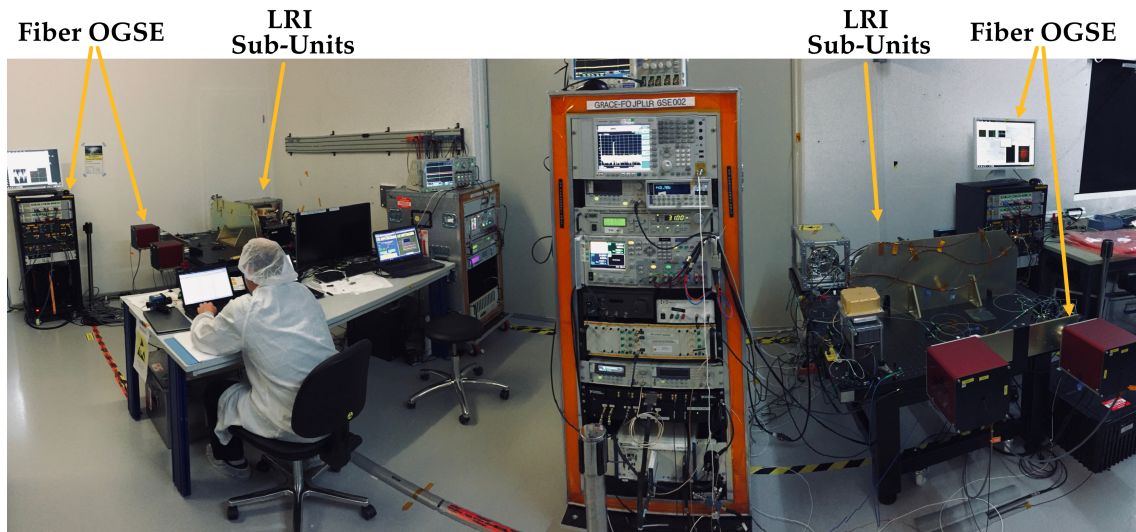
Figure 3.17: The photograph shows the LRI during sub-system level testing in a cleanroom at STI facilities near Immenstaad, Germany. The Fiber OGSE is attached to S/C interface simulators (see the red boxes and racks at the left and right sides of the image). The usage of the photograph was kindly permitted by STI and JPL.
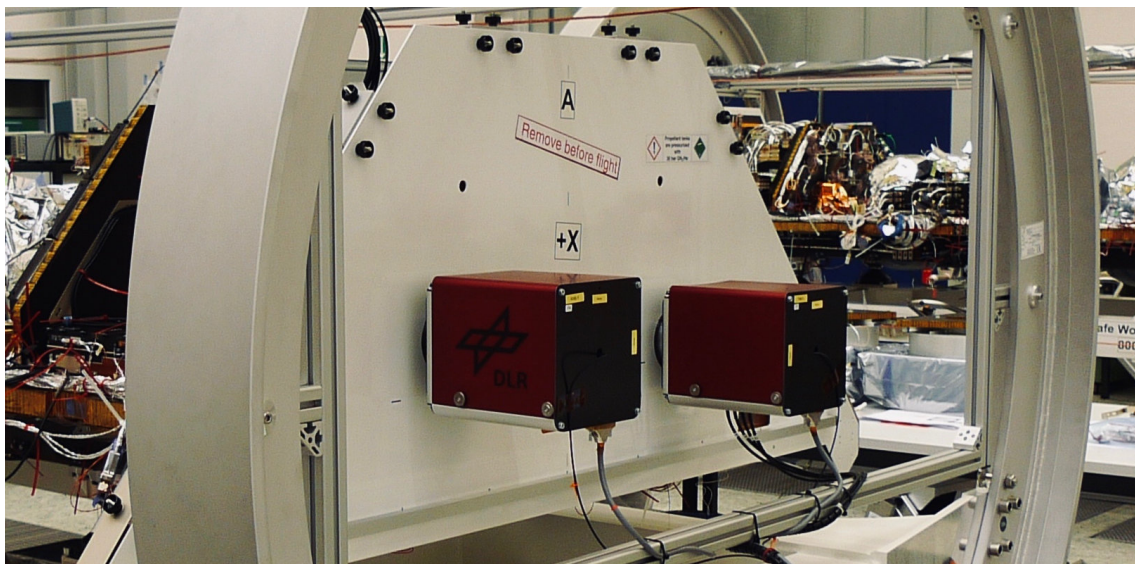
Figure 3.18: The picture shows the Fiber OGSE attached to one of the GRACE-FO S/C in a cleanroom at Airbus Defence & Space in Friedrichshafen, Germany. The usage of the photograph was kindly permitted by Airbus Defence & Space.

Chapter 4

Processing of LRI in-orbit measurements

This chapter presents detailed analyses of actual flight data, in contrast to the simulations and laboratory experiments that were presented previously. First, the data obtained in the LRI's initial laser link acquisition runs from June 13th and 14th, 2018 is presented and analyzed. This analysis led to the unambiguous detection of the angular line of sight (LOS) offsets of the LRI on both S/C and the frequency offset of the transponder laser with respect to the master. Immediately after uploading the obtained set-points to the S/C, the LRI transitioned into the science mode on the first try.

In the second part of this chapter, flight data is used to analyze small TMA imperfections, the so-called co-alignment errors (CAEs). These misalignment angles would cause a drop of the optical power that is received by distant the S/C if they are not compensated for. Not only are the CAEs quantified, but also a trade-off study is presented which shows how these angles can be optimally compensated.

4.1 As-run initial laser link acquisition

On June 13th and 14th, 2018 the LRI was commanded to run two initial laser link acquisition scans. Each acquisition run took about 9 hours to complete. Two runs were scheduled in order to allow a swap of the S/C master and transponder roles. This was done to verify the functionality of all LRI sub-units on both S/C, e.g. the cavities which are only used on the S/C which is in the master mode. Additionally, it allowed for a slightly more robust statistical analysis, as not only one, but two sets of data per S/C could be analyzed.

As was detailed in the previous chapters, during the initial acquisition procedure the fast steering mirrors (FSMs) perform spatial scans while the laser frequency on the transponder S/C is swept. The fast Fourier transform (FFT) amplitudes of the beat note signals are recorded together with the current FSM angles and the frequency set-point (only on the transponder S/C). During the initial acquisition runs, hundreds of datapoints with high SNR were recorded by each S/C.

Figure 4.1: The figure illustrates the definition of the LRI optical reference frame LOF.
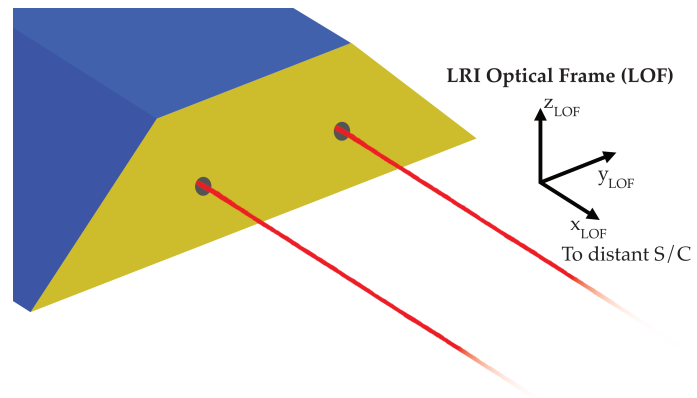
The master FFT amplitudes and FSM angles are readily usable and directly provide a best estimate of the local S/C misalignment with respect to the LOS (see e.g. the right plot in Fig. 4.4). The data from the transponder S/C, however, shows a slightly distorted scan pattern with respect to its fast scan axis which is actuated with a frequency of $f = 100\,\text{Hz}$ (see Figs. 4.3 and 4.4). This behavior was expected and already studied extensively on ground. The reason for this is an electronic delay on the order of $\sim$175 µs between the reporting of the measured FSM angles (the so-called Position Sensing Subsystem (PSS) readings) and the corresponding FFT amplitude. This delay must not be confused with the error between the commanded and performed FSM scans in the laboratory experiments, depicted in Chapter 3.

The delay needs to be identified before the transponder measurements can be used to obtain a best estimate of the transponder's LOS misalignment. It can be neglected for the hexagonal scan angles on the master S/C and the slow axis of the transponder scan, as the FSM here can be considered stationary on the time scales of the FFT-to-PSS delay.

4.1.1 Estimation of the FFT-to-PSS readout delay

A set of MATLAB scripts was developed to estimate the FFT-to-PSS delay from raw data, that was recorded by the Laser Ranging Processors (LRPs). These scripts were adapted from a collection of Python scripts that were initially developed by C. Mahrdt at the AEI for the analysis of simulated initial acquisition data.

After loading the raw initial acquisition data, various scaling factors are applied. These corrections ensure that the considered angles describe *optical* beam tilts (in contrast to the mechanical tilt angles of the FSM) and are referred to the LRI optical frame (LOF) (see Fig. 4.1). In a next step, the so-called *reference direction* is subtracted from the FSM angles. This is a unit vector that represents the current best estimate of the LOS that is sent to the LRPs by the S/C main computer. The LRPs then add this vector onto the FSM pointing commands. If this were omitted, S/C attitude jitter would couple into the current LRI pointing substantially, as the S/C orbit the Earth about six times during one complete initial acquisition scan. This must then be reversed in post-processing of the FSM data.
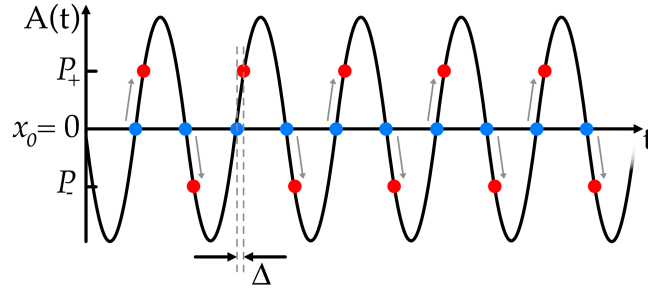
Figure 4.2: The figure illustrates the effect of a readout delay on the recorded FSM angles. The solid black line illustrates a sinusoidal oscillation of an FSM with an arbitrary frequency. The blue dots mark the FSM angle that should be recorded (here chosen to be zero, $x_0 = 0$). Due to the delay Δ, the LRP associates the FSM angles shown in red (P_+ and P_-) with the FFT peaks.

Figure 4.2 shows a sinusoidal oscillation with amplitude A(t) and illustrates the effect of a delay Δ on the readout of an instantaneous angle x_0. Transferring the situation that is illustrated in Fig. 4.2, to the oscillation of an FSM, a PSS reading in one axis, $P(t)$, can be described as

$$P(t) = v(t) \cdot \Delta + x_0(t). \tag{4.1}$$

Here, $x_0(t)$ is the true FSM angle. $v(t)$ is the velocity of the FSM at time t and Δ the delay. As can be obtained from the figure, the recorded FSM angles are either too large or too small, depending on the current scan direction, i.e. the sign of $v(t)$. The fact that $v(t)$ can be positive and negative can be used to estimate the delay. The mean value of the recorded PSS readings, $\overline{P}_\pm$, can be expressed as a function of the delay Δ, the mean of the corresponding FSM velocity $\overline{v}_\pm$ and the true FSM angle x_0:

$$\overline{P}_+ = \overline{v}_+ \cdot \Delta + x_0 \tag{4.2}$$

$$\overline{P}_- = \overline{v}_- \cdot \Delta + x_0. \tag{4.3}$$

As the FSMs on the transponder S/C perform pure sinusoidal oscillations, their velocities can easily be calculated as the derivative of the known commanded scan. Based on their position along the scan track, the PSS angles are then divided into subsets with positive and negative entries. The same is done for the corresponding velocities. $\overline{P}_\pm$ and $\overline{v}_\pm$ are then simply calculated as the mean of the respective set of values. Using these parameters and combining Eqs. (4.2) and (4.3) yields the sought for delay:

$$\Delta = \frac{\overline{P}_+ - \overline{P}_-}{\overline{v}_+ - \overline{v}_-}. \tag{4.4}$$

4.1.2 Results of the initial acquisition runs

Figure 4.3 shows FFT amplitudes as a function of the raw FSM angles that were recorded by GF-1 on June 13th, 2018 when it was set to the transponder role. As can be seen in the plot, numerous datapoints were obtained. A cross-shaped distribution of the FFT
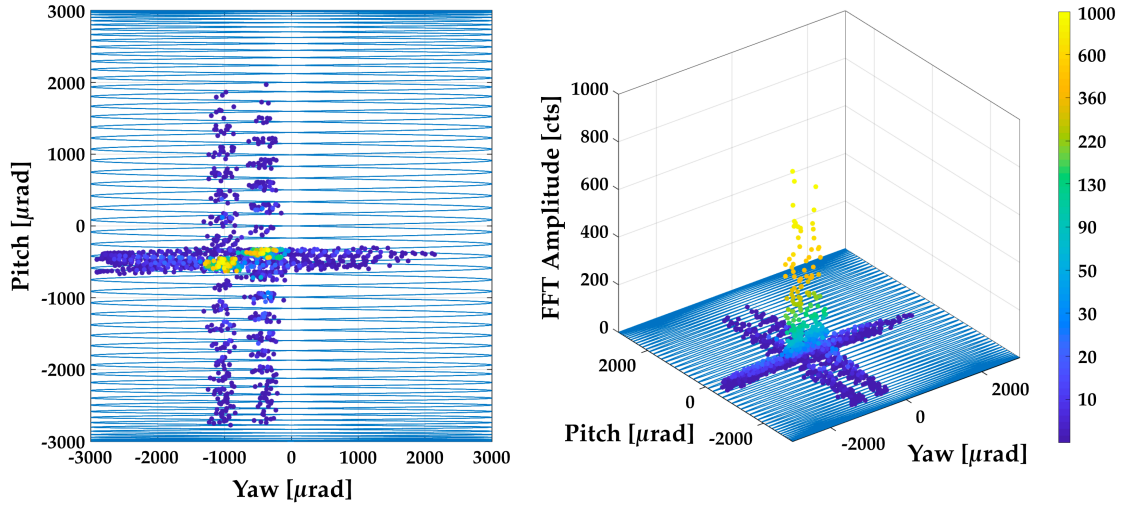
Figure 4.3: Top and side views of FFT amplitudes as a function of the raw FSM angles that were recorded by GF-1 in transponder mode. The initial acquisition run from June 13$^{\text{th}}$, 2018 was evaluated.

amplitude is visible which is caused by the insensitive slits of the QPRs [46]. Also clearly visible is a double peak structure of the FFT amplitudes which is caused by the FFT-to-PSS readout delay Δ.

This data was processed with the procedure that was outlined in the previous section. A threshold was implemented in order to prevent the low amplitude detections in the side lobes of the cross-shaped distribution of the FFT peaks (see Fig. 4.3, especially the wide-spread region around a pitch angle of $\sim$-600 µrad) from influencing the delay. Datapoints, whose FFT amplitudes were below 100 counts, were not used for the estimation of the delay. With this procedure, the following FFT-to-PSS delay on GF-1 could be obtained:

$$\Delta_{\text{GF}-1} = -175\,\mu\text{s}. \tag{4.5}$$

The left plot in Fig. 4.4 shows the peak FFT amplitudes as a function of the FSM angles that were corrected by $\Delta_{\text{GF}-1}$.

The LOS misalignment angles were then obtained by calculating the weighted sum of the corrected FSM angles. For the i-th yaw, α_{i}, and pitch angle, β_{i}, the weighting function w_i was defined as the normalized FFT amplitude $A_{\text{FFT,i}}$:

$$w_i = \frac{A_{\text{FFT,i}}}{\sum\limits_{i=1}^{n} A_{\text{FFT,i}}} \tag{4.6}$$

with the total number of datapoints n .
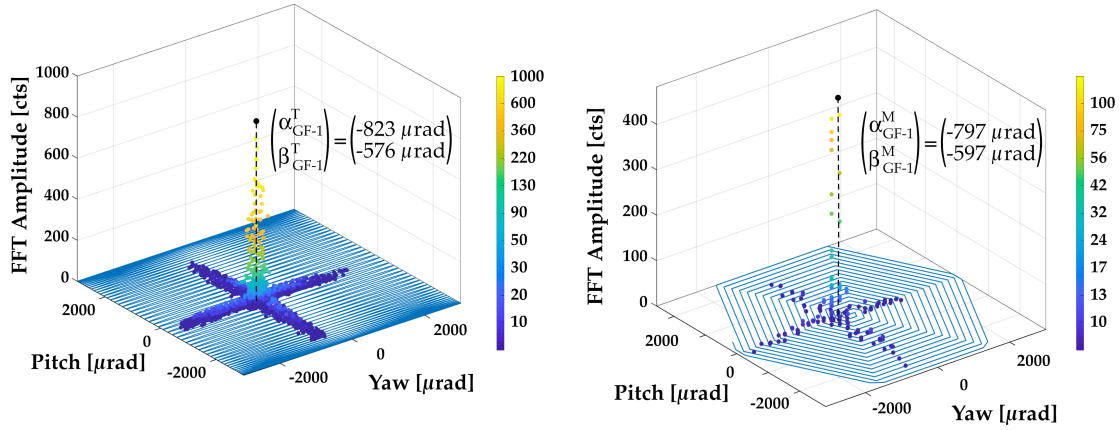
Figure 4.4: The figure shows plots of the peak FFT amplitudes that were recorded by the LRI on **GF-1**. The plot on the left shows the results that were obtained in transponder mode on June 13th, 2018 and the plot on the right shows the results from master mode, which were obtained on June 14th. The dashed lines indicate the obtained LOS offsets.

The yaw and pitch LOS misalignment angles then follow as:

$$\alpha = \sum_i (\alpha_i \cdot w_i) \tag{4.7}$$

$$\beta = \sum_i (\beta_i \cdot w_i) . \tag{4.8}$$

The LOS misalignment angles of GF-1 in transponder mode that were found with this method were:

$$\alpha_{GF-1}^{T} = -823\,\mu\text{rad} \tag{4.9}$$

$$\beta_{GF-1}^{T} = -576\,\mu\text{rad} \tag{4.10}$$

for yaw and pitch, respectively (see Fig. 4.4). It should be mentioned that the LRI on GF-1 was misaligned with respect to the LOS by $\left(-\alpha_{GF-1}^{T}, -\beta_{GF-1}^{T}\right)$. The angles that were presented above compensate this misalignment and, therefore, have the opposite sign.

The total uncertainty space for these angles was ± 3 mrad [66]. The fact that the obtained values are within ± 1 mrad is an indicator for the high precision of the integration of the LRI sub-systems as well as the structural stability of the S/C. Additionally, a frequency set-point for the transponder laser was found. Also this value was well within its expected uncertainty range. As the frequency offset shows a strong dependency on temperature. Hence, the number that was obtained in the summer of 2018 is not very informative and is therefore omitted here.

The right plot in Fig. 4.4 shows the results that were obtained for GF-1 when it was set to master role during an initial acquisition scan that was carried out on June 14th, 2018. The FSM angles do not need to be corrected by the FFT-to-PSS delay here, as the master (hexagonal) scan is slow compared to the delay.
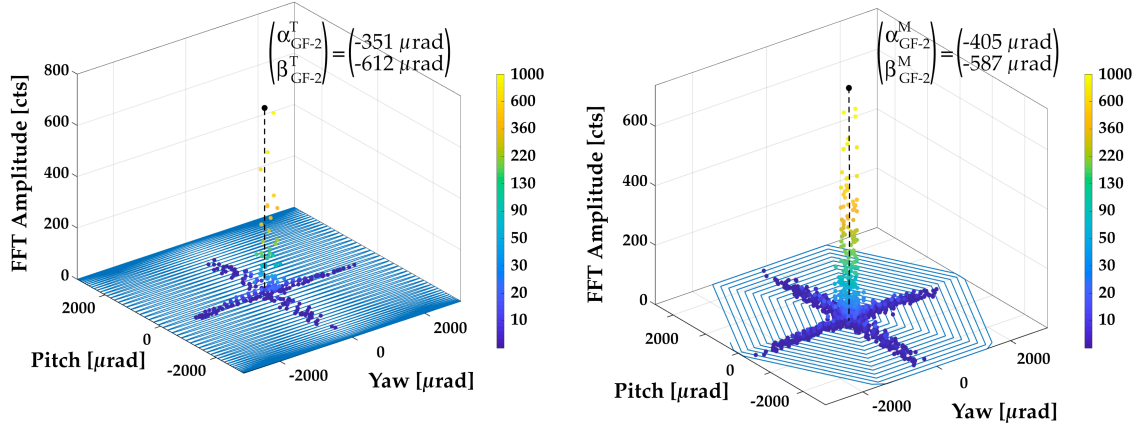
Figure 4.5: The figure shows the results of the initial acquisition scans obtained on **GF-2**. On June 13th, 2018 GF-2 was set to the master role (right figure) and on the 14th it was set to the transponder role (left figure). The dashed lines indicate the obtained LOS offsets.

The LOS offsets that were obtained from this scan, were

$$\alpha_{\text{GF}-1}^{\text{M}} = -797\,\mu\text{rad} \tag{4.11}$$

$$\beta_{\text{GF}-1}^{\text{M}} = -597\,\mu\text{rad}. \tag{4.12}$$

The differences between the measurements in transponder and master role are $\delta\alpha_{\text{GF}-1} = 26\,\mu\text{rad}$ and $\delta\beta_{\text{GF}-1} = 21\,\mu\text{rad}$. Such small deviations were expected. They can be explained by the grid error of the scan patterns, errors from imperfect information on the S/C reference directions and temporal variations of the LOS misalignment. Furthermore, they are well below the scan range of the re-acquisition scans of $\pm300\,\mu\text{rad}$ which means that the remaining uncertainty of the GF-1 LOS offset did not impose any risk to the establishment of the laser link (see Sec. 2.2.5).

Figure 4.5 shows the results that were obtained from the two initial acquisition scans that were carried out by GF-2. Again, the left plot shows the results obtained in transponder mode (from June 14th, 2018) and the right plot shows the results from master mode (from June 13th, 2018). The Lissajous scan data was corrected with the procedure that was detailed in the previous section. For the estimation of the FFT-to-PSS delay, again only those datapoints were used, whose FFT amplitude exceeded 100 counts. The obtained delay was

$$\Delta_{\text{GF}-2} = -179\,\mu\text{s} \tag{4.13}$$

which is in good agreement with the value that was obtained for GF-1: $\Delta_{\text{GF}-1} = -175\,\mu\text{s}$. The LOS offset angles that were found while the LRI on GF-2 was in transponder mode was:

$$\alpha_{\text{GF}-2}^{\text{T}} = -351\,\mu\text{rad} \tag{4.14}$$

$$\beta_{\text{GF}-2}^{\text{T}} = -612\,\mu\text{rad}. \tag{4.15}$$

The LOS offsets that were obtained from the master scan were:

$$\alpha^{\mathrm{M}}_{\mathrm{GF}-2} = -405\,\mu\mathrm{rad} \tag{4.16}$$

$$\beta^{\mathrm{M}}_{\mathrm{GF}-2} = -587\,\mu\mathrm{rad}. \tag{4.17}$$

The LOS offsets obtained in master and transponder role differ by $\delta\alpha_{\mathrm{GF}-2} = 54\,\mu\mathrm{rad}$, for yaw, and $\delta\beta_{\mathrm{GF}-2} = 25\,\mu\mathrm{rad}$, for the pitch angle. Again, these values are well below the re-acquisition scan range. Also, with GF-2 in transponder mode, an unambiguous frequency set-point could be found whose absolute value is again omitted here for the same reason as above.

4.2 In-flight analysis of TMA co-alignment errors

The triple mirror assemblies (TMAs) on-board of the GRACE-FO S/C play a central role in the architecture of the LRI (see Sec. 2.1.1.1). They consist of three mutually perpendicular mirrors which form a virtual retroreflector. The mirrors are connected by a 60 cm long carbon fiber reinforced polymer (CFRP) tube. Due to the TMAs' unique properties, the LRI effectively measures the intersatellite distance from the center of mass (CoM) of one S/C to the CoM of the other (see Sec. 2.1.1.2). Furthermore, the LRI relies on another key property of a retroreflector: the outgoing laser beam stays anti-parallel to the incoming beam, even under rotations of the TMA.
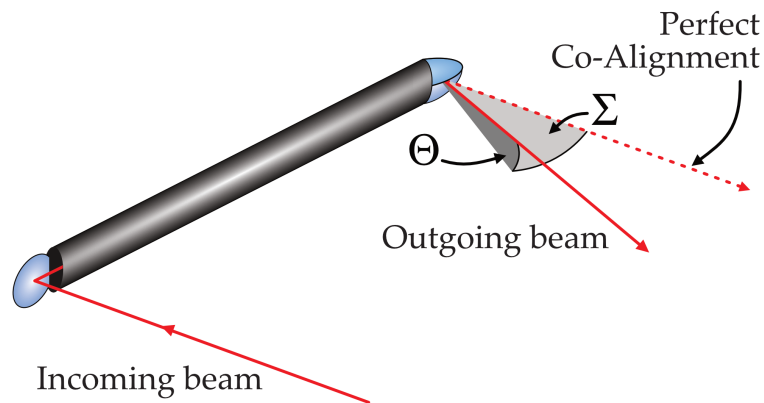
Figure 4.6: The figure shows a TMA with imperfectly aligned mirror surfaces. This results in a so-called co-alignment error (CAE) of the outgoing laser beam with respect to the incoming beam. The horizontal (yaw) component of the CAE is labeled Σ and the vertical component (pitch) Θ. If the three mirror surfaces were perfectly perpendicular to each other, incoming and outgoing laser beams would be perfectly anti-parallel. The CAE is shown exaggerated.

The parallelism of the two laser beams is a direct consequence of the perpendicularity of the TMA's three mirror surfaces. Hence, small angular misalignments between the mirror surfaces are translated to so-called co-alignment errors (CAEs) of the incoming and outgoing laser beams (see Fig. 4.6 and the Appendix of [44]).

Because the TMA is placed in the path of the TX laser beam behind the OB, these small CAEs are not measurable on the local OBs (cf. Fig. 2.2). As the RX laser beams can be considered to have spherical wavefronts, the heterodyne efficiency on the receiving S/C is, at least to first order, not affected by the CAE on the transmitting S/C. The CAE there manifests itself as a reduction of the received laser power.

The CAEs were subject to many measurement campaigns and detailed analyses on ground. The latest on-ground measurements that were carried out at the Vandenberg Airforce Base on December 19th and 20th, 2017 yielded CAEs in yaw (Σ) and pitch (Θ) of

$$(\Sigma, \Theta)_{\text{GF}-1} = (28, -107) \; \mu\text{rad} \tag{4.18}$$

$$(\Sigma, \Theta)_{\text{GF}-2} = (48, 72) \; \mu\text{rad}. \tag{4.19}$$

These values were measured at $20°\,$C and corrected for deformations due to the gravity on ground of $1\,$g, such that they describe the anticipated CAEs in orbit. However, it was expected that the values in orbit differ from the ground measurements due to several effects: insufficiently modeled deformations due to the gravity on ground vs. $0\,$g in orbit, outgassing of the CFRP and the glue, as well as temperature dependent distortions of the TMA components.

Therefore, as part of the commissioning phase of the LRI, on July 18th, 2018 a dedicated procedure was executed to identify the CAEs of the two TMAs in orbit. In order to monitor possible temporal variations of the CAEs, follow-up tests were carried out. For this thesis, in total three such tests were evaluated: one test from July 2018 and two from June 2019. After the completion of this thesis, more tests were scheduled. An overview of the design, manufacturing and testing of the TMAs was being prepared for publication by the time of writing of this thesis.

This section is structured as follows: First, the procedure is explained which was carried out to identify the CAEs. The recorded data is then used to estimate the CAEs of the two TMAs. Eventually, a trade-off analysis to identify DWS offsets which optimally compensate the CAEs is presented.

4.2.1   The DWS offset scan procedure

In this section, the procedure that was carried out to identify the CAEs is explained. It is based on the application of dedicated differential wavefront sensing (DWS) offsets. The procedure that was carried out on July 18th, 2018 is explained in detail. The two scans that were carried out in the summer of 2019 used the same pattern, but fewer datapoints. The motivation for this was to reduce the required scanning time. Additionally, the temperature of the TMA was varied between the three different scans to check for a possible temperature dependency of the CAEs.

From this two-dimensional scan on each S/C, the CAEs could be estimated by identifying
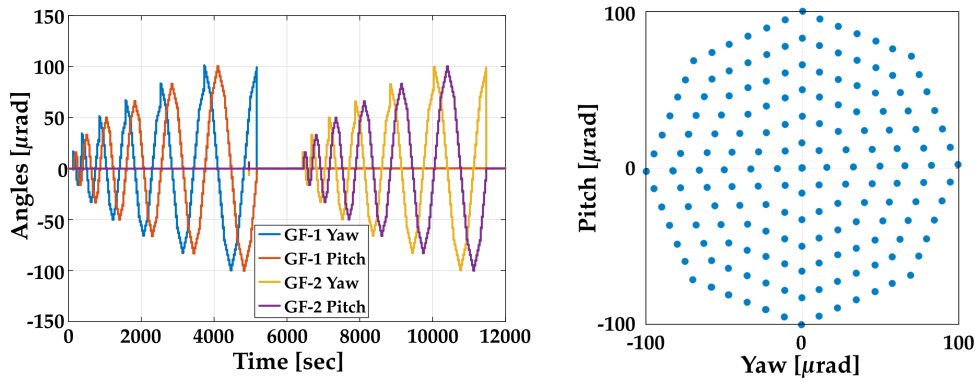
Figure 4.7: Sequence of the DWS offset scans on the two S/C (left) as well as a 2D representation of the scan pattern (right). The DWS offsets were converted to units of FSM angles.

those DWS offsets at which the maximum RX power was measured. Thereby, GF-1 records a maximum RX power when GF-2 applied a DWS offset that compensated its local CAE and vice versa.

4.2.1.1   Description of the DWS offset scan procedure

The DWS offset scan procedure was executed while the LRI was in science mode. Hence, both S/C tracked the local heterodyne beat note and the DWS control loops were locked. This ensured that the local oscillator (LO) was kept parallel to the RX laser beam on both S/C. That means that for small misalignments of those two laser beams, which can occur due to S/C attitude jitter, an error signal is produced by the DWS readout. This is forwarded to the FSM which then compensates the S/C motion.

Within the procedure that is explained in this section, deliberate DWS offsets were added to these small error signals. These caused the local heterodyne efficiency to decrease, because RX and LO beams were no longer aligned to each other. Additionally, the RX power on the distant S/C was affected. The DWS offsets were applied on one S/C first and then on the other. Figure 4.7 shows the sequence of the DWS offsets as well as a 2D representation of the scan pattern.

4.2.1.2   Description of the analyzed signals

The photocurrents from the two redundant QPRs on each S/C are nominally summed up segment-wise in the analog domain. Thus, for each S/C four heterodyne beat note amplitudes can be analyzed. These are referred to as the four *channels* of the QPR. The heterodyne amplitude of channel j, A_j, is calculated by combining the I and Q values (see [52]) of the respective dPLLs, i_j and q_j, while taking into account the digital gain g_j that is

introduced by the LRP:

$$A_j = g_j^{-1} \cdot \sqrt{i_j^2 + q_j^2}. \tag{4.20}$$

These amplitudes can be combined to form the so-called *incoherent sum* S^{ICS}:

$$S^{\mathrm{ICS}} = A_1 + A_2 + A_3 + A_4. \tag{4.21}$$

Another quantity that is calculated by the LRPs is the *coherent sum* S^{CS} of the four QPR channels (also referred to as the "phaselocker" channel). This is the signal that the transponder LRP uses to lock the local laser to. It is defined by the addition of the four channels' complex amplitudes, taking into account the respective electrical phase ϕ_j:

$$S^{\mathrm{CS}} = A_1 e^{i\phi_1} + A_2 e^{i\phi_2} + A_3 e^{i\phi_3} + A_4 e^{i\phi_4}. \tag{4.22}$$

In practice, the coherent sum does not need to be calculated manually, because the LRP directly records it in units of an ASD. In the binary data that is stored by the LRP this parameter is called "fftSNR". More details on the calculation of the coherent and incoherent sums of QPR segments in the LRI-context can be found in [83].

Additionally, the noise spectral density of the coherent sum of the four channels is recorded by the LRP. To be more precise, the parameters that are recorded are called *noise*$_{89}$ and *noise*$_{11\_12}$. They describe the noise ASD in the frequency range of 8-9 MHz and 11-12 MHz, respectively. If it is assured that the beat note frequency is not within these ranges, which was the case for the presented analysis, the mean value of these two parameters can be used as representation of the noise spectral density, here described by $\tilde{n}_{cs}$. The carrier-to-noise density (C/N_0) of the coherent sum in units of dBHz can then be calculated as:

$$C/N_0 \left(S^{\mathrm{CS}} \right) = 20 \cdot \log_{10} \left(\frac{\mathrm{fftSNR} \cdot \sqrt{f_s}}{\tilde{n}_{cs}} \right). \tag{4.23}$$

A scaling factor of $\sqrt{f_s}$, with $f_s = 10\,\mathrm{kHz}$, is required to convert "fftSNR" from an ASD to rms amplitude.

On both S/C each of the four beat note amplitudes A_j is tracked by an individual dPLL. These dPLLs can only reliably track signals above a certain C/N_0 threshold. It is thus desirable to also know the single channel C/N_0. However, the corresponding single channel noise spectral densities were not recorded by the LRP during the DWS offset scan procedure. It is therefore not straight forward to calculate the C/N_0 of the single channels. A calibration of the single channel C/N_0 in the context of the DWS scans was carried out. It was based on data that was recorded during a different diagnostic scan. This calibration is presented in the next section.
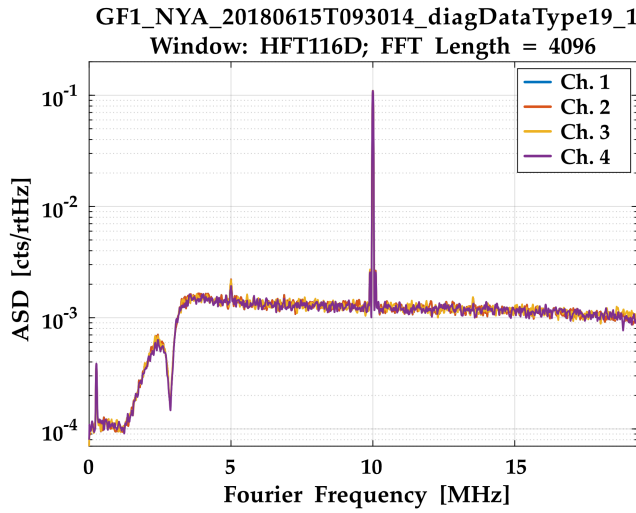
Figure 4.8: ASD of the single channels that were recorded during a diagnostic scan on GF-1 on June 15th, 2018.

4.2.1.3 Single channel C/N$_0$ calibration

On June 15th, 2018 a measurement of the raw ADC voltages of each individual channel was carried out with a high sampling frequency of about 38 MHz [1]. During this diagnostic scan, the S/C were in science mode, the lasers were enabled and the beat note frequency was at 10 MHz. GF-1 was set to the master and GF-2 to the transponder role. From the recorded data, the single channel amplitudes, noise spectral densities and consequently also the C/N$_0$ can be calculated. Under the assumption that the laser power and the single channel noise did not change between June 15th and mid-July, when the first DWS offset scan procedure was carried out, the C/N$_0$ of the individual channels on July 18th can be calibrated.

From the data taken on June 15th, ASDs were calculated (see Fig. 4.8). A flat-top window function (HFT116D, [84]) with an FFT length of 4096 samples was used. Flat-top windows, like the one used for this analysis, are beneficial when reliable estimates of sinusoidal signal amplitudes are of interest. However, they should only be used in situations with high SNR, which was the case for the data used here. The C/N$_0$s of this data were then calculated by dividing the rms amplitudes of the peaks at the beat note frequency of 10 MHz with the mean noise in the frequency bands of 8..9 MHz and 11..12MHz, $\tilde{n}_{8\_9/11\_12}$, according to:

$$\mathrm{C/N}_0\left(A_j\right) = 20 \cdot \log_{10}\left(\frac{A_{j,\mathrm{rms}}}{\tilde{n}_{8\_9/11\_12}}\right). \tag{4.24}$$

The obtained single channel C/N$_0$s are listed in Tab. 4.1. The single channel C/N$_0$s during the DWS offset scan procedure were then estimated by using the recorded single channel amplitudes A_j and adjusting the corresponding noise such that the resulting C/N$_0$s matched the values that are provided in Tab. 4.1.

The C/N$_0$s, obtained from the June 15th data, are only valid for perfectly aligned beams. Therefore, only the amplitudes at those time segments from the July 18th data were used,

---

[1]"GF1_NYA_20180615T093014_diagDataType19_1.bin", "GF2_NYA_20180615T110517_diagDataType19_1.bin"

Table 4.1: Single channel C/N_0s obtained from a diagnostic scan on both S/C with a sampling frequency of $f_s = 38\,\text{MHz}$, carried out on June 15th, 2018.

Spacecraft	Channel	C/N_0 [dBHz]
GF-1	1	84.85
GF-1	2	84.85
GF-1	3	84.65
GF-1	4	84.92
GF-2	1	85.03
GF-2	2	85.03
GF-2	3	84.67
GF-2	4	84.89

where the DWS offsets were zero (see Fig. 4.7). The single channel noise was evaluated in units of digital counts. Their absolute value in this unit is not very informative and is therefore omitted here. With this calibration, the single channel heterodyne amplitudes, as well as the incoherent sums, could be expressed in terms of C/N_0s in units of dBHz.

4.2.1.4   Parametrization of the time series data

For further analysis, each recorded data stream was fitted with a 2D fit as a function of the yaw and pitch angles of the S/C that conducted the DWS offset scan. The following expression was used:

$$I_{\text{fit}} = I_{\text{max}} \cdot \exp\left(-(K_1^2 + K_2^2)\right), \tag{4.25}$$

where

$$K_1 = \frac{(\sigma - \sigma_0) \cdot \cos(\beta) + (\theta - \theta_0) \cdot \sin(\beta)}{w_1} \tag{4.26}$$

$$K_2 = \frac{-(\sigma - \sigma_0) \cdot \sin(\beta) + (\theta - \theta_0) \cdot \cos(\beta)}{w_2}. \tag{4.27}$$

This describes a general expression for a 2D elliptical Gaussian function where the $1/e^2$ width along each axis is defined by w_1 and w_2. The angle β allows for arbitrary rotations of this ellipse. I_{max} is the distribution's maximum amplitude in units of digital counts, σ and θ describe the yaw and pitch angles of the DWS offset scan. σ_0 and θ_0 describe the offsets of the distribution's maximum from zero, along yaw and pitch.

4.2.2   Determination of the co-alignment errors

The CAEs of the two TMAs can be obtained from the DWS offset scans by identifying those FSM angles at which both S/C detect the highest RX power. To be more precise, the respective distant S/C's RX power must be analyzed to obtain information on the local CAE. This is because the DWS offsets at the respective maximum compensate the
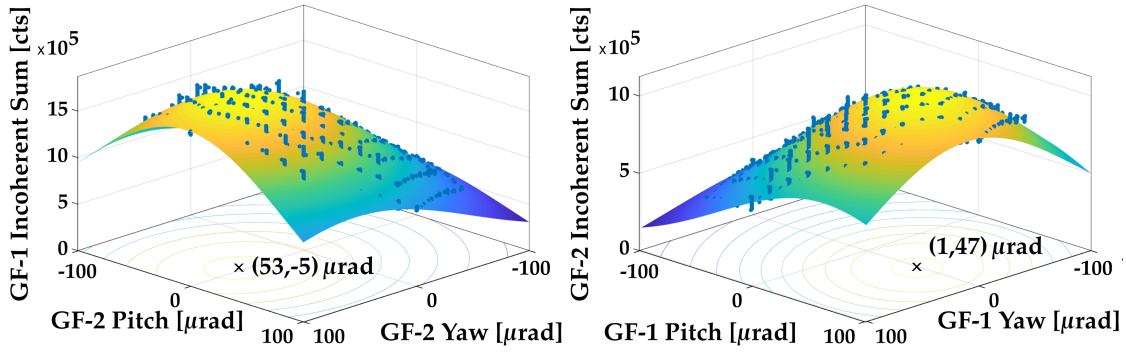
Figure 4.9: Plots of the measured and fitted incoherent sums on GF-2 (left) and GF-1 (right) are shown that were recorded while the respective other S/C applied DWS offsets. The fits were done according to Eq. (4.25). The shown data was obtained during the scans that were carried out on July 18$^{\text{th}}$, 2018. The position of the maxima of both distributions is marked by a cross. All angles describe optical tilts, referred to the LOF.

transmitting S/C's CAE. The incoherent sum of the four QPR channels was used to evaluate the total RX power of a S/C (see Eq. (4.21)).

The position of the maximum of the incoherent sum on GF-1, while GF-2 applied DWS offsets, yields information on the CAE on GF-2. Similarly, to obtain information on the CAE on GF-1, the maximum of the incoherent sum on GF-2 must be searched. By inverting the sign of the found angles, the CAEs of the transmitting S/C's TMA are obtained.

Figure 4.9 shows measurements (blue dots) and fits according to Eqs. (4.25)–(4.27) of $S_{\text{GF-1}}^{\text{ICS}}(\sigma_{\text{GF-2}}, \theta_{\text{GF-2}})$ (left plot) and $S_{\text{GF-2}}^{\text{ICS}}(\sigma_{\text{GF-1}}, \theta_{\text{GF-1}})$ (right plot). The data was obtained during the scans that were carried out on July 18$^{\text{th}}$, 2018. The angles at which the fits have their maxima (σ_0, θ_0) are marked by black crosses. These angles compensate the CAEs of the S/C that conducted the scan. Thus, by inverting them, the CAEs of the TMA on the scanning S/C are obtained. With $(\text{yaw}, \text{pitch}) = (-\sigma_0, -\theta_0) = (\Sigma, \Theta)$ the following CAEs on GF-1 and GF-2 were obtained:

$$(\Sigma, \Theta)_{\text{GF-1}}^{2018} = (-1, -47) \ \mu\text{rad} \tag{4.28}$$

$$(\Sigma, \Theta)_{\text{GF-2}}^{2018} = (-53, 5) \ \mu\text{rad}. \tag{4.29}$$

The provided values are defined as optical angles in the LOF. The TMA's temperature, defined as the value at the TMA thermal reference point (TRP), was 14.5 °C during these scans.

For the second scan, about one year later on June 13$^{\text{th}}$, 2019, the TMA on GF-1 was heated up by almost 6 °C to 20.2 °C. The temperature of the TMA on GF-2 remained at 14.7 °C.

The CAE that were obtained from this data were:

$$(\Sigma, \Theta)_{\text{GF}-1}^{2019-\text{I}} = (10, 6) \ \mu\text{rad} \tag{4.30}$$

$$(\Sigma, \Theta)_{\text{GF}-2}^{2019-\text{I}} = (6, 0) \ \mu\text{rad}. \tag{4.31}$$

A third scan was carried out on June 14$^{\text{th}}$, 2019, one day after the second scan. Here, the temperature of the TMA TRP on GF-1 was 19.3 °C, almost 1 °C cooler than for the second scan. The obtained CAEs were:

$$(\Sigma, \Theta)_{\text{GF}-1}^{2019-\text{II}} = (10, 6) \ \mu\text{rad} \tag{4.32}$$

$$(\Sigma, \Theta)_{\text{GF}-2}^{2019-\text{II}} = (5, 0) \ \mu\text{rad}. \tag{4.33}$$

The same angles were obtained by an independent analysis, that was carried out by other members of the LRI team [85]. The difference of the CAE on GF-2 from June 13$^{\text{th}}$ and 14$^{\text{th}}$ of about 1 µrad is well within the uncertainty range of the used analysis methods and is therefore not considered to be significant. No temperature dependency of the CAEs was observed in these scans. The significant reduction of the CAE on both S/C from the measurement in 2018 to the ones from 2019 can not be attributed to the temperature of the TMAs. This is because the temperature on GF-2 remained very similar to the value from the first scan in 2018. The high CAE that was measured in 2018 is explained by an expansion of the glue that was used to connect the mirrors to each other and the CFRP structure, due to humidity on Earth. The moisture was then gradually released from the glue after the S/C were launched into space, which caused the mirrors to settle into their designed position. This led to a reduction of the CAEs to the values that are provided by Eqs. (4.32) and (4.33).

Before the second and third set of DWS offset scans were performed in 2019, a trade-off study of how to optimally compensate the non-negligible CAEs that were observed in the first measurements by adding dedicated, constant DWS offsets to the DWS control loop set-point was carried out. This analysis is presented in the following sections.

4.2.3 Search for optimal DWS offset angles

As the CAEs have decreased significantly over the first twelve months in orbit, a complicated compensation of this error is not necessary at this moment. However, the TMAs might degenerate in the future. In such a situation, the CAEs might need to be compensated. For the sake of the trade-off study presented in this section, the CAEs that were measured in July, 2018 are used.

The goal of the analysis presented here was to identify yaw and pitch offset angles for the DWS control loops on both S/C that yield an optimum compensation of the CAE of both TMAs. This requires a trade-off study, because the compensation of the CAE implies that the FSMs point the LOs away from the optimum value that the DWS control loop

commands. Hence, a correction of the CAE has the potential of enhancing the RX power at the distant S/C, but at the same time, the heterodyne amplitude on the local S/C is reduced.

The definition of the goal of the trade-off study to "optimally" compensate the CAEs leaves room for various solutions. One attempt at such an optimal solution is presented in this section. First, the current in-orbit situation with zero DWS offsets and the resulting losses due to the presence of CAEs are presented. Here, the loss of each signal is compared to the individual maximum value. The analyzed signals for each S/C are the four heterodyne amplitudes (cf. Eq. (4.20)), as well as their incoherent (cf. Eq. (4.21)) and coherent sums (cf. Eq. (4.22)).

The obtained results are not very representative because the optimization of each of these signals yields different optimal DWS offsets which contradict each other. Obviously, it is not possible to apply a single DWS offset which realizes this optimum for all signals simultaneously. That is why in the next and final part of this section, a figure of merit (FoM) is defined which is then used to derive DWS offsets that optimize those signals that were deemed important. The benefit of the application of optimized DWS offsets is quantified by comparing the gain of each signal with the currently experienced losses that are due to zero DWS offsets.

4.2.3.1 No static DWS offsets

The results that are presented in this section assume the CAEs measured in 2018 (see Eqns. (4.28) and (4.29)).

Without applying any DWS offsets, the CAEs are not compensated. The DWS control loop on each S/C simply ensures that the LO and RX beams are aligned, by maximizing the local heterodyne efficiency. The CAEs only manifest themselves as a drop of the RX power at the distant S/C. The losses of the single channels and of the incoherent and coherent sums of both S/C are summarized in Figs. 4.10 (GF-1 master) and 4.11 (GF-2 master). For this, all signals were expressed in units of dBHz, using Eqs. (4.23) and (4.24). In Figs. 4.10 and 4.11, the total loss in each signal (light blue) is split into the amount that is due to the angles on GF-1 (dark blue) and GF-2 (green).

As can be seen in the figures, the coherent sum on each S/C experiences no loss due to the local DWS offset angles on that S/C. This was expected, because these are the signals that the DWS loops drive to zero. Furthermore, one can see that the by far largest contribution to the single channel losses is the misalignment caused by the respective distant S/C. These two observations visualize the previously mentioned fact that without compensation through DWS offsets, the CAEs manifest themselves only as drops of the RX laser powers.
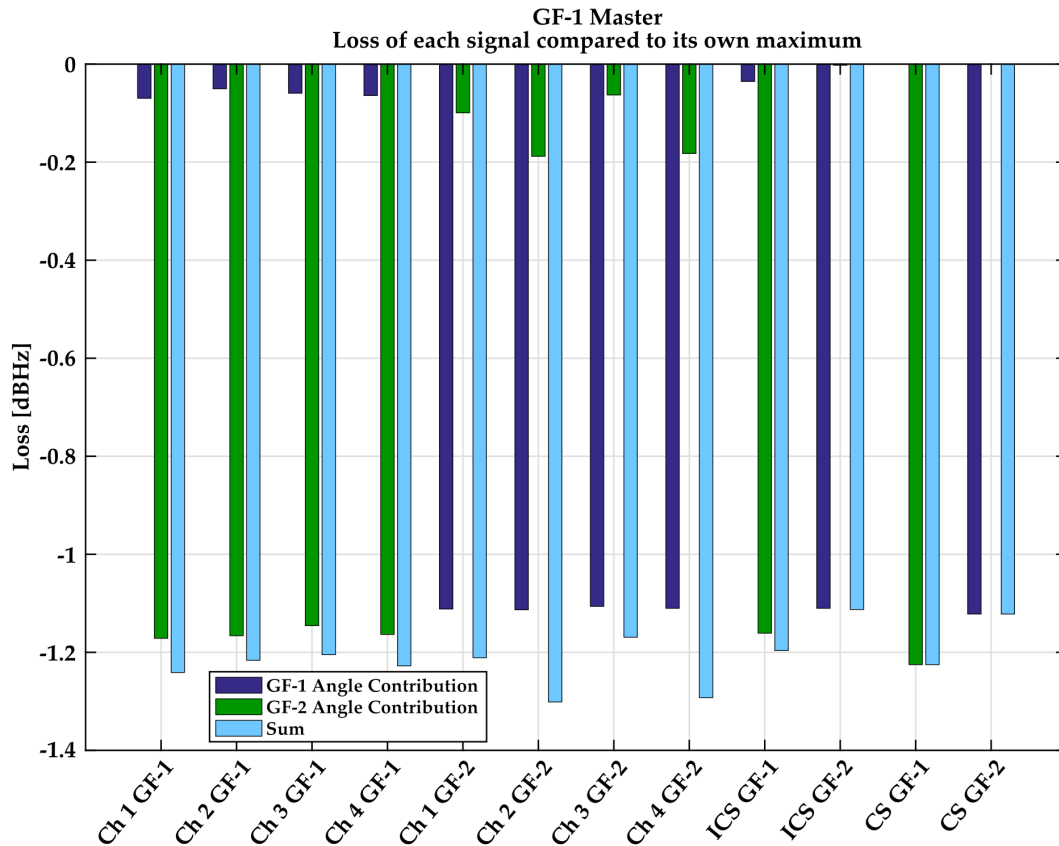
Figure 4.10: The figure shows losses of all signals of interest on GF-1 and GF-2 when no DWS offsets are present. The loss of a signal is referred to its respective maximum. GF-1 was in master role and GF-2 was the transponder.

The loss of each signal, presented in this section, is scaled relative to the signal's own maximum. This means that each signal has by definition a loss of zero dBHz at its respective maximum. Because each signal has its maximum at a slightly different DWS offset, it is obviously not possible to reach this optimum for all signals at the same time. However, in the upcoming description of an optimized compensation of the CAEs, the signal losses with zero DWS offsets serve as a reference because they describe the current situation in orbit. The absolute values of the individual signals' maxima are not important anymore, once the losses after the optimization were expressed relative to the results shown in Figs. 4.10 and 4.11.

4.2.3.2 Definition of a figure of merit

The goal of this analysis is to provide DWS offset angles that optimally compensate the CAEs of the two TMAs. For this optimization, one or multiple figures of merit (FoM) have to be defined.

On the master S/C, the individual QPR channels are tracked in science mode. On the transponder, the coherent sum of the QPR channels is tracked. These signals must be
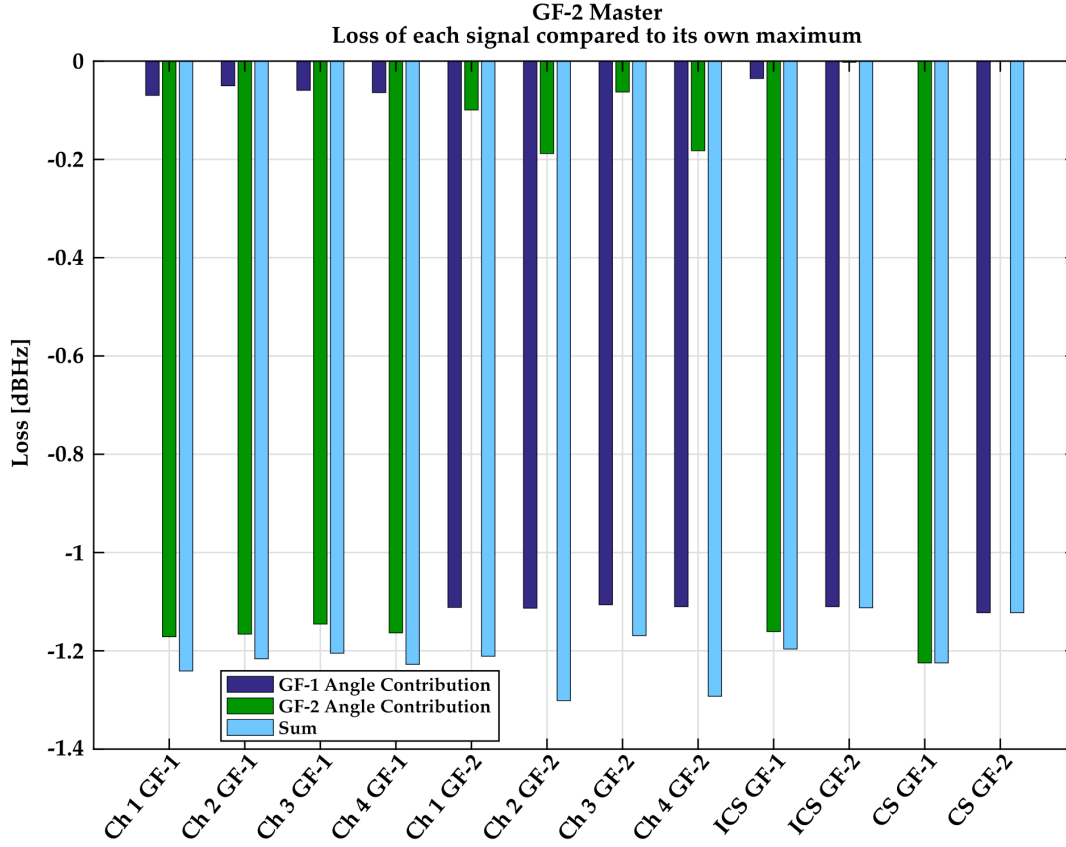
Figure 4.11: The figure shows losses of all signals of interest on GF-1 and GF-2 when no DWS offsets are present. The loss of a signal is referred to its respective maximum. GF-1 was in transponder role and GF-2 was the master.

reflected by the FoM. For simplicity, the incoherent sum of the four channels on the master S/C could be used for the FoM, instead of the individual channels. Both, the coherent and the incoherent sums are functions of all four DWS offset angles $(\sigma_{\mathrm{GF}-1}, \theta_{\mathrm{GF}-1}, \sigma_{\mathrm{GF}-2}, \theta_{\mathrm{GF}-2})$.

These dependencies were accounted for in a three step process. First, the incoherent and coherent sums from both S/C were fitted separately for the scans of GF-1 and GF-2, using Eqs. (4.25)–(4.27). This resulted in eight expressions:

$$S_{\mathrm{GF}-1}^{\mathrm{ICS}}\left(\sigma_{\mathrm{GF}-1}, \theta_{\mathrm{GF}-1}\right) \tag{4.34}$$

$$S_{\mathrm{GF}-1}^{\mathrm{ICS}}\left(\sigma_{\mathrm{GF}-2}, \theta_{\mathrm{GF}-2}\right) \tag{4.35}$$

$$S_{\mathrm{GF}-1}^{\mathrm{CS}}\left(\sigma_{\mathrm{GF}-1}, \theta_{\mathrm{GF}-1}\right) \tag{4.36}$$

$$S_{\mathrm{GF}-1}^{\mathrm{CS}}\left(\sigma_{\mathrm{GF}-2}, \theta_{\mathrm{GF}-2}\right) \tag{4.37}$$

$$S_{\mathrm{GF}-2}^{\mathrm{ICS}}\left(\sigma_{\mathrm{GF}-1}, \theta_{\mathrm{GF}-1}\right) \tag{4.38}$$

$$S_{\mathrm{GF}-2}^{\mathrm{ICS}}\left(\sigma_{\mathrm{GF}-2}, \theta_{\mathrm{GF}-2}\right) \tag{4.39}$$

$$S_{\mathrm{GF}-2}^{\mathrm{CS}}\left(\sigma_{\mathrm{GF}-1}, \theta_{\mathrm{GF}-1}\right) \tag{4.40}$$

$$S_{\mathrm{GF}-2}^{\mathrm{CS}}\left(\sigma_{\mathrm{GF}-2}, \theta_{\mathrm{GF}-2}\right). \tag{4.41}$$

In a next step, each of these functions was normalized, using the amplitude at
$(\sigma, \theta) = (0, 0)\,\mu\text{rad}$ as reference. In a last step, a combined expression for the coherent and incoherent sums was then obtained by multiplying the corresponding pairs. For the incoherent sum on GF-1, this was done according to:

$$\overline{S_{\text{GF}-1}^{\text{ICS}}}\left(\sigma_{\text{GF}-1}, \theta_{\text{GF}-1}, \sigma_{\text{GF}-2}, \theta_{\text{GF}-2}\right) = \overline{S_{\text{GF}-1}^{\text{ICS}}}\left(\sigma_{\text{GF}-1}, \theta_{\text{GF}-1}\right) \cdot \overline{S_{\text{GF}-1}^{\text{ICS}}}\left(\sigma_{\text{GF}-2}, \theta_{\text{GF}-2}\right). \quad (4.42)$$

Thereby, the bars denote the normalization of the expressions. The same procedure was applied to the incoherent sum on GF-2, as well as the coherent sums on GF-1 and GF-2. The sum of these functions was then used for the FoM:

GF-1 Master, GF-2 Transponder:

$$\mathcal{F}_1 = \overline{S_{\text{GF}-1}^{\text{ICS}}}\left(\sigma_{\text{GF}-1}, \theta_{\text{GF}-1}, \sigma_{\text{GF}-2}, \theta_{\text{GF}-2}\right) + \overline{S_{\text{GF}-2}^{\text{CS}}}\left(\sigma_{\text{GF}-1}, \theta_{\text{GF}-1}, \sigma_{\text{GF}-2}, \theta_{\text{GF}-2}\right) \quad (4.43)$$

GF-1 Transponder, GF-2 Master:

$$\mathcal{F}_2 = \overline{S_{\text{GF}-1}^{\text{CS}}}\left(\sigma_{\text{GF}-1}, \theta_{\text{GF}-1}, \sigma_{\text{GF}-2}, \theta_{\text{GF}-2}\right) + \overline{S_{\text{GF}-2}^{\text{ICS}}}\left(\sigma_{\text{GF}-1}, \theta_{\text{GF}-1}, \sigma_{\text{GF}-2}, \theta_{\text{GF}-2}\right) \quad (4.44)$$
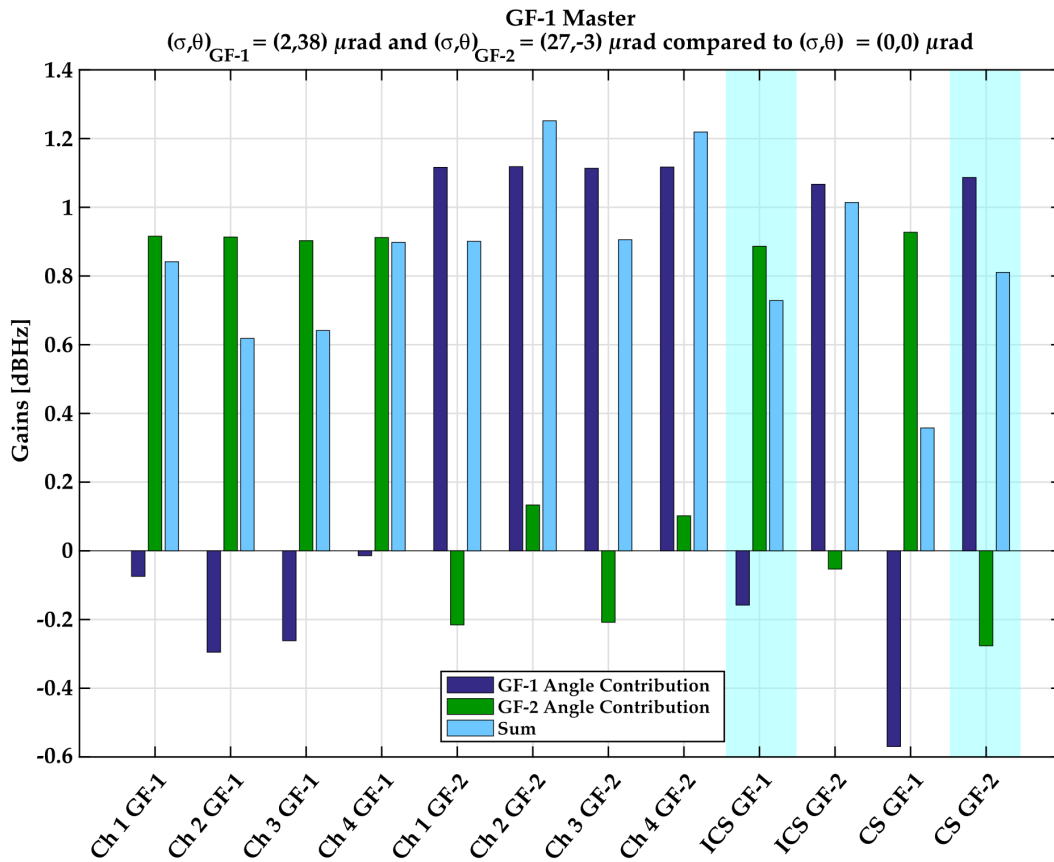
Figure 4.12: The figure shows losses (or gains) of all signals of interest on GF-1 and GF-2 relative to the situation without DWS offsets. GF-1 was in master role and GF-2 was the transponder.

4.2.3.3 Optimized DWS offsets

Optimized DWS offsets were obtained by minimizing $(-\mathcal{F}_1)$ and $(-\mathcal{F}_2)$ with the help the Nelder-Mead simplex algorithm [86]. Based on the role of each S/C, the following optimum DWS offsets were found:

GF-1 Master, GF-2 Transponder

$$(\sigma, \theta)_{\text{GF}-1} = (2, 38) \ \mu\text{rad} \tag{4.45}$$

$$(\sigma, \theta)_{\text{GF}-2} = (27, -3) \ \mu\text{rad} \tag{4.46}$$

GF-1 Transponder, GF-2 Master

$$(\sigma, \theta)_{\text{GF}-1} = (1, 26) \ \mu\text{rad} \tag{4.47}$$

$$(\sigma, \theta)_{\text{GF}-2} = (43, -4) \ \mu\text{rad} \tag{4.48}$$
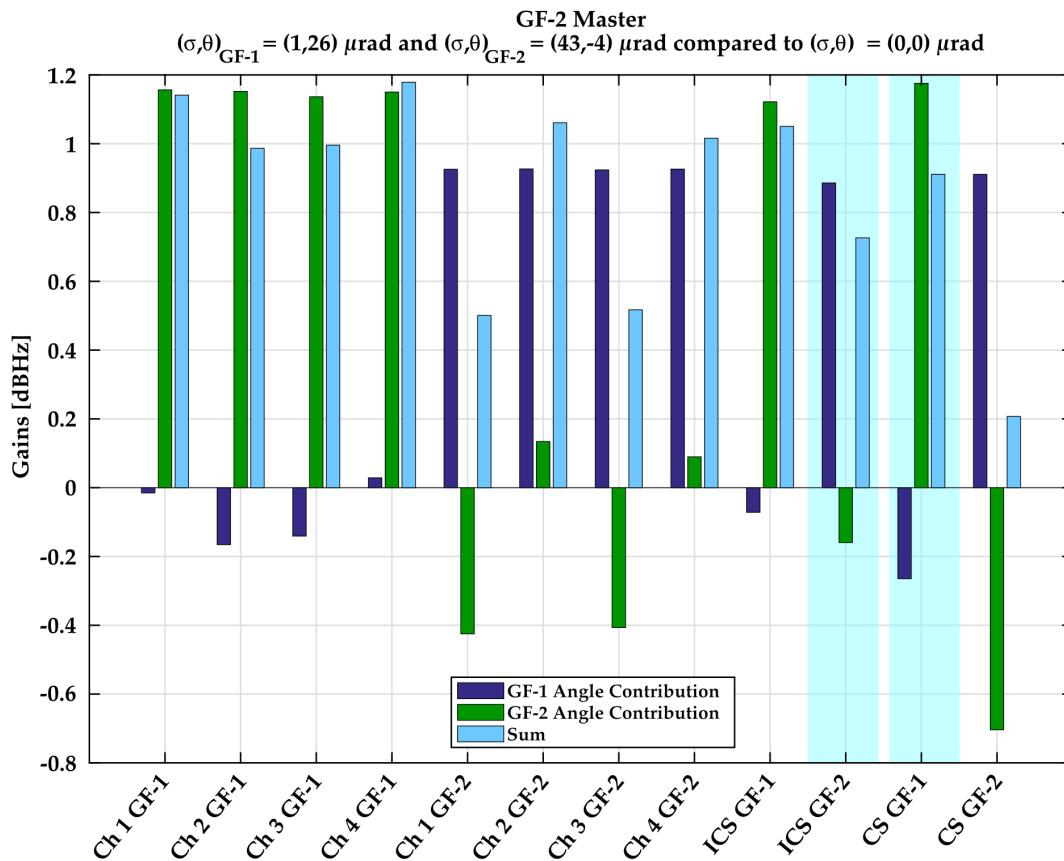
Figure 4.13: The figure shows losses (or gains) of all signals of interest on GF-1 and GF-2 relative to the situation without DWS offsets. GF-1 was in transponder role and GF-2 was the master.

Calculating the difference between the gain that each signal experiences with the optimized DWS offsets and the losses with zero DWS offsets (see Figs. 4.10 and 4.11) yields the results that are presented in Figs. 4.12 and 4.13. The signals that were used by the respective FoM are highlighted in light blue. As can be obtained from the figures, most signals benefit from optimized DWS offsets with relative signal gains of up to 1.2 dBHz.

4.3 Summary

Only a few weeks after the launch of GRACE-FO, the initial laser link acquisition procedure was executed. As was presented in Sec. 4.1 of this chapter, unambiguous LOS offset angles for both S/C $((\alpha, \beta)_{\mathrm{GF-1}} \approx (-800, -600)\,\mathrm{\mu rad}, (\alpha, \beta)_{\mathrm{GF-2}} \approx (-400, -600)\,\mathrm{\mu rad})$ and a frequency set-point for the transponder laser could be found. All obtained values were found to be well within their expected uncertainty range ($|\alpha, \beta| < 3\,\mathrm{mrad}$, $\Delta f < 360\,\mathrm{MHz}$ [66]). After the initial acquisition procedure was run, the found pointing and frequency offsets were uploaded to the LRPs and the S/C were commanded into the re-acquisition state. By the time of the next ground station contact, both S/C reported that they had successfully transitioned into science mode.

In the second part of this chapter, an analysis of the TMAs CAEs was presented. The TMAs' CAEs were subject to numerous test campaigns on ground, prior to launch. Not only ground tests were performed, but also in-orbit measurements were carried out that had the goal of quantifying these angles. The analysis of the obtained data was presented in this chapter. As was shown, the first in-orbit measurement from July 2018 yielded CAEs within $\pm 50\,\mathrm{\mu rad}$ around zero. Subsequent tests of the angles, about one year after the launch, revealed that the errors were reduced to below $10\,\mathrm{\mu rad}$. This reduction was explained by moisture release from the used glue and a corresponding shift of the TMA mirrors. Nevertheless, the CAEs will be closely monitored throughout the operation of the LRI in the future.

In the last part of this chapter, a trade-off study was presented which can be used to derive DWS offset angles that optimally compensate the CAEs. The framework of this study can be used, should the CAEs increase again in the future. It was shown that with the values of the CAEs from July 2018, the application of optimized DWS offsets yields $\mathrm{C/N_0}$ enhancements of the individual QPR channels, as well as of their coherent and incoherent sums of up to 1.3 dBHz.

By the time of this writing, the LRI has been successfully operating in science mode for the majority of the time since the launch of the S/C in May 2018. The instrument has been performing exceptionally well and it could already be shown that its performance is orders of magnitude below the requirement across the frequency range that was so far assessable [19].

Part II

Laser link acquisition for future gravity missions

Chapter 5

The experimental Laser Link Simulator

In this chapter the design, construction and characterization of an experimental *laser link simulator* (LLS) is described in detail. The LLS is a test bed for intersatellite laser interferometers such as the LRI on GRACE-FO or a novel laser ranging instrument aboard a Next Generation Gravity Field Mission (NGGM). In its current state the LLS is capable of connecting two OBs. However, it could be extended and used in the context of LISA, as the laser ranging instruments of these missions have significant technological overlap (see e.g. [87]). To account for the fact that different mission scenarios, e.g. the LRI on-board of GRACE-FO or a laser ranging instrument aboard NGGM, can be simulated with the LLS, the term "laser ranging instrument" is used synonymously for these kinds of instruments within this chapter.

The LLS is based on the experiences gained from designing, building and operating the Fiber OGSE which was used for on-ground tests of the LRI as detailed in Chapter 3 (see e.g. Fig. 3.1). The Fiber OGSE was built by the DLR in Bremen in close collaboration with the author of this thesis.

What makes the LLS unique is that it was designed to enable testing of the laser link acquisition modes. Furthermore, the test bed allows for the calibration of scaling factors and similar measurements. However, as the underlying architecture of the test bed relies on the use of optical fibers, optical path length stability tests of laser interferometers are not possible in the usually required regime of nm or pm at mHz frequencies due to the strong effect of temperature changes on the optical fibers.

In Sec. 5.1 requirements on the LLS are derived from its above-mentioned foreseen applications. The experimental setup is then explained in detail in Sec. 5.2. This is followed by an analysis of the performance of the LLS in terms of error between the desired and realized received (RX) output power, the stability of the optical phase and the power stability of the output signal. A discussion of the obtained results and a comparison of the LLS with other, similar, experimental test beds concludes this chapter.

5.1   Requirements on the Laser Link Simulator

The LLS shall render end-to-end testing of intersatellite laser interferometers possible. This implies a few generic functionalities of a LLS test bed: The angle of the transmitted (TX) laser beam must be measured and the corresponding RX power at the *distant* S/C must be determined. The LLS must then generate a laser beam at the receiving optical bench (OB) which resembles an RX laser beam as it would be present at the receiving S/C if they would be separated by hundreds (or millions) of kilometers. This includes the correct shape of the wavefront, the distribution of the intensity and the optical power of the beam. Obviously, all this needs to happen simultaneously for each laser link. In the case of the GRACE-FO LRI or an instrument on-board of NGGM this means: twice. In order not to disturb the logic behind the operating modes of the instrument, the LLS should not introduce delays that are significantly larger than the light travel time of the respective mission.

As was previously mentioned, the LLS was designed to enable tests of the laser link acquisition mode of intersatellite laser interferometers. Therefore, the required functionalities of the LLS are defined by the link acquisition procedures that shall be tested. In Sec. 2 a detailed description of the LRI and the link acquisition mode was provided which is not repeated here. Table 5.1 summarizes key parameters of the laser ranging instrument on-board of GRACE-FO and NGGM. Also those parameters of the initial acquisition modes are listed that have an impact on the design of the LLS.

Table 5.1: Key properties of the laser ranging instruments on GRACE-FO and NGGM that have an impact on the requirements on the LLS [22, 19, 18, 67]

Parameter	GRACE-FO	NGGM
LO power	20 mW	100 mW - 500 mW
Maximum RX power	0.5 nW - 1.4 nW[1]	8 nW - 40 nW[2]
Field of View (FoV)	135 µrad	100 µrad - 150 µrad[3]
Doppler Shifts	$< \pm 1\,\mathrm{MHz}$	$< \pm 5\,\mathrm{MHz}$
FSM scan frequencies	~2 & 100 Hz	N/A
FSM scan amplitude	3 mrad	2 mrad
Light Travel Time	0.6 ms - 0.9 ms[4]	0.3 ms

Most of the parameters listed in Tab. 5.1 can be considered merely constraints on the design of the LLS. The fast FSM scanning frequency in the GRACE-FO case, however, imposes one of the most important requirements on a test bed. As no detailed FSM scanning algorithm has been developed for an instrument on NGGM so far, the GRACE-FO parameters are used as requirements on the LLS instead. This fast 100 Hz scan results in a flash of light that is received by the S/C in ~220 km distance which only lasts for an

---

[1]The values account for S/C separations of 270 km and 170 km, respectively.
[2]A receiving aperture radius of 4 mm was assumed. The values account for different LO powers.
[3]The values account for different LO powers.
[4]The values account for S/C separations of 170 km and 270 km, respectively.
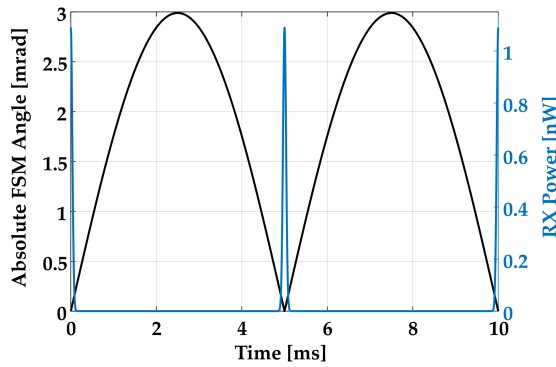
Figure 5.1: Absolute value of a sinusoidal spatial scan of the FSM with $f = 100\,\text{Hz}$ (black). In blue the corresponding optical RX power is plotted. It was assumed that the transmitting S/C is aligned to the LOS.
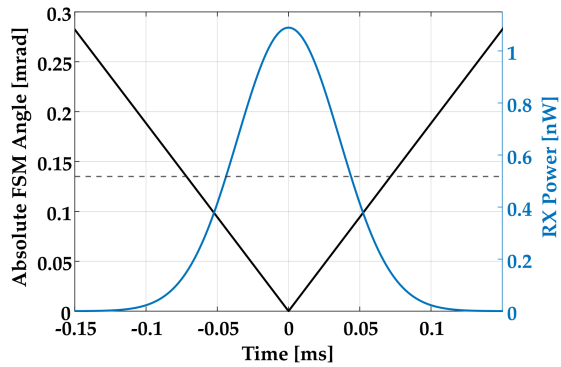
Figure 5.2: Zoom into the time series from Fig. 5.1. Additionally a dashed line marks the LRI FoV of 135 µrad.

extremely short amount of time (cf. Eq. (2.14)). Figure 5.1 shows the absolute value of a sinusoidal scan of the FSM with $f_{\text{scan}} = 100\,\text{Hz}$ together with the corresponding optical RX power which the far S/C would receive. It was assumed that the transmitting S/C (OB) is perfectly aligned to the LOS. Figure 5.2 shows a zoom into one of these flashes of RX power. As can be seen in the plots, the complete LRI FoV of 135 µrad is covered within a time interval of less than 0.2 ms. Thus, the LLS needs to transition from a phase where its output is zero (FSM angle $\gamma \gg 135\,$µrad) to output powers in the nW range within very brief time intervals.

5.2 Implementation of the LLS

Figure 5.3 shows a schematic overview drawing of the LLS experimental setup. The LLS is currently equipped with two LRI-like OBs. These OBs are the same devices that were developed for the tests of the LRI laser link acquisition procedure described in Sec. 3.2. They were used in all experimental laboratory setups that are described in this thesis. If tests with a dedicated acquisition sensor (see Chapter 6) should be done, the OBs could be augmented with such sensors. This illustrates the scope of the LLS as a test bed for novel instrument designs: It was developed using LRI-type OBs and will be available in the future as versatile test bed for the development of novel OB and instrument designs. In the following sections, the individual parts of the complete setup are explained in detail.

5.2.1 The optical benches and peripherals

Figure 5.4 shows a detailed schematic drawing of a subset of the LLS. The focus here lies on one OB which is mounted on top of a hexapod. Also shown are the laser, the RX beam
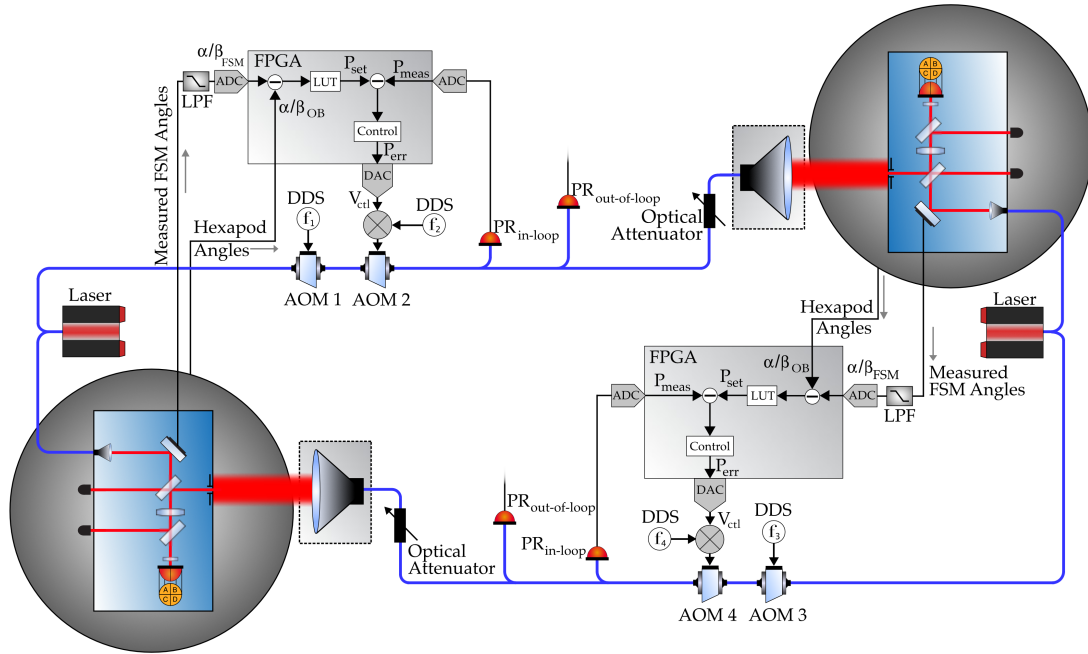
Figure 5.3: The figure shows the schematic layout of the LLS together with two OBs which are placed on hexapods. The setup is shown highly simplified. Details about the sub-units of the LLS are found in the following sections. Optical fibers are shown in blue, electrical cables in black and the free laser beams are illustrated in red.

fiber collimator, all the required electronic controllers and a phasemeter. The individual components are explained in the following paragraphs.

5.2.1.1   The optical benches, phasemeters and lasers

The same OBs as were used for the tests described in Section 3.2 were used. However, careful investigation of the OB shown in Figure 5.3 and 5.4 reveals that the TX beam is not guided to the respective receiving OB as was done during the previous tests, but is in fact dumped. Instead, a part of the light from the laser is directly guided to the LLS as TX beam. This decision was made possible because the absolute path length of the interferometric signal was determined to not be of interest for tests with the LLS. Doing this simplifies the design of the LLS controller. That is because launching the TX beam into an optical fiber and sending it to the LLS and the subsequent "distant" OB would introduce an angle dependent gain to the LLS output power [77]. Therefore, this simplified design was chosen. By using one laser as source for the local oscillator (LO) and TX beam on each OB, it is, however, ensured that the absolute laser frequency is unique to each OB and the light that is sent to the other OB as RX beam.

The LOs are Gaussian laser beams with waist radii $w_{0,\text{LO1}}$ $=$ 2.7 mm and $w_{0,\text{LO2}}$ $=$ 2.8 mm (see Sec. 3.2.2.1). LO and RX beams are interfered on the recombination beamsplitter (BS-Rec) and imaged onto the QPR by an imaging system which is formed by the two lenses L1 and L2. Following the design of the GRACE-FO OBs, a
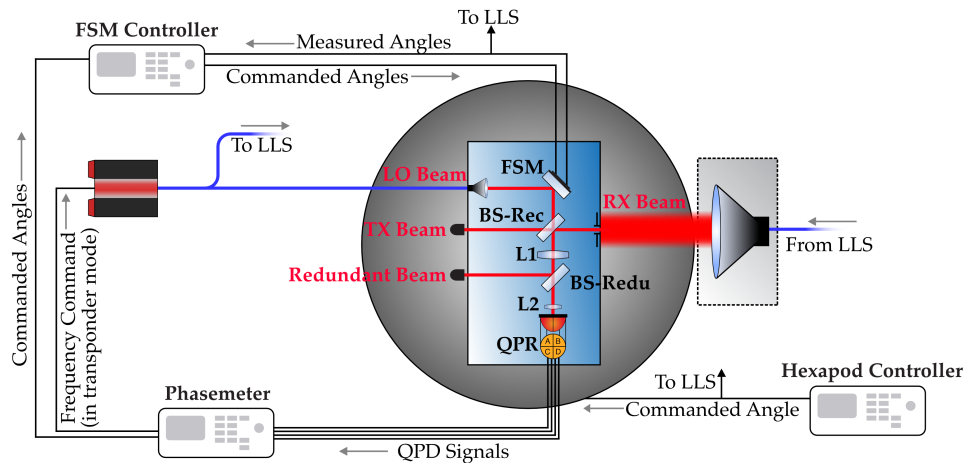
Figure 5.4: Detailed schematic drawing of a subset of the LLS setup: one OB, mounted on a hexapod, together with all the required controllers, the RX beam, the laser and the phasemeter. Optical fibers are shown in blue and cables in black. Arrows indicate where signals and the laser are connected to the remaining LLS setup. FSM: fine steering mirror, BS-Rec: recombination beamsplitter, L1: lens 1, L2: lens 2, BS-Redu: redundancy beamsplitter, QPR: quadrant photoreceiver.

redundant output port was added to the interferometer, which is, however, also dumped in the current design. If desired, this port could be used for out-of-loop measurements. The QPRs are the same as the ones used during the tests described in Sec. 3.2. The QPR signals are processed by a phasemeter. During the initial link acquisition procedure the latter also sends commands to the FSM controller which forwards the corresponding signals to the FSM head. If the OB is set to the role of transponder, the phasemeter sends a voltage to the laser controller to ramp the LO and the TX beam's frequency according to the chosen initial acquisition procedure. At the same time the phasemeter continuously calculates FFTs of the QPR signals and forwards the current frequency and amplitude of any received beat note to a host PC. As many data points could be accumulated quite fast during a long scan, an option can be set to only store those data points with the n highest FFT amplitudes, where n is adjustable.

As was done for the previous tests described in Sec. 3.2, standard off-the-shelf laser systems are used. The free-running Nd:YAG NPRO Mephisto from the company Innolight can be used as transponder laser. Its counterpart Prometheus, whose frequency is stabilized to an iodine hyperfine structure, could be used as master laser.

5.2.1.2 The received beams

The received (RX) beams are simulated with the same fiber collimator model as was used for the Fiber OGSE (Schäfter & Kirchhoff 60FC-T-4-M200-37, see Fig. 5.5). As was already discussed earlier in this thesis, the RX beams that an LRI-like instrument in space would produce are laser beams with diameters of dozens of meters. It is a valid approximation

Figure 5.5: The figure shows a photograph of the RX beam fiber collimator from Schäfter & Kirchhoff (model 60FC-T-4-M200-37). The collimator is held by a tip/tilt mount which is attached to a two DoF translation mount to allow for proper alignment to the OB.
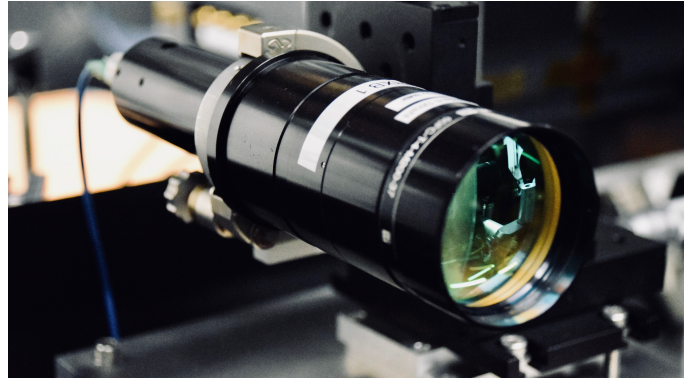
to describe these beams as having spherical wavefronts, where the center of curvature of the wavefront is located in or close to the transmitting S/C. Thus, to an instrument with a defining RX aperture of only a few millimeters diameter, such as the LRI on GRACE-FO where $r_{ap} = 4\,mm$, such laser beams seem to have a flat wavefront and homogeneous intensity distribution transversal to the optical axis. Such beams are referred to as *top-hat* laser beams.

The used fiber collimator (see Fig. 5.5) uses a large lens with 2" diameter to collimate the output of the connected optical fiber to a beam of roughly 4 cm diameter. Due to its large size, this beam has a homogeneous intensity distribution if only its central part is considered. Furthermore, the beam's wavefront can be made relatively flat by properly aligning the collimator lens to the fiber end. These properties make it an adequate imitation of an actual top-hat laser beam. The beams that were generated with the two used fiber collimators show a degradation of their intensity over a disc of 8 mm diameter of 10 % and 7 %, respectively (see Fig. 5.6). As the intensity is distributed completely rotationally symmetric through a cross-section of the beam, only a one-dimensional fit was used to obtain these numbers. A simple exponential model was fitted to the recorded data. The data was recorded with the help of a 1" complementary metal-oxide-semiconductor (CMOS) sensor (WinCamD-LCM from Dataray Inc.).
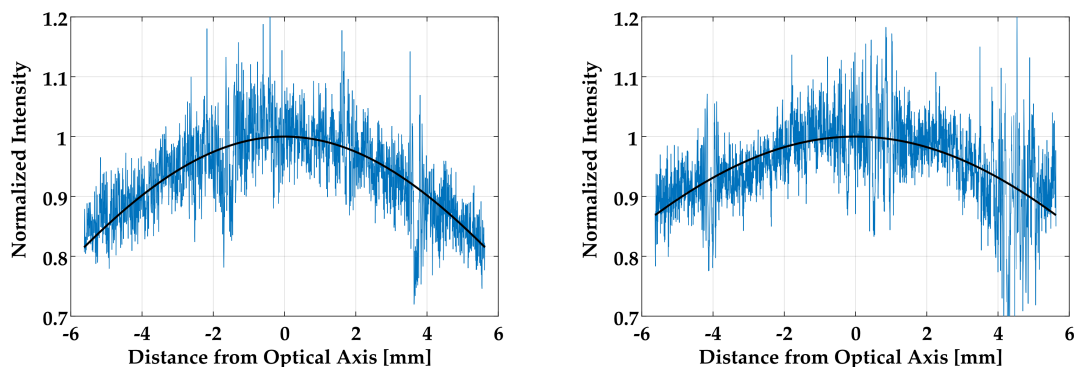
Figure 5.6: The plots show the normalized intensities along a cross-section of the RX beams 1 (left) and 2 (right). A simple exponential fit is shown in black.
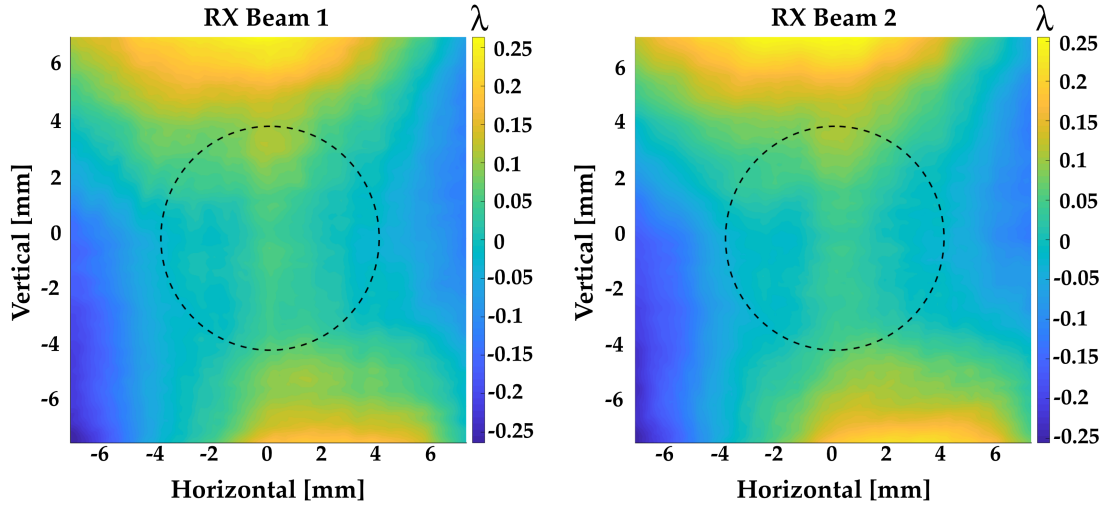
Figure 5.7: The wavefronts of the two used RX beam fiber collimators are plotted. Additionally, a dashed circle of 8 mm diameter illustrates the section of the laser beams that are transmitted through the apertures on the OBs. The color indicates the deviation of the wavefront from a reference surface and is scaled in units of wavelength, where $\lambda = 1064$ nm.

In order to judge the quality of the wavefronts of these beams their wave front error (WFE) is analyzed. Throughout this thesis this value is always defined as the rms deviation of the wavefront under test from a *flat reference surface*, following this definition:

$$\Omega_{\mathrm{wfe}} = \sqrt{\frac{\sum\limits_{i=1}^{N} \left(\Phi_i - \Phi_{ref}\right)^2}{N}} \qquad \Phi_{ref} \equiv \mathrm{const.} \tag{5.1}$$

It is important to stress this definition, as throughout literature various other reference surfaces are used but often not specified. Figure 5.7 shows the wavefronts of the two output beams of the used RX beam FCs. This data was recorded with the help of a Shack-Hartmann sensor (HASO3 128 GE2 from Imagine Optic). Over the complete data set shown, the total rms WFE of the two laser beams is $\Omega_{\mathrm{wfe}} = \lambda/11$, where $\lambda = 1064$ nm. However, as only an area of 8 mm diameter in the center of the recorded data is of interest (indicated by dashed circles in Fig. 5.7), the WFE within this range of interest (ROI) is $\Omega_{\mathrm{wfe}}^1 = \lambda/26$ and $\Omega_{\mathrm{wfe}}^2 = \lambda/29$, respectively for the two beams.

Both, the intensity and the WFE, were investigated in a distance of about 20 cm from the front of the collimators. This value corresponds to the separation of the collimators and the apertures on the optical benches in the later experiments.

5.2.1.3 The hexapods and the introduction of OB misalignments

For the real LRI in space, a tilt of the local S/C with respect to the LOS would manifest itself solely as a tilt of the incoming flat wavefront, if the distant TX laser beam is perfectly aligned to the LOS. This is a consequence of the sphericity of the RX beams' wavefronts.

The received optical power is not affected. Such local S/C tilts are simulated in the experiment with the help of hexapods (see the photographs in Fig. 5.8). These are parallel kinematic motion devices that provide six DoF, three translational and three rotational DoF. Various types of hexapods exist that vary substantially in size, load capacity, tilt and translation range, precision, accuracy and many other properties. What unites them is that the underlying functional principle is always the same: six one-dimensional motors (hence the name) control the attitude and position of a mounting interface to which arbitrary loads can be attached. The used hexapods (HXP100-MECA from Newport) were chosen because they provide a sufficient centered load capacity of 20 kg, travel ranges of a few centimeters and degrees and minimum incremental rotations / motions of a few µrad / µm [88].
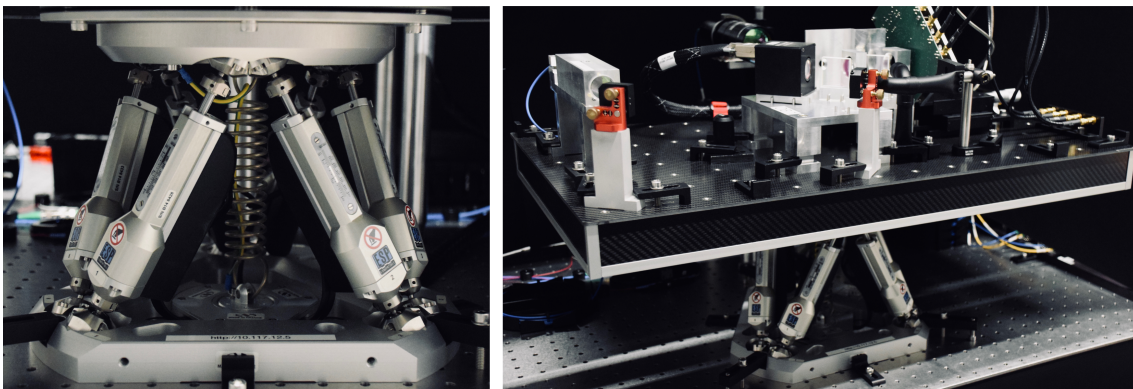
Figure 5.8: Photographs of a hexapod and the mock-up LRI, mounted on a hexapod.

The pivot point of the hexapod motion is adjustable by software and was placed in the center of the aperture of the respective OB. Furthermore, the coordinate system in which the tilts are introduced was aligned with the axes of the OBs. By doing so it is ensured that a rotation of the OB by the hexapod does not result in a transversal translation of the RX beam with respect to the OB. This minimizes coupling of wavefront deviations from a perfectly flat reference surface and effects of a changing laser intensity into the measurements done on the OBs. This precaution is taken because, as was shown in the previous section, the RX beams are no perfect top-hats.

5.2.1.4   The fast steering mirrors

Low-pass filters were placed between the fast steering mirror (FSM) controller output channels and the LLS ADCs. Here, a simple combination of a resistor (R $=$ 10 kΩ) and a capacitor (C $=$ 15 nF) yields a cut-off frequency of $f_{\mathrm{lp}} = 1/(2\pi RC) \approx 1060$ Hz. This cut-off frequency allows for the transmission of the scanning frequency, whose fastest component is 100 Hz. A margin of $\sim$900 Hz was chosen for two reasons: (a) higher frequency components of the FSM response are still visible up to the cut-off frequency and (b) the introduced electronic delay of the transmitted signal is still acceptable. In theory, this value is zero at DC and $-\pi/4 = -45°$ at the cut-off frequency. The delay
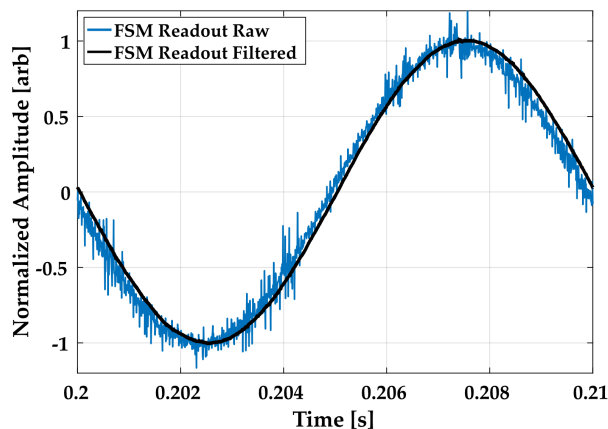
Figure 5.9: The figure shows the raw and low-pass filtered FSM angles that are read out internally by the FSM controller. The used filter had a cut-off frequency of approximately 1 kHz. The introduced electronic delay was estimated to about $\Delta t_{\text{lp}} = 130\,\mu s$.

was measured by driving the FSM with a $f = 100\,\text{Hz}$ signal from a signal generator. The internal readout channel of the FSM controller is split. One output is low-pass filtered and both outputs are connected to a data acquisition system. This way, the delay of the internal delay of the FSM (controller) is also measured. The delay can then be deduced from the phase shift of the two signals. A value of $\Delta t_{\text{lp}} = 130\,\mu s$ was obtained (see Fig. 5.9). This delay is part of the total delay that the LLS introduces between the FSM scanning angles on its input side to the realization of the corresponding RX power at its output. As is presented in Table 5.1, for the NGGM scenario, an overall delay that corresponds to the light travel time of $\Delta t_{\text{tot}} = 0.3\,\text{ms}$ is desirable. For an analysis of the achieved delay see Section 5.3.

5.2.2 The controller sub-system

Figure 5.10 shows a drawing of a sub-system of the LLS. The image illustrates the closed-loop controller that regulates the RX laser power as a function of the FSM angles on the transmitting OB. As was discussed in the previous section, the TX laser beams are not directly forwarded to the receiving OBs but are in fact dumped. Instead, the laser that provides the LO also provides an input to the LLS which processes the light and delivers it to the receiving OB as the RX beam.

The controller is implemented on an FPGA (National Instruments NI PCIe-7852R with Virtex-5-LX50-FPGA) that is connected to a PC via PCIe for fast data transfer via direct memory access (DMA). The FPGA operates on a 40 MHz on-board clock and a derived 80 MHz clock. The latter is used for the timing of the LLS controller. It hosts an 8-channel ADC with 16 bit resolution, corresponding to $\pm 10\,\text{V}$, and a maximum sampling rate of 750 kS/s per channel (the S stands for "sample") and an 8-channel digital-to-analog converter (DAC), also with 16 bit resolution, again corresponding to $\pm 10\,\text{V}$, and a maximum single channel update rate of 1 MS/s [89].

The controller itself as well as all required auxiliary functions (e.g. saving data, setting of scaling factors and monitoring of the system state) have been implemented with the
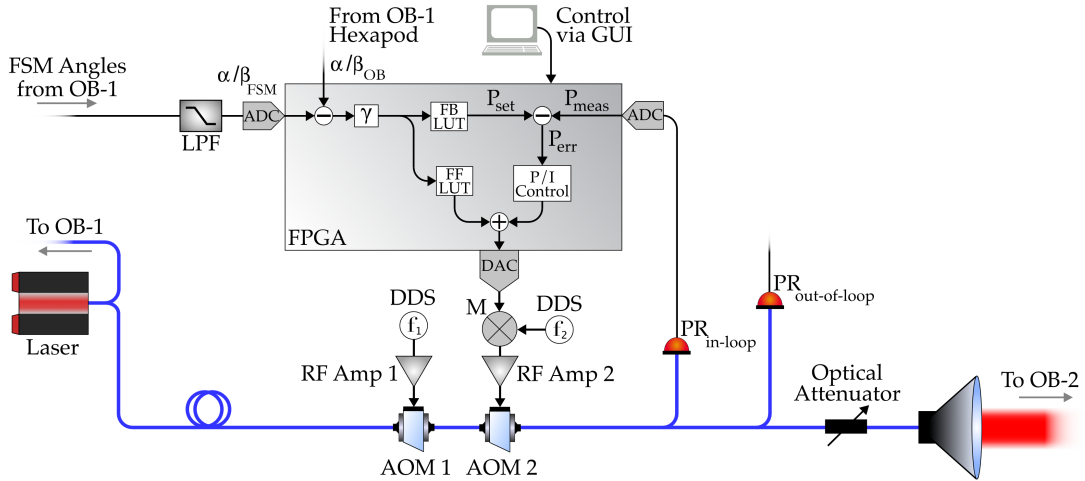
Figure 5.10: The figure shows a detailed schematic drawing of the controller sub-system of the LLS. Optical fibers are shown in blue and cables in black. The hexapod that is used to simulate a misalignment of OB-1 with respect to the LOS is labeled "OB-1 Hexapod". The user can control the LLS via a GUI on a PC (see Appendix C). LPF: low-pass filter, ADC: analog-to-digital converter, FB LUT: feed-back look-up table, FF LUT: feed-forwad look-up table, DAC: digital-to-analog converter, DDS: direct digital synthesizer frequency generator, M: multiplier, RF Amp: RF amplifier, AOM: Acousto-optic modulator, PR: photoreceiver (here: fiber-coupled).

software LabVIEW from National Instruments. The FPGA code is designed in LabVIEW and then compiled by the software to a bit file that is readable by the FPGA. Within the context of LabVIEW programming, all programs are referred to as LabVIEW virtual instruments (VIs). Two such VIs comprise all required functionalities. One of these is the actual code that is run by the FPGA. Here, all components that require near real-time processing are included: the processing of the FSM angles and the control of the RX laser power. This VI will from now on be referred to as the *FPGA VI*. The second VI runs on the host computer and allows for monitoring of the system state, setting of scaling factors, saving of data and the overall operation of the setup. It will be referred to as *Host VI*. Data is transferred between these two VIs via DMA. Key parts of these VIs is shown and explained in Appendix C.

The angles of the transmitting OB's FSM are continuously measured by the FSM controller and forwarded to the LLS controller where they are low-pass filtered and digitized by the ADCs ($\alpha/\beta_{\mathrm{FSM}}$ in Fig. 5.10). The current misalignment angles of the transmitting OB ($\alpha/\beta_{\mathrm{OB}}$) are forwarded from the respective hexapod controller to the LLS. The differences of these angles are used to calculate the half-cone misalignment angle γ:

$$\gamma = \sqrt{(\alpha_{\mathrm{FSM}} - \alpha_{\mathrm{OB}})^2 + (\beta_{\mathrm{FSM}} - \beta_{\mathrm{OB}})^2}. \tag{5.2}$$

Thereby, the misalignment of the transmitting OB with respect to the LOS, $\alpha/\beta_{\mathrm{OB}}$, and the current FSM angle, $\alpha/\beta_{\mathrm{FSM}}$, are expressed relative to the nominal position of the FSM (see Fig. 5.11). As was mentioned earlier, the RX laser beam is rotational symmetric around the optical axis. It thus suffices to describe the RX power as a function of the half-cone
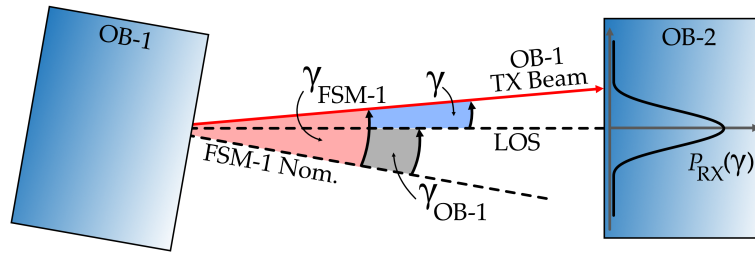
Figure 5.11: Illustration of the definition of the half-cone angle γ. The misalignment of OB-1 with respect to the LOS, $\gamma_{\mathrm{OB-1}}$, and the current FSM angle, $\gamma_{\mathrm{FSM-1}}$, are expressed relative to the nominal zero position of the FSM on OB-1 (FSM-1 Nom.).

angle γ. Thus, the currently desired RX power is obtained by feeding γ to a LUT which contains the normalized distribution of P_{RX} according to Eq. (2.14). The output of the LUT is the set-point of the controller ($\mathrm{P_{set}}$ in Fig. 5.10). The actual value $\mathrm{P_{meas}}$ is obtained with the help of the in-loop sensor. Here, a high bandwidth, low noise PR (Newport, model 2053-FC-M) is used. The difference of $\mathrm{P_{set}}$ and $\mathrm{P_{meas}}$ is the error signal $\mathrm{P_{err}}$ that is then processed by the feed-back control loop.

The controller output is converted to a voltage by the DAC and fed to the actuator. The latter is made up by a combination of an analog multiplier (Analog Devices ADL5391), a direct digital synthesizer (DDS) RF signal generator (Novatech Instruments, model 409B, 4 channels, 171 MHz frequency range) and a fiber-coupled AOM (Gooch & Housego Fibre-Q, nominal operating frequency 150 MHz). The underlying principle that is used for the actuation process is that the optical output power of an AOM, $P_{\mathrm{AOM-out}}(t)$, is proportional to the product of the power of the driving RF signal, $P_{\mathrm{RF}}(t)$, and the optical input power to the AOM, $P_{\mathrm{AOM-in}}$:

$$P_{\mathrm{AOM-out}}(t) \propto P_{\mathrm{RF}}(t) \cdot P_{\mathrm{AOM-in}}. \tag{5.3}$$

Deviations from linearities are not critical here, as the AOMs are operated in a closed-loop controller.

The DDS signal generator produces an RF signal at the required frequency (nominally 150 MHz) with a constant amplitude. This signal is then modulated with the DAC output (see Fig. 5.10) by the multiplier which creates the time dependent RF power $P_{\mathrm{RF}}(t)$ used in the equation above. A subsequent voltage-controlled attenuator (VOA) is used to apply a static attenuation to the this signal, which is usually in the µW range, such that the desired RX power in the pW to nW range is realized. An additional PR (same model as the in-loop sensor) allows for an out-of-loop measurement of the optical power behind the AOMs. All these signals (half-cone misalignment angle γ, LUT output, DAC output, error signal, in-loop signal and out-of-loop signal) can be monitored in the Host VI (see Appendix C).

The scenario, for which the controller is used, can be considered an optical power stabilization with a rapidly changing operating point. The classical disturbances to such power

stabilization scenarios, mostly temperature effects and laser output power variation, can be neglected on the time scales on which the RX power is required to differ from zero (<1 ms). Hence, the only perturbations are the dynamics of the FSM scans. As these are well known, not only a feed-back controller scheme is used, but a combination of feed-back and feed-forward control is implemented. The feed-forward filter drastically reduces the dynamic range of the error signal that the feed-back controller needs to cope with. The basic controller design and the characteristics of its components are explained in the next section.

5.2.2.1 Controller parts characterization

In this section, important calibration measurements of crucial parts of the controller, namely the AOMs, the multipliers and the VOAs are presented. Several units of each of these devices are used in the LLS. Each unit was calibrated individually and it was found that the obtained parameters or calibration results are very similar. Thus, in the following sections only one respective calibration result per device is presented in order to emphasize the qualitative dependencies of these parameters.

Acousto-optic modulators

As can be obtained from Fig. 5.10, in total two AOMs are used for the simulation of one laser link. AOMs use the acousto-optic effect to shift the frequency of the light that passes through them [69]. The applied frequency shift is thereby defined by the frequency of the RF signal that is used to drive the AOM. Moreover, as an AOM realizes this frequency shift by diffracting the light on a grating-like structure that is induced within the AOM's crystal, the AOM can be designed to use the *first* or the *minus first* order of diffraction. This has the consequence that the AOM operating frequency is *added to* (first order diffraction) or *subtracted from* (minus first order diffraction) the laser light frequency.

The desired frequency shifts are on the order of a few MHz (cf. Tab. 5.1). As there are no AOMs that realize such small shifts, a combination of two AOMs is used. One of them adds its operating frequency, it thus uses the first order diffraction, while the second AOM subtracts its operating frequency. Here, both AOMs have the same nominal operating frequency of 150 MHz. The total nominal frequency shift is thus *zero*. Small detuning of the operating frequencies from their nominal value then realize the desired frequency shifts of a few MHz.

The optical output power of an AOM depends on the current RF frequency and the power of the driving RF signal. The corresponding calibration measurements were carried out. The obtained results, as well as fits of the data, are shown in the left and right panels of Fig. 5.12. For a given optical input power to the AOM, the calibration results can be combined to obtain the dependency of the optical output power of an AOM P_{AOM} on the
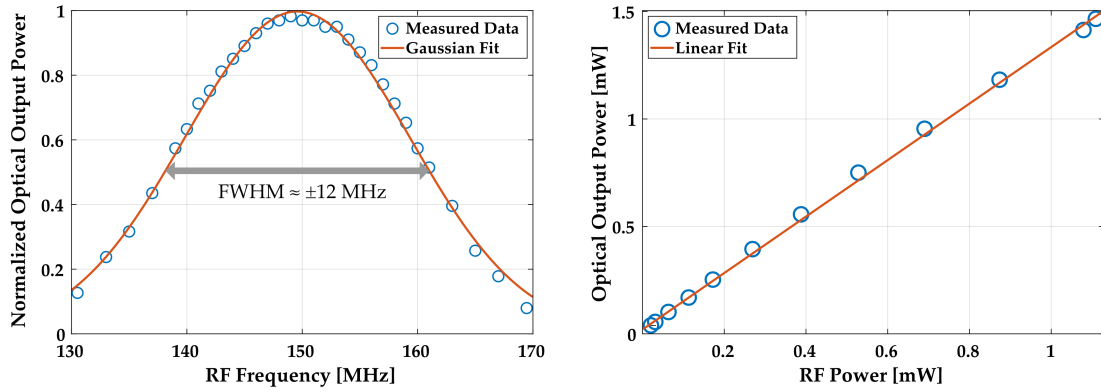
Figure 5.12: The plots show the optical output power of an AOM as a function of the RF frequency (left) and the RF power (right). The distribution in the left panel was normalized.

RF power P_{RF}, expressed in mW, and the RF frequency f, in MHz:

$$P_{AOM}\left(P_{RF}, f\right) = \left[G_{AOM} \cdot P_{RF} + P_o\right] \cdot e^{-\Delta f^2/w^2} \tag{5.4}$$

with $G_{AOM} = 1.3\,\mathrm{mW}^{-1}$, $P_o = 23\,\mu\mathrm{W}$ being the results of the linear fit, shown in the right panel of Fig. 5.12, and $\Delta f = (f - 150\,\mathrm{MHz})$ and $w = 13.9\,\mathrm{MHz}$ being the results from the frequency calibration (left panel in Fig. 5.12). It should be noted that G_{AOM} includes the gain of the RF amplifier (ZHL-2-12 from MiniCircuits). However, as the amplifier gain only constitutes a constant factor in the frequency range of interest, it is not separately analyzed here. It should be noted that the model presented in Eq. (5.4) simply fits the recorded data well, but does not aim to explain the more complex interior workings of the analyzed AOM circuit.

The desired Doppler shifts can now be introduced by keeping the frequency of AOM 2 (cf. Fig. 5.10) constant and changing the frequency of AOM 1. The power of the driving RF signal for AOM 1 is adapted such that the optical output power of AOM 1 remains constant. The required values for P_{RF} can be obtained by solving Eq. (5.4) for P_{RF} and providing the desired value for the optical output power P_{AOM} and the current operating frequency f. Correcting the output power of AOM 1 in this feed-forward manner allows for the introduction of Doppler shifts while not affecting the working point of the LLS controller. This functionality is implemented as part of the LabVIEW Host VI.

Even though fit residuals are not provided, a minor inconsistency between the linear fit and the data shown in the right panel of Fig. 5.12 is visible by eye. The linear fit does not seem to be an adequate representation of the data for $P_{RF} > 0.7\,\mathrm{mW}$. A quadratic fit would have been a better parametrization of the recorded data. However, the residuals to a linear fit were assessed to be acceptable. The nature of the observed deviation will be explained in the discussion of the calibration of the multiplier, in the next paragraphs.

Figure 5.13: Plot of the optical output power of an AOM whose driving signal is the product of a constant RF voltage, generated by the DDS, and the control voltage, V_{ctl}. Additionally, second and third order fits to the data are plotted. The second order fit was only applied to the voltages $V_{ctl} < 1.3\,V$.
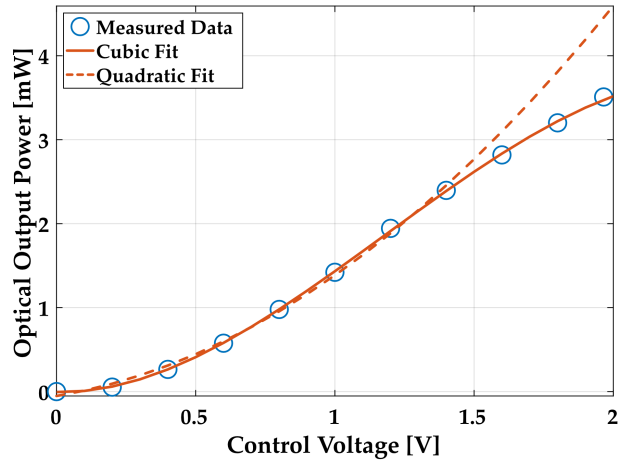
Multipliers

The used multipliers (Analog Devices ADL5391) are specified to provide linear operation according to $V_{out} = V_{in1} \cdot V_{in2}$ for Fourier frequencies up to the GHz regime [90]. The device offers even more options, e.g. scaling and offsetting of the output. However, these features are currently not used.

The transfer functions of the multipliers were measured. For this purpose, one of the inputs was kept constant, $V_1 = \text{const.}$, while a swept sine signal was connected to the other input, $V_2(t) \propto \cdot \sin\left(2\pi f(t) \cdot t\right)$. The obtained transfer functions were found to be constant up to the highest measurable Fourier frequency of $30\,MHz$. This supports the manufacturers claim of GHz operation and proves that the devices have enough bandwidth for their foreseen application.

The multipliers are used in this experiment to allow the controller output to modulate the amplitude of the RF signal that is produced by the DDS. Therefore, knowledge about the relationship of the AOM optical output power and the controller output, V_{ctl}, for a constant RF amplitude is required. The result of the associated calibration measurement is shown in Fig. 5.13. According to Eq. (5.4), a linear relationship between P_{AOM} and the driving RF signal *power* is expected. As the DDS voltage was kept constant for this measurement, the power of the RF signal should only be proportional to the square of the controller output voltage: $P_{RF} \propto V_{ctl}^2$. In addition to the measurement, Fig. 5.13 shows a quadratic fit to the data, for $V_{ctl} < 1.3\,V$. Additionally, a cubic fit is displayed. As can be obtained from the plot, a second order fit only describes the relationship reasonably well up to control voltages of $\sim 1.3\,V$. For higher values, a cubic fit seems to be a better choice.

For a constant optical input power, the shown third order fit is defined by:

$$P_{\text{AOM}}(V_{\text{ctl}}) = G_3 \cdot V_{\text{ctl}}^3 + G_2 \cdot V_{\text{ctl}}^2 + G_1 \cdot V_{\text{ctl}} + G_0 \qquad \text{[mW]} \quad (5.5)$$

$$G_3 = -0.59 \, \text{mW V}^{-3} \tag{5.6}$$

$$G_2 = 2.1 \, \text{mW V}^{-2} \tag{5.7}$$

$$G_1 = -0.07 \, \text{mW V}^{-1} \tag{5.8}$$

$$G_0 = -5.5 \cdot 10^{-3} \, \text{mW.} \tag{5.9}$$

It was ensured that the applied RF power levels were well below the maximally acceptable values for the AOMs. Thus, the deviation from the above-mentioned proportionality of the optical output power to the RF power level is not expected to be due to a nonlinear response of the AOMs. However, the maximum input voltage to the multiplier is specified as $\pm 2\,\text{V}$. Therefore, the inconsistency is attributed to a nonlinearity of the multiplier output that only becomes visible towards its maximum ratings. The other combinations of RF amplifiers, DDS channels and multiplier qualitatively show the same result. The relationship that is expressed by Eq. (5.5) is therefore used henceforth to describe the multiplier output.

The inadequacy of the linear fit shown in the right panel of Fig. 5.12, that was mentioned before, is also attributed to the multiplier. This is because the shown data was recorded with the multiplier connected to input of the RF amplifier. The calibration was done by varying the DDS output and keeping the control voltage set to a constant level of $V_{\text{ctl}} = 1\,\text{V}$. The effect seems to be not as dominant as in Fig. 5.13. This is simply caused by the DDS output power being smaller than the corresponding range of applied control voltages.

As the multiplier is part of the controller's actuator, its nonlinear response to a change of the control voltage affects the output of the LLS. The feed-back controller compensates the dependency expressed by Eq. (5.5). For the feed-forward filter, on the other hand, the actuator response needs to be accounted for. In Sec. 5.2.2.2 it is explained how this is realized.

Voltage-controlled optical attenuators
The required maximum output power of the LLS is on the order of pW to nW. Even though low-noise PR are used for the in-loop and out-of-loop sensors, such low powers would barely exceed the noise floor of these devices. Therefore, the power levels on the sensors are kept in the µW range and are then subsequently attenuated to the required pW to nW range.

Fiber-coupled voltage-controlled attenuators (VOAs) (single channel MEMS variable optical attenuators from OZ Optics) are used to realize these RX signal powers at the output of the LLS. An advantage of *voltage-controlled* attenuators over manual fiber-coupled attenuators is the repeatability of the attenuation factor and the fact that it can be enabled and disabled by the push of a button. Especially the latter makes debugging

Figure 5.14: Plot of the relative optical output power of a voltage-controlled, fiber-coupled attenuator as a function of the applied voltage.
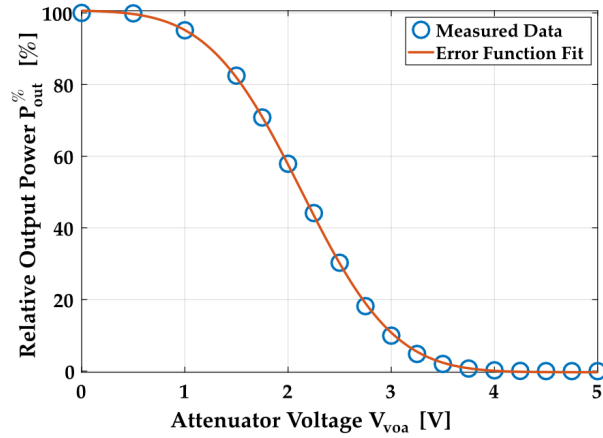
of the experimental setup very convenient. Figure 5.14 shows the relative optical output power of a VOA $P_{\text{out}}^{\%}$ as a function of the applied voltage V_{voa}. An error function was found to be a good representation of this relationship:

$$P_{\text{out}}^{\%} = [1 - \text{erf}(V_{\text{voa}} - 2.13\,\text{V})] \cdot 50.5 \qquad\qquad [\%]. \quad (5.10)$$

5.2.2.2   Controller design

The LLS controller consists of a feed-forward and a feed-back part –see Fig. 5.10. To account for the high dynamic range of the error signal, the feed-back control loop includes a nonlinear correction of the controller gains. These filters are explained in the following sections.

Feed-forward filter

As was already mentioned, the signal dynamics within the control frequency band in the kHz range are well known. In such situations it is advisable to employ a feed-forward controller. The corresponding filter is defined by calculating the desired controller output and adapting it by the measured actuator response. The requested output of the LLS is the distribution of the RX power as a function of the TX beam angle, as it would be detected by a S/C in orbit, as described in Chapter 2 in Eqs. (2.14) and (2.11). For the design of the controller, the absolute amplitude of the distribution is not important, as it can later be adjusted to the required level. The parameters should only be chosen such that the involved components (e.g. sensors, actuators, ADCs and DACs) can operate far above their respective noise floor. It must only be ensured that enough optical power is transmitted by the LLS for all beam angles such that it can later be adjusted to the required absolute value in the pW or nW range by the VOAs (see Fig. 5.10).
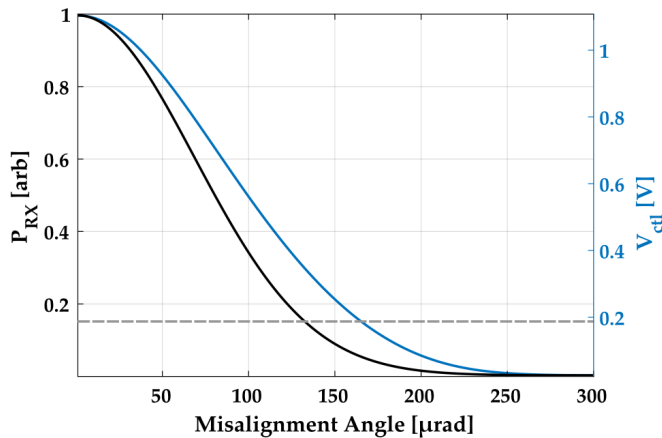
Figure 5.15: The black curve shows the distribution of the normalized RX power as defined by Eqs. (2.14) and (2.11). As the intensity of the RX beam is symmetric around the optical axis, the RX power only depends on the half-cone misalignment angle of the beam. Additionally, the RX power at the edge of the FoV of the LRI is indicated by the dashed line. The feed-forward filter, which takes the measured actuator nonlinearity into account, is shown in blue.

As was also already mentioned, the distribution of the RX power is expressed as a function of the half-cone misalignment angle of the TX laser beam. The FoV of the laser ranging instruments on GRACE-FO or NGGM is on the order of $\pm 150\,\mu$rad (cf. Tab. 5.1). This implies that the output power of the LLS must be a faithful representation of the RX power according to Eqs. (2.14) and (2.11) within this range. For angles much larger than $\pm 150\,\mu$rad the output of the LLS can simply be set to zero. Therefore, a range of 300 µrad around $\gamma = 0\,\mu$rad was chosen to be actively processed by the LLS. The output of the LLS is set to zero for $\gamma > 300\,\mu$rad. This range was chosen to include ample margin. Possible transient effects between the region of active control of the output power and the passive range for $|\gamma| > 300\,\mu$rad, that might disturb the distribution of the RX power, are moved outside of the range that is detectable by the laser ranging instrument. The black curve in Fig. 5.15 shows the desired distribution of the RX power as a function of the TX beam half-cone misalignment angle γ as it is defined by Eqs. (2.11) and (2.14).

The actuator of the control loop consists of the combination of an AOM, the associated RF amplifier, a multiplier, a DDS signal generator and the DAC. All of the components that make up the actuator show an individual response, which is in general not linear. As was outlined in the previous section, these responses must be taken into account for the derivation of the feed-forward filter. More precisely, the actuator response to a change of V_{ctl} must be considered. The associated calibration was already explained earlier and shown in Fig. 5.13. The feed-forward filter is implemented on the FPGA as a LUT that uses the half-cone misalignment angle γ as an input and produces values for the controller voltage V_{ctl}. The blue curve in Fig. 5.15 shows the corrected distribution of V_{ctl} as a function of the half-cone beam misalignment angle. V_{ctl} was obtained by multiplying the desired optical power with the response of the actuator. The latter was obtained by numerically solving Eq. (5.5) for each desired value of the optical power.

Measurements were carried out to characterize the functionality of the feed-forward controller. The shown data was sent from the FPGA VI to the Host VI via DMA where it was then recorded with a high sampling rate of $\sim$800 kHz. Figure 5.16 shows time series plots of various data streams while the FSM horizontal axis was driven with a sinusoidal
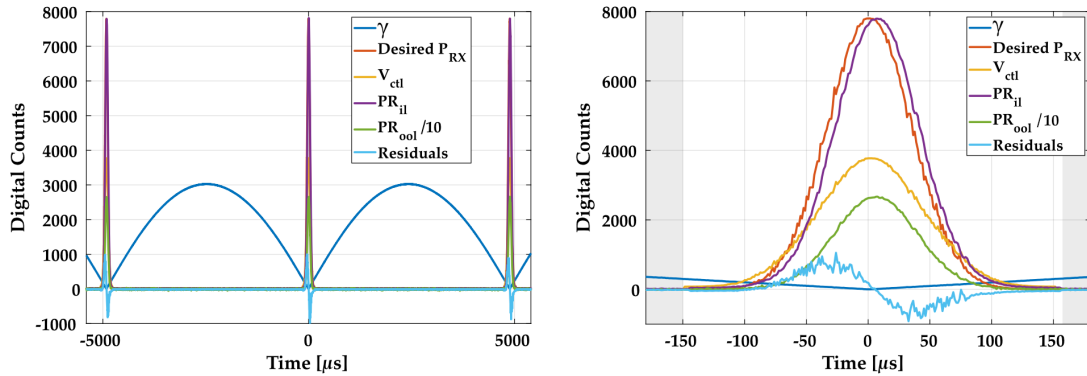
Figure 5.16: Time series plots of the half-cone misalignment angle γ, the desired RX power, the controller output V_{ctl}, the in-loop and out-of-loop PR voltages and the residual error between desired and achieved output power. The left plot shows an overview for a longer time segment, while the right plot shows a zoom into one flash of RX power. In the right plot, the gray shaded area indicates times during which $|\gamma| > 300\,\mu\text{rad}$, where the controller output is hard-coded as zero. For better visualization the amplitude of the out-of-loop signal was divided by 10 to match the range of amplitudes of the other signals.

signal with $f = 100\,\text{Hz}$ and an amplitude of 1.5 mrad. A laser beam that is reflected off the mirror oscillates with an amplitude of 3 mrad, thus covering the complete parameter range of an initial acquisition scan (cf. Tab. 5.1). Consequently, this process well approximates the most challenging part of the initial acquisition procedure that the LLS must be capable of realizing. As can be obtained from Fig. 5.16 the in-loop and the out-of-loop sensor data well matches with the desired distribution of the RX power. It should be noted that the absolute amplitudes of the shown signals are not important. The necessary calibration from units of digital counts to optical power at the receiving OB will be presented in Sec. 5.3. However, it was ensured that the optical power at the output of the LLS is above its required value for all possible angles.

From the data that is shown in Fig. 5.16 a delay of about 5.5 µs between the desired and the measured output can be derived. It is attributed to the phase shifts that are introduced by cables and the ADCs and DACs. As will be shown in the following section, the feed-back controller corrects for this effect.

Figure 5.17 shows an ASD plot of the LLS controller set-point and the residual error with the feed-forward filter activated. Just as was done before, the FSM was excited by a 100 Hz signal with an amplitude of 1.5 mrad. Both signals show a clear peak at twice the excitation frequency (200 Hz) and a steep roll off towards Fourier frequencies above $\sim$10 kHz. The shown residuals, with the feed-forward filter activated, are between one and two orders of magnitude lower than the controller set-point. The remaining error must be mitigated with the help of a closed-loop controller. From the ASD it can be deduced that the closed-loop controller should have a unity gain frequency (UGF) of about 20 kHz. The UGF is the frequency where the open-loop system has a gain of one. A lower value would cut off a part of the signal and a higher value would introduce an unnecessary amplification of noise as no signal is present at such high frequencies.
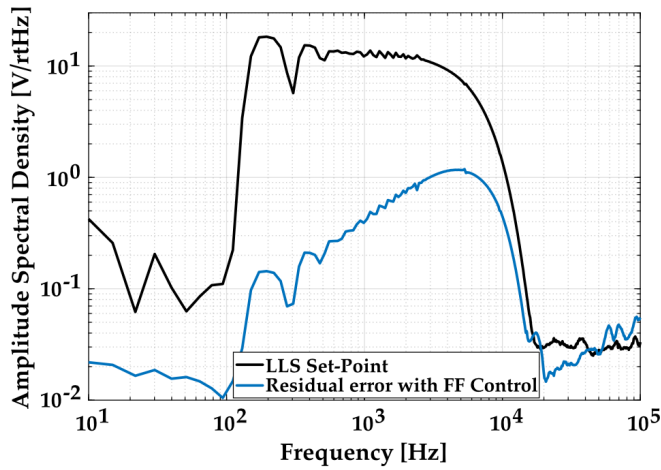
Figure 5.17: ASD plot of the LLS controller set-point and the residual error of the control loop with the feed-forward filter activated. For the calculation the Fourier bins were logarithmically scaled [91, 92].

Feed-back filter

The implemented feed-back controller architecture consists of a proportional (P) and an integrating (I) part. The schematic representation of the feed-back loop is shown in Fig. 5.18. The error signal follows as the difference between the set-point and the sensor output: $e(t) = P_{\text{set}}(t) - P_{\text{meas}}(t)$. Just as was done for the feed-forward filter, the set-point is defined by a LUT. The LUT for the feed-back controller is again described by Eqs. (2.14) and (2.11) (see black trace in Fig. 5.15). The actuator in Fig. 5.18 describes the combination of the DAC, the multiplier, the DDS output, the RF amplifier and the AOM (AOM 2 in Fig. 5.10). Here, $s = \sigma + jw$ is the Laplace variable σ and $w = 2\pi f$ the real and imaginary parts. $A(s)$ denotes the Laplace transform of $A(t)$ [93]. $A(s)$ describes the transfer function of the actuator. $P(s)$ describes the transfer function of the experimental setup. It is defined by the optical output power as a function of frequency. The controller's sensor, described by D(s), is a fiber-coupled PR. Following the nomenclature from Fig. 5.18, the output of the controller $u(t)$ can be described in the time domain as:

$$u(t) = K_p \, e(t) + K_i \int_0^t e(\tau) \, d\tau \tag{5.11}$$

with the proportional gain K_p and the integral gain K_i. The combination of a proportional and an integrator part was chosen because a proportional controller alone would result
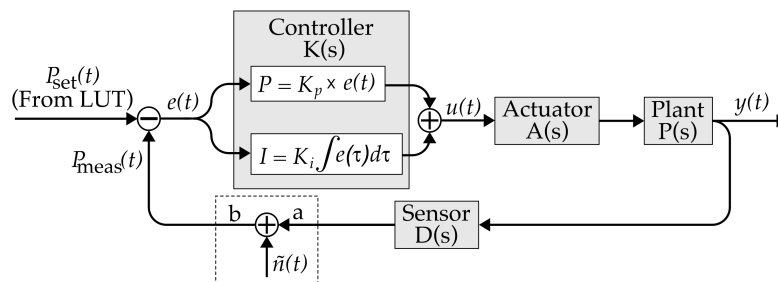
Figure 5.18: Schematic drawing of the closed-loop controller system. The output of the LLS controller $y(t)$ is the time-dependent optical RX power that a S/C receives. The adder in the dashed area is only used for the measurement of the OLTF $G_{\text{ol}}(s)$.
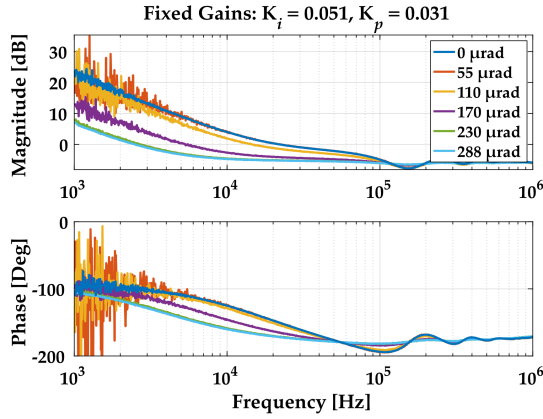
Figure 5.19: Bode plots of the OLTF measured at different FSM angles $0 < \gamma < 300\,\mu\text{rad}$ with fixed gains $K_i = 0.051$ and $K_p = 0.031$.
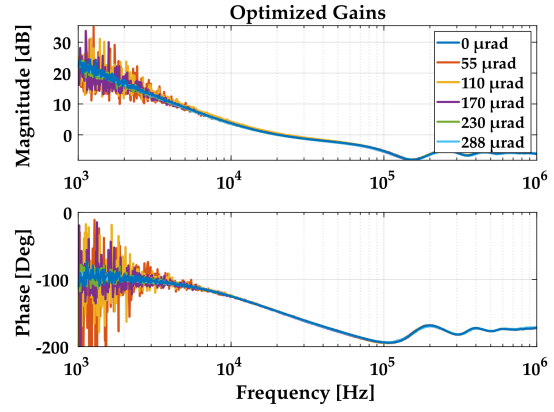
Figure 5.20: Bode plots of the OLTF for different FSM angles with optimized gains K_i and K_p.

in a steady-state error between actual and desired output power. This is due to the gain K_p being finite which leads to insufficient suppression of the error signal towards DC frequencies. To compensate this offset, an additional integral controller is used. Its error signal is constructed by integrating the error. Hence, also very small deviations of desired and actual output will eventually result in substantial error signals.

There exist various approaches to finding optimal values for K_i and K_p, e.g. the method by Ziegler and Nichols [94]. In the present case, optimized values for these gains were obtained by starting off with empirically derived best estimates and subsequent fine-tuning. This was done while monitoring the system's resulting OLTF $G_{\text{ol}}(s)$. This function describes the complete system's response to small harmonic excitations in the Laplace domain:

$$G_{\text{ol}}(s) = K(s)\, A(s)\, P(s)\, D(s). \tag{5.12}$$

$G_{\text{ol}}(s)$ is measured with the help of a network analyzer (Keysight E5061B) by adding a small harmonic excitation $\tilde{n}(t)$ to the circuit between the points a and b, indicated in Fig. 5.18, and measuring the controller's response.

The OLTF is used to tune the controller gains K_i and K_p such that the closed-loop system becomes stable as will be shown in the following paragraphs. The corresponding closed-loop transfer function (CLTF), $G_{\text{cl}}(s)$, can be derived from the OLTF:

$$G_{\text{cl}}(s) = \frac{G_{\text{ol}}(s)}{1 + G_{\text{ol}}(s)}. \tag{5.13}$$

It becomes obvious that the response of the closed-loop system is infinite if $G_{\text{ol}} = -1$. In such a situation the system is unstable. For obvious reasons this condition and its vicinity should be avoided. Two stability criteria for closed-loop controllers can be derived from this: there must be sufficient (i) *phase margin* with respect to $\phi = \pm 180°$ at the UGF and enough (ii) *gain margin* when $\phi = \pm 180°$ in the OLTF.
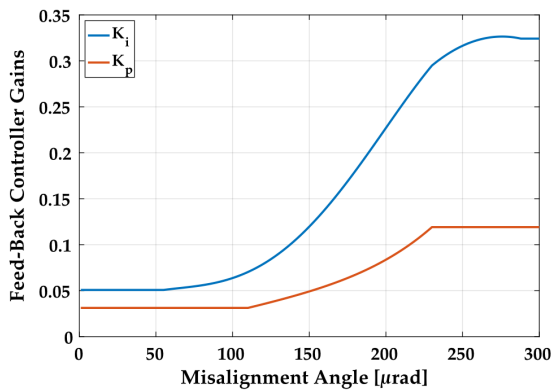
Figure 5.21: Obtained nonlinear gains K_i and K_p that ensure a constant system OLTF for all possible FSM angles.
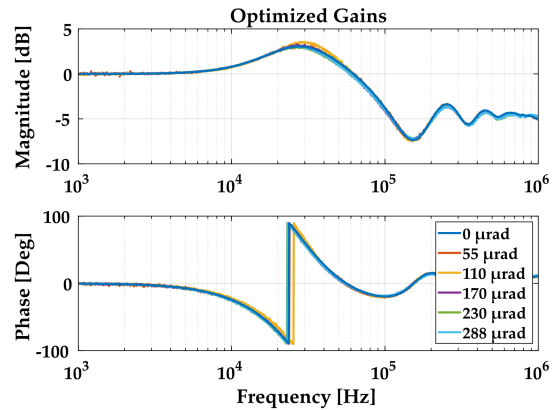
Figure 5.22: Bode plots of the CLTF for different FSM angles with optimized gains K_i and K_p. The shown data was calculated with Eq. (5.13) from the OLTFs shown in Fig. 5.20.

For $\gamma = 0\,\mu$rad the gains K_p and K_i were tuned such that generally accepted values for the phase margin of around 30° and for the gain margin of around 3 dB could be achieved [95, 96]. The obtained OLTF had a UGF of $f(|G| = 1) \approx 20\,$kHz, a corresponding phase margin of $\phi = 32°$ and a gain margin of 2.8 dB (see Fig. 5.19). However, for FSM angles that deviate from zero, the shape of the OLTF is distorted and the UGF for $\gamma \geq 200\,\mu$rad is reduced by almost a factor of ten.

This is a consequence of the high dynamic range of the desired LLS output as a function of γ which directly affects the size of the controller's error signal. To mitigate this effect, a nonlinear filter was added to the feed-back controller which ensures that K_i and K_p are optimized for each FSM angle γ. This filter was again implemented as a LUT which provides values for K_i and K_p as a function of the half-cone misalignment angle. For five different FSM angles the corresponding values were obtained by modifying the controller gains such that the OLTFs match the OLTF at $\gamma = 0\,\mu$rad. Figure 5.20 shows the resulting OLTFs that were obtained with this procedure. K_i and K_p were then interpolated for all possible angles $0 < \gamma < 300\,\mu$rad. The resulting LUTs are displayed in Fig. 5.21. Eq. (5.13) was used to calculate the CLTF from the open-loop data (see Fig. 5.22). As can be obtained from the plot, the closed-loop system shows reasonable values of gain peaking of approximately 3 dB at frequencies between 20 kHz and 30 kHz.

Finally, time series data was recorded with the Host VI while the feed-forward and feed-back controllers were activated. Figure 5.23 shows the obtained data around one instance where $|\gamma| < 300\,\mu$rad. A comparison with Fig. 5.16 reveals that the delay between the RX power, which is here illustrated as the feed-back LUT output, and the controller output could be eliminated.

Figure 5.23: Time series plots of the half-cone misalignment angle γ, the corresponding LUT output, the controller output V_{ctl}, the in-loop and out-of-loop PR voltages and the controller's error signal. The gray shaded area indicates time spans during which $|\gamma| > 300\,\mu rad$, where the controller output is hard-coded as zero. For better visualization the amplitude of the out-of-loop signal was divided by 10 to match the range of amplitudes of the other signals.
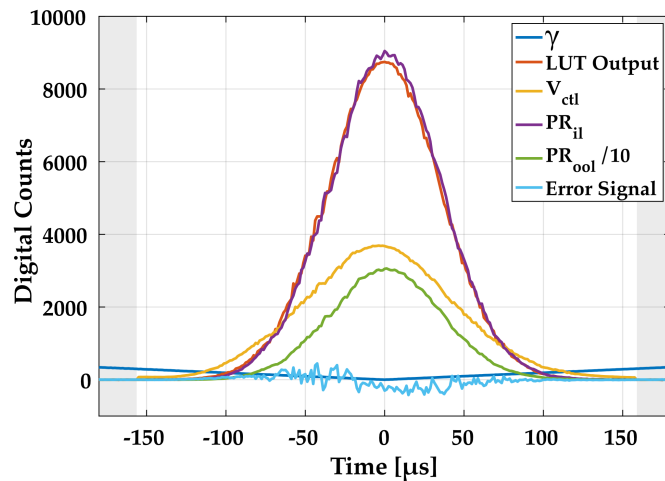
5.3   LLS controller performance

In this section the performance of the LLS is analyzed. First, the out-of-loop error of the controller output is characterized. For this analysis, the LLS was tuned to realize the expected RX power levels of the NGGM mission scenario. This is followed by a study of the delay that is introduced by the LLS between the command of a scanning angle on the transmitting OB to the realization of the associated optical RX power at the receiving OB. Finally, the stability of the LLS output is evaluated. This includes analysis of the achievable path length stability and the polarization state of the LLS output signal.

5.3.1   Out-of-loop error analysis

The in-loop sensor data of a control circuit is not a suitable indicator for the quality of the controller output. That is because in-loop sensor data directly enters the controller's error signal which is minimized by the control loop. Noise or other disturbing influences that the in-loop sensor is not sensitive to are not suppressed by the controller. Additionally, the in-loop sensor noise is imprinted onto the controller output. Therefore, an out-of-loop sensor, that is placed as close to the system's output as possible, is used to properly evaluate the quality of the controller output.

In the case of the LLS a fast, low noise and high gain photoreceiver (Newport 2053-FC-M), placed just before the VOA, is used for this purpose. This scheme allows for reliable measurements with the out-of-loop sensor far above its noise floor. The combination of the fiber beamsplitter that is used to include the out-of-loop sensor in the setup and the subsequent VOA then realizes the required power levels of the RX beam.

As was mentioned before, the absolute optical power at the output of the control loop was not considered for the development of the LLS. However, it was ensured that the output

power is always above the required level. The calibration of the absolute output power is explained in the following paragraphs.

As the LLS is currently tuned to simulate the NGGM mission scenario, the desired output power is between 8 nW and 40 nW for the different optical LO powers (cf. Tab. 5.1). From these values the minimum received power, $P_{\mathrm{RX}} = 8$ nW, is chosen as desired output power as it constitutes the most pessimistic value which must still be measurable by a laser ranging instrument.

To find the required attenuation through the VOA, the output power of the LLS for $\gamma = 0$ µrad was determined while the feed-back and feed-forward controllers were activated. A powermeter was therefore placed directly behind the aperture on the OB. The determined output power was $P_{\mathrm{LLS}} = 123$ nW. Thus, the LLS output power must be reduced to $\kappa_{\mathrm{VOA}} = 8\,\mathrm{nW}/123\,\mathrm{nW} \,\widehat{=}\, 6.5$ % of its initial value. The VOA must thus introduce an attenuation of 93.5 %. Using the calibration of the VOA (see Fig. 5.14), the corresponding voltage $V_{\mathrm{VOA}} = 3.3$ V is obtained.

Before the out-of-loop error can be evaluated, scaling factors must be identified that translate the measured out-of-loop signal and the LUT set-point, which are recorded in units of digital counts, to units of optical watts. To do so, time series data of the out-of-loop sensor and the LUT set-point were recorded with the LabVIEW Host VI. The half-cone misalignment angle was first set to $\gamma = 0$ µrad and then to $\gamma > 300$ µrad, each for a time span of about 1 s. Next, the mean of the recorded amplitude of the out-of-loop PR, $\overline{A}_{\mathrm{OOL}}$, and the LUT set-point, $\overline{A}_{\mathrm{LUT}}$, were calculated for both of the $\sim$1 s long segments. The scaling factors are then obtained by referring the values during the times where $\gamma = 0$ µrad to the output power of 8 nW:

$$\sigma_{\mathrm{OOL}} = 8\,\mathrm{nW}/\overline{A}_{\mathrm{OOL}}|_{\gamma=0\,\mu\mathrm{rad}} = 2.86 \cdot 10^{-13}\,\mathrm{nW/cts} \tag{5.14}$$

$$\sigma_{\mathrm{LUT}} = 8\,\mathrm{nW}/\overline{A}_{\mathrm{LUT}}|_{\gamma=0\,\mu\mathrm{rad}} = 9.51 \cdot 10^{-13}\,\mathrm{nW/cts}. \tag{5.15}$$

In addition to these scaling factors, the out-of-loop sensor shows a small offset which can be obtained from the recorded data where $\gamma > 300$ µrad. Here the output of the LLS is zero by definition. Hence, the out-of-loop PR's mean amplitude is the sought offset:

$$\Theta_{\mathrm{OOL}} = \overline{A}_{\mathrm{OOL}}|_{\gamma>300\,\mu\mathrm{rad}} = 24\,\mathrm{cts}. \tag{5.16}$$

The LUT set-point does not have an offset. Using these expressions, the recorded out-of-loop data and the LUT set-point can be translated to units of optical watts:

$$A_{\mathrm{OOL}}^{\mathrm{nW}} = \left(A_{\mathrm{OOL}}^{\mathrm{cts}} - \Theta_{\mathrm{OOL}}^{\mathrm{cts}} \right) \cdot \sigma_{\mathrm{OOL}}^{\mathrm{nW/cts}} \tag{5.17}$$

$$A_{\mathrm{LUT}}^{\mathrm{nW}} = A_{\mathrm{LUT}}^{\mathrm{cts}} \cdot \sigma_{\mathrm{LUT}}^{\mathrm{nW/cts}}. \tag{5.18}$$

The superscripts indicate the unit of the respective parameter. The out-of-loop error is now evaluated by subtracting the out-of-loop signal from the associated LUT set-point. Using
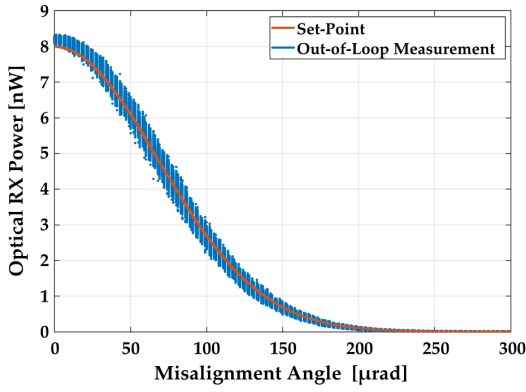
Figure 5.24: Controller set-point and out-of-loop measurement as a function of the half-cone misalignment angle. Both quantities were converted to units of optical nW using Eqs. (5.17)–(5.18).
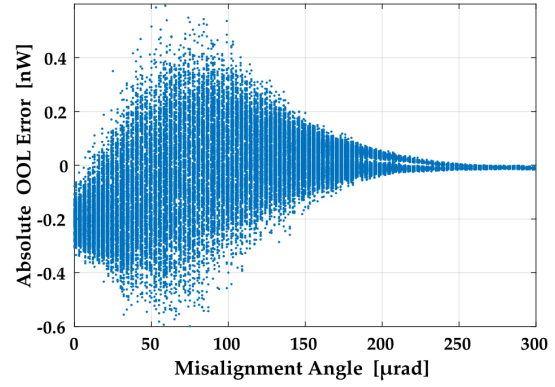
Figure 5.25: The figure shows the absolute out-of-loop error of the LLS controller, as defined by Eq. (5.19), as a function of the half-cone misalignment angle.

Eqs (5.17) and (5.18), both quantities were expressed in optical watts before calculating the error. The time series data, that was used for the evaluation, was once again obtained by driving the horizontal axis of the FSM with a 100 Hz signal with an amplitude of 1.5 mrad.

Figure 5.24 shows the set-point for the LLS feed-back controller and the out-of-loop measurement, both expressed in units of nW, as a function of the FSM half-cone misalignment angle. A time series of approximately two seconds was evaluated. With an FSM scanning frequency of 100 Hz this results in about 400 flashes of RX power that are plotted on top of each other. The absolute out-of-loop error, expressed in units of nW, is now defined as:

$$\epsilon^{\mathrm{nW}} = A_{\mathrm{LUT}}^{\mathrm{nW}} - A_{\mathrm{OOL}}^{\mathrm{nW}}. \tag{5.19}$$

For the recorded time series, this error is shown in Fig. 5.25 as a function of the half-cone misalignment angle γ. As can be obtained from the plot, the maximum absolute out-of-loop error is in the range of a few hundred pW. The largest error occurs for half-cone angles between about 30 μrad and 100 μrad. A small offset of about -200 pW is visible for $\gamma \approx 0$ μrad. Perhaps even more insightful than the absolute error is the relative out-of-loop error which is defined as:

$$\epsilon^{\%} = \frac{A_{\mathrm{LUT}}^{\mathrm{nW}} - A_{\mathrm{OOL}}^{\mathrm{nW}}}{A_{\mathrm{LUT}}^{\mathrm{nW}}} \cdot 100. \tag{5.20}$$

This relative error is displayed in Fig. 5.26. As can be obtained from the plot, the mean relative out-of-loop error at an angle of $\gamma = 0$ μrad is $\sim 2.5\%$. Towards the NGGM FoV of about 150 μrad it increases to about 10 %. For angles above ~ 275 μrad the maximum relative error is as high as 1000 %. This range is not shown in Fig. 5.26 to enhance the resolution in the more important range of $\gamma \approx$ FoV. Figure 5.27 shows plots of the PSD of the controller set-point which was translated to units of nW and the error signal, also expressed in nW. It can be obtained from the figure that the error signal is between five
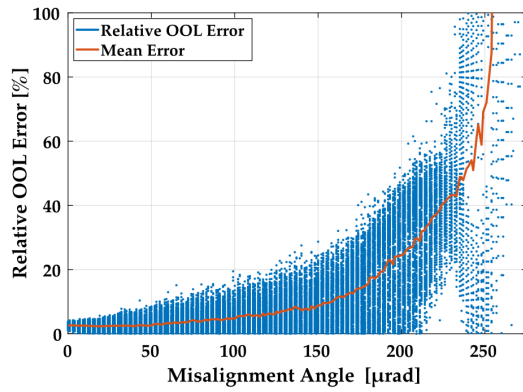
Figure 5.26: The figure shows the relative out-of-loop error of the LLS controller, as defined by Eq. (5.20), for $0 < \gamma < 300\,\mu\text{rad}$ together with its mean value.
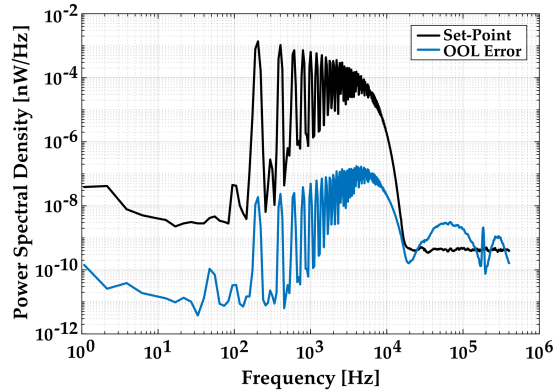
Figure 5.27: Plot of the PSD of the controller set-point and the out-of-loop error, as defined by Eq. (5.19), with feed-forward and feed-back controllers activated.

($f = 200\,\text{Hz}$) and three ($f = 5\,\text{kHz}$) orders of magnitude below the desired output power.

5.3.2 LLS time delay

There exists a delay between the command of an FSM angle and the realization of the corresponding RX power at the receiving OB. This is due to delays that are introduced by the FSM itself, the used cables, the limited sampling frequencies of the ADCs and DACs and the FPGA latency.

A frequency generator was used to generate a signal of $f = 100\,\text{Hz}$. The output of the frequency generator was split. One part was connected to a data acquisition (DAQ) system and the other was used to drive the FSM. With this setup, the delay between the input to the FSM and the output of the LLS could be determined. Figure 5.28 shows a short section of the recorded time series data. The mean delay $\overline{\Delta t}$ is obtained by calculating the average value of Δt over a time series of 0.5 s. A value of $\overline{\Delta t} = 540\,\mu\text{s}$ was found. As was
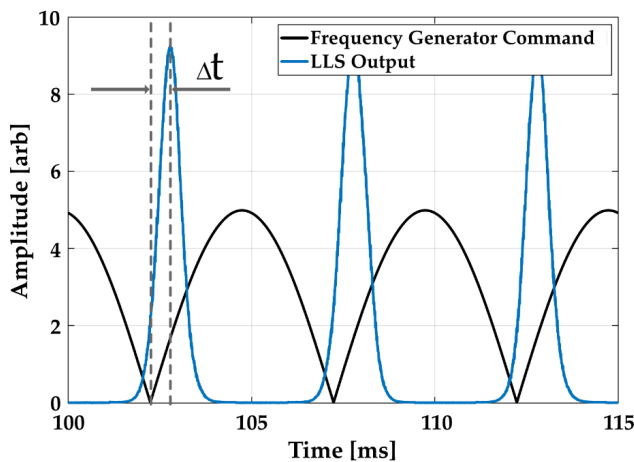
Figure 5.28: The figure shows a short segment of time series data of FSM commands and the corresponding LLS output.

mentioned before, this delay is caused by various parts within the LLS. A comparison of $\overline{\Delta t}$ with the light travel times of missions like GRACE-FO and NGGM, as well as a comment on how to change the delay is given in the summary of this chapter –see Sec. 5.4.

5.3.3 LLS output stability

In this section, two quantities are analyzed that characterize the stability of the LLS optical output: the polarization of the released laser beam and the path length stability of the beat note signal, recorded with the help of one LRI-like OB.

The polarization of the light is of high interest, because it directly affects the achievable heterodyne amplitude of the beat note signals on the OBs. This is because only those light fields interfere on the recombination beamsplitter that are polarized along the same axis. As was explained in Sec. 3.2.2.1, the LOs show linear p-polarization. Therefore, the output of the LLS must also be p-polarized.

The LLS setup is composed of fiber-optical components. All these components use polarization maintaining (PM) fibers.However, the polarization is never perfectly preserved. An important figure of merit that describes the quality of the polarization at the output of such components is the polarization extinction ratio (PER). It is defined as the logarithmic ratio of a optical powers of a light field's components in the p- and s-polarization states:

$$\mathrm{PER} = 10\log_{10}\left(\frac{P_p}{P_s}\right). \tag{5.21}$$

It should be noted that the definition in Eq. (5.21) could also be given with P_p and P_s swapped. The presented definition is used here as p-polarization is the desired polarization state. The PER is, thus, usually positive and larger values are preferable.

As polarization maintaining fibers only maintain the polarization state of a perfectly aligned input, the combination of multiple fiber components becomes a process which is crucial to the combined PER. Throughout the experimental setup described here, two fibers are combined by pressing their end surfaces together with the help of fiber mating sleeves. The alignment of the two fibers' axes is thereby determined by the quality of the used mating sleeve. No components are currently used which would allow for an active control of the polarization state of the light that is guided by the fibers. Thus, the combined PER of all the used components can only be determined but not optimized.

The overall PER is measured by placing a polarimeter (Schäfter & Kirchhoff SK010PA) directly behind the large FC that generates the RX beam and carrying out the built-in PER measurement. During this process the polarization of the light is recorded by the polarimeter for several seconds while the fibers under test are stressed. One of the simplest ways to induce stress, is to moderately heat up the fibers. The applied stress results in a varying phase shift between P_p and P_s. Of interest is the minimum value of the PER that can be recorded this way. For the LLS this value was PER = 18.5 dB, which corresponds
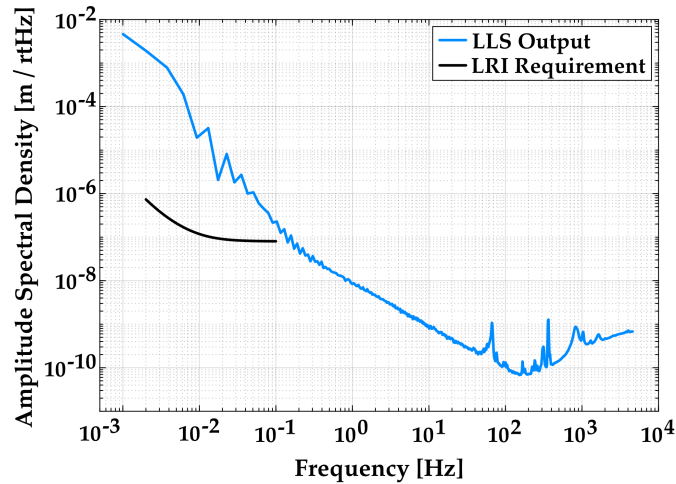
Figure 5.29: The figure shows the stability of the optical path length, that was recorded with one of the OBs while the LLS provided the RX beam. To reduce the visible noise at higher frequencies, logarithmically scaled Fourier bins were used for the calculation. For comparison the requirement on the path length noise of the LRI is shown.

to a linear ratio of about 100 to 1 between p- and s-polarization. This value agrees well with the PER of the used fiber-coupled AOMs that is provided by their manufacturer. It can be deduced from this that not the fiber-to-fiber connections, but the AOMs limit the reachable PER.

As was outlined in the introduction of this chapter, the LLS was not designed to provide a path length stability of its output signal that is compatible with the usual stability of intersatellite laser interferometers in the nano- or picometer range at mHz frequencies. Nevertheless, the path length stability of an interferometric signal that uses the LLS to provide the RX laser beam was characterized. For this one LRI-like OB and a phasemeter, that was previously used for the tests described in Chapter 3, were used. The LO power was 20 mW and the LLS was set to provide an RX power in the nW range. Both, the feed-back and feed-forward control loops were activated. The phasemeter tracked and recorded the beat note frequency, which was set to 1 MHz by detuning the driving frequency of AOM 1 by to 149 MHz. In post-processing, the tracked beat note frequency was then referred to an optical phase by integrating it and converting it from radians to meters by accounting for the laser wavelength of $\lambda = 1064$ nm. A plot of the ASD of this signal is shown in Fig. 5.29. The obtained path length stability is a combination of the phase stability of the output of the LLS, the dimensional stability of the OB, which is made out of aluminum, the phase stability of the LO and the performance of the used phasemeter. However, the stability of the LLS is deemed to be the dominant contributor. Additionally, the figure shows the path length noise requirement of the LRI of $80\,\text{nm}/\sqrt{\text{Hz}} \times \text{NSF}$ as reference.

5.4   Summary and discussion

In this chapter, the design, construction and performance of the LLS test bed was explained. Key properties of the LRI on GRACE-FO and a laser ranging instrument for NGGM were used as input to the derivation of requirements on the LLS. Here, special focus was laid upon the initial acquisition mode of the instruments as this imposes the highest requirements on the test bed. The design of the LLS is based on the successful Fiber OGSE, which was jointly developed by the DLR Institute of Space Systems and the AEI as part of the OGSE for GRACE-FO (see Chapter 3). However, the LLS was not subject to the same, tight requirements that the Fiber OGSE had to fulfill: e.g. transportability and the intricacies that are related with flight hardware testing. Therefore, numerous improvements could be implemented.

As the lasers were accessible during experiments with the LLS, in contrast to testing of flight hardware that is integrated into a S/C, the TX beams were not needed to be processed by the LLS but the lasers' outputs could be used directly instead. This eliminated an additional, FSM angle dependent gain that had to be accounted for by the Fiber OGSE. Additionally, this reduced the complexity of the setup as the TX beam angle did not need to be measured by a custom sensor. The internal FSM sensor could be used instead. This was legitimate as the FSM and its controller were not subject to investigations during tests with the LLS. However, should this change in the future, an independent measurement of the FSM angle could be included in the setup. Furthermore, the LLS controller was extended by a feed-forward filter. This helped to reduce the dynamic range of the error signal for the feed-back controller which in turn helped to relax the requirements on the latter. The use of VOAs in contrast to mechanical attenuators, as were used for the Fiber OGSE, allowed for a much more reproducible setting of the RX power. Moreover, debugging of the LLS setup and the OBs was significantly eased by this.

The LLS controller showed a closed-loop bandwidth of $\sim$30 kHz where gain peaking of $\sim$3 dB occured. The Fiber OGSE on the other hand has a bandwidth of about 50 kHz [77]. However, this is accompanied with slightly higher resonance peaks at this frequency. Analysis of the PSD of the out-of-loop error (see Fig. 5.27) revealed that the largest contribution to the error occurred in the frequency range between a few kHz and 20 kHz. This implies that the LLS would in fact benefit from a higher UGF. To achieve this, the existing PI-controller could be tuned for a higher UGF. However, this could only be realized at the cost of less phase margin which leads to more gain peaking. Alternatively, the use of an additional differential component to the controller could provide the required gain at higher frequencies. It could be shown that the relative out-of-loop error of the LLS output was below 10 % for half-cone misalignment angles $\gamma < 150$ µrad, which corresponds to the FoV of the laser ranging instruments on GRACE-FO or NGGM (cf. Tab. 5.1). This good performance shows that there is currently no pressing need for an increase of the controller bandwidth.

The polarization extinction ratio (PER) corresponded to the expected value that was

introduced by the AOMs. A linear ratio of approximately $P_p/P_s \approx 100/1$ was achieved. The expected effect on the achievable heterodyne beat note signals seemed marginal. Therefore, further control of the state of polarization was not deemed necessary. The achieved phase stability at frequencies below 10 Hz was poor in comparison to the typical levels of intersatellite laser interferometers (see Fig. 5.29). This was expected and was attributed to the strong effect of temperature variations on the dimensional stability of the used fibers. As the LLS was not designed to enable phase stability measurements in this frequency range, this circumstance was not deemed as troubling. If the stability of the setup needs to be enhanced in the future, optical elements that allow for an active control of the state of polarization of the light could be included. Furthermore, the fibers' temperature could be better controlled or even actively stabilized.

The delay between a changing FSM angle and the realization of the corresponding RX power at the output of the LLS was found to be ~540 µs (see Fig. 5.28). The desired value, which corresponds to the light travel time between one S/C and another, is ~300 µs for NGGM or 600 µs ... 900 µs for GRACE-FO. Currently, it seems that the achieved value cannot be lowered with the existing setup, because the ADCs, DACs and the FPGA clock were already operated at their respective maximum frequency. The FSM angles that were read out by the FSM controller were low-pass filtered as the raw signals were very noisy. These filters introduced a delay of about 130 µs. It could be investigated if a custom-made sensor, to read out the FSM angles, could help to reduce this part of the total delay. Further optimization of the FPGA code regarding latency could also be contemplated. Enlarging the delay to simulate larger S/C separations (e.g. for LISA) could be realized by using longer first in first out (FIFO) registers for digital storing of the half-cone misalignment angle. However, the available space on the FPGA could be a limiting factor. Additionally, the sampling frequencies of the ADCs and DACs could be reduced. Instead of using the 80 MHz FPGA clock, a slower derived clock could be used.

If parts of an instrument for a mission like LISA should be tested with the LLS further changes should be made. The output power of the LLS would have to be reduced to the pW level. However, this can be realized by using the full range of the VOAs or, if necessary, adding additional attenuators. Even changing the distribution of the RX power as a function of the TX beam angle is possible by exchanging the respective LUTs. By doing this, e.g. a fiber mode could be implemented as distribution of the RX power (see e.g. [46]). If required, the FPGA code could even be adapted to process the two components of the half-cone misalignment angle separately. This could be done to realize distributions of the RX power that are not rotational symmetric around the LOS. For a mission like LISA, laser beam steering is realized by slow tilts of the complete S/C or by pointing of the telescope and the OB. The bandwidth of the LLS control loops, that was discussed at length above, is not of importance in this context. Obviously, the LLS in its current form can only be used to connect two OBs, thus simulating two laser links. As the laser ranging instrument for LISA employs six laser links, the LLS would have to be expanded significantly to enable a full system test, if this should be desired. Additionally, the LLS

currently simulates the RX laser beams by using fiber collimators (FCs) which generate Gaussian laser beams of about 4 cm diameter. Due to the currently envisaged architecture of the laser ranging instrument for LISA, this implies that telescope simulators would be required to replace the FCs (see [97, 98, 99]). These devices can be used to create faithful replicas of the output of the LISA telescope that then serve as RX beam on the OB. As, to the knowledge of the author, only one such device has been constructed so far in a rather elaborate process, it might be advisable to design simpler alternatives that create LISA-like RX beams.

Chapter 6

Investigation of different sensor types as acquisition sensor

As was presented in Chapter 4, the initial acquisition process on the GRACE-FO mission worked flawlessly. A similar procedure can only be used for a mission like LISA, if a fast steering mirror (FSM) is placed within the interferometer path. Due to orbital dynamics, the line of sight (LOS) between either two LISA S/C will change by about $\pm 1°$ per year [100, 101]. The decision in favor or against an FSM on the optical bench (OB) is part of the answer to the question of how to compensate for this "breathing" of the constellation. Two options were considered: the implementation of a steering mirror, this is referred to as "in-field pointing", and tilting of a whole sub-system of the instrument, consisting of telescope, OB and test mass, which is called "telescope pointing". As a consequence of a risk analysis, the telescope pointing scheme is currently foreseen as the baseline [100]. Hence, no steering mirror will be implemented as part of the interferometer. Therefore, spatial scanning of the laser beam during the initial link acquisition procedure will either be realized by rotations of the S/C themselves or by telescope pointing, or a combination of both. However, such S/C maneuvers consume large amounts of propellant. Furthermore, neither of the two mentioned mechanisms allows for fast scans of the laser beam. Therefore, it was decided to implement dedicated acquisition sensors with a wide field of view (FoV) that allow for a reduction of the spatial uncertainty space. Additionally, the degrees of freedom (DoF) that need to be calibrated by the initial acquisition procedure, are decoupled when dedicated sensors are used. The link acquisition procedure for a Next Generation Gravity Field Mission (NGGM) is not yet well defined. However, it would most certainly be simplified and be made more reliable by the usage of dedicated acquisition sensors. The term *constellation acquisition sensor* (CAS), which was coined in the context of LISA, is used throughout this thesis to describe such dedicated acquisition sensors.

Two alternative detectors were investigated within this thesis: a position sensitive photodetector (PSPD) and an InGaAs focal plane array (FPA) camera. Both detector types have advantages and disadvantages. A PSPD is comparably cheap and requires a rather simple electronic readout circuit. However, in order to distinguish the impinging laser beam from

stray light and the detector noise, the laser beam must be amplitude modulated, which requires additional hardware on, or close to, the OBs. An InGaAs camera on the other hand requires more complex electronics for the readout of the data. However, due to the high quantum efficiency (QE) of InGaAs for a wavelength of 1064 nm and the possibility of using long exposure times, the detection of low power signals is feasible, even with high SNRs.

It should be mentioned that within this thesis the abbreviation "PSPD" for Position Sensitive PhotoDetector is used, instead of the more common term "PSD", to avoid confusion with the abbreviation of the power spectral density.

In the following section, a short description of an initial acquisition process with a dedicated acquisition sensor is given. This is followed by an overview of the design parameters for an acquisition sensor system for LISA and NGGM. The characteristics of both analyzed sensor types and the achievable resolution of the measurement of the laser beam position are discussed in detail in the subsequent sections. This chapter is concluded by a discussion of the obtained results and a comparison of the studied sensors with alternative sensor types or materials.

6.1 Laser link acquisition with dedicated acquisition sensors

In this section, a brief overview of the initial acquisition mode with dedicated acquisition sensors is given, in order to expose the benefits of utilizing such sensors. However, the processes that are described here are merely a description of a generic link acquisition procedure with dedicated sensors. They should not be understood as a proposed procedure for a specific mission.

The initial acquisition procedure that was used by the LRI on-board of GRACE-FO was presented in Sec. 2.2. The LRI does not use any dedicated acquisition sensors. Therefore, this procedure is based on using the quadrant photoreceivers (QPRs) on the OBs as only sensors in the initial acquisition mode. As a consequence, five DoF had to be matched simultaneously: two laser beam angles per S/C and the laser frequency on the transponder S/C. Only when all these parameters were within narrow ranges around their corresponding optimum, did the QPRs detect signals. Thereby, the laser beam angles were scanned with the help of FSMs. They were able to conduct fast spatial scans with scanning frequencies of up to 100 Hz. However, even with such high scanning frequencies, the total time that was required for a scan of the complete uncertainty space took about 9 hrs.

For a mission like LISA where it is planned to rotate the complete S/C, or at least large parts like the telescopes, to introduce tilts of the transmitted laser beams, the corresponding scanning frequencies are far below 100 Hz. A scan of an uncertainty space that is similar to the GRACE-FO case would require an immense amount of time and propellant. Hence, the LRI initial acquisition procedure is not directly applicable for a mission like LISA.

Instead, procedures that make use of dedicated acquisition sensors could be used. These sensors would be designed such that they are sensitive to the DC power of impinging light. This should be understood in contrast to the MHz beat note signals that the QPRs are sensitive to, which are only proportional to the square root of the optical power levels. Depending on the sensor type, amplitude modulation of the laser beam in the low kHz range might be required to unambiguously distinguish the weak incoming beam from background noise or starlight. Instead of detecting heterodyne signals, only the RX beams would be incoherently measured by the acquisition sensors. Hence, no alignment below a certain threshold of the received and the local beam is required. Additionally, the frequency difference of these two beams is irrelevant. This splits up the five DoF that need to be calibrated into three scans with 2+2+1 DoF: One spatial scan in two axes per S/C and a frequency scan of the transponder laser.

A dedicated acquisition sensor is used to infer the tilt of the local OB with respect to the laser ranging instrument's LOS in one of these spatial scans. This is accomplished by precisely measuring the position of a laser beam on the sensor surface by means of incoherent power detection. An imaging system in front of the sensor translates a tilt of the local S/C, and consequently of the local OB, into beamwalk on the sensor. By prior calibration of beamwalk on the sensor to beam tilt relative to the LOS, the desired tilt angle of the OB can be deduced. The used imaging system should thereby be optimized such that the complete spatial uncertainty space is imaged onto the sensor surface. This is referred to as the FoV of the acquisition sensor.

Once a S/C has determined its misalignment with respect to the LOS, it should be rotated such that this angle is minimized. After all involved S/C have corrected their misalignment angles, a subsequent scan of the laser frequency on the transponder S/C must be carried out. The correct transponder laser frequency is identified as soon as the QPRs on the OBs detect a heterodyne signal. Hereafter, the DWS pointing control loops and the laser frequency lock should be enabled to maintain the obtained constellation and to further optimize the amplitudes of the AC beat note signals.

Of course this procedure is overly simplified. Many factors, e.g. the amplitude and dynamics of the residual jitter of the S/C during the spatial scans or the frequency acquisition scan, were not considered. Additionally, only the acquisition of the laser link between two S/C was described. Acquiring all six links of the LISA constellation clearly introduces substantial complications that were not discussed here. However, as was stated at the beginning of this section, no specific mission scenario was described here. The goal of this short section was to present the key advantage of using dedicated acquisition sensors, namely splitting up the five DoF that are required for the acquisition of a single laser link into three independent scans of 2+2+1 DoF.

6.2   Design parameters for a CAS system for NGGM and LISA

Throughout this thesis, the combination of a constellation acquisition sensor (CAS), corresponding imaging optics and the readout electronics are referred to as a *CAS system*. Using the LISA Payload Description Document [100] and the results of the e^{2}motion study [22], design parameters for such a CAS system for LISA and NGGM are established. The listed parameters should be considered preliminary. This is even more important for the NGGM scenario, as the e^{2}motion report merely constitutes an early study on a possible successor to GRACE-FO. LISA, in contrast, is currently in its Phase A. Furthermore, it should be noted that only parameters regarding the optical properties of a CAS system are investigated here. This chapter does not focus on environmental properties of the sensors, like size and weight, electric power consumption or the emitted heat. Table 6.1 summarizes the obtained design parameters.

Table 6.1: Design parameters for a CAS system for NGGM and LISA [100, 22]

Parameter	NGGM	LISA
Field of View (FoV)	± 3 mrad	± 33.5 mrad
Centroiding Accuracy	30 µrad	100 µrad
Max. Opt. Power	$(8\,\text{nW–}40\,\text{nW})\cdot\mathcal{R}$	25 pW
Min. Opt. Power	TBD	1 pW
Frame Rate	TBD	10 Hz
Nom. Operating Temperature	$\sim 20\,°\text{C}$	$20\,°\text{C}$
Operating Mode	Link Acquisition Mode	Link Acquisition Mode Star Tracker Mode

The maximal optical power on a CAS describes the power level that the sensor receives when the distant S/C points its laser beam directly towards the receiving S/C. For NGGM, this power is not yet defined. While the total received power is known ($8\,\text{nW}-40\,\text{nW}$), there will be optical elements that split off a part of the RX beam for the CAS. This introduces attenuation factors which cannot be defined before the laser ranging instrument has been properly designed. These factors are described by the parameter $\mathcal{R}$ in Tab. 6.1. A typical order of magnitude for this parameter is $1\,\%-10\,\%$. The minimum optical power that a CAS on NGGM must be able to detect is defined by the maximum optical power and the grid error of the laser beam's spatial scan on the distant S/C. Both of these parameters have not yet been defined. Therefore, also the expected minimum power remains currently undefined. However, due to the high maximum optical power, in comparison with the LISA parameters, it can be expected that this value will be higher or equal to the corresponding value for LISA. The provided nominal operating temperature of the CAS on NGGM is an estimate. It was assumed that the CAS is exposed to the same thermal environment as the OB, which is usually at room temperature.

It is planned to use a CAS for LISA in two operating modes: a link acquisition mode and a star tracker mode. In the latter, a dedicated acquisition sensor will be used to measure

the bias angle between the OBs and the star trackers on a S/C. This will be realized by using the CAS to localize one or more bright stars on the sky. The determined positions of the stars are then compared to the corresponding results that were obtained with the actual star trackers. The difference between these measurements yields information about the angular misalignment between the local OB and the S/C reference frame. By doing this the required scanning range of the link acquisition mode that needs to be covered by subsequent S/C steering is severely reduced. On NGGM, a star tracker mode is currently not foreseen. According to the e^{2}motion study, either a FSM can be used to scan the laser beam, as was done on GRACE-FO, or a dedicated laser source with large beam divergence in the mrad range can be used to ease the link acquisition procedure. In both scenarios there is no need for a reduction of the spatial uncertainty space beyond the GRACE-FO level. This is because FSM scanning allows for quick scans, even of large uncertainty spaces. If a dedicated acquisition light source were used, e.g. a beacon beam as described in [102], the spatial uncertainty on the transmitting S/C would either be eliminated completely or at least be severely reduced, depending on the relationship of the beacon beam size and the uncertainty space.

The ratio of the required centroiding accuracy and the total FoV of the sensor is a useful parameter that allows for easy comparison of mission requirements on the one hand and the realized functionality of a CAS system on the other. For the LISA requirements, this ratio is $\Gamma_{\text{LISA}} = \frac{0.1\,\text{mrad}}{67\,\text{mrad}} = 1.5 \cdot 10^{-3}$. Thus, the required centroiding accuracy corresponds to 0.15 % of the FoV. For NGGM this value is $\Gamma_{\text{NGGM}} = \frac{0.03\,\text{mrad}}{6\,\text{mrad}} = 5 \cdot 10^{-3}$, or 0.5 %. Thus, the NGGM requirements, regarding centroiding accuracy and FoV, can be considered about three times less stringent compared to LISA.

6.3 Investigation of a position sensitive photodetector as CAS

A two dimensional position sensitive photodetector (PSPD) (*2L10 PSD* from SiTek Electro Optics [103]) was studied as possible CAS in the LISA context. The investigated PSPD is a duo-lateral type photodiode made of silicon [104]. Such devices have two resistive layers, each of which is connected to two electrodes on opposing sides (see Fig. 6.1). A proper combination of the photocurrents that are generated by the two anodes and two cathodes yields information on the position of the beam on the sensor [105, 106]. Within a constrained area, that is usually specified by the manufacturer, the relationship between the beam position in one axis and the corresponding photocurrents is linear. Hence, PSPDs have found wide application throughout industry and science, whenever the position or orientation of a device is of interest (see e.g. [107, 108]).
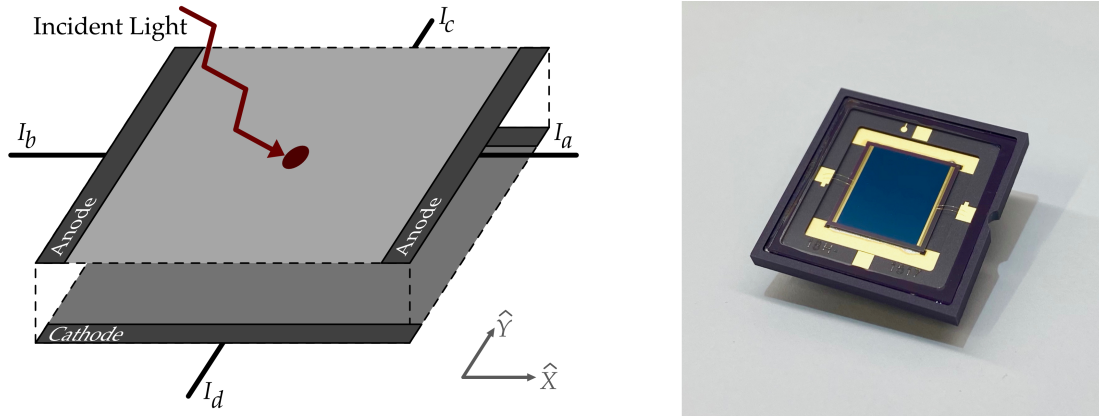
Figure 6.1: Schematic drawing (left) and photograph (right) of a PSPD . In the drawing, the PSPD's two resistive layers are shown in gray and the four electrodes in dark gray. The four currents I_a, I_b, I_c and I_d can be combined to obtain information on the spot position of the incident laser beam along two axes, $\hat{X}$ and $\hat{Y}$, which are defined by the sensor topology.

Within the linear range, the position of a laser beam spot on a PSPD is defined for the two orthogonal detector axes, $\hat{X}$ and $\hat{Y}$, by the following equations:

$$\hat{x} = k_x \frac{I_a - I_b}{I_a + I_b} \tag{6.1}$$

$$\hat{y} = k_y \frac{I_c - I_d}{I_c + I_d} \tag{6.2}$$

with scaling factors k_x and k_y. Normalizing the differences by the sums of the currents yields output signals that are independent of beam power level variations. In order to separate the desired signal from background light or other noise sources in the DC range, it is advisable to modulate the laser beam's amplitude with a frequency in the kHz range [109, 110]. When amplitude modulation is applied, the signals I_a–I_d, used in Eqs. (6.1) and (6.2), describe the amplitudes of the AC photocurrents.

The work that is described in this chapter was carried out in parts by the author of this thesis and in parts by a master student, Vrushabha Raja Marlur Sunder Kumar, under supervision of the author. Therefore, parts of the ideas and results that are presented here were already published in [111].

In the next section, the PSPD readout electronics are explained. This is followed by a presentation of calibration results and a short discussion.

6.3.1 PSPD readout electronics

Fig. 6.2 shows the schematic design of the circuit that was developed to readout and combine the PSPD currents. The first part (see red boxes in Fig. 6.2) contains electronics that are used for the application of a bias voltage to the PSPD. The second part is made up by TIAs (blue boxes). These amplifiers are used to convert the photocurrents to voltages and to amplify the signals. In order to remove DC offsets from the signals which could

saturate the second amplifier stages and to limit the noise in the AC domain, subsequent bandpass filters (BPFs) are used (turquoise boxes). Finally, the differences and the sum of the signals are calculated by difference and sum amplifiers (purple and green boxes). Additionally, these circuits are used to apply a second stage of amplification to the signals. The combination of the differences and the sum is then done in post-processing.
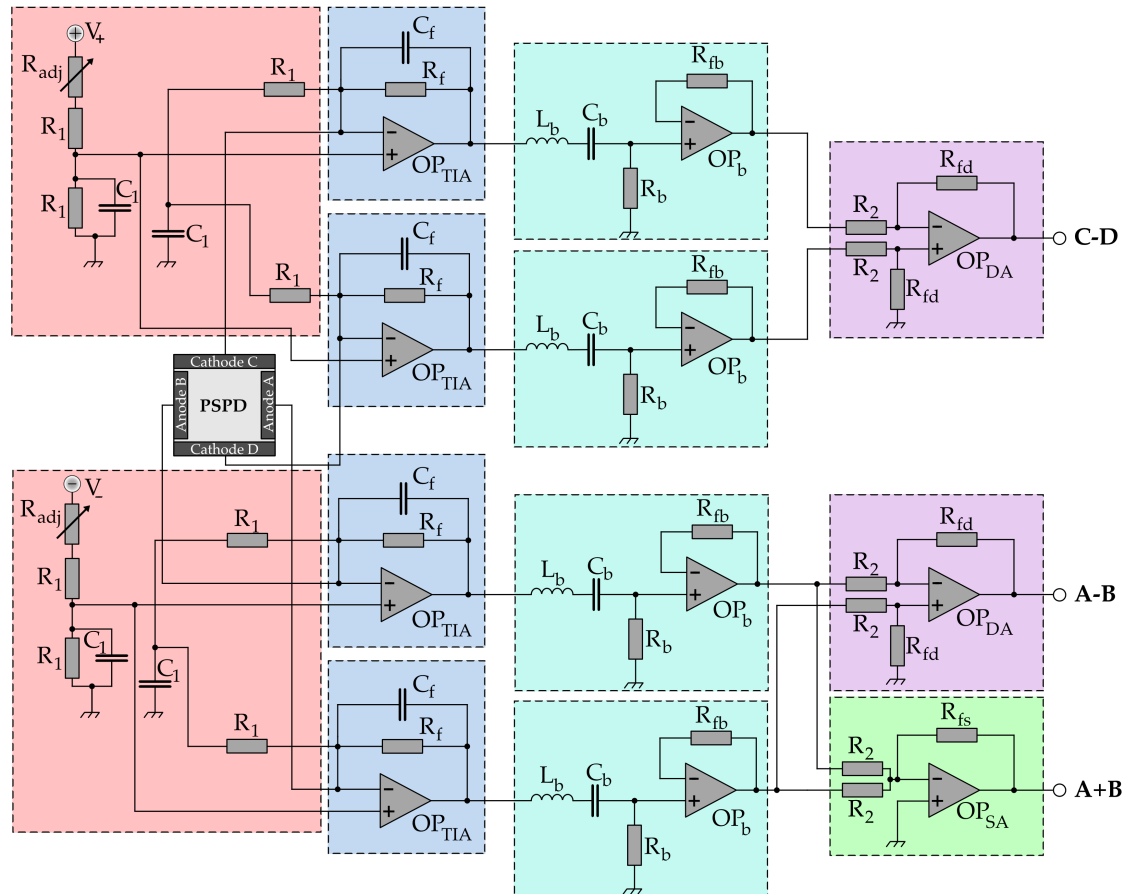
Figure 6.2: Schematic drawing of the electronic readout circuit that was designed to provide information on the horizontal and vertical position of a laser beam that hits the PSPD. The circuit can be divided into five groups: electronics related to the application of the bias voltage to the PSPD (red boxes), TIAs (blue boxes), BPFs (turquoise boxes), difference amplifiers (purple boxes) and the sum amplifier (green box).

6.3.1.1 Design of transimpedance amplifiers

Just like for a normal photodiode (PD), the application of a reverse-bias voltage to a PSPD increases the width of the depletion layer which leads to a higher bandwidth. At the same time, the capacitance of the detector is significantly reduced. This helps to reduce the input-referred current noise (ICN). However, in contrast to a normal PD, a duo-lateral PSPD does not provide accessible ports which can be used to connect a bias voltage. Therefore, the transimpedance amplifier (TIA) design had to be extended to allow for the application of a bias voltage. The electronic components shown in the red boxes in Fig. 6.2

were used to apply offset voltages to the inputs of the operational amplifiers (OPAs) which then led to the required voltage over the cathode - anode junction of the PSPD. The outputs of the TIAs remained unaffected by this bias voltage. In the used design, the positive and negative supply voltages of the OPAs, $V_\pm$, were also used as bias voltage. A symmetric design was chosen, where $V_+/2$ is applied to the cathodes and $V_-/2$ to the anodes. With $V_\pm = \pm 5\,\text{V}$, and choosing $R_1 = 1\,\text{k}\Omega$, the total bias voltage applied to the detector was $V_\text{bias} = -5\,\text{V}$. The resistors R_adj were used to compensate for tolerances of the R_1 resistors. Capacitors $C_1 = 1\,\mu\text{F}$ were used to suppress fluctuations of V_bias and the ground potential.

For the design of the TIAs, two properties were especially important: the 3 dB bandwidth and the input-referred current noise (ICN). As amplitude modulation of the laser beam in the low kHz range is envisaged, the TIA bandwidth must be high enough to process the modulated signals. A bandwidth of $\geq 10\,\text{kHz}$ seems appropriate. As the ICN describes the input referred noise of the TIA, its noise floor basically determines the minimum optical current that a TIA can properly process. The PSPD is made from silicon. Therefore, a typical value for the responsivity of $\rho_\text{PSPD} \approx 0.25\,\text{A/W}$ for a wavelength of 1064 nm was assumed [112]. For the LISA scenario, the maximum expected signal power on the PSPD is $P_\text{max} = 25\,\text{pW}$ (cf. Tab. 6.1). Therefore, the corresponding peak-to-peak amplitude of the sum of either the anode or the cathode photocurrents turns out as:

$$I_\text{pk-pk} = \rho_\text{PSPD} \cdot P_\text{max} \tag{6.3}$$
$$= 0.25\,\text{A/W} \cdot 25\,\text{pW}$$
$$\approx 6\,\text{pA}.$$

For this calculation, a modulation depth of 1 was assumed. The rms noise follows from the ICN as is shown in the following equation [84]:

$$\tilde{n}_\text{rms} = \sqrt{\int_{f_1}^{f_2} \text{ICN}^2(f)\mathrm{d}f}. \tag{6.4}$$

For frequencies in the kHz range, the ICN can be considered constant [45]. This expression can then be simplified to:

$$\tilde{n}_\text{rms} = \sqrt{\int_{f_1}^{f_2} \text{ICN}^2\mathrm{d}f} \tag{6.5}$$

$$= \sqrt{\text{ICN}^2 \cdot \int_{f_1}^{f_2} \mathrm{d}f} \tag{6.6}$$

$$= \text{ICN} \cdot \sqrt{\Delta f}. \tag{6.7}$$

As the TIA output will be filtered by a bandpass filter (BPF) (see Fig. 6.2), the scaling factor $\sqrt{\Delta f}$ is defined by the passband frequency range of this component. Considering the PSPD scenario, a typical value for this frequency range could be $\Delta f = 1\,\text{kHz}$. The
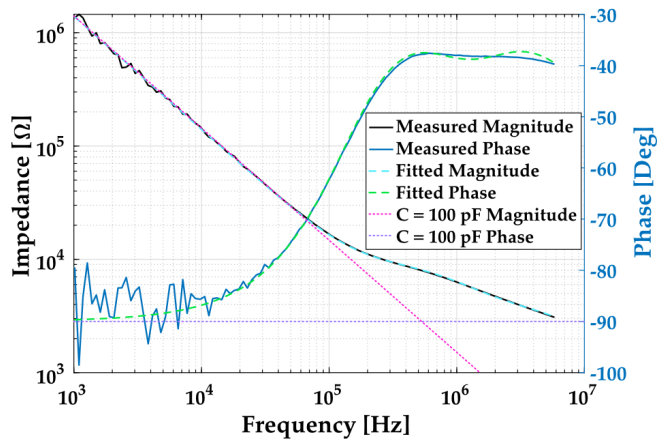
Figure 6.3: The figure shows plots of the amplitude and phase of the measured and fitted impedance of the PSPD. Additionally, the magnitude and phase of a pure capacitance with $C = 100\,\text{pF}$ is shown.

scaling factor in Eq. (6.7) then becomes $\sqrt{\Delta f} \approx 32\,\sqrt{\text{Hz}}$. Hence, in order for the TIA ICN to not dominate a pA level photocurrent that is expected to be generated by a weak RX signal (cf. Eq. (6.3)), the ICN noise floor must be below ICN $= 1/32\,\text{pA}/\sqrt{\text{Hz}} \approx 30\,\text{fA}/\sqrt{\text{Hz}}$. Furthermore, the TIA gain R_f should be chosen as large as possible. Therefore, a value of $R_f = 1\,\text{M}\Omega$ was used. It was found that higher values jeopardize the proper functionality of the OPAs.

Before the remaining parameters of the TIA circuit were defined, the impedance of the bare PSPD was measured for a bias voltage of $V_{\text{bias}} = -15\,\text{V}$. A theoretical model, consisting of three parallel combinations of a resistor and a capacitor in series, was fitted to the data. The model does not have any physical meaning, it simply allows for a good parametrization of the measured data. Figure 6.3 shows the measured data and the fit result. As can be obtained from the figure the impedance of the PSPD can be well approximated by a capacitance of $C_i \approx 100\,\text{pF}$ for frequencies below 10 kHz.

A capacitor C_f is used in the feed-back path of the TIAs to stabilize its output (see Fig. 6.2). A maximally flat response of the system, as described in [113], was aspired. C_f then follows from R_f, the OPA's gain bandwidth product (GBWP) and C_i, the capacitance of the PSPD as:

$$C_f = \frac{1}{4\pi\,R_f\,\text{GBWP}} \cdot \left(1 + \sqrt{1 + 8\pi\,R_f\,C_i\,\text{GBWP}}\right). \tag{6.8}$$

The chosen R_f, C_f according to Eq. (6.8), the fitted PSPD impedance as well as various OPA-specific parameters were then used in a simulation of the complete TIA circuit with the tool LISO. LISO is a program for **Li**near **S**imulation and **O**ptimization of analog electronic circuits [114]. The goal of the simulation was to find suitable OPAs that provide a 3 dB bandwidth of at least 10 kHz and a ICN in the low kHz range that is below the pA/$\sqrt{\text{Hz}}$ level.

For all the investigated OPAs, the bandwidth criterion was met. Hence, it did not impose a constrain on the choice of a suitable OPA. The achievable ICN, on the other hand, was strongly influenced by the respective properties of the different OPAs. Here, the input referred voltage and input referred current noise terms must be as low as possible.

Figure 6.4: LISO simulation result of the total input-referred current noise (ICN) of the PSPD at the input of a TIA which uses the AD820 OPA.
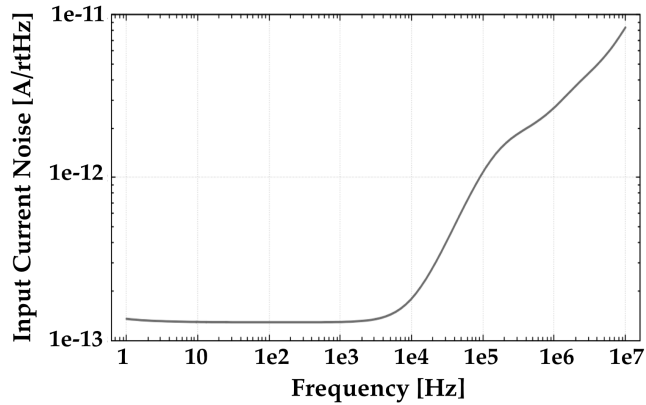
Especially regarding the input current noise, OPAs that are based on field effect transistor (FET) topologies usually provide the best performance. However, while many such FET OPAs were investigated, it quickly became obvious that for the frequency range of interest in the low kHz range, the achievable ICN was already limited by thermal noise, often also called Johnson noise, of the feed-back resistor. For a resistance R at temperature T, expressed in Kelvin, the input referred ASD of the Johnson noise is described by [115]:

$$\widetilde{I}_J = \sqrt{\frac{4k_B T}{R}} \tag{6.9}$$

with the Boltzmann constant $k_B \approx 1.38 \cdot 10^{-23}$ J/K. Therefore, the Johnson noise of the feed-back resistor with $R_f = 1\,M\Omega$ at room temperature, is $\widetilde{I}_J(R_f) \approx 0.13\,pA/\sqrt{Hz}$.

The LISO simulation result regarding ICN for the OPA AD820, from Analog Devices, is shown in Fig. 6.4. A feed-back capacitance of $C_f = 4\,pF$ was calculated with Eq. (6.8). According to the simulation, the ICN at frequencies below about 10 kHz corresponds well to the Johnson noise of the feed-back resistor of $\widetilde{I}_J(R_f) \approx 0.13\,pA/\sqrt{Hz}$. For higher frequencies, the voltage noise of the OPA dominates the total noise. As the noise introduced by the AD820 does not dominate the ICN in the low kHz range and as it also fulfills the bandwidth criterion, it was used henceforth as OPA for the TIAs.

In summary, the optimization of the TIA regarding a high gain, sufficient bandwidth and a low ICN yielded the following parameters:

$$R_f = 1\,M\Omega \tag{6.10}$$

$$C_f = 4\,pF \tag{6.11}$$

$$OP_{TIA} = AD820. \tag{6.12}$$

Using the obtained parameters, the TIA circuit, as drawn in Fig. 6.2, was realized. As was stated above, a bias voltage of $V_{bias} = -5\,V$ was used. Figure 6.5 shows a measurement of the transfer functions of the completed TIAs. As can be obtained from the plots, the 3 dB bandwidth of all four channels was about 30 kHz which matched well with the
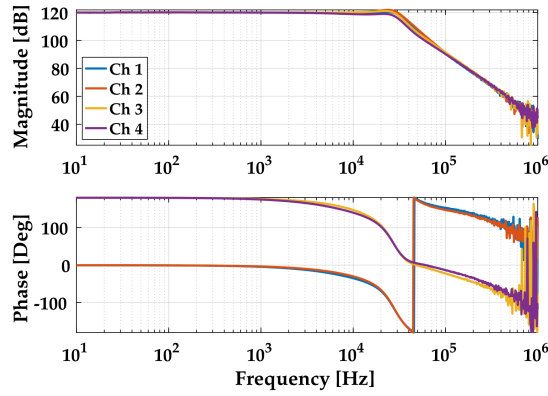
Figure 6.5: Bode plots of the PSPD TIAs transfer functions.
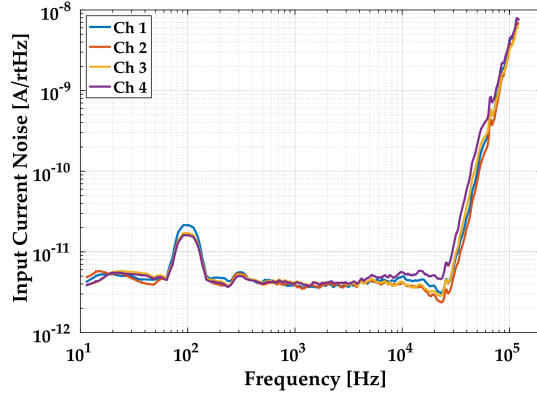
Figure 6.6: Plots of the PSPD TIAs input-referred current noise (ICN).

simulated value. This bandwidth was deemed sufficient, as an amplitude modulation of the laser beam in the low kHz range was foreseen. The phase difference at DC of 180° between channels 1/2 and 3/4 was due to the sign difference of the cathode and anode photocurrents.

In a next step, the achieved ICN was measured and compared to the LISO simulation result. This was done by performing a dark measurement with the TIAs and referring the obtained noise spectral density back to the input of the TIAs by dividing it by the DC gain of $R_f = 1\,\text{M}\Omega$ and the normalized transfer function. The result of this is displayed in Fig. 6.6. A noise floor of $\widetilde{I}_{\text{ICN}} \approx 4\,\text{pA}/\sqrt{\text{Hz}}$ could be measured for frequencies below 10 kHz. The excess noise at 100 Hz is not attributed to the TIAs, but is expected to be due to residual background illumination during the dark measurements. The noise floor of the used data acquisition system (National Instruments PCIe-6351) was measured and found to be well below the noise floor of the dark measurement.

The difference between the LISO simulation and the measurement is attributed to an additional impedance at the input of the TIAs. This is expected to be introduced by the electronic parts that are used for the application of the bias voltage to the PSPD (see red boxes in Fig. 6.2) and a cable of about 1 m length (LEMO 4-pole) which were not part of the simulation. Furthermore, the used bias voltage was only $V_{\text{bias}} = -5\,\text{V}$ instead of $V_{\text{bias}} = -15\,\text{V}$ which was assumed for the simulation. This caused the actual impedance of the PSPD to be higher than the value which was assumed by the simulation. Unfortunately, the bias voltage could not be enhanced in the present design, as the OPAs were supplied with a voltage of only $V_{\pm} = \pm 5\,\text{V}$.

6.3.1.2   Design of bandpass filters

Bandpass filters (BPFs) were used to remove DC offsets from the TIA outputs and to suppress noise at frequencies above the optical amplitude modulation frequency. As the TIAs provide a bandwidth of about 30 kHz, a modulation frequency below this values
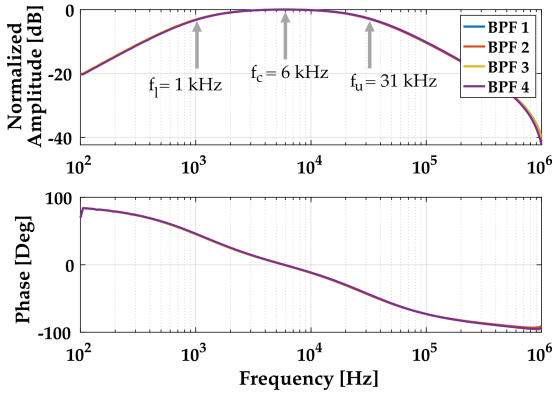
Figure 6.7: Bode plots of the transfer functions of the bandpass filters. Arrows indicate the cutoff and center frequencies.
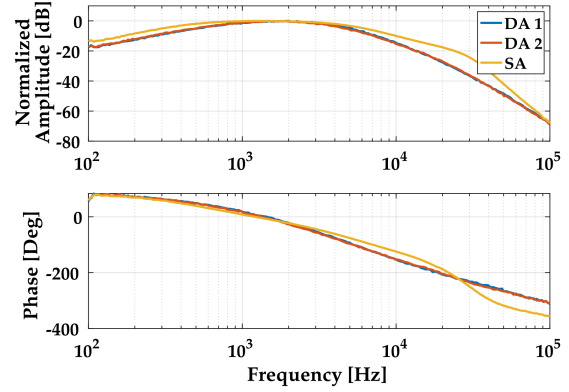
Figure 6.8: Bode plots of the transfer functions of the complete PSPD setup: PSD-TIA-BPF-DA/SA.

was desired. A combination of a coil, a capacitor and a resistor was used as BPF (see the turquoise boxes in Fig. 6.2). The output of the BPF was connected to an active buffer to isolate the inputs of the subsequent difference and sum amplifiers from the output impedance of the BPF. The center frequency of such a filter is defined by [116]:

$$f_c = \frac{1}{2\pi\sqrt{L_b C_b}}. \tag{6.13}$$

The lower and upper frequencies, at which the amplitude of the output of the filter has dropped by $3\,\mathrm{dB}$, are described by [116]:

$$f_l = -\frac{R_b}{4\pi L_b} + \sqrt{\left(\frac{R_b}{2L_b}\right)^2 + \frac{1}{L_b C_b}} \tag{6.14}$$

$$f_u = +\frac{R_b}{4\pi L_b} + \sqrt{\left(\frac{R_b}{2L_b}\right)^2 + \frac{1}{L_b C_b}}. \tag{6.15}$$

With $R_b = 619\,\Omega$, $C_b = 220\,\mathrm{nF}$ and $L_b = 3.3\,\mathrm{mH}$ the following frequencies were obtained:

$$f_c = 6\,\mathrm{kHz} \tag{6.16}$$

$$f_l = 1.1\,\mathrm{kHz} \tag{6.17}$$

$$f_u = 31\,\mathrm{kHz}. \tag{6.18}$$

Figure 6.7 shows the measured transfer functions of the four implemented BPFs. As can be seen in the plots, the calculated frequencies are matched well by the measurements. According to this design, the optical signal should be modulated with a frequency of $6\,\mathrm{kHz}$. The buffer uses an OP27 from Analog Devices as OPA and is operated at unity gain. According to the data sheet, this requires a feed-back resistor of $R_{fb} \approx 500\,\Omega$ [117].

6.3.1.3 Design of sum and difference amplifiers

For the calculation of the position of an impinging laser beam on the PSPD, the difference and sum of the photocurrents produced by the cathodes and the anodes are required. As the sum of the cathode photocurrents equals the sum of the anode photocurrents, $|I_a + I_b| = |I_c + I_d|$, only one sum amplifier is built to keep the electronic design as simple as possible. For a schematic drawing of the sum amplifier see the green box in Fig. 6.2. Again the AD820 OPA was used. Its low voltage noise makes it an appropriate solution for this amplifier stage. The sum amplifier gain is defined by

$$G_{SA} = -R_{fs}/R_2. \tag{6.19}$$

See Fig. 6.2 for the corresponding notation. A gain of $G_{SA} \approx 511$ was achieved by using $R_{fs} = 511\,k\Omega$ and $R_2 = 1\,k\Omega$.

The AD820 was also used for the difference amplifiers (see purple boxes in Fig. 6.2). The gain of a difference amplifier is defined by:

$$G_{DA} = R_{fd}/R_2. \tag{6.20}$$

By choosing $R_{fd} = 511\,k\Omega$ and $R_2 = 1\,k\Omega$, also here a gain of $G_{DA} \approx 511$ was achieved. These gains seemed to be the maximum without introducing distortions of the OPA output signal.

Figure 6.8 shows measurements of the transfer functions of the conjunction of TIAs, BPFs and the difference and sum amplifiers. The obtained frequency response had its maximum at ~2 kHz. This value slightly deviates from the expected maximum at 6 kHz which was visible in the transfer functions of the BPFs (cf. Fig. 6.7). However, the transfer functions of the BPFs were measured independently. It is expected that the deviation of the maximum frequency that is observed here, is due to an impedance mismatch of the TIAs, the BPFs and the difference and sum amplifiers. Consequently, the optical signal should be modulated with a frequency of 2 kHz.

6.3.2 Spatial calibration of the PSPD

The manufacturer's claim of a linear relationship between laser beam position on the PSPD and the sensor signals, described by Eqs. (6.1) and (6.2), was tested. To do so, a laser beam with an optical power in the nW range and a Gaussian diameter of 490 µm ±40 µm in the plane of the PSPD sensor was generated. The beam's intensity was modulated with the help of an elecotro-optical amplitude modulator (EOAM) with a modulation frequency of 2 kHz (see Fig. 6.9). The PSPD was mounted on a 2D translation stage and was roughly centered with respect to the laser beam by minimizing the difference amplifier signals. It was then moved with the linear stages along a 2D grid that spanned from -5.25 mm to +5.25 mm in the horizontal and vertical axis. The scan range was chosen to cover the
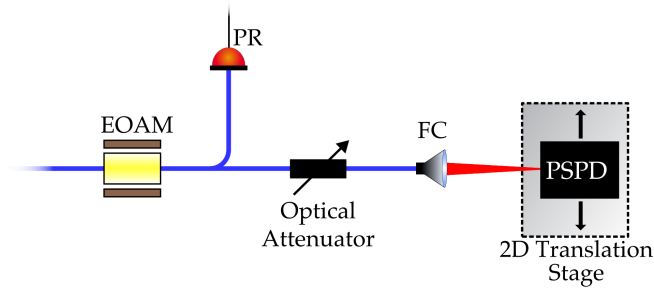
Figure 6.9: Schematic drawing of the experimental setup that was used for the spatial calibration of the PSPD readout. The 2D translation stage can move the PSPD along two axes orthogonal to the optical axis (only one axis is shown). EOAM: Electro-optical amplitude modulator, PR: Photoreceiver, FC: Fiber collimator, PSPD: Position Sensitive Photodetector

complete sensor area plus a little margin. A scan step size of 0.25 mm was chosen for the area outside of the inner ±4 mm of the sensor. Within this region, the step size was relaxed to 2 mm to reduce the scanning time. The denser grid towards the edges of the sensor was chosen, to properly map the nonlinear response expected in this area.

The difference and sum amplifier output signals were recorded and divided in post processing. The PSPD signal for the horizontal axis is defined by $\delta_h = V_{DA-1}/V_{SA}$, with V_{DA-1} the amplitude of the voltage that is produced by one of the difference amplifiers and V_{SA} the amplitude of the sum amplifier signal. For the vertical axis the signal follows analogously: $\delta_v = V_{DA-2}/V_{SA}$. The corresponding values are plotted in the top panels of Fig. 6.10.

As can be seen in the plots, δ_h and δ_v seem to be well described by 2D first order polynomials for beam positions within about ±4 mm around the PSPD center. Therefore, the data from this are was fitted by such polynomials. The resulting fit residuals are illustrated in the bottom plots of Fig. 6.10. The polynomial and the obtained fit parameters for the horizontal axis are defined by:

$$\delta_{h,fit} = p_{0h} + p_{10h}x + p_{01h}y \tag{6.21}$$

$$p_{0h} = 0.004317 \tag{6.22}$$

$$p_{10h} = 0.2512 \tag{6.23}$$

$$p_{01h} = -0.004489 \tag{6.24}$$

with the horizontal beam position x and the vertical position y. For the vertical axis the obtained fit parameters are:

$$\delta_{v,fit} = p_{0v} + p_{10v}x + p_{01v}y \tag{6.25}$$

$$p_{0v} = -0.0009276 \tag{6.26}$$

$$p_{10v} = 0.003463 \tag{6.27}$$

$$p_{01v} = 0.2529. \tag{6.28}$$
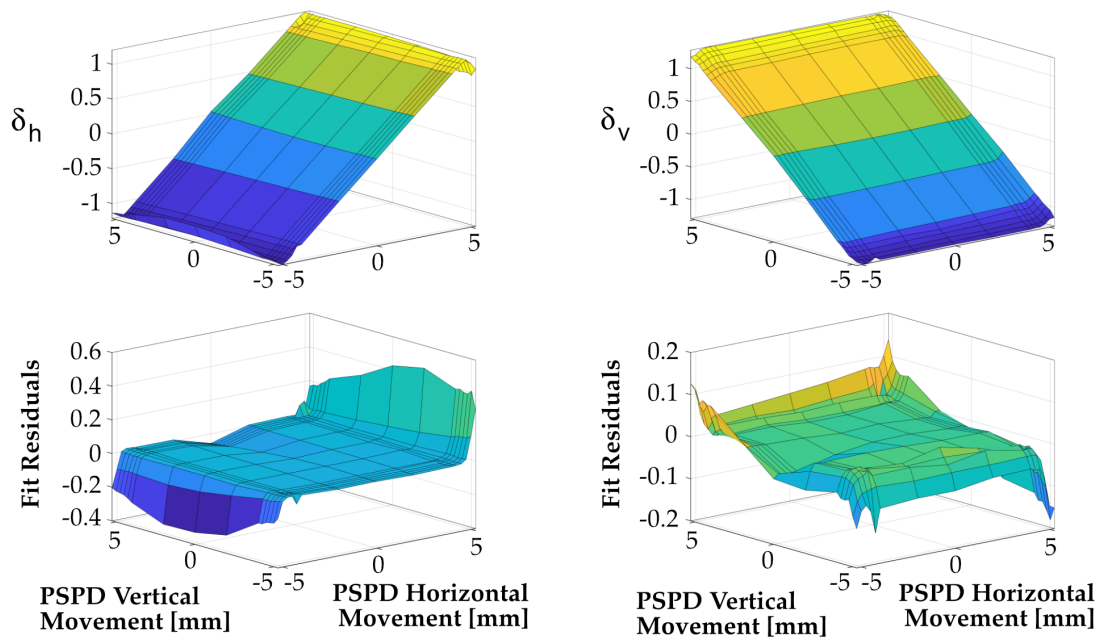
Figure 6.10: Top panels: horizontal (left) and vertical (right) signal of the PSPD, defined by $\delta_h = V_{DA-1}/V_{SA}$ and $\delta_v = V_{DA-2}/V_{SA}$. Bottom panels: fit residuals to first order 2D polynomials. The fits were only applied to the sensor data from the inner $\pm 4\,mm$ region.

As can be seen in the bottom plots in Fig. 6.10, the fit residuals within the $\pm 4\,mm$ area around the PSPD center are small. Within this area the rms residuals are only $\sim 1\,\%$. If also the data from outside of the $\pm 4\,mm$ area around the center is taken into account, the rms fit residuals increase to about $10\,\%$. This was expected and matches the manufacturer's claim of linear operation within $80\,\%$ of the sensor length ($=\pm 4\,mm$) [103].

If the complete sensor area should be used, higher order fits must be applied to the data that properly map the complete sensor. However, for the analysis that is presented here, the laser beam position was instead constrained to the inner $\pm 4\,mm$ part of the PSPD and the obtained linear fits were used. If measurements of δ_h and δ_v are made, the desired beam positions along the horizontal and vertical axes, x and y, are obtained by numerically solving Eqs. (6.21) and (6.25) for x and y.

Verification of the PSPD calibration
The spatial error of the PSPD readout, using the calibration from Eqs. (6.21) and (6.25), while searching the position of an impinging beam is of highest interest. To investigate this error, the PSPD was illuminated with the same amplitude modulated laser beam, as was already used for the calibration. The power of the laser beam was then reduced until the PSPD output voltages were barely visible above the noise. This occurred at power levels of about $10\,nW$. The PSPD was then moved orthogonally to the impinging laser beam, with the help of a translation stage, as illustrated in Fig. 6.9. A stepper motor was

used to actuate the translation stage with a constant step size. By doing so, it could be assumed that the laser beam moved over the PSPD along a straight line. The position of the impinging laser beam was then obtained for each scan step by numerically solving Eqs. (6.21) and (6.25) for x and y while using the measured signals δ_h and δ_v as inputs. The residuals of a linear fit to these obtained positions then served as indicator for the error of the PSPD readout. Three linear scans with a total number of $\sim$40 measurements were carried out.

For each of the linear scans, rms fit residuals of 8 µm, 10 µm and 20 µm were obtained. A combined rms value is not calculated due to the low number of scans and scan points. Instead, the worst value of 20 µm will be used henceforth to describe the achieved resolution of the PSPD.

6.3.3   Discussion

In this section, results of a study of a PSPD as possible CAS for LISA were presented. The obtained results should be considered preliminary and with potential for improvement. This assumption bases on the discrepancy between the measured noise floor of the TIAs of about $4\,\mathrm{pA}/\sqrt{\mathrm{Hz}}$ and the obtained minimum power that the conjunction of TIAs, BPFs, difference and sum amplifiers could process. The latter turned out to be about 10 nW. The cause for the enhanced noise floor is currently not understood. If the idea of using a PSPD as a CAS for an intersatellite laser interferometer is further pursued, it is strongly suggested to perform a thorough analysis of the noise performance of all the amplifier stages. However, at this point it remains uncertain, if the required minimum power level can be reduced far below the nW range.

For the current implementation of the PSPD-based CAS system, the laser beam was amplitude modulated in the low kHz range to suppress the coupling of background or stray light into the position determination procedure. If a CAS system with a PSPD is further studied, the effect of stray light on the achievable resolution should be thoroughly examined.

It could be shown that the achieved rms residuals of the determination of the impinging laser beam's position was $\leq$20 µm. The ratio of these residuals to the sensor edge length is $\Gamma_{\mathrm{PSPD}} = \frac{20 \cdot 10^{-6}\,\mathrm{m}}{10 \cdot 10^{-3}\,\mathrm{m}} = 2 \cdot 10^{-3}$. Equivalently, it could be expressed as 0.2 % of the sensor size. If it is assumed that optics in front of the sensor would image the FoV that is required by a CAS onto the complete sensor area, this number can be compared to the ratio of the required angular resolution to the FoV, which was presented in Sec. 6.2. The corresponding numbers are $\Gamma_{\mathrm{LISA}} \leq$0.15 % for LISA and $\Gamma_{\mathrm{NGGM}} \leq$0.5 % for NGGM. Thus, the realized system met the requirements for NGGM while the achieved ratio falls just short of the LISA requirement. Furthermore, the PSPD system provides a signal in the kHz range. Thus, the LISA frame rate requirement of 10 Hz could be met. All measurements were carried out at a room temperature of about 20 °C. However, an analysis of the achieved

SNR of the laser beam position readout has not been conducted. This should be done, if a PSPD is further studied.

However, the realized PSPD system is designed to work with AC signals. The star tracker mode, that is required by the LISA mission, can not be implemented by such a system. Even if the PSPD system were capable of detecting DC signals, it could only properly detect the position of one such signal. This imposes various challenges on a star tracker mode with a PSPD. If light from more than one star is incident on the sensor, the position readout is biased. Hence, it would have to be ensured that only one star at a time is visible in the FoV of the PSPD. This does not seem feasible. Therefore, a PSPD is no suitable option for a CAS for LISA.

It was shown that the error of the position determination is compatible with the requirements for NGGM. While the achieved minimum power level of 10 nW is still too high for an application of the PSPD as CAS for NGGM, it does not exceed the expected levels by orders of magnitude. Hence, depending on the exact implementation of a laser ranging instrument for NGGM, a PSPD might be an option for a CAS for this type of mission.

6.4 Study of an InGaAs camera as CAS

An indium gallium arsenide (InGaAs) FPA sensor was investigated as possible CAS for LISA and NGGM. The model *OWL SW1.7 CL-320* from Raptor Photonics was used (see photograph in Fig. 6.11). This sensor provides an array of 256×320 InGaAs pixels, of 30 μm×30 μm size [118]. The active sensor area is thus 7.68 mm×9.6 mm. InGaAs was chosen in favor of silicon due to its higher QE at $\lambda = 1064$ nm [119]. At this wavelength, the used sensor provides a QE of about 0.65 electrons/photon [118]. The sensor features a
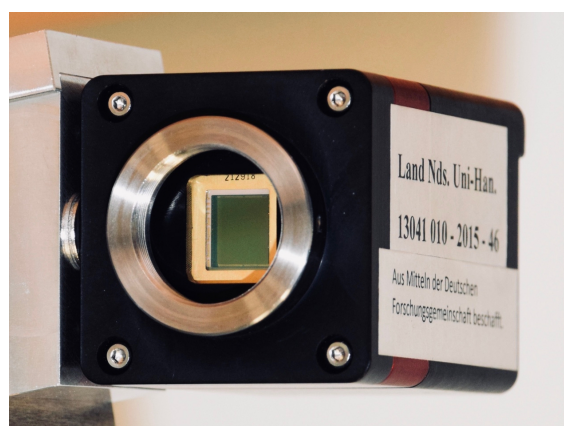
Figure 6.11: Photograph of the *OWL SW1.7 CL-320* InGaAs FPA from Raptor Photonics. The dark area inside the golden square is the InGaAs chip.

CMOS-based readout integrated circuit (ROIC) to read out the pixels. In such a scheme, each individual pixel is directly connected to its own pre-amplifier. Effects like *streaking*, which classical CCD sensors can suffer from if single pixels start to saturate [120], do not

occur. However, the pixels' pre-amplifiers in a CMOS-based ROICs, as well as individual column amplifiers cause a non-uniform response of the sensor that is visible in every recorded image. This is referred to as fixed pattern noise (FPN) [121]. Before an image can be processed, the FPN must be corrected for. A procedure that is often referred to as non-uniformity correction (NUC) is applied for this purpose. It includes the correction of each pixel gain in reference to the mean gain, a subtraction of each pixel's offset and the application of a bad pixel map (BPM) to the complete sensor data. The BPM accounts for pixels that are *cold*, such pixels show no response to incident radiation, *hot*, these are always saturated independent of the incident light level and pixels that show an otherwise abnormal behavior, e.g. a relative gain which is far above or below the mean value.

The sensor is equipped with a dedicated FPGA which is used for the pre-processing of the raw image data. The FPGA offers the option of actively controlling the temperature of the ROIC with the help of a thermoelectric cooler. Another provided function is the automatic gain control (AGC) mode. In this mode, the FPGA continuously optimizes the exposure time and the camera's digital gain to make optimal use of the dynamic range. Furthermore, a pre-calibrated NUC function is implemented within the FPGA. The corresponding correction matrices, that are provided by the manufacturer, were determined at a sensor temperature of 15 °C. However, a CAS on LISA or NGGM should be operated at ∼20 °C (see Tab. 6.1). Especially the pixel offset partly depends on the temperature-dependent dark current. Hence, the built-in NUC does not provide the necessary correction matrices to fully compensate effects like the dark current offset. Therefore, the built-in NUC functionality is not used. The same is true for the AGC. Instead, the NUC is applied manually in post-processing of the data. This way, more control over the applied correction factors is preserved.

The sensor uses the Base Camera Link interface to exchange data with a frame grabber (FG) [122]. The *ADM-XRC-7Z1* FG-board from Alpha Data is used for communication with the sensor [123]. It is connected to a breakout board, *ADC-XMC-Breakout*, also from Alpha Data, to provide an interface for a standard ATX 24-pin power supply and sufficient interfaces for the exchange of data, e.g. USB and ethernet sockets [124]. The decision for such a stand-alone system, in contrast to a FG which is connected to a host PC via PCIe, was made to enable more realistic testing of the whole CAS system at later stages. For example, such an independent system could eventually be directly connected to a phasemeter for advanced system testing of the link acquisition mode without the need for a computer in the loop.

The FG board is constituted by a system on chip (SoC) which consists of an FPGA that handles the transfer of data to and from the camera and a microcontroller (μC). On the μC runs an embedded Linux. A C++ program was developed, which is based on an application programming interface (API) provided by Alpha Data, that runs on the FG's Linux system. It is used to receive data from the camera or to send commands to it, e.g. to set parameters like the exposure time. For all the experiments that are explained in this thesis, a computer is used to connect to the μC via the RS232 serial interface. The C++
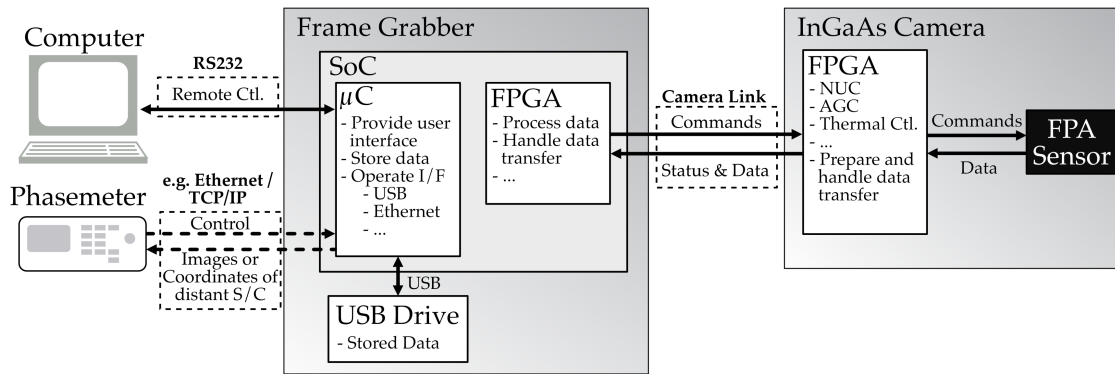
Figure 6.12: The figure shows an overview of the complete InGaAs camera system including the frame grabber and remote computer. Additionally, the flow of data and the respective protocols are shown. For advanced tests of a CAS system, the FG could directly be connected to a phasemeter. This possible connection is indicated by dashed arrows. SoC: System on chip, µC: Microcontroller, FPGA: Field-Programmable Gate Array, NUC: Non-uniformity correction, AGC: Automatic gain control, FPA: Focal plane array.

program is then remotely controlled by this computer. Figure 6.12 shows an overview of the complete system.

Parts of the C++ program were developed by an intern student, Ekin Celikkan, who was supervised by the author of this thesis. The FG and the InGaAs sensor were commissioned together with a Bachelor student, Christoph Gentemann, also under supervision of the author. Early experiments with the setup were published in his Bachelor thesis [125]. Parts of the work that is described in this chapter were already made publicly available to the LISA consortium in a technical note [126].

In the next section, the calibration measurements that were needed for a proper NUC, are explained. This is followed by an analysis of the dominating sensor noise sources of the InGaAs camera. A template-based readout procedure of the sensor data is presented in the subsequent section together with a detailed simulation of the procedure that takes into account the measured camera noise. In the last part of this section, an experimental investigation of the achievable resolution of the template-readout scheme is presented.

6.4.1 Calibration of the InGaAs camera

Figures 6.13 and 6.14 show an uncorrected dark image that was taken with the InGaAs camera at an exposure time of $t_e = 1\,\text{ms}$. The ROIC temperature was actively stabilized at $20\,°\text{C}$. The camera's internal NUC, as well as the AGC mode, were disabled for this image. Various features are visible in the image that must be corrected for: hot and cold pixels as well as a rather large offset of approximately $4000\,\text{cts}$. A feature that is not visible to the naked eye, are the different gains of the pre-amplifiers of the individual pixels. These cause a slight variation in the response of each pixel to a uniform illumination of the sensor. What can be seen in the images is a striped structure that is caused by the
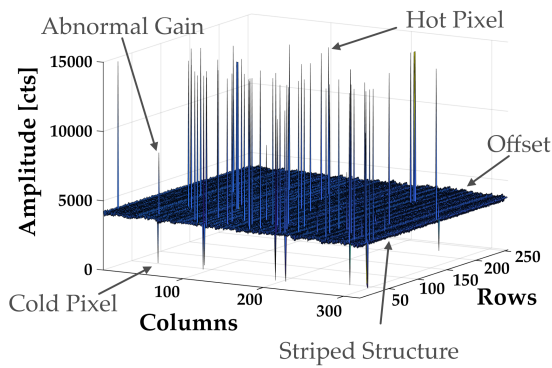
Figure 6.13: The figure shows a plot of an uncorrected dark image that was taken with the InGaAs camera at an exposure time of 1 ms at a temperature of 20 °C.
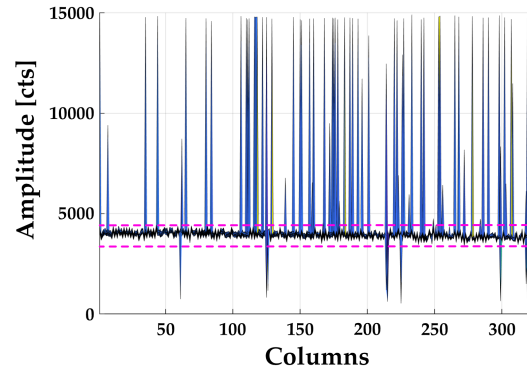
Figure 6.14: The figure shows a side view of Fig. 6.13. The pink dashed lines indicate the thresholds that were used for the definition of a bad pixel map (BPM).

different gains of the column amplifiers. Within this section, two calibrations of the sensor are presented: the derivation of a BPM and the calibration of the relative gains by means of a flat field correction.

Bad pixel correction

The hot and cold pixels that are visible in the uncorrected dark image shown in Figs. 6.13 and 6.14 must be excluded from any image before it can be further processed. This is realized by the introduction of a bad pixel map (BPM). A straight forward approach was used to define a BPM B_{ij}:

$$B_{ij} = \begin{cases} 1 & T_l < \mathcal{A}_{ij} < T_u \\ 0 & \text{otherwise} \end{cases} \qquad (6.29)$$

Here, $\mathcal{A}_{ij}$ is the amplitude of pixel (i, j) in units of digital counts. The lower and upper thresholds, T_l and T_u, indicated in Fig. 6.14 by the pink, dashed lines, were defined as $T_l = 3000$ cts and $T_u = 4400$ cts.

The shown data was obtained at an exposure time of $t_e = 1$ ms. However, nonlinear relative gains of the individual pixels can lead to a pixel being defined as a bad pixel only for higher exposure times. That is why the BPM should be compared with an uncorrected dark image for each exposure time and should be adapted, if necessary. It could be pondered, if using a single BPM derived at a very long exposure time to identify all bad pixels also for lower exposures is favorable. However, pixels that are still operational at these low exposure times would be excluded a priori, which seems unnecessary. Therefore, an individual BPM was derived for each set of measurements by recording a dark image at the same exposure time and defining proper thresholds T_l and T_u. By using this approach, it was accounted for the fact that inoperative pixels could come back to nominal functionality and vice versa. The camera's manufacturer claims a pixel functionality of $> 99\,\%$ [118]. Measurements with an exposure time of 1 ms yielded a functionality of ~98.5 %. With an exposure time of $t_e = 200$ ms, which was the maximum value used
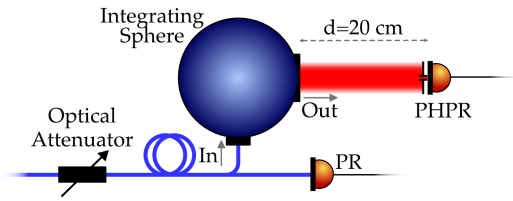
Figure 6.15: Schematic drawing of the experimental setup that was used for the evaluation of the intensity distribution of the light emitted by the integrating sphere. For the flat-field correction, the PHPR was replaced by the InGaAs sensor.
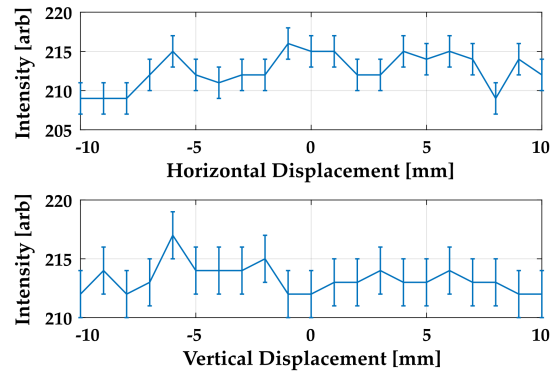
Figure 6.16: Obtained intensity profile along two orthogonal axes that was used for the flat field correction of the InGaAs sensor. The plots also show the error bars of the intensity measurement.

throughout all experiments, a pixel functionality of $> 95\%$ was found. The BPMs, that were defined with the scheme explained above, thus, excluded slightly more pixels than were expected. However, as the obtained numbers were still comparable to the provided value, this was not deemed as troubling.

Flat field correction

As each pixel is read out by an individual pre-amplifier, every pixel shows a unique response to incident radiation. The same is true for each column of pixels. This leads to a non-uniform response of the sensor to a homogeneous illumination of the complete chip. This behavior must be corrected for. A technique called *flat field correction* was applied to correct for these pixel-to-pixel sensitivity variations by identifying the relative gains of the pixels to a homogeneous illumination.

An integrating sphere (*819D-SL-3.3* from Newport / Labsphere) was used to create a light beam with a homogeneous intensity distribution over an area that was large enough to illuminate the complete InGaAs sensor. This distribution was realized by diffuse scattering of an input beam on the sphere's inner surface. To realize a high number of scattering processes, and, therefore, improve the quality of the output beam, the sphere's inside is coated with a highly reflective, diffusive coating for $\lambda = 1064\,\text{nm}$ (R $\approx 99\%$ [127]). As is indicated in Fig. 6.15, a bare fiber end is connected to the sphere's input port. A lens was omitted here on purpose, to further improve the homogeneity of the output beam. It was found that an optimal trade-off between a flat intensity distribution and a sufficiently high output power level was achieved at a distance of 20 cm from the output port of the integrating sphere.

Before this output beam could be used to calibrate the InGaAs pixel's response, its intensity distribution had to be characterized. Due to limitations of the laser setup, the achieved

Figure 6.17: The figure shows a histogram of all relative pixel gains G_{ij}. The corresponding standard deviation was found to be about 10 %.
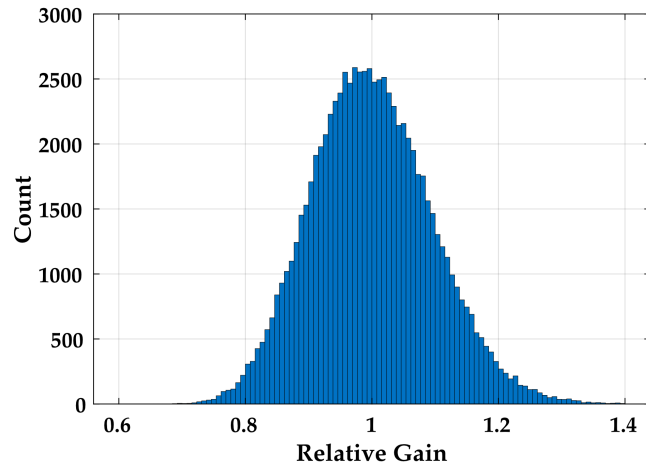
power level of the output beam was comparably low. Unfortunately, no 2D sensor, as e.g. a calibrated CCD camera, was available that had a high enough optical gain to perform the calibration measurements. Instead, the intensity distribution was characterized with the help of a high gain PHPR. The pinhole had a diameter of 1 mm. It was ensured that the PHPR was properly shielded from any background illumination. By moving the PHPR through the light field and taking measurements at various positions, the intensity along two axes, orthogonal to the optical axis, was measured (see Fig. 6.16). Under the assumption that the light field, emitted by the integrating sphere, is rotationally symmetric around the optical axis, the obtained intensity distribution was considered sufficiently homogeneous to perform the flat field correction of the InGaAs camera.

Once the intensity profile's homogeneity was verified, the PHPR was replaced by the InGaAs sensor. The response of the pixels to different optical power levels could then be evaluated. An optical attenuator, shown in Fig. 6.15, was used to change the power of the laser beam. The relative power changes were recorded with the help of an auxiliary PR. As the absolute gains of the pixels were not of interest for this calibration, also the absolute relationship between the power seen by the PR and the power on the InGaAs sensor was not important. Under the assumption that the power on the PR was proportional to the power level on the InGaAs sensor, the gain of each pixel could be assessed. Each pixel's amplitude, $\mathcal{A}_{ij}$, was fitted by a first order polynomial as a function of the relative incident power P that was assumed constant for all pixels:

$$\mathcal{A}_{ij} = G_{ij} \cdot P + O_{ij}. \tag{6.30}$$

G_{ij} is the gain of pixel (i, j). The *relative* gains were then obtained by dividing G_{ij} by the mean gain of all pixels, $\overline{G}$. Here it had to be ensured that the bad pixels did not affect the calculation of the mean value. Thus, the relative gain of pixel (i, j) is described by:

$$G_{ij}^{\mathrm{r}} = G_{ij}/\overline{G}. \tag{6.31}$$

Even though the relative gains G_{ij} were derived with data that was taken with an exposure
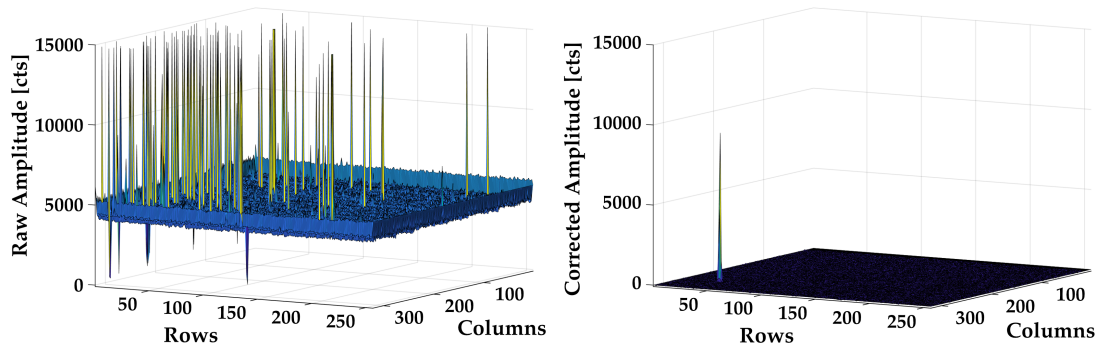
Figure 6.18: In the left plot, a raw image taken with the InGaAs camera at an exposure time of $t_\mathrm{e} = 50\,\mathrm{ms}$ is shown. The right plot shows the same data after application of the correction procedure. A clear signal peak has become visible in the data that was dominated by sensor noise and bad pixels prior to the correction.

time of 1 ms, they remain valid for all other integration times because they were normalized by the mean value. However, this is not the case for the fit offsets O_{ij}. These values vary, depending on the integration time. Hence, they are discarded and not used for the correction of the pixel offset in raw images. Instead, each image is additionally corrected by a dark measurement which was recorded at the same exposure time. This provides the added benefit that residual stray light due to background illumination is also subtracted from the image. Figure 6.17 shows a histogram of the obtained relative gains G_{ij}^r. The standard deviation of the relative gains is $\sim 10\,\%$.

Correction of raw images

Any raw image was corrected, using the correction factors that were derived above. A pixel's corrected amplitude, $\mathcal{A}_{ij}^c$, is obtained by applying the following procedure:

$$\mathcal{A}_{ij}^c = \frac{\mathcal{A}_{ij} - \mathcal{A}_{ij}^\mathrm{D}}{G_{ij}^\mathrm{r}} \cdot B_{ij} \tag{6.32}$$

Thereby, A_{ij}^D is the amplitude of pixel (i, j) that was obtained by taking a dark image. The correction defined by Eq. (6.32) was applied to all the data that was taken with the InGaAs sensor that is shown throughout this thesis.

In the left part of Fig. 6.18 a raw image is shown that was recorded with an exposure time of $t_\mathrm{e} = 50\,\mathrm{ms}$. All the artifacts that were discussed above, are visible. Additionally, the four outermost pixel columns and rows show visibly enhanced offsets. While the origin of this offset is currently not understood, its visibility in this image is due to the 50 times higher exposure time, compared to the raw image shown in Fig. 6.13. This is a prominent example, why the BPM should be adapted to the exposure time. After applying the correction procedure, described by Eq. (6.32), the data shown in the right part of Fig. 6.18 is obtained. A clear signal peak is now visible that was previously buried in the sensor artifacts.

6.4.2   InGaAs camera noise investigation

The intrinsic noise of the InGaAs sensor defines the minimum optical power level that it can measure. As low power functionality is required, if the sensor is used as CAS for LISA or NGGM, the noise of the sensor is of highest interest. The intrinsic noise as well as the achievable SNRs were investigated experimentally and are discussed in this section.

300 dark images were recorded at each integration time between $1\,\mu s$ and $100\,ms$. This was done for ROIC temperatures of $0°C$ and $20°C$. In total, more than 5000 dark images were recorded and analyzed.

As was already mentioned, read noise, caused by the pixel pre-amplifiers, and shot noise due to dark current are expected to be the dominating contributions to the total noise [121]. As these terms are uncorrelated, they are summed in quadrature to yield the total noise [121]:

$$n_{\text{total}} = \sqrt{n_{\text{read}}^2 + n_{\text{shot}}^2(t_e)}. \tag{6.33}$$

The read noise, n_{read}, is independent of the exposure time t_e. In order to describe all noise sources in a common unit, it is usually expressed in rms electrons. The shot noise is defined by:

$$n_{\text{shot}}(t_e) = \sqrt{\Phi \cdot t_e} \tag{6.34}$$

with Φ the flux of electrons. For the analysis of the dark noise of the camera, Φ describes the flux of dark electrons: $\Phi = \Phi_{\text{dark}}$. The shot noise follows a Poisson distribution [128], which means that its variance equals the expected value. In this case, this can be replaced by the arithmetic mean, such that:

$$\text{Var}(n_{\text{shot}}) = \overline{n_{\text{shot}}}. \tag{6.35}$$

A model, according to Eq. (6.33) was fitted to the dark measurements. Therefore, for each exposure time, the mean of each pixel from 299 images was calculated. One image per exposure time served as dark image for the correction of the data, according to Eq. (6.32). The effect of the averaging and of the subtraction of a dark image on the noise statistics was properly accounted for. The derivation of the corresponding scaling factor is shown in Appendix A.

In a next step, the recorded pixel amplitudes were converted from units of digital counts to electrons. The corresponding conversion factor is defined by the ratio of the well capacity of the pixels, N_{well} to the corresponding range in digital counts. N_{well} describes the maximum number of electrons that one pixel can contain before overflow into adjacent pixels occur. N_{well} was taken from the sensor's data sheet [118].

For both analyzed temperatures of the ROIC, $T = 20°C$ and $T = 0°C$, the total noise as a function of the exposure time is shown in Fig. 6.19. The figure shows the measured noise as well as models according to Eq. (6.33) that were fitted to the data. The parameters of
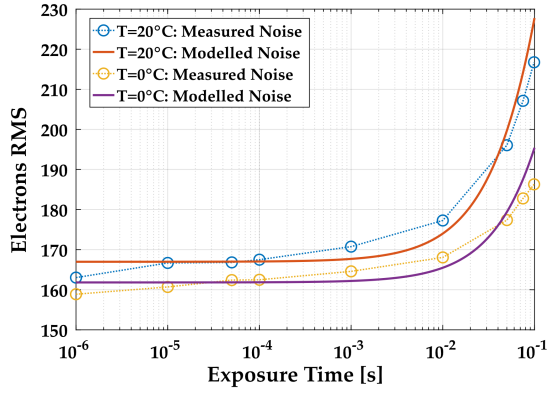
Figure 6.19: The figure shows the measured noise of the InGaAs sensor in units of electrons rms for T = 20°C and 0°C. A noise model according to Eq. (6.33) is also plotted.
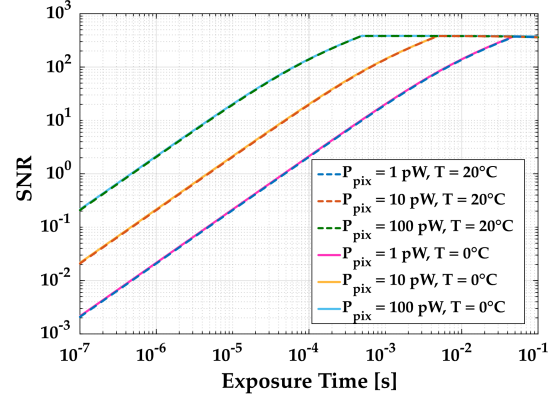
Figure 6.20: Plots of the achievable SNR for power levels of 1 pW, 10 pW and 100 pW impinging on a *single pixel*.

the noise models obtained at both temperatures are:

$$T = 0°C: \quad n_{\text{read}} = 161 \, e^- \tag{6.36}$$

$$\Phi_{\text{dark}} = 120.000 \, e^-/s \tag{6.37}$$

$$T = 20°C: \quad n_{\text{read}} = 167 \, e^- \tag{6.38}$$

$$\Phi_{\text{dark}} = 240.000 \, e^-/s. \tag{6.39}$$

As can be obtained from Fig. 6.19, the shot noise due to dark current dominates the total sensor noise for exposure times above ~10 ms. Cooling the camera to 0°C only has a marginal effect on the read noise. However, the dark current is severely reduced.

As the sensor should be used with signals of very low optical power, the SNR that follows from the determined sensor noise was calculated. This was done for three different power levels: P = 1 pW, P = 10 pW and P = 100 pW. Thereby, it was assumed that the optical power was incident on a single pixel. Before the signal power and the noise can be compared, the optical power, so far expressed in units of W, was converted to the corresponding number of electrons that are deposited in a single pixel:

$$N_{e^-} = \frac{\rho \cdot t_e}{q_e} \cdot P_W \tag{6.40}$$

with the elementary charge $q_e = 1.602 \cdot 10^{-19}$ C, the exposure time t_e and the optical power in units of W, P_W. The pixel responsivity ρ, expressed in units of A/W, can be derived from the QE by the following equation [129]:

$$\rho = \frac{QE \, \lambda \, q_e}{h \, c} \tag{6.41}$$

with $\lambda = 1064$ nm, $h \approx 6.626 \cdot 10^{-34}$ Js the Planck constant and c the speed of light. According to the datasheet, the quantum efficiency of the used InGaAs camera is QE = 0.65 [118]. Using Eq. (6.41), it follows $\rho \approx 0.56$ A/W. The noise must now also

include shot noise due to the flux of signal electrons, Φ_{sig}:

$$n_{\text{total}} = \sqrt{n_{\text{read}}^2 + n_{\text{shot}}^2(t_{\text{e}})} \tag{6.42}$$

$$= \sqrt{n_{\text{read}}^2 + (\Phi_{\text{dark}} + \Phi_{\text{sig}}) \cdot t_{\text{e}}}. \tag{6.43}$$

The obtained SNRs as a function of exposure time for different incident optical power levels per pixel and different temperatures of the ROIC are shown in Fig. 6.20. As can be obtained from the plots, a reduction of the sensor temperature does not have a significant effect on the achievable SNR. This is because the shot noise due to the optical signal dominates the SNR. The maximally achievable SNR is $\sim$400. This is due to the number of signal electrons reaching the well capacity of the pixels. A SNR of one is achieved at $t_{\text{e}} = 50\,\mu\text{s}$, $t_{\text{e}} = 5\,\mu\text{s}$ and $t_{\text{e}} = 0.5\,\mu\text{s}$ for optical power levels of 1 pW, 10 pW and 100 pW.

As a result from this noise analysis, it can be stated that the investigated sensor seems suitable for measurements of optical signals with power levels in the pW range. As the corresponding SNR does not significantly improve, cooling of the sensor below room temperature does not seem necessary. Depending on the incident optical power, the exposure time must be adjusted in the µs to ms range to achieve SNRs of up to 400.

6.4.3 Study of a template-based readout procedure of the InGaAs camera

Depending on the mission scenario, the position of a laser beam must be found with an accuracy of $\Gamma_{\text{LISA}} \approx 0.15\,\%$ or $\Gamma_{\text{NGGM}} \approx 0.5\,\%$ of the sensor size. This assumes that the FoV is imaged onto the complete sensor surface. Hence, to calculate the corresponding required resolution for the InGaAs sensor, the FoV must be imaged onto the shorter edge length of the sensor of $L = 7.68\,\text{mm}$. The required resolution R must then fulfill $\Gamma_{\text{FPA}} = R/L < 0.15\,\%$ for the LISA scenario or $\Gamma_{\text{FPA}} < 0.5\,\%$ for NGGM. It follows that $R \approx 11.5\,\mu\text{m}$ for LISA and $R \approx 38\,\mu\text{m}$ for NGGM. As the sensor's pixel have a length of $30\,\mu\text{m}$, the LISA scenario requires sub-pixel resolution for the centroiding procedure.

A template-based procedure was developed to find the position of a laser beam that is incident on the InGaAs sensor. In the first part of this procedure, the cross-correlation of a pre-computed template that matches the expected intensity distribution of the laser beam on the sensor, and the sensor data is calculated. A subsequent quadratic fit is then applied to a sub-matrix of the sensor data around the obtained maximum of the cross-correlation. Such a scheme offers the benefit of determining the sought for laser beam position even in noisy data. A template of the intensity distribution is readily calculable as the distribution of an RX laser beam within the sensor plane of an acquisition sensor is easily predictable.

Similar procedures have found wide applicability throughout various scientific fields. GW signals are for example searched for by calculating the cross-correlation of the noisy detector data and different templates of GWs [24]. Here, the used templates are defined in the time domain. These are referred to as *matched filters*. However, also matched filtering
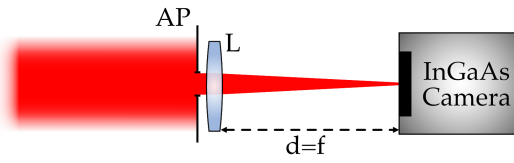
Figure 6.21: Schematic drawing of the simulated experimental setup. The image plane of the InGaAs sensor is placed in the focal plane of the lens. AP: Aperture $r_{\text{ap}} = 4\,\text{mm}$, L: Lens.
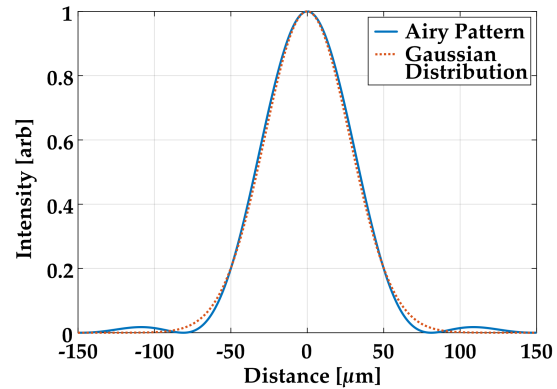
Figure 6.22: The figure shows the intensity distribution of an Airy disk and a Gaussian intensity distribution.

in the spatial domain is widely applied for the detection of patterns in noisy data (see e.g. [130, 131]).

In order to assess the applicability of a template-based search for an impinging laser beam's position on an acquisition sensor, a detailed simulation of such a procedure was carried out. The goal of the simulation was twofold. The first figure of merit was the achievable resolution of the procedure. Within this thesis, this term is described by the spatial error of the determination of the beam position on the sensor from the true position. The second figure of merit is the achievable SNR of the algorithm. This must not be confused with the SNR of a signal with respect to the camera noise, which was illustrated in Fig. 6.20. The SNR that is of interest here, is the ratio of the "amplitude" of a detection to a parameter that is a measure for the detection of noise. A proper description of the SNR will be given later in this chapter, once terms like the "amplitude" of a detection have been introduced. If the resolution and the corresponding SNR of the procedure are deemed sufficient, optimal parameters for a CAS system with the InGaAs sensor are derived. These include optimum beam spot sizes on the sensor and the required exposure times.

The parameters and the determined noise of the InGaAs sensor, that were presented above, served as input to the simulation. The simulated experimental setup is shown in Fig. 6.21. As can be seen in the figure, it is assumed that a single thin lens is used to focus a laser beam that was clipped on a circular aperture on the InGaAs sensor. Hereby, the sensor is placed in the focal plane of the lens. Due to beam clipping on the aperture, this leads to the formation of an Airy disk on the sensor ([132], see Fig. 6.22). The diameter of this intensity distribution, measured as the distance between the first diffraction minima, is defined by:

$$D_{\text{Airy}} = 1.22 \frac{\lambda f}{2\, r_{\text{ap}}} \tag{6.44}$$

for a lens with focal length f, an optical wavelength λ and the radius of the aperture r_{ap}.
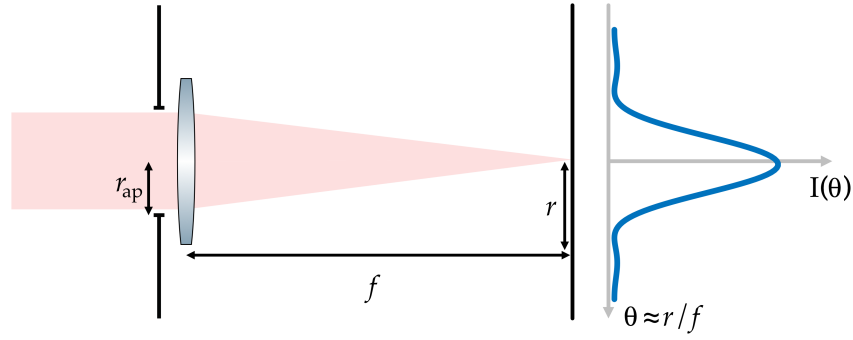
Figure 6.23: Drawing of the formation of an Airy pattern by a laser beam that is clipped by a circular aperture and then focused onto a screen by a lens.

For the simulation a radius of $r_{ap} = 4\,\text{mm}$ was assumed. However, this does not limit the validity of the obtained results for other scenarios in any way.

In laser optics, the Gaussian beam diameter is a commonly used parameter to describe the size of a laser beam spot. For the study that is presented in this section, it was deemed sufficiently accurate to describe the diameter of the Airy pattern by the diameter of a matched Gaussian intensity distribution. To illustrate their similarity, both distributions are shown in Fig. 6.22. A normalized Gaussian intensity distribution according to the following equation is shown in the figure:

$$I_{\text{Gauss}}(r) = \exp\left(\frac{-2\,r^2}{w_0^2}\right) \tag{6.45}$$

with r the radial distance from the center of the distribution and w_0 the Gaussian radius. Hence, all laser beam sizes are from now on expressed as Gaussian beam diameters. By enforcing that the Gaussian intensity distribution matches the amplitude of a corresponding Airy pattern (as is shown in Fig. 6.22), the diameter of the Gaussian distribution, defined at an intensity of $1/e^2$, can be expressed as [133]:

$$D_{\text{Gauss}} = 2\,w_0 = 1.68\frac{\lambda\,f}{2\,r_{ap}}. \tag{6.46}$$

Within the simulation, the position of the Airy pattern on the sensor is randomly varied. For each position, the template-based readout procedure is carried out and the error between true and obtained position is calculated. The simulation requires the following inputs to be made: the total optical power incident on the sensor, a range of focal lengths that should be simulated, an interval of integration times and the number of simulation runs for each combination of the other parameters. The latter parameter is required to obtain meaningful statistics of the outputs of the simulation: the SNR of the procedure and the error of the determination of the position of the incident laser beam. The structure of the simulation is explained in the following paragraphs.
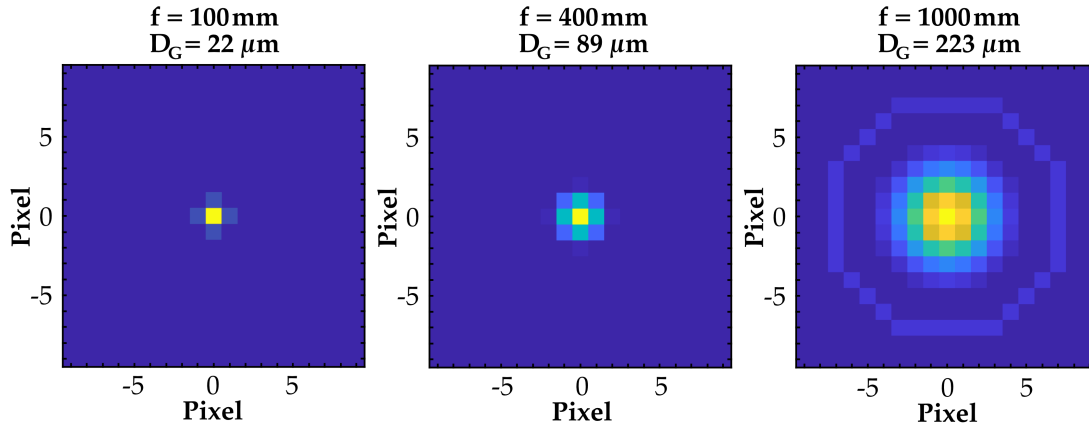
Figure 6.24: The figure shows examples of three different templates that were calculated for lenses with focal lengths of $f = 100\,\text{mm}$, $f = 400\,\text{mm}$ and $f = 1000\,\text{mm}$. The corresponding Gaussian beam diameters are $D_{\text{f100}} = 22\,\mu\text{m}$, $D_{\text{f400}} = 89\,\mu\text{m}$ and $D_{\text{f1000}} = 223\,\mu\text{m}$. A pixel has an edge length of $30\,\mu\text{m}$.

Calculation of templates

For each focal length, and consequently each beam diameter, an individual template is calculated. This is done by integrating the intensity of the Airy distribution for each pixel of a 19×19 pixel matrix. Thereby, the intensity at an angle θ, that is expressed relative to the optical axis, see Fig. 6.23, is defined by:

$$I(\theta) = I_0 \cdot \left[\frac{2\,J_1\left(k\,r_{\text{ap}}\,\sin\left(\theta\right)\right)}{k\,r_{\text{ap}}\,\sin\left(\theta\right)} \right]^2 \tag{6.47}$$

with J_1 the Bessel function of the first kind of order 1 and $k = 2\,\pi/\lambda$ the wave number. The usual small angle approximation, $\tan\left(\theta\right) \approx \theta$, can be applied, such that θ can be expressed as:

$$\theta = r/f \tag{6.48}$$

$$= \sqrt{x^2 + y^2}/f \tag{6.49}$$

with x and y the distance from the optical axis in horizontal and vertical axis and f the focal length. The maximum intensity, I_0 is defined by

$$I_0 = \frac{P_0\,\pi r_{\text{ap}}^2}{\lambda^2\,f^2} \tag{6.50}$$

with P_0 the total optical power within the aperture. It was found that proper scaling of I_0 is not necessary for the template. The subsequent calculation of the cross-correlation, as well as the corresponding SNR, are not affected by the templates amplitude. Thus, it was set to $I_0 = 1$. Therefore, a new template is only calculated when a new focal length is simulated, but not when the exposure time changes.

Three templates that were obtained by integrating Eq. (6.47) for $f = 100\,\text{mm}$, $400\,\text{mm}$ and

1000 mm for each pixel of a 19×19 matrix are shown as an example in Fig. 6.24. The pixel size was 30 μm×30 μm. As can be obtained from the plots, the chosen template size of 19×19 pixels is sufficient to contain even large beams of more than 200 μm diameter.

Calculation of the signal and dark matrices

Just as was done for the template, the signal is obtained by integration of the Airy intensity pattern, described by Eq. (6.47). Thereby, the center of the Airy pattern is randomly placed on a pixel. Due to practical reasons, the intensity is integrated over a 20×20 matrix. Here, the intensity at the center of the distribution is properly calculated, according to Eq. (6.50). The resulting pixel amplitudes are then converted to units of digital counts by applying the same conversion factors that were already used for the calculation of the sensor noise (Eqs. (6.40) and (6.41)).

A complete matrix with 256×320 pixels is created that contains the large sensor offset (~4000 cts), an offset due to dark current, the sensor noise, as calculated in the previous section, and the 20×20 sub-matrix with the integrated signal. Also shot noise due to signal electrons is accounted for. The sub-matrix is placed at a random position in the large matrix. In a next step saturation of the pixels is accounted for by limiting the amplitudes of all pixels to 2^{14} cts, which corresponds to the maximum pixel amplitude. The resulting 256×320 matrix is referred to as the *signal matrix*. Plot (a) in Fig. 6.25 shows a a simulated signal matrix, obtained with $f = 400$ mm and $t_e = 5$ ms. A second matrix with 256×320 pixels is created that contains only the large sensor offset, the offset due to dark current and the noise. This is referred to as the *dark matrix*.

As both, the noise and the signal, change with the exposure time, these matrices are updated for every change of the focal length f and the exposure time t_e. Additionally, as the position of the incident laser spot on the sensor is varied during the calculation of the signal matrix, the dark and signal matrices are updated for each iteration of the simulation.

Implementation of the template-based readout procedure

In a first step, the dark matrix is subtracted from the signal matrix to correct for the ~4000 cts offset and the introduced sensor noise. As no bad pixels and individual pixel gains were used for the calculation of the signal and dark matrices, these do not need to be corrected for. The corrected signal matrix is shown in plot (b) in Fig. 6.25.

The next step is the calculation of a normalized cross-correlation value $\gamma(u, v)$ for each element of the signal matrix M(x, y). This calculation is done in the spatial domain, as the normalized correlation coefficient usually does not have a simple and efficient frequency domain expression [134]. $\gamma(u, v)$ is a measure for the similarity of the signal matrix with a
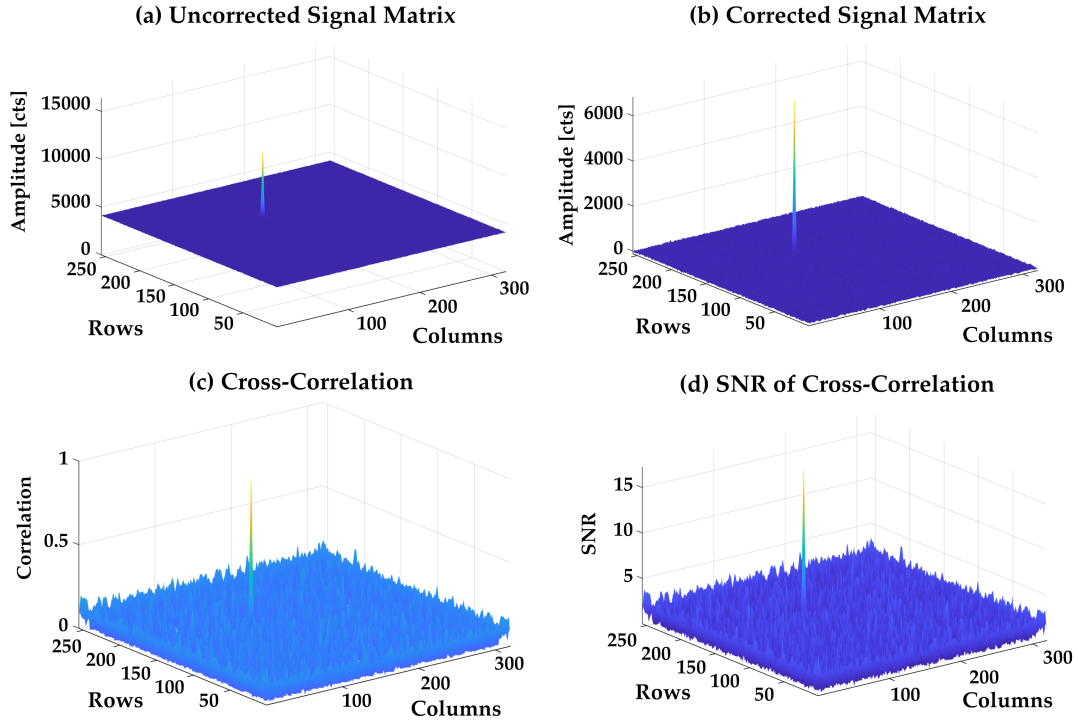
Figure 6.25: (a) Shows a simulated signal matrix for $f = 400\,\text{mm}$ and $t_e = 5\,\text{ms}$. (b) Shows the simulated signal matrix, corrected by a dark image. (c) Shows the cross-correlation of the signal matrix with a pre-computed template. (d) Shows the SNR of the cross-correlation. The used template was also calculated for $f = 400\,\text{mm}$ and is shown in the center plot of Fig. 6.24.

template T, positioned at (u, v). $\gamma(u, v)$ is defined by [134, 135, 136]:

$$\gamma(u, v) = \frac{\sum_{x,y} \left[\mathrm{M}(x, y) - \overline{\mathrm{M}}_{u,v} \right] \left[\mathrm{T}(x - u, y - v) - \overline{\mathrm{T}} \right]}{\sqrt{\sum_{x,y} \left[\mathrm{M}(x, y) - \overline{\mathrm{M}}_{u,v} \right]^2 \sum_{x,y} \left[\mathrm{T}(x - u, y - v) - \overline{\mathrm{T}} \right]^2}}. \qquad (6.51)$$

Here, $\overline{\mathrm{M}}_{u,v}$ is the mean of the signal matrix $\mathrm{M}(x, y)$ within the area spanned by template that was shifted to (u, v):

$$\overline{\mathrm{M}}_{u,v} = \frac{1}{N_x N_y} \sum_{x=u}^{u+N_x-1} \sum_{y=v}^{v+N_y-1} \mathrm{M}(x, y), \qquad (6.52)$$

with N_x and N_y the size of the template, here: $N_x = N_y = 19$. $\overline{\mathrm{T}}$, the mean of the template, is calculated analogously. The obtained normalized cross-correlation of the template and the corrected signal matrix is referred to as γ_{signal}, it is shown in plot (c) in Fig. 6.25.

Additionally, the cross-correlation of the template and the dark matrix, γ_{dark}, is calculated. This allows for the expression of a SNR of this template-based readout algorithm.

The SNR is obtained by normalizing γ_{signal} by the rms value of γ_{dark}:

$$\text{SNR} = \frac{\gamma_{\text{signal}}}{\gamma_{\text{dark,rms}}} \tag{6.53}$$

$$\gamma_{\text{dark,rms}} = \sqrt{\frac{\sum_u \sum_v \gamma_{\text{dark}}^2(u,v)}{256 \times 320}} \tag{6.54}$$

The resulting SNR matrix is shown in plot (d) in Fig. 6.25. The maximum of the SNR matrix defines the beam spot position with integer pixel resolution. In a next step, the maximum SNR should be determined to sub-pixel resolution. This is done here, by applying a least-squares fit of a 2D second order polynomial to a 3×3 pixel sub-matrix of the signal matrix. This matrix, that will be referred to as $\widehat{M}_{3\times3}$, is thereby centered around the beam position that is defined by the maximum of the SNR matrix. The nomenclature, used to address the elements of this matrix, is shown in Fig. 6.26. As is indicated by the gradient coloring of the plot, $M_{0,0}$ is the pixel with the highest SNR. A quadratic relationship between the amplitude of each element of $\widehat{M}_{3\times3}$ and the pixel index can be expressed as:

$$M_{x_i, y_j} = a_1 + a_2 \cdot x_i + a_3 \cdot y_j + a_4 \cdot x_i^2 + a_5 \cdot y_j^2 + a_6 \cdot x_i y_j. \tag{6.55}$$

Here, $x_i \in [-1, 0, 1]$ enumerates the columns and $y_j \in [-1, 0, 1]$ enumerates the rows of $\widehat{M}_{3\times3}$. $a_1 - a_6$ are the fit coefficients that must be determined. When all these entries are combined in a vector $\vec{M}_{3\times3}$, a system of linear equations can be established:

$$\begin{pmatrix} M_{-1,1} \\ M_{0,1} \\ M_{1,1} \\ M_{-1,0} \\ M_{0,0} \\ M_{1,0} \\ M_{-1,-1} \\ M_{0,-1} \\ M_{1,-1} \end{pmatrix} = \begin{pmatrix} 1 & -1 & 1 & 1 & 1 & -1 \\ 1 & 0 & 1 & 0 & 1 & 0 \\ 1 & 1 & 1 & 1 & 1 & 1 \\ 1 & -1 & 0 & 1 & 0 & 0 \\ 1 & 0 & 0 & 0 & 0 & 0 \\ 1 & 1 & 0 & 1 & 0 & 0 \\ 1 & -1 & -1 & 1 & 1 & 1 \\ 1 & 0 & -1 & 0 & 1 & 0 \\ 1 & 1 & -1 & 1 & 1 & -1 \end{pmatrix} \cdot \begin{pmatrix} a_1 \\ a_2 \\ a_3 \\ a_4 \\ a_5 \\ a_6 \end{pmatrix}. \tag{6.56}$$

With the coefficients $a_1 - a_6$ described by the vector $\vec{C}$, this can be rewritten as:

$$\vec{M}_{3\times3} = \widehat{A} \cdot \vec{C}. \tag{6.57}$$

The entries of $\vec{M}_{3\times3}$ are known. Thus, Eq. (6.57) can be solved for $\vec{C}$, to obtain the sought for coefficients $a_1 - a_6$, by applying the least-squares approach:

$$\left(\widehat{A}^{\mathrm{T}} \widehat{A}\right)^{-1} \cdot \widehat{A}^{\mathrm{T}} \cdot \vec{M}_{3\times3} = \mathbb{1} \cdot \vec{C}. \tag{6.58}$$

The maximum of the quadratic fit is then obtained by calculating the partial derivatives

of Eq. (6.55), setting them to zero, solving for x and y and using the obtained coefficients $a_1 - a_6$. Combining this results with the maximum of the SNR yields the desired information about the position of the impinging laser beam to sub-pixel resolution. As the *true* position of the laser beam is also known within the simulation, the error of the procedure can be calculated. The rms error is obtained by combining the error of all iterations of the simulation for each combination of f and t_e. As was mentioned at the beginning of this section, this rms error describes the *resolution* of the template-based readout algorithm.

Figure 6.26: The figure shows a graphical representation of $\widehat{M}_{3\times3}$ to illustrate the chosen labeling of the elements.

Discussion of the simulation results

Figure 6.27 shows the mean SNR and the rms error of a simulation run with an impinging beam power of 25 pW, as a function of the exposure time t_e and for different beam spot sizes, expressed as Gaussian beam diameters. The rms error is expressed in units of pixels. Each combination of f and t_e was iterated 100 times.

The two plots in the top half of the image show the complete parameter space. In the bottom plots, only those datapoints are shown that correspond to combinations of beam size and exposure time that did not lead to a saturation of pixels due to overexposure. Furthermore, to enhance the resolution in the interesting rms error range below 0.5 pixels, all larger errors are hidden.

As can be obtained from Fig. 6.27, combinations of sensible exposure times in the µs to ms range and beam spot sizes of a few pixels should lead to SNRs of up to 19 and rms errors of well below 10 % of the pixel size. For beam diameters on the order of the pixel length of $L = 30\,\mu m$, the error is approximately 25 % of the pixel size. For larger values it is reduced significantly. The smallest errors are obtained for beam diameters between 100 µm and 200 µm, which correspond to about three to six pixels. For even larger beam sizes, longer exposure times are required to yield similar centroiding errors. This was expected and is due to the peak intensity being reduced for larger beams.

Figure 6.28 shows another simulation run that was carried out for a total beam power of 1 pW. Again, each combination of f and t_e was iterated 100 times. The plots in the top and bottom of the figure show the same data, however, in the bottom row datapoints that belong to saturated pixels or showed errors above 0.5 pixel were again hidden. As can be obtained from the plots, the achievable rms error and the SNR are similar to the results
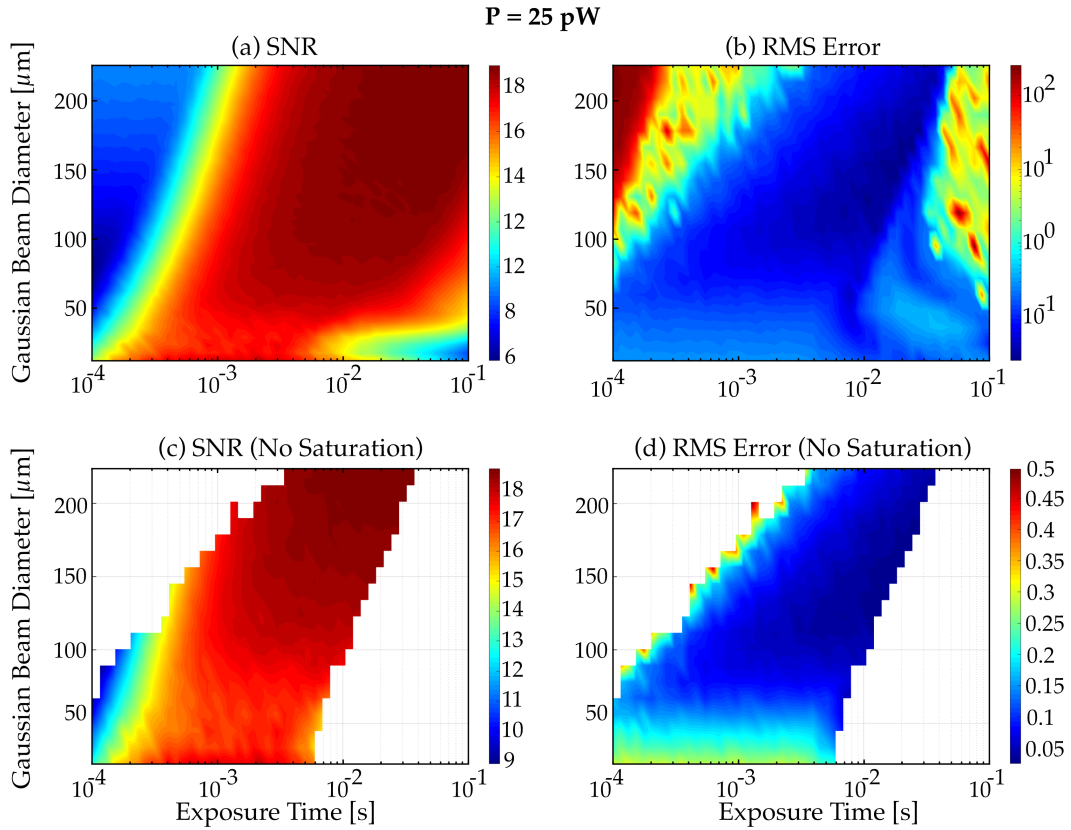
Figure 6.27: Simulation results for the SNRs and the achievable rms error of the template-based readout scheme. The simulated optical power was P = 25 pW. Each combination of focal length and exposure time was simulated 100 times. The top plots show the full parameter ranges and the bottom plots only show those datapoints that were obtained without saturation of the sensor. Additionally, all datapoints were excluded in the bottom plots where the rms error was greater than 0.5 pixel, to enhance the resolution of the plot in the range of interest.

that were obtained with a power of 25 pW. It can be stated that, in general, about one order of magnitude higher exposure times are necessary for an incident power of 1 pW.

Therefore, it can be stated that the carried out simulations confirmed that the template-based readout scheme seems appropriate to identifying the position of a laser beam on the InGaAs camera. A selection of values for the beam sizes and the exposure time should be tested by experiment to validate the simulation results. Beam diameters between one and four pixels are expected to produce SNRs and rms errors that are interesting for a CAS system for NGGM and LISA. Thereby, it is expected that beam sizes of $\geq 100\,\mu m$ yield minimum errors in the determination of the position of the laser beam below 10 % of the pixel size, or $\leq 3\,\mu m$. If the required FoV is imaged onto the complete sensor, this would correspond to a ratio of resolution to sensor size of $\Gamma_{\text{FPA,sim}} = \frac{3 \cdot 10^{-6}\,\text{m}}{7.68 \cdot 10^{-3}\,\text{m}} \approx 4 \cdot 10^{-4}$, or 0.04 % of the sensor size. If these numbers are proven to be correct by an experiment, the presented template-based readout scheme of the InGaAs camera data is capable of providing sufficient resolution with ample margin for LISA ($\Gamma_{\text{LISA}} \leq 0.15\,\%$) or NGGM ($\Gamma_{\text{NGGM}} \leq 0.5\,\%$).
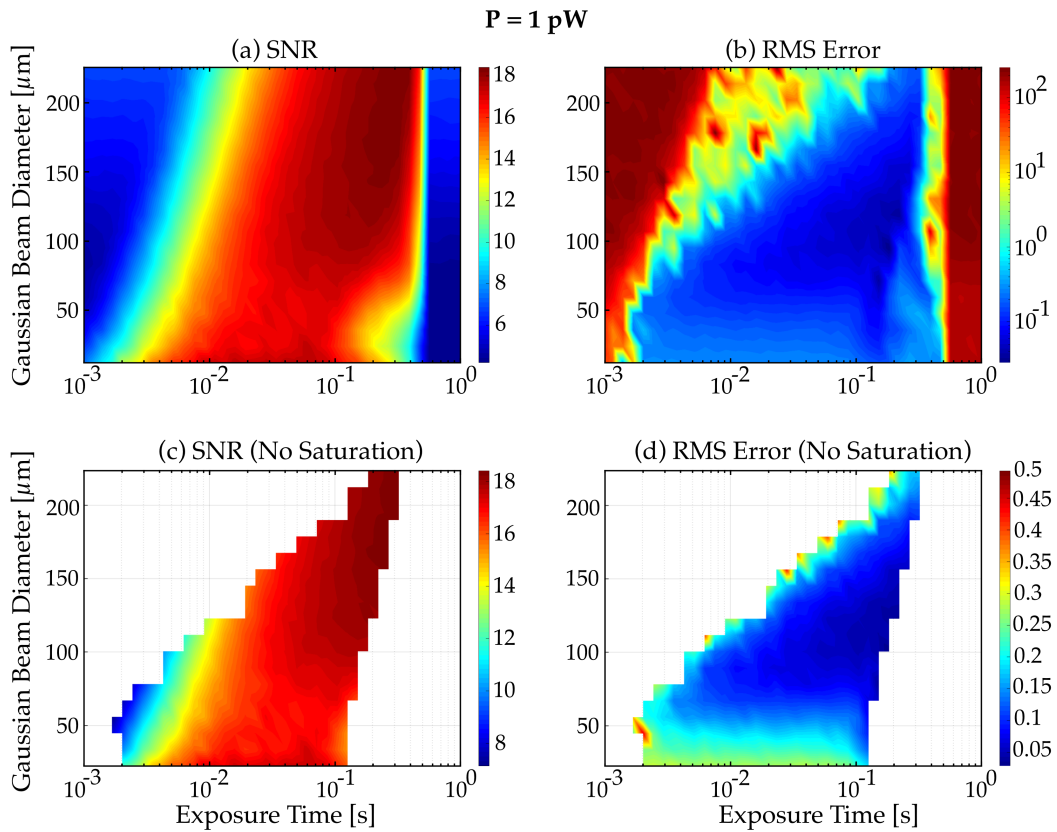
Figure 6.28: Simulation results for the SNRs and the achievable rms error of the template-based readout scheme. The optical power was $P = 1\,\mathrm{pW}$. Each combination of focal length and exposure time was simulated 100 times. The top plots show the full parameter ranges and the bottom plots only show those datapoints that were obtained without saturation of the sensor. Additionally, all datapoints were excluded in the bottom plots where the rms error was above 0.5 pixel, to enhance the resolution of the plot in the range of interest.

6.4.4 Experimental investigation of the template-based readout procedure

In this section, an experiment is explained that was carried out to validate the simulation results presented in the previous section. Thus, different laser beam spot sizes were generated in the InGaAs sensor plane and the template-based readout procedure was used to find the position of the impinging beam.

An experimental setup according to Fig. 6.21 was used. A photograph of the realized system is shown in Fig. 6.29. A laser beam of about 4 cm Gaussian diameter was generated with a large FC and then clipped at a circular aperture of 8 mm diameter. Just as was done before (see Sec. 5.2.1.2), the FC was aligned such that the transmitted laser beam had a homogeneous intensity profile and a flat wavefront. Again, a calibrated CCD camera and a Shack-Hartmann sensor were used for the alignment of the FC. Similar results as were presented previously (see Fig. 5.7 and 5.6), were obtained. A lens, placed just behind the aperture, was used to focus the laser beam to an Airy pattern on the InGaAs sensor. Therefore, the InGaAs sensor was placed within the focal plane of the lens. Different beam
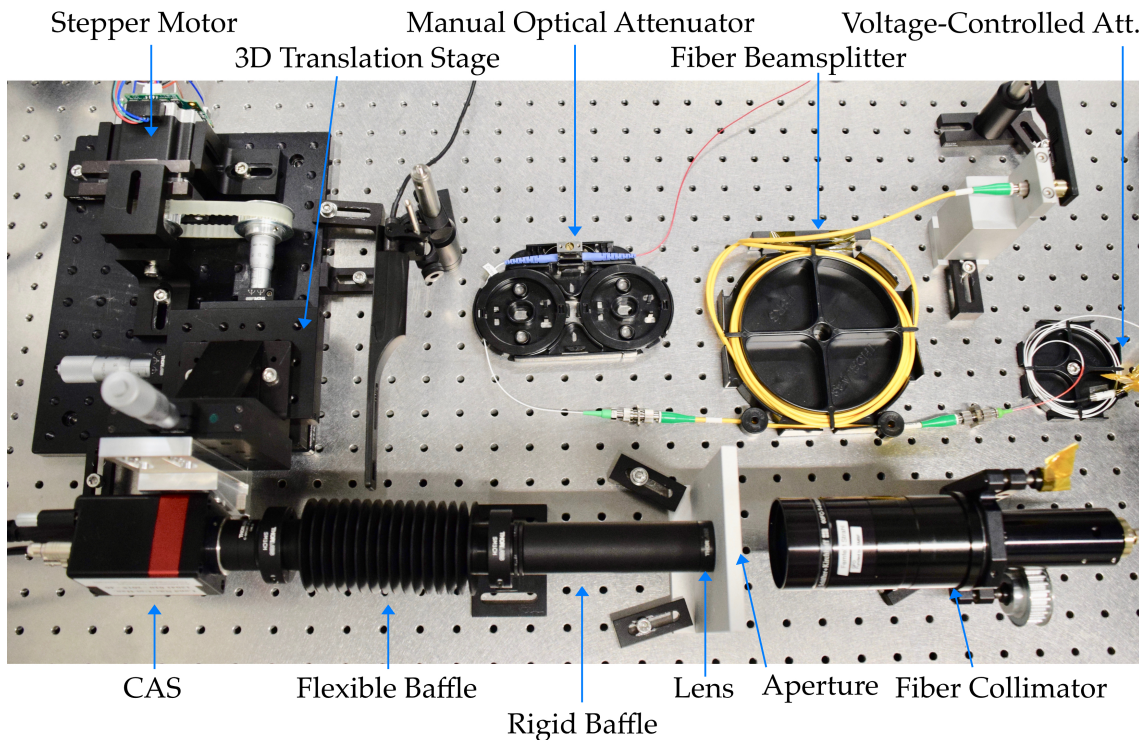
Figure 6.29: Photograph of the experimental setup that was used to test the template-based readout of the InGaAs sensor data.

sizes were then generated by replacing the lens. It was decided to only use such *focal systems*, to ensure that the generated laser beams can always be described by Airy patterns. This simplifies the comparison of the experimental results with the simulation results. Partly flexible baffles were used to isolate the sensor from stray light.

A laser power of $P = 1\,\text{pW}$ was used for all experiments. This low value was chosen to carry out the tests with the minimum power that a CAS is expected to receive (cf. Tab. 6.1). It was adjusted with the help of a manual and a voltage-controlled optical attenuator. The same calibration procedure of the attenuators as was applied for the LLS was used (see Sec. 5.2.2.1).

Instead of moving the laser beam to random positions on the sensor, as was assumed in the simulation, the whole sensor was moved relative to the laser beam. To implement this, the CAS was attached to a 3D translation stage. Thereby, the horizontal axis of the stage was actuated by a stepper motor which allowed for movements of the CAS in precise steps along this axis.

The key figure of merit of this experiment was the rms error of the template-based readout procedure and the achievable SNR. In the simulation, the error was obtained by subtracting the *true* position of the laser beam from the value that was obtained by the correlation with the matched template. However, in this experiment the *true* position is not known, as there is no absolute reference frame available. Therefore, a relative reference frame is used instead. The translation stage, that was actuated by the stepper motor, was used to move the sensor with a repeatable and precise step size along a straight line. For each step the
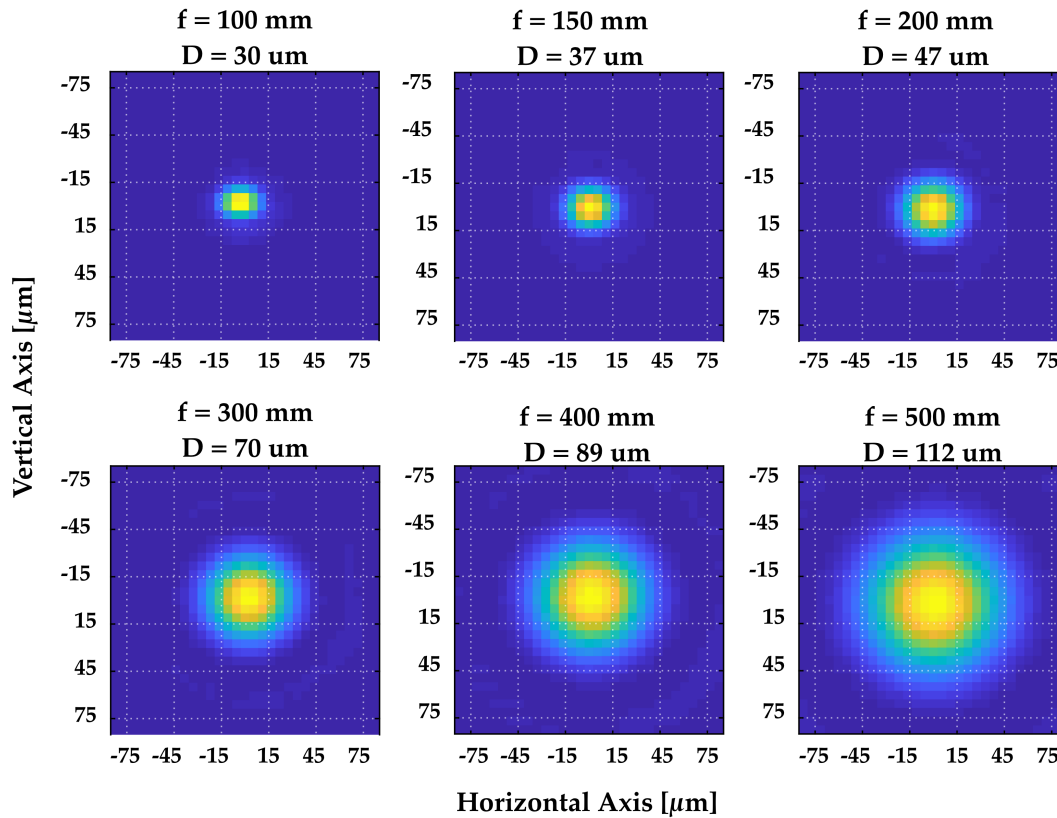
Figure 6.30: Plots of the laser beam spot intensity distributions that were generated on the WinCam sensor. The camera was placed in the focal plane of the lenses. The white grid lines are separated by 30 µm, such that the grid resembles the pixel size of the InGaAs camera. The provided beam diameters, D, were measured and are expressed as Gaussian beam diameters.

sensor was configured to perform a measurement. As also dark images were recorded, the data could be corrected, as is described by Eq. (6.32). Processing of this corrected data then yielded the position of the impinging laser beam in the horizontal and vertical sensor axes. As it could assumed that the sensor moved along a straight line, these datapoints were then fitted by a first order polynomial. The residuals to this linear fit were then interpreted as the error of the template-based readout procedure. By calculating the rms residuals for many such scan lines, a representative error of the template-based readout procedure as a function of the used beam diameter was produced.

Different lenses with focal lengths $f = 100 \, \text{mm}$, $150 \, \text{mm}$, $200 \, \text{mm}$, $300 \, \text{mm}$, $400 \, \text{mm}$ and $500 \, \text{mm}$ were tested. Figure 6.30 shows an overview of the laser beams that were generated with these lenses. The shown data was recorded with the help of a CCD camera (WinCam LCM-D) that provided a much higher spatial resolution than the InGaAs camera itself ($5.5 \, \mu\text{m} \times 5.5 \, \mu\text{m}$ per pixel). The WinCam was aligned such that its sensor was in the focal plane of the lens. After the WinCam was properly aligned and the laser beam's intensity distribution was characterized, the camera was replaced by the InGaAs sensor. Thereby, a special mount was used which ensured that the sensor planes of the two cameras were at the same distance to the lens.
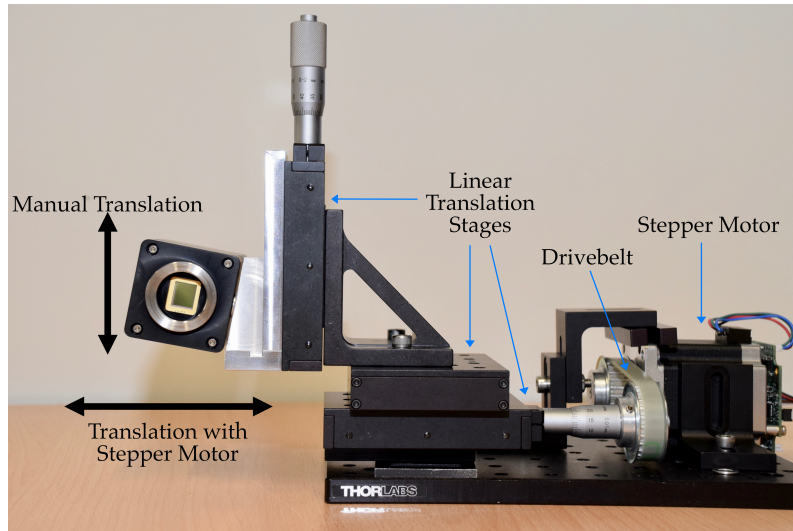
Figure 6.31: Photograph of the CAS, attached to the linear translation stages. The CAS was mounted under a 10° angle with respect to the vertical axis. A stepper motor was used to drive one of the linear stages. This motion occurred in the horizontal plane. Manual translation of the CAS was possible along the vertical axis and along the horizontal axis, that was aligned with the laser beam optical axis.

In general, the measured beam diameters, provided in the titles of Fig. 6.30, matched well the theoretical value that can be calculated with Eq. (6.46). Only for $f = 100$ mm, the measured value (D = 30 μm) slightly deviates from the theoretical one (D = 22 μm). The difference is expected to be due to a slightly afocal alignment of the WinCam and the CAS.

As was explained above, the sensor was moved parallel to the optical table with the help of the motorized linear stage. For each step of the motor, a measurement was carried out. By changing the position of the vertical translation stage, this process could be repeated for various other positions of the CAS along the vertical axis. Thereby, the CAS was attached to the translation stage under an angle of 10°, such that it could be ensured that the laser beam impinges on different positions on the pixels for each measurement (see photograph in Fig. 6.31).

The results that were obtained from one linear scan with a lens with focal length $f = 100$ mm are illustrated in Fig. 6.32. The obtained positions of the laser beam in the two sensor axes, here denoted x and y, are shown in the upper graph. One datapoint was excluded from the analysis. This is a step at which the template-based readout of the data did not properly find the position of the laser beam, due to the beam impinging on a bad pixel. As can be seen, both axes were fitted with linear fits independently. The individual and combined fit residuals are shown in the center graph. Thereby, the combined residuals were obtained by summing the individual components in quadrature: $\Delta_{\text{tot}} = \sqrt{\Delta_x^2 + \Delta_y^2}$. The bottom graph shows the SNR of the template-based readout procedure at the obtained beam position for each scan step. Multiple such scans were carried out. Figure 6.33 shows all of these scans plotted on top of each other. As is stated in the plot title, the total number of processed scan steps was $N = 146$. The combined rms residuals amounted to 0.2 pixel.
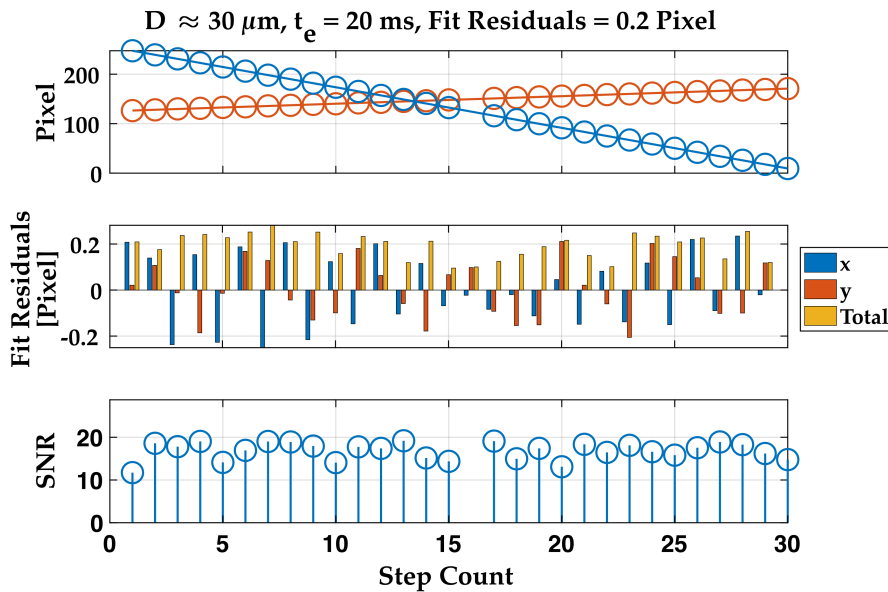
Figure 6.32: The figure shows the results that were obtained from one linear scan that was carried out with a lens a with focal length of $f = 100\,\text{mm}$. The resulting spot had a Gaussian beam diameter of about $30\,\mu\text{m}$. The upper plot shows the found beam positions in the two sensor axes, the center plot shows the residuals to linear fits and the bottom plot shows the corresponding SNRs.
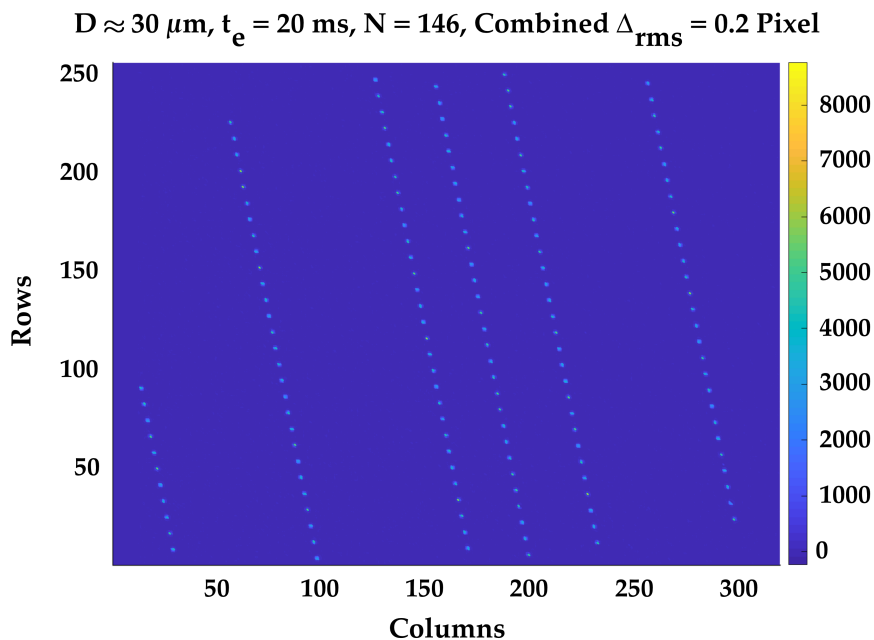
Figure 6.33: The figure shows all linear scans that were carried out with the $f = 100\,\text{mm}$ lens plotted on top of each other. The combined rms residuals of all scans amounted to $\Delta_{\text{rms}} = 0.2$ pixel.
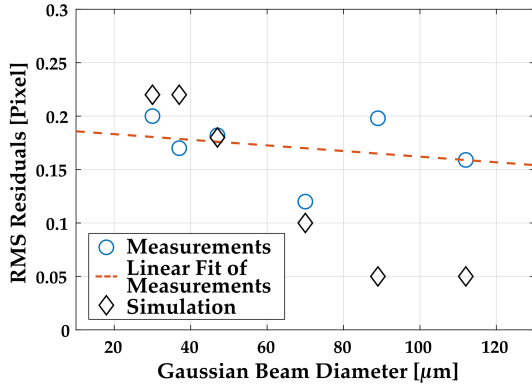
Figure 6.34: Overview of the rms residuals that were achieved with different beam sizes. Additionally, the simulation result is plotted.
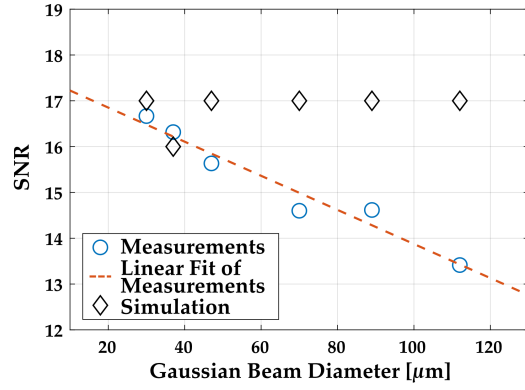
Figure 6.35: The figure shows the achieved mean SNR as a function of the beam size. Additionally, the simulated SNR is plotted.

Corresponding measurements were carried out with the remaining lenses. Thereby, the exposure time had to be adjusted in a range from 20 ms to 100 ms, for beam diameters of 30 μm to 112 μm. Thereby, the exposure times were chosen such that the peak signal amplitudes amounted to about 80 % of the dynamic range of the pixels. Figure 6.34 summarizes the results that were obtained with six different beam sizes, ranging from 30 μm to 112 μm. In addition to the obtained data, also a linear fit and the corresponding simulation results are shown. With the beam diameter D in units of μm and the rms fit residuals Δ_{rms} in units of pixels, the obtained fit is:

$$\Delta_{\mathrm{rms}}(\mathrm{D}) = -2.6 \cdot 10^{-4} \, \frac{1}{\mu\mathrm{m}} \times \mathrm{D} + 0.19. \tag{6.59}$$

In Fig. 6.35, the corresponding mean SNRs of the template-based readout method is plotted as a function of the beam size together with the simulated SNR. A corresponding linear fit is defined by:

$$\mathrm{SNR}(\mathrm{D}) = -3.7 \cdot 10^{-2} \, \frac{1}{\mu\mathrm{m}} \times \mathrm{D} + 17.6. \tag{6.60}$$

6.4.5   Discussion

Six different sized Airy patterns were generated by placing the InGaAs sensor in the focal plane of different lenses. The Gaussian beam diameters of the generated laser beams ranged from 30 μm to 112 μm. As can be obtained from the shown plots in Figs. 6.34 and 6.35, the achieved rms error ranged from ∼ 20 % to ∼ 15 % of the pixel size of 30 μm. The corresponding SNRs were found between ∼ 17 and 13. The achieved errors for beam diameters above 80 μm are slightly higher than the simulation results. It is expected that this is due to structural instabilities of the experimental setup. The central assumption that was made for the processing of the linear scans was that the CAS was moved along a

straight line by the motorized linear stage. However, the linear translation stage does only provide a finite precision for this linear motion. Especially if mechanically stressed, this motion might be slightly instable. Such stress could be induced by the "flexible" baffle that was mounted between CAS and the lens. This effect could be especially strong for the lenses with long focal lengths, as here also the used baffles are the longest. Therefore, special attention was paid to the distribution of the fit residuals. However, no systematic features were visible in these residuals from which a nonlinear motion of the translation stage, e.g. wobbling, could be inferred. An additional error source could have been the drivebelt that was used to transmit the motor's torque to the translation stage. By always moving the motor in the same direction during measurements, it was tried to minimize hysteresis effects. However, residual slack or play could have had an effect on the precision of the step size.

Also the achieved SNRs slightly deviate from the simulated values. As can be obtained from Fig. 6.35 and the corresponding linear fit, the SNR of the measurements seems to linearly decrease for larger beams. According to the simulation, a constant SNR is expected. However, the maximum deviation amounts to about 25 %. As was mentioned earlier, it was tried to optimize the exposure time for each beam size such that the peak amplitude reaches about 80 % of the full well capacity of the pixels. The achievable SNR strongly depends on this peak amplitude. Hence, it is expected that this discrepancy is caused by non-optimal choice of the exposure time which led to too low peak amplitudes. However, it can be stated that in general the measurements support the simulation. The observed deviations regarding the achieved SNR and the rms resolution, were not deemed substantial.

It could be shown by experiment that the SNR of the template-based readout algorithm exceeded a value of 10 for all tested configurations. Therefore, the LISA requirement (SNR>10, cf. Tab. 6.1) was fulfilled. Even though the observed rms errors exceeded the expectations, the obtained residuals of about 15 % of a pixel for a beam diameter of 110 µm correspond to a spatial resolution of about 5 µm. If an imaging system would image the complete FoV on the sensor surface, this corresponds to $\Gamma_{\text{FPA}} = {}^{5\cdot10^{-6}\,\text{m}}/_{7.68\cdot10^{-3}\,\text{m}} \approx 6.5 \cdot 10^{-4}$, or 0.065 % of the sensor surface. In comparison with the required values for LISA and NGGM ($\Gamma_{\text{LISA}} \leq 0.15\,\%$ and $\Gamma_{\text{NGGM}} \leq 0.5\,\%$) it can be stated that the template-based readout of the analyzed sensor is more than sufficient for both mission scenarios.

Furthermore, as the laser power was set a value of 1 pW, it was shown that the InGaAs FPA together with the applied readout method is qualified for the required low-power application (cf. "Min. Opt. Power" of 1 pW in Tab. 5.1). No showstoppers were identified that would prevent the sensor from working with even lower optical power levels. Only the exposure time would have to be further increased. In order to be in accordance with a required frame rate of 10 Hz, a value of 100 ms should not be exceeded. However, as was shown in Fig. 6.28 and by experiment, the required exposure time for a beam power of 1 pW varies between a few ten and one hundred ms. Hence, there exists margin to further reduce the beam power.

As was briefly mentioned in the context of the analysis of the data that was obtained with the lens with $f = 100\,\mathrm{mm}$, individual measurements were disturbed by bad pixels. The number of disturbed detections increased with increasing beam diameters. This is of course expected as the probability of the beam partly illuminating a bad pixel is enhanced with increasing beam diameter. However, the effect of this overlap on the error in the determination of the beam position decreases for larger beams. Also this is expected as smaller beams could be completely swallowed by bad pixels which could lead to errors of the template-based readout as large as the sensor size. Whereas the correlation between a partly obstructed large beam with a template is less likely to be affected strongly. Hence, beam diameters that are significantly larger than one pixel provide more robust detections. Additionally, the rms error of the detection of the beam position is reduced for larger beam diameters.

6.5   Consideration of different sensor types and materials for a CAS

An acquisition sensor yields information on the tilt of the local S/C with respect to the LOS. The wavefront of a received laser beam can be considered flat for the studied intersatellite laser interferometers, where the S/C separation is on the order of hundreds or millions of km. Therefore, a tilt of the local S/C with respect to the LOS yields a tilt of the incoming wavefront relative to the local S/C reference frame. The sought for information on the local tilt can then be obtained by using dedicated imaging optics in front of a CAS that translate a tilt of the wavefront into beamwalk on the sensor. Now a sensor is required that provides information on the position of an impinging laser beam. A prior, on-ground calibration of beamwalk to wavefront tilt is then applied to find the S/C tilt. Sensors that fulfill this criterion are e.g. PSPDs or a matrix detectors, such as CCDs or the investigated InGaAs FPAs.

A PSPD as possible CAS was studied and the results were presented in this thesis. With an achieved resolution of 0.2 % of the sensor size, the preliminary requirement on a CAS for NGGM could be fulfilled. However, it fell just shy of the required value for LISA. Furthermore, in order not to have noise in the DC range and stray light affecting the readout of the sensor, usually AC signals are used. However, this implies that a PSPD cannot be used in a star tracker mode. As this is required for the LISA mission to calibrate the angle between the S/C reference frame and the OB reference frame, a PSPD cannot be used for a CAS for LISA.

However, the achieved resolution and the proven operation of a PSPD with low optical power levels in the nW range make it a possible solution for a CAS for NGGM. Even though, the achieved minimum required optical power is most likely not sufficient for NGGM, it is expected that this could be further lowered. One possibility to achieve this would be the choice of a different semiconductor material. The investigated sensor was

made from silicon, which has a comparably low responsivity for laser light at $\lambda = 1064\,\text{nm}$. Large area PSPDs, that have diameters of about 10 mm, made of InGaAs exist and provide a much higher responsivity for 1064 nm. However, such large InGaAs sensors have a very high capacitance, compared to silicon (see e.g. [137, 57]). This lowers the achievable bandwidth of the TIA and increases the electronic noise. Therefore, a thorough analysis of the required sensor size should be carried out. Depending on the outcome of this analysis, the required bandwidth and the minimum optical power, the semiconductor material can be chosen. Additionally, the presented prototype readout electronics should then also undergo extensive investigations, regarding a possible optimization. Even though the PSPD was used with an amplitude-modulated laser beam, the effect of stray light on the achievable resolution regarding the determination of the position of the impinging beam, should be analyzed.

Most multi pixel sensors, such as CCDs or FPA sensors, are also made of either silicon or InGaAs. However, due to the low responsivity of silicon at a wavelength of 1064 nm, standard silicon-based sensors are not recommended for the application as CAS for either LISA or NGGM. Previous experiments at the AEI support this claim, during which it was observed that incident radiation with a wavelength of 1064 nm was transmitted by the thin silicon chip and disturbed the readout electronics underneath the sensor surface. Another option to the materials listed above is fully depleted silicon. A sensor that is based on this manufacturing process was presented in [138]. It provides 265×265 pixels of 51 µm edge length. As the semiconductor material is silicon, the bandgap energy yields a low dark current in comparison to an InGaAs FPA. Hence, the sensor provides a lower noise level than an InGaAs sensor. By enlarging the depletion region, the quantum efficiency of this semiconductor was enhanced from <0.3 electrons/photon for silicon to about 0.6 electrons/photon , which is comparable to InGaAs. Additionally, a CCD of similar type was used for the high throughput European Photon Imaging Camera (EPIC) on XMM and the German ABRIXAS x-ray satellite mission [139]. Hence, in addition to the promising characteristics regarding the sensitivity at 1064 nm, the high technical readiness level (TRL) of the sensor on XMM makes this technology an interesting candidate for a CAS on LISA and NGGM.

Within this thesis, a thorough analysis of a FPA made of InGaAs was presented. InGaAs provides a high quantum efficiency for radiation at 1064 nm. Furthermore, it was shown that the readout and dark noise of the investigated sensor are sufficiently low for the expected optical power levels in the pW range. High SNRs of up to 400 are achievable, even at room temperature. An algorithm was presented which was used to find the position of an impinging laser beam, based on the correlation of the sensor data with a pre-calculated template. The achieved resolution of this method was about 15 % of the pixel size of 30 µm, or $\sim$5 µm. There exists a large heritage of different centroiding algorithms for Shack-Hartmann sensors or star tracker applications that could also be applied for the readout of the CAS data (see e.g. [140, 141]). Also in the context of a CAS for LISA, various centroiding algorithms were already studied [142, 143, 144]. The investigated methods

provided a similar precision as the template-based correlation method, which was studied here. This is supported by another publication which showed that the algorithms that were also studied in the publications cited above yield similar residual errors, at least for high photon fluxes [145]. The computation time required for the template-based correlation method was found to be about three times higher than the time required for a center of gravity approach, which was used as benchmark due to its prevalence in the field of centroiding applications [145]. However, due to the comparably low required frame rate for the readout of a CAS for LISA, this does not seem to be a limiting factor. Additionally, it is expected that the progress in available computation power from the time of publication of [145] (2006) to today, further reduces the required computation time. Also for the InGaAs sensor, a proper analysis of stray light on the achievable centroiding resolution should be carried out. Due to the possibility of subtracting a dark image from the sensor data before it is further processed, the effect of stray light can be minimized. However, the dynamic range of the pixels is reduced by incident stray light which could in turn reduce the maximum SNR of a detection.

In summary it can be stated that an InGaAs FPA sensor, as was studied in this thesis, together with the template-based correlation readout method seems to be a good candidate for a CAS for LISA. A PSPD system could be used for the NGGM scenario. However, of course also the InGaAs FPA would be an appropriate solution for a CAS on NGGM. As was stated at the beginning of this chapter, only the optical properties of the studied sensors were investigated. The used InGaAs sensor, for example actively stabilizes the temperature of the ROIC. This will most likely not be possible for a CAS on LISA, due to the excess heat that the sensor produces and the stringent requirements on the power that a CAS is allowed to dissipate. Therefore, the proposal to use an InGaAs FPA, that was made above, only relates to the sensor type and not the exact model. In addition to the studied InGaAs-based sensor, a CCD that uses fully depleted silicon also seems to be an adequate solution. The corresponding CAS imaging system should be designed such that the required FoV is imaged onto the complete sensor surface. For the InGaAs sensor, a laser beam of about $100\,\mu m$ Gaussian beam diameter should be generated in the sensor plane of the CAS. As the investigated FPA has a pixel pitch of $30\,\mu m$, this corresponds to a beam diameter of about three pixels. It is expected that also for a fully depleted silicon-based CCD, the optimum beam size corresponds to about three by three pixels. The experiment with the InGaAs camera has shown that the position of an incident laser beam with $P = 1\,pW$ on the sensor can be detected with a ratio of resolution to sensor size of about $\Gamma_{FPA} = 0.065\,\%$ with a SNR of 15.

Chapter 7

Conclusion and Outlook

In the first part of the thesis, key components of the Laser Ranging Interferometer (LRI) on-board of GRACE-FO, as well as its laser link acquisition mode were introduced. This is a calibration scan in five degree of freedom (DoF) that was required to be carried out at the beginning of the mission. The aim of the procedure was to obtain estimates of offset angles of the LRI with respect to the line of sight (LOS). Furthermore, the frequency offset between the lasers on the master and the transponder S/C had to be identified.

Realistic mock-up optical benches (OBs) were designed and built for on-ground tests of this procedure that were carried out at the AEI. An elaborate test bed was used, to experimentally simulate the laser link. This setup was jointly developed by members of the DLR Institute of Space Systems in Bremen and the author of this thesis, originally for on-ground testing purposes of LRI flight hardware. Various tests of the initial acquisition procedure were carried out with this configuration. The obtained results confirmed the simulations that had been done previously and provided valuable insights for the whole LRI project team. After the tests of the initial acquisition procedure, the test bed accompanied the LRI from sub-system level testing at STI, to the instrument integration at Airbus Defence & Space facilities, to system level testing at IABG, to final system tests just before launch on the Vandenberg Airforce Base.

The GRACE-FO S/C were successfully launched on May 22nd, 2018. On June 13th and 14th, just a few weeks after the launch, the initial laser link acquisition procedure was carried out in orbit. As was presented in Chapter 4, for each OB pointing offset angles were found just below $\pm 1\,\text{mrad}$, well within the expected range of $\pm 3\,\text{mrad}$. Additionally, the initial acquisition procedure yielded correct set-points of the laser frequency offset on the transponder S/C. After the obtained pointing and frequency set-point offsets were uploaded to the S/C, the LRI autonomously transitioned into science mode on the first attempt. By doing so, the LRI on-board of GRACE-FO established the first intersatellite laser interferometer.

As was presented in the second part of Chapter 4, additional spatial calibration scans of the LRI were carried out within and after the instrument's commissioning phase. These differential wavefront sensing (DWS) offset scans were done to identify possible pointing errors of the triple mirror assemblies (TMAs). These so-called co-alignment errors (CAEs)

are not measurable on the local OB of a S/C, as the TMAs are placed behind the OBs along the transmitted (TX) beam's path towards the distant S/C. If the CAEs are not corrected for, they manifest themselves as a drop of the received (RX) power on the distant S/C. Hence, too large values could have fatal effects on the laser link. Processing of the first scans from July 2018 revealed absolute values of the CAEs between 0 and ∼50 µrad. The trade-off study that was presented in Sec. 4.2, demonstrated that the CAEs could potentially be partially compensated by the introduction of static DWS offsets. The carrier-to-noise density (C/N_0) of the heterodyne beat note signals on both S/C could be enhanced by such offsets by about 1 dBHz.

As was shown, subsequent DWS scans in June 2019 revealed that the CAE seem to have cured. Absolute values between 0 and about 10 µrad were found. Hence, currently it is not necessary to implement dedicated DWS offsets. However, the received signal strengths should be closely monitored throughout the mission life time to observe re-emerging CAEs. Should the CAEs increase, the analysis that was presented in this thesis can be applied to obtain DWS offset angles that optimally compensate these. This becomes especially important at later stages of the mission, when the laser power, and, consequently also the received signal amplitudes, start to degrade.

Since after the completion of the commissioning phase, the LRI has been operating flawlessly. The ranging noise was found on the order of $1\,\mathrm{nm}/\sqrt{\mathrm{Hz}}$ for frequencies above $0.1\,\mathrm{Hz}$, well below the requirement of $80\,\mathrm{nm}/\sqrt{\mathrm{Hz}}$ [19]. However, the noise floor is not yet assessable in the full frequency range due to the Earth's gravity dominating the ranging signal. The LRI data was made publicly available in the summer of 2019. By the time of writing of this thesis, publications of the first gravity field solutions from LRI data are expected. Once these solutions have been derived, the dominating component of the ranging signal that is due to gravity can be subtracted from the total ranging signal and the true instrument noise floor is assessable.

The main topic of the second part of this thesis was technology development for the laser link acquisition mode of future gravity missions. Specifically, the LISA mission and a possible Next Generation Gravity Field Mission (NGGM) were studied. An experimental test bed was developed that allows for end-to-end tests of two laser links between LRI-like OBs. This laser link simulator (LLS) was presented in Chapter 5. One of the key features of the LLS is its ability to process fast spatial scans of the TX laser beams with frequencies in the range of 100 Hz. It could be shown that the received signal power as a function of the TX beam angle could be faithfully reconstructed by the LLS with a relative out-of-loop error below 10 %. The LLS can be used for testing novel OB topologies for NGGM, e.g. proposed in-line configurations [44, 146]. Such designs are tempting, as they do not require a retroreflector with a large lateral beam offset, like the TMA. Additionally, due to the technological overlap of the laser ranging instruments on LISA and GRACE-FO, the LLS could also be used to test components of the LISA interferometer.

In Chapter 6, different sensor types were investigated regarding their applicability as dedicated acquisition sensor for missions like LISA and NGGM. Two sensors were tested: a single-element position sensitive photodetector (PSPD) and a multi-pixel InGaAs camera. Prototype readout electronics for the PSPD were developed that allowed for the determination of the impinging laser beam position with an rms error of about $20\,\mu$m. This corresponds to a ratio of resolution to detector size of $\Gamma_{\text{PSPD}} \mathrel{\hat{=}} 0.2\,\%$. With this value, the preliminary requirements of NGGM, $\Gamma_{\text{NGGM}} \leq 0.5\,\%$, could be fulfilled, while the obtained value fell just short of the LISA requirement, $\Gamma_{\text{LISA}} \leq 0.15\,\%$. The designed prototype electronics required a minimum optical signal power of $\geq 10\,$nW. This value is too high for LISA and NGGM. However, the obtained results are promising and suggest that further development of PSPD readout electronics towards a lower electronic noise floor could yield a possible constellation acquisition sensor (CAS) for NGGM.

In addition to a PSPD, an InGaAs camera with $256{\times}320$ pixels was investigated as possible CAS. A template-based readout of the sensor data to obtain information on the impinging laser beam position was proposed. A detailed simulation of this procedure with a realistic model of the sensor noise was carried out. The results suggested that the procedure and the investigated sensor were very promising for both mission scenarios. This was verified by experiments. It could be shown that a signal of $1\,$pW optical power on the sensor could be detected with high SNR and more than sufficient spatial resolution. A value of $\Gamma_{\text{FPA}} \mathrel{\hat{=}} 0.065\,\%$ was found. All tests were carried out with a temperature of the sensor of $20\,°$C. Additionally, it could be shown that the combination of presented sensor and template-based readout scheme fulfilled all preliminary requirements on a CAS for LISA and NGGM. However, it should be noted that no environmental properties of the sensor, e.g. the amount of emitted heat or the sensor size, were investigated. Furthermore, the possibility of utilizing a CCDs that is based on fully depleted silicon was briefly discussed. Due to the sensor's quantum efficiency (QE), which was enhanced by a factor of $\sim$2 compared to regular silicon, such sensors were found to be a viable alternative to InGaAs-based cameras for a CAS. A clear advantage over InGaAs would be the lower electronic noise of an un-cooled sensor.

Once mature requirements on a CAS for LISA or NGGM exist, a detailed CAS system should be designed. The imaging optics should be optimized such that the required field of view (FoV) covers the complete sensor area and that an optimal spot size for the readout algorithm is realized within the constraints of the provided envelope for the whole CAS system. Additionally, the handshaking between the CAS system, which includes the frame grabber, and the phasemeter or a S/C's on-board computer must be developed. Furthermore, processes need to be defined, which allow for the usage of the CAS pointing results by the S/C's AOCS. Testing of such a system could then be carried out in the LLS test bed.

Appendix

Appendix A

Effect of averaging and dark image subtraction on sensor noise

In Sec. 6.4.2, the dark and read noise of a single image of an InGaAs FPA camera with 256×320 pixels was analyzed. In the process, multiple images without any incident light ("dark images") were acquired for a pre-defined set of parameters (exposure time, sensor temperature, etc.). These single images were averaged and another dark image was subtracted. The last step was required to correct for static offsets of the whole sensor, as well as its columns. The rms value of all pixels of this corrected image was then used as representation of the noise of the acquired image.

However, it needs to be taken into account, that averaging and the subtraction of a dark image affect the noise. The scaling factor, that converts the noise of the corrected image to the noise of a single image is derived in the following paragraphs. The obtained factor was used to produce the numbers that were presented in Sec. 6.4.2.

When two images are added, the signal in single pixels adds up linearly. However, the uncorrelated noise within those images, $n_{1/2}$, adds in quadrature [121]. The noise of an image, that was obtained by adding two images, is thus defined as:

$$n_{\text{total}} = \sqrt{n_1^2 + n_2^2}. \tag{A.1}$$

Extending this to a sum over N images yields:

$$n_{\text{N}} = \sqrt{\sum_{k=1}^{N} n_{\text{k}}^2}. \tag{A.2}$$

Images, that were acquired with the same settings (exposure time, sensor temperature, etc.), show the same noise. The noise of a single image will be described by n_{s}. With that, Eq. (A.2) becomes:

$$n_{\text{N}} = \sqrt{N \cdot n_{\text{s}}^2} \tag{A.3}$$

$$= \sqrt{N} \cdot n_{\text{s}}. \tag{A.4}$$

In the following few lines, the effect of averaging N images on the noise of the resulting averaged image is described. A single image will be denoted by M_k. The average over N images, thus follows as:

$$M_{avg} = \frac{1}{N} \sum_{k=1}^{N} M_k. \tag{A.5}$$

Here, the sum denotes a pixel-wise summation of the matrices M_k. It was shown above, that the noise of the images M_k, adds in quadrature. Using Eq. (A.4), the noise of the average over N images follows as:

$$n_{avg} = \frac{1}{N} \cdot \sqrt{N} \cdot n_s \tag{A.6}$$

$$= \frac{n_s}{\sqrt{N}}. \tag{A.7}$$

Subtraction of a dark image, M_{dark}, from M_{avg} has the same effect on the noise as the *addition* of an image. According to Eq. (A.1) and (A.7) and assuming that the dark image shows the same noise as all other single images, the resulting total noise is defined by:

$$n_{tot} = \sqrt{n_{avg}^2 + n_{dark}^2} \tag{A.8}$$

$$= \sqrt{\left(\frac{n_s}{\sqrt{N}}\right)^2 + n_s^2} \tag{A.9}$$

$$= \sqrt{n_s^2 \left(\frac{1}{N} + 1\right)} \tag{A.10}$$

$$= n_s \sqrt{\frac{1}{N} + 1}. \tag{A.11}$$

By rearranging this equation, the noise of a single image is obtained:

$$n_s = n_{tot} \cdot \left(\sqrt{\frac{1}{N} + 1}\right)^{-1}. \tag{A.12}$$

Appendix B

QPR electronic schematics

Schematics of transimpedance amplifiers (TIAs) for a 1 mm diameter InGaAs QPD, that were designed by B. Sheard at AEI as prototypes for the GRACE-FO LRI are presented here. The QPRs were used as part of the mock-up OBs during the experiments, described in Chapter 3 and Chapter 5.
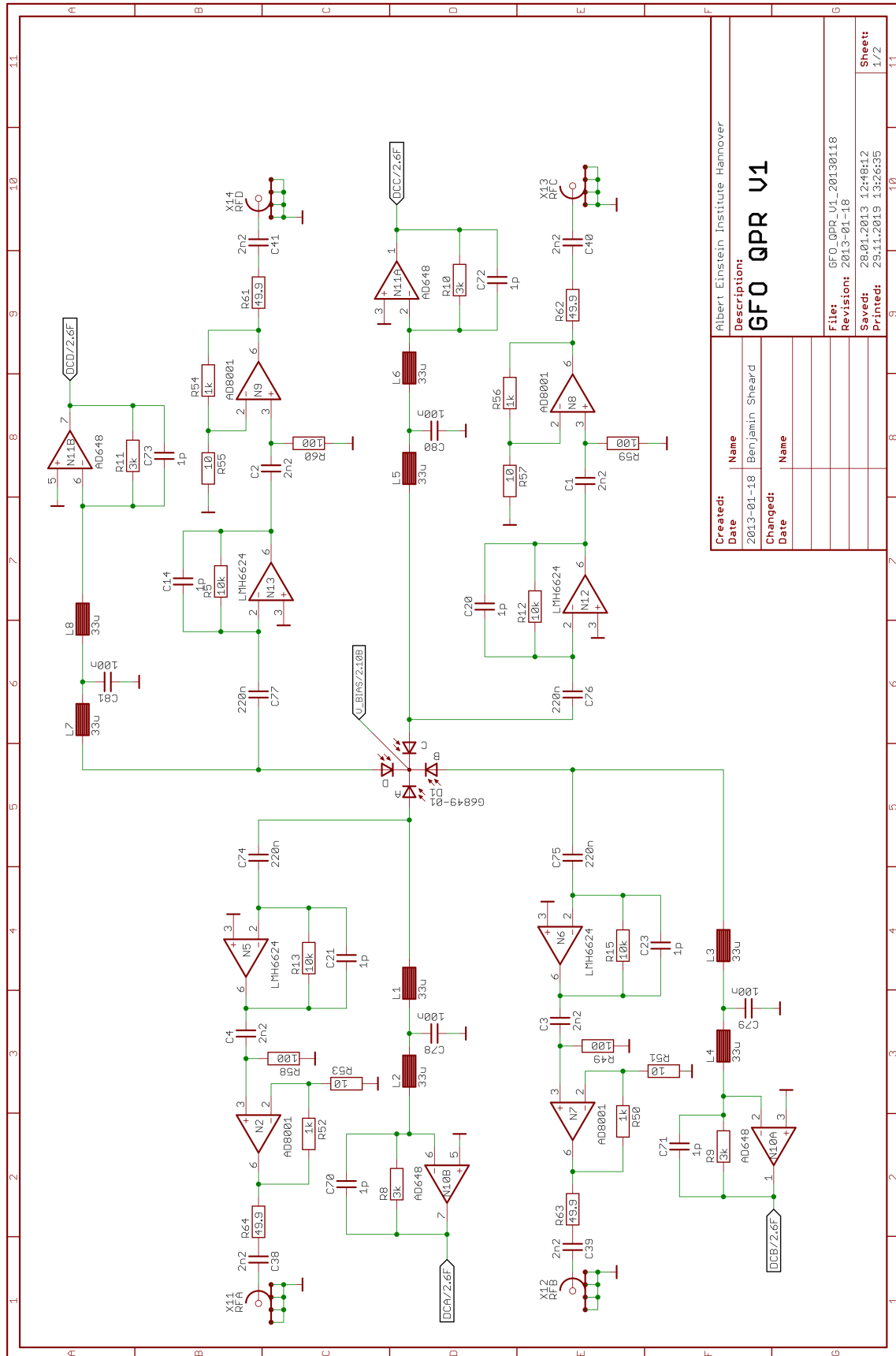
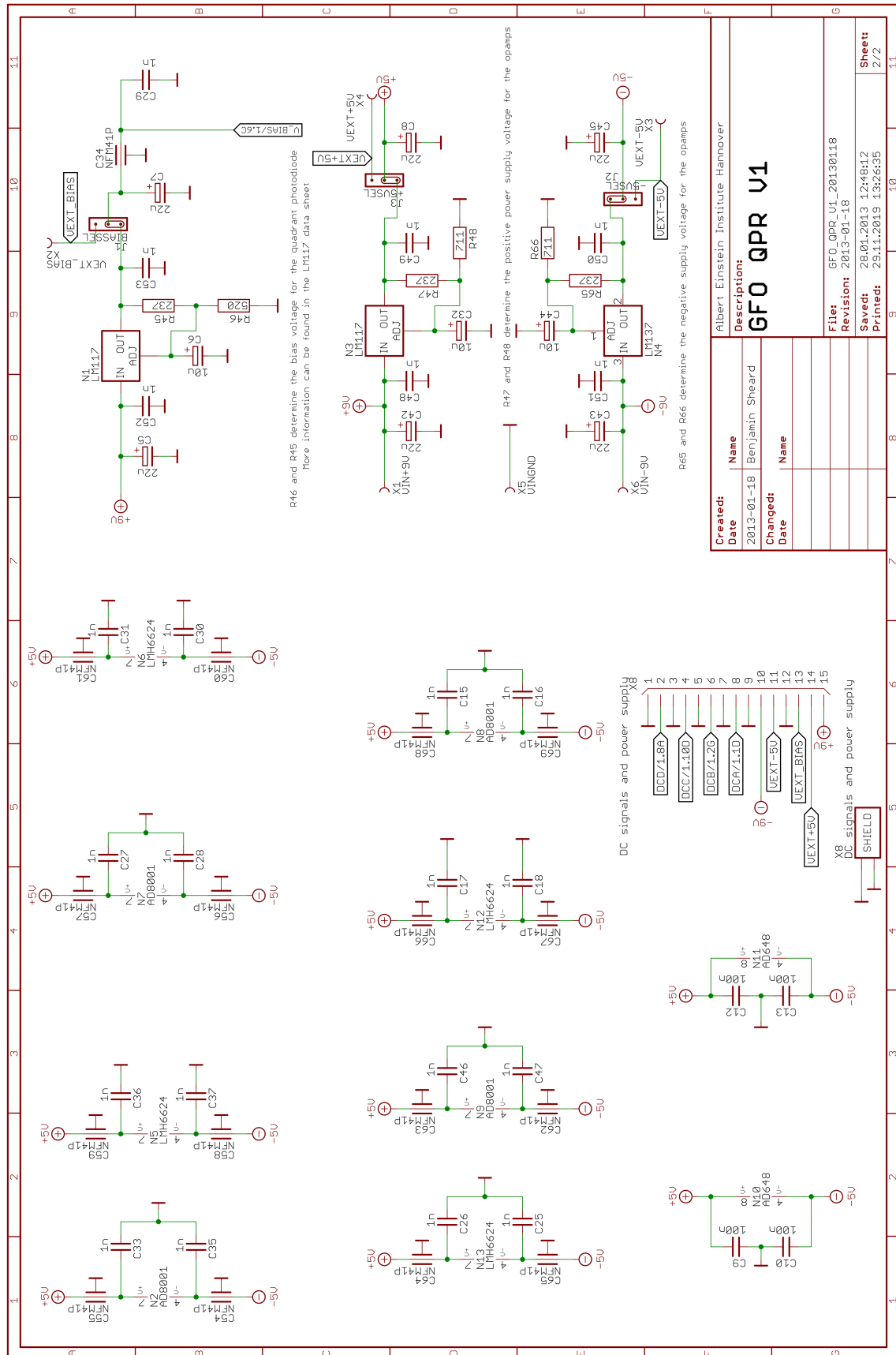**Figure B.1:** Schematic of the QPR front-end electronics with split AC and DC amplifiers for each QPD segment.

Figure B.2: Schematic of the power supply for the OPAs and of the generation of the QPD bias voltage.

Appendix C

LLS controller LabVIEW VIs

Key components of the LLS controller LabVIEW FPGA VIs are shown in Figs. C.1 to C.5. Annotations are marked by yellow boxes. The GUI, that is provided by the Host VI, is shown in Fig. C.6.
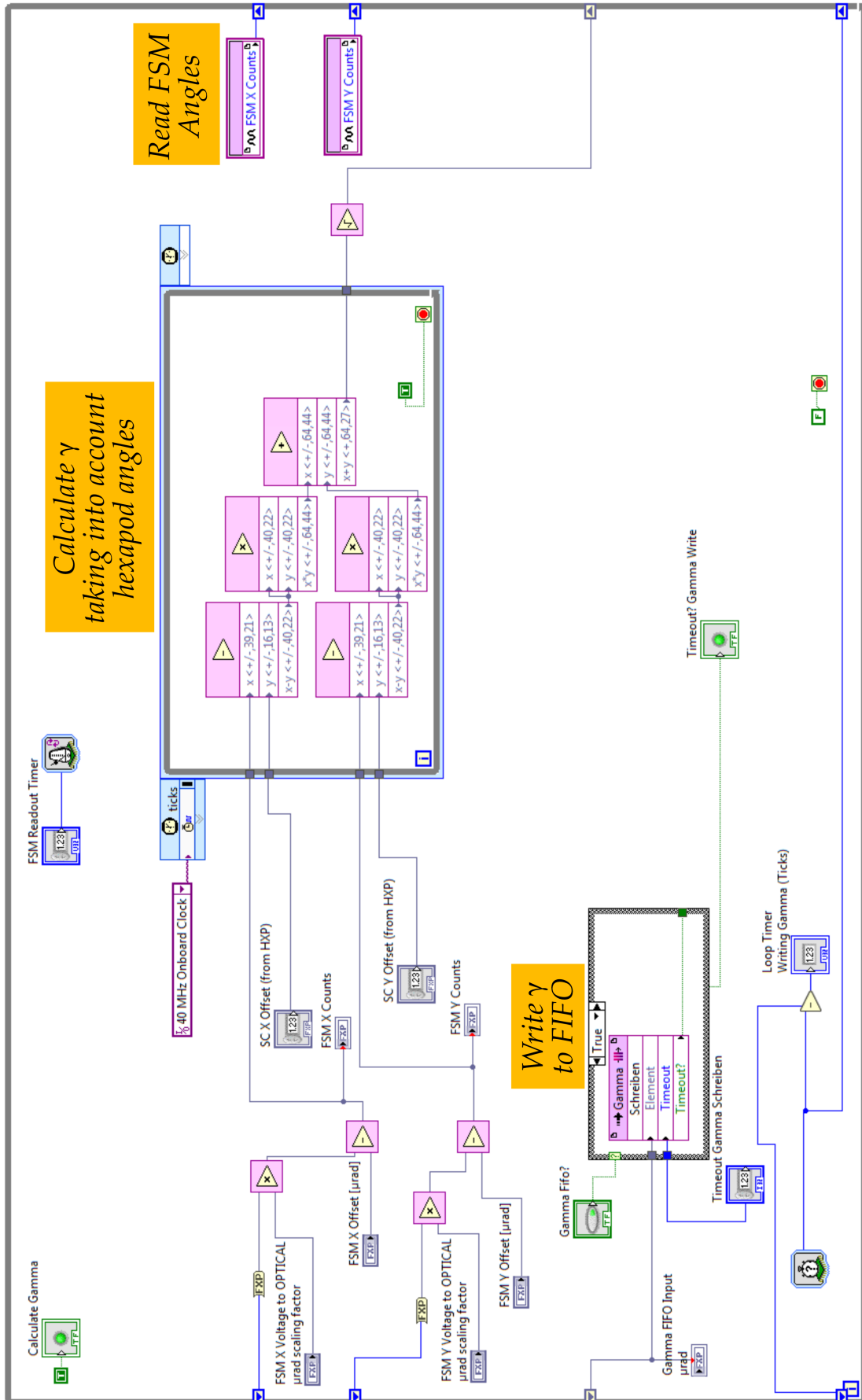
Figure C.1: γ is calculated and written to a FIFO register. The current hexapod angles are taken into account, such that $\gamma = 0$, when the distant OB's FSM angle coincides with the current local hexapod orientation.
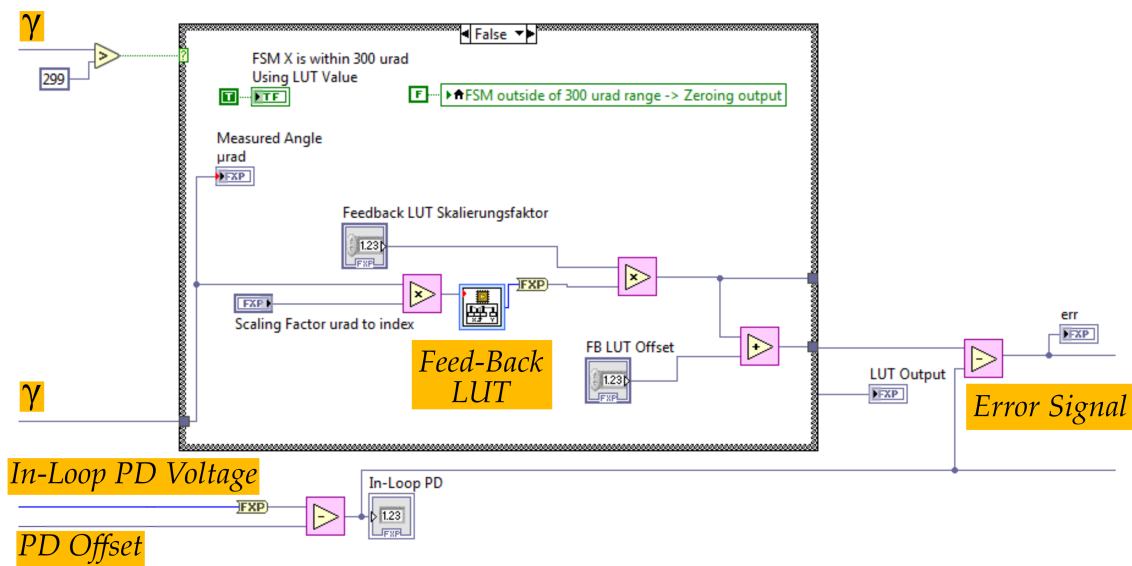
Figure C.2: If $\gamma < 300$ µrad, an error signal is calculated. This is the difference between the current in-loop PR signal and the output of the feed-back LUT (see black line in Fig. 5.15).
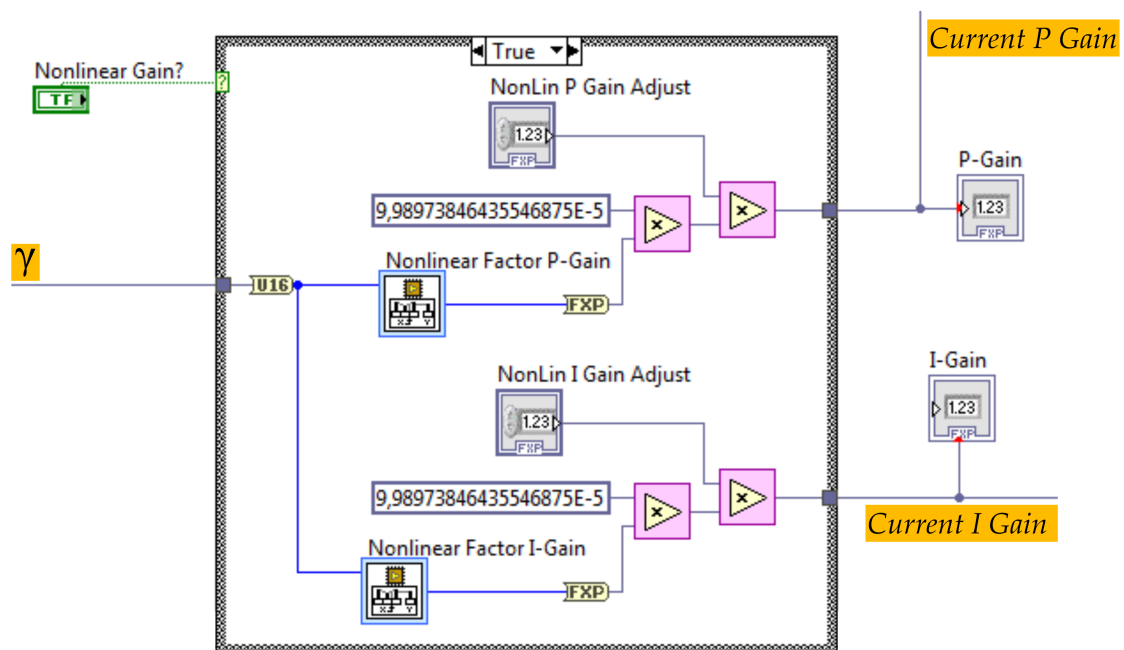

Figure C.3: The nonlinear gains are determined as a function of the current half-cone angle γ. The content of the LUTs is illustrated in Fig. 5.21.
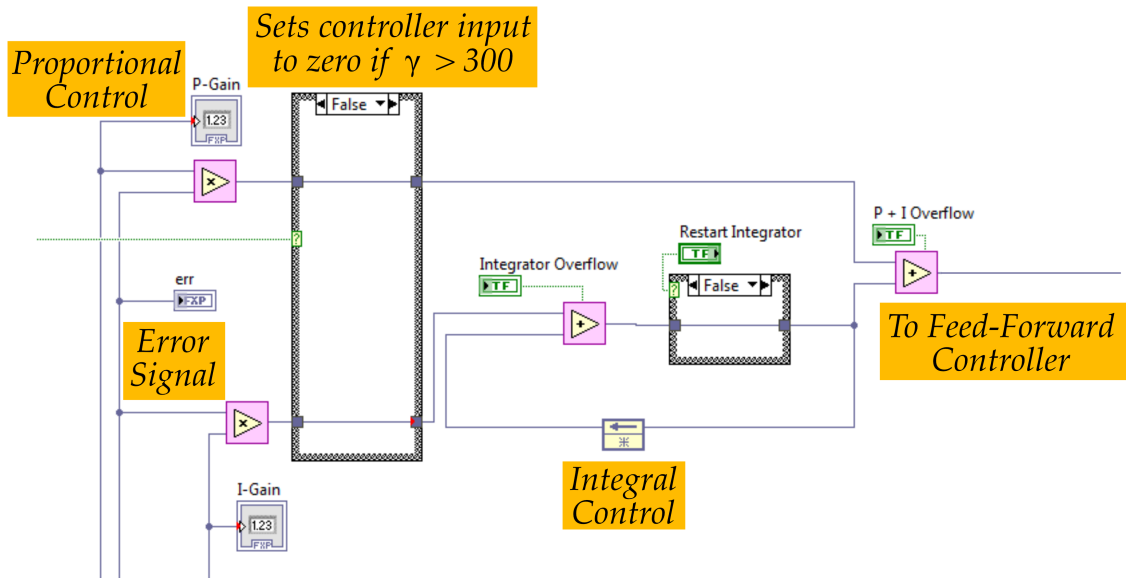
Figure C.4: The error signal is multiplied with the P-gain and integrated by the integral controller. The controller is deactivated when $\gamma > 300\,\mu$rad.
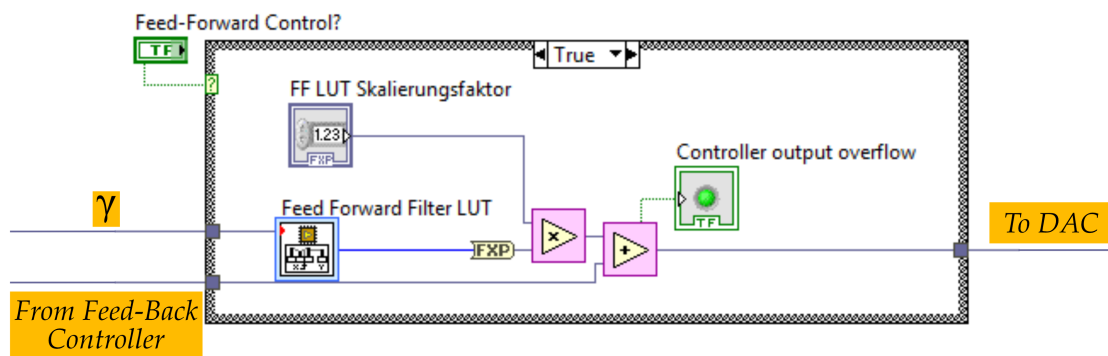
Figure C.5: The feed-forward signal (see blue line in Fig. 5.15) is added to the output of the feed-back controller. The sum is then sent to the DAC.
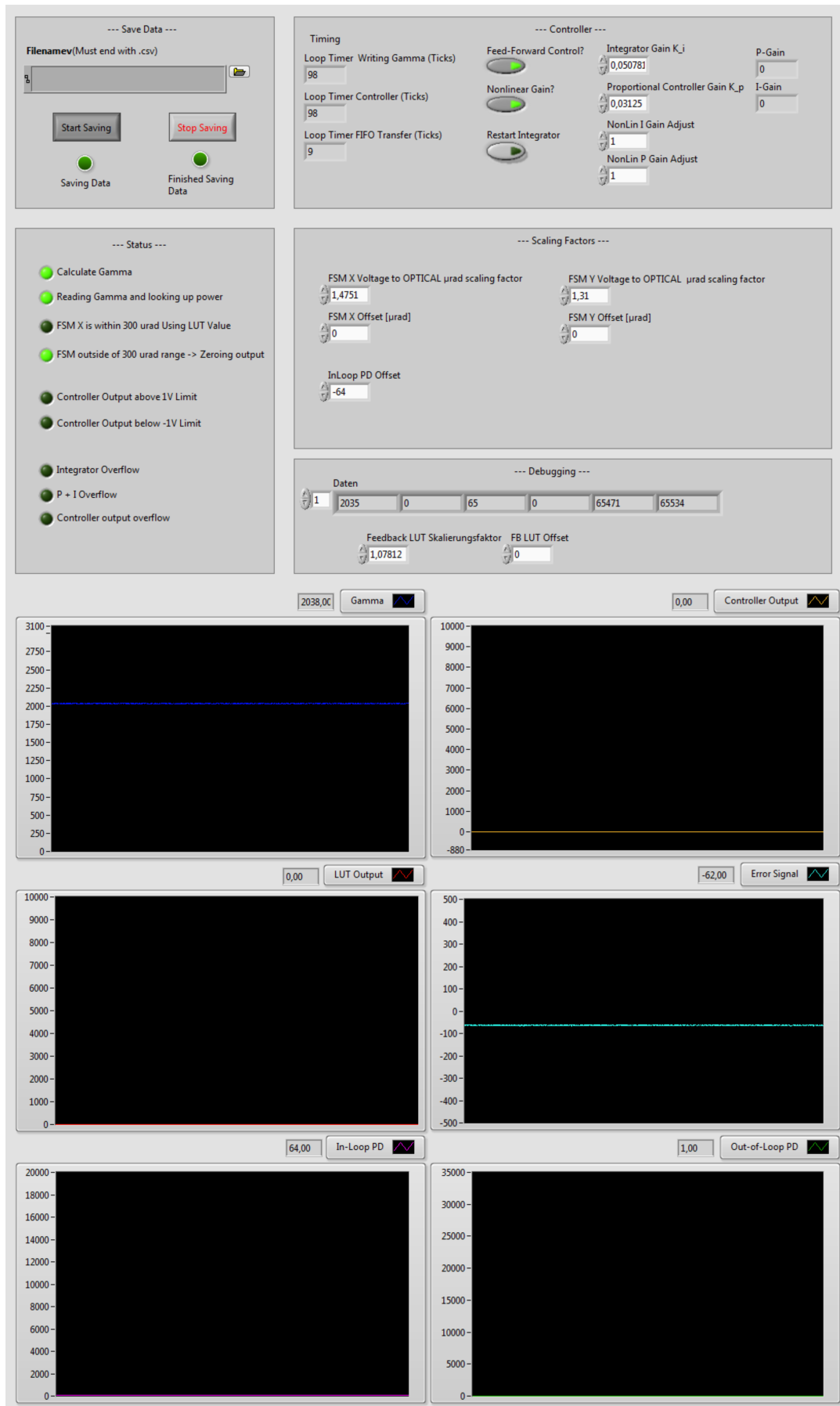
Figure C.6: GUI of the LLS LabVIEW Host VI. The user can save data at a sampling frequency of about 800 kHz. The feed-forward controller as well as the utilization of nonlinear gains can be enabled or disabled. Various scaling factors can be set by the user. The current half-cone angle γ, the controller output that is sent to the DAC, the feed-back LUT output, the error signal, the in-loop PR signal and the out-of-loop PR signal are illustrated in graphs.

Bibliography

[1] Iridium Satellite LLC. *Iridium NEXT Engineering Statement*. 2013. URL: https://fcc.report/IBFS/SAT-MOD-20131227-00148/1031348.pdf.

[2] Günter Seeber. *Satellite geodesy: foundations, methods, and applications*. Walter de Gruyter, 2003.

[3] C. Reigber, P. Schwintzer, and H. Lühr. "The CHAMP geopotential mission". In: *Bollettino di geofisica teorica ed applicata* 40.3-4 (1999), pp. 285–289.

[4] Reigber, C. et al. *A High Resolution Global Gravity Field Model Combining CHAMP and GRACE Satellite Mission and Surface Gravity Data: EIGEN-CG01C*. Tech. rep. Deutsches GeoForschungsZentrum Potsdam, 2006. DOI: 10.2312/GFZ.b103-06075.

[5] NASA. *Gravity model figure of Europe and Africa prepared by The University of Texas Center for Space Research as part of a collaborative data analysis effort with the NASA Jet Propulsion Laboratory and the GeoForschungsZentrum Potsdam. Image Credit: NASA / University of Texas Center for Space Research*. 2008. URL: https://appel.nasa.gov/2008/03/01/the-road-to-grace/.

[6] NASA. *Gravity Recovery and Climate Experiment Follow-On (GRACE-FO)*. 2014. URL: https://www.nasa.gov/image-feature/gravity-recovery-and-climate-experiment-follow-on-grace-fo.

[7] M.R. R. Drinkwater et al. *Earth Gravity Field from Space - from Sensors to Earth Sciences. GOCE: ESAs first Earth Explorer Core mission*. Ed. by G.B. Beutler et al. Kluwer Academic Publishers, 2003.

[8] J. Ebbing et al. "Earth tectonics as seen by GOCE - Enhanced satellite gravity gradient imaging". In: *Nature: Scientific Reports* 8.16356 (2018). DOI: 10.1038/s41598-018-34733-9.

[9] J. Berge, B. Christophe, and B. Foulon. "GOCE accelerometers data revisited: stability and detector noise". In: *Proceedings: ESA Living Planet Symposium 2013* (2013).

[10] B. D. Tapley et al. "The gravity recovery and climate experiment: Mission overview and early results". In: *Geophys. Res. Lett.* 31 (2004).

[11] C. Dunn et al. "The Instrument on NASAs GRACE Mission: Augmentation of GPS to Achieve Unprecedented Gravity Field Measurements". In: *Proceedings of the 15th International Technical Meeting of the Satellite Division of The Institute of Navigation (ION GPS 2002)* (2002), pp. 724–730.

[12] Deutsches GeoForschungsZentrum (GFZ) Helmholtz-Zentrum Potsdam. *GRACE and GRACE-FO Related Publications*. 2019. URL: http://www-app2.gfz-potsdam.de/pb1/op/grace/references/sort_date.html.

[13] M. Bevis et al. "Accelerating changes in ice mass within Greenland, and the ice sheets sensitivity to atmospheric forcing". In: *Proceedings of the National Academy of Sciences* 116.6 (2019). DOI: 10.1073/pnas.1806562116.

[14] Z. Liu et al. "Monitoring Groundwater Change in Californias Central Valley Using Sentinel-1 and GRACE Observations". In: *Geosciences* 9 (2019). DOI: 10.3390/geosciences9100436.

[15] S. Adhikari et al. "Sea-level fingerprints emergent from GRACE mission data". In: *Earth System Science Data* 11 (2019), pp. 629–646. DOI: 10.5194/essd-11-629-2019.

[16] K. Ahmed et al. "The changing characteristics of groundwater sustainability in Pakistan from 2002 to 2016". In: *Hydrogeology Journal* 27 (2019), pp. 2485–2496. DOI: 10.1007/s10040-019-02023-x.

[17] S. Kayali, P. Morton, and M. Gross. "International challenges of GRACE Follow-On". In: *IEEE Aerospace Conference* (2017). DOI: 10.1109/AERO.2017.7943615.

[18] B. S. Sheard et al. "Intersatellite laser ranging instrument for the GRACE follow-on mission". In: *J. Geod.* 86 (2012), pp. 1083–95. DOI: 10.1007/s00190-012-0566-3.

[19] Abich, K. et al. "In-Orbit Performance of the GRACE Follow-on Laser Ranging Interferometer". In: *Physical Review Letters* 123 (3 2019). DOI: 10.1103/PhysRevLett.123.031101.

[20] K. Abich et al. "GRACE Follow-On Laser Ranging Interferometer: German Contribution". In: *10th International LISA Symposium*. J. Phys. Conf. Ser. 2014. DOI: 10.1088/1742-6596/610/1/012010.

[21] F. Flechtner et al. "What Can be Expected from the GRACE-FO Laser Ranging Interferometer for Earth Science Applications?" In: *Surv. Geophys.* (2015). DOI: 10.1007/s10712-015-9338-y.

[22] NGGM-D Team. *e2.motion Earth System Mass Transport Mission (Square) - Concept for a next generation gravity field mission*. Verlag der Bayerischen Akademie der Wissenschaften, 2014.

[23] P. L. Bender, D. N. Wiese, and R. S. Nerem. "A possible dual-GRACE mission with 90 degree and 63 degree inclination orbits". In: *Proceedings of the 3rd International Symposium on Formation Flying, Missions and Technologies*. 2008.

[24] B. P. Abbott et al. "Observation of Gravitational Waves from a Binary Black Hole Merger". In: *Physical Review Letters* 116.6 (2016). DOI: 10.1103/PhysRevLett.116.061102.

[25] The Royal Swedish Academy of Sciences. *Press release: The Nobel Prize in Physics 2017*. 2017. URL: https://www.nobelprize.org/prizes/physics/2017/press-release/.

[26] B. P. Abbott et al. "GWTC-1: A Gravitational-Wave Transient Catalog of Compact Binary Mergers Observed by LIGO and Virgo during the First and Second Observing Runs". In: *Physical Review X* 9.3 (2019). DOI: 10.1103/PhysRevX.9.031040.

[27] The LIGO Scientific Collaboration. "Advanced LIGO". In: *Classical and Quantum Gravity* 32 (2015). DOI: 10.1088/0264-9381/32/7/074001.

[28] F. Acernese et al. "Advanced Virgo: a second-generation interferometric gravitational wave detector". In: *Classical and Quantum Gravity* 32 (2015). DOI: 10.1088/0264-9381/32/2/024001.

[29] K. L. Dooley et al. "GEO 600 and the GEO-HF upgrade program: successes and challenges". In: *Classical and Quantum Gravity* 33 (2016). DOI: 10.1088/0264-9381/33/7/075009.

[30] T. Akutsu for the KAGRA Collaboration. "The status of KAGRA underground cryogenic gravitational wave telescope". In: *arXiv preprint arXiv:1710.04823* (2017).

[31] S. Fairhurst. "Improved source localization with LIGO-India". In: *Journal of Physics: Conference Series* 484 (2014). DOI: 10.1088/1742-6596/484/1/012007.

[32] A. Einstein. "Die Grundlage der allgemeinen Relativitätstheorie". In: *Annalen der Physik* 354.7 (1916), pp. 769–822. DOI: 10.1002/andp.19163540702.

[33] A. Einstein. "Näherungsweise Integration der Feldgleichungen der Gravitation". In: *Sitzungsber. Preuss. Akad. Wiss.* (June 22, 1916), pp. 688–696. DOI: 10.1002/3527608958.ch7.

[34] A. Einstein. "Über Gravitationswellen". In: *Sitzungsber. Preuss. Akad. Wiss.* (Feb. 14, 1918), pp. 154–167. DOI: 10.1002/3527608958.ch12.

[35] Gerhard Heinzel. "Advanced optical techniques for laser-interferometric gravitational-wave detectors". PhD thesis. Leibniz Universität Hannover, 1999.

[36] Gregory M. Harry (for the LIGO Scientific Collaboration). "Advanced LIGO: the next generation of gravitational wave detectors". In: *Classical and Quantum Gravity* 27 (2010). DOI: 10.1088/0264-9381/27/8/084006.

[37] S. A. Hughes and K. S. Thorne. "Seismic gravity-gradient noise in interferometric gravitational-wave detectors". In: *Physical Review D* 58.12 (1998). DOI: 10.1103/PhysRevD.58.122002.

[38]   P. Amaro-Seoane et al. "Laser Interferometer Space Antenna: A proposal in re-
       sponse to the ESA call for L3 mission concept". In: *arXiv preprint arXiv:1702.00786*
       (2017).

[39]   F. Antonucci et al. "The LISA Pathfinder mission". In: *Classical and Quantum Gravity*
       29.12 (2012). DOI: 10.1088/0264-9381/29/12/124014.

[40]   M. Armano et al. "Sub-Femto-g Free Fall for Space-Based Gravitational Wave
       Observatories: LISA Pathfinder Results". In: *Physical Review Letters* 116.23 (2016).
       DOI: 10.1103/PhysRevLett.116.231101.

[41]   M. Armano et al. "Beyond the Required LISA Free-Fall Performance: New LISA
       Pathfinder Results down to 20 µHz". In: *Physical Review Letters* 120.6 (2018). DOI:
       10.1103/PhysRevLett.120.061101.

[42]   M. Armano et al. "LISA Pathfinder Performance Confirmed in an Open-Loop
       Configuration: Results from the Free-Fall Actuation Mode". In: *Physical Review
       Letters* 123.11 (2019). DOI: 10.1103/PhysRevLett.123.111101.

[43]   ESA. *Gravitational wave mission selected, planet-hunting mission moves forward*. 2017.
       URL: https://sci.esa.int/s/ABZzKKA.

[44]   Vitali Müller. "Design Considerations for Future Geodesy Missions and for Space
       Laser Interferometry". PhD thesis. Leibniz Universität Hannover, 2017.

[45]   Germán Ferndández Barranco. "Photodetection in intersatellite laser interferome-
       ters". PhD thesis. Leibniz Universität Hannover, 2018.

[46]   Christoph Mahrdt. "Laser Link Acquisition for the GRACE Follow-On Laser Rang-
       ing Interferometer". PhD thesis. Leibniz Universität Hannover, 2014.

[47]   Daniel Schütze. "Intersatellite Laser Interferometry: Test Environments for GRACE
       Follow-On". PhD thesis. Leibniz Universität Hannover, 2015.

[48]   B. Ware et al. "Phase Measurement System for Inter-Spacecraft Laser Metrology".
       In: *Earth Science Technology Conference* (2006).

[49]   B. Bachman et al. "Flight phasemeter on the Laser Ranging Interferometer on the
       GRACE Follow-On mission". In: *IOP Conf. Series: Journal of Physics: Conf. Series* 840
       (2017). DOI: 10.1088/1742-6596/840/1/012011.

[50]   R. W. P. Drever et al. "Laser phase and frequency stabilization using an optical
       resonator". In: *Applied Physics B* (1983). DOI: 10.1007/BF00702605.

[51]   R. Thompson et al. "A Flight-Like Optical Reference Cavity for GRACE Follow-on
       Laser Frequency Stabilization". In: *Frequency Control and the European Frequency
       and Time Forum (FCS), 2011 Joint Conference of the IEEE International* (2011). DOI:
       10.1109/FCS.2011.5977873.

[52] Oliver Gerberding. "Phase Readout for Satellite Interferometry". PhD thesis. Leibniz Universität Hannover, 2014.

[53] A. Wilson. "The internal photoelectric effect in crystals". In: *Nature* 130.913 (1932). DOI: 10.1038/130913a0.

[54] First Sensor. *Datasheet QP1-6 TO*. 2018. URL: https://www.first-sensor.com/cms/upload/datasheets/QP1-6_TO_5000029.pdf.

[55] D. Z. Anderson. "Alignment of resonant optical cavities". In: *Applied Optics* 23.17 (1984), pp. 2944–2949. DOI: 10.1364/AO.23.002944.

[56] D. Schütze et al. "Laser beam steering for GRACE Follow-On intersatellite interferometry". In: *Opt. Exp.* 22.20 (2014), pp. 24117–32. DOI: 10.1364/OE.22.024117.

[57] Hamamatsu. *Datasheet G12180 InGaAs Photodiode, 5 mm*. 2019. URL: https://www.hamamatsu.com/resources/pdf/ssd/g12180_series_kird1121e.pdf.

[58] H.-J. Eichler et al. *Lehrbuch der Experimentalphysik - Band 3*. Ed. by Heinz Niedrig. Walter de Gruyter & Co, 1993.

[59] K. Asakawa et al. *Handbook of Lasers and Optics*. Ed. by F. Träger. Springer, 2012.

[60] F. Guzman Cervantes et al. "Characterization of photoreceivers for LISA". In: *Classical and Quantum Gravity* 28.9 (2011). DOI: 10.1088/0264-9381/28/9/094010.

[61] Z. W. Barber et al. "Shot noise statistics and information theory of sensitivity limits in frequency- modulated continuous-wave ladar". In: *Journal of the Optical Society of America A* 30.7 (2013). DOI: 10.1364/JOSAA.30.001335.

[62] W. Schottky. "Über spontane Stromschwankungen in verschiedenen Elektrizitleitern". In: *Annalen der Physik* 362 (23 1918), pp. 541–567. DOI: 10.1002/andp.19183622304.

[63] E. R. Peck. "Theory of the Corner-Cube Interferometer". In: *Journal of the Optical Society of America* 38.12 (1948), pp. 1015–1024. DOI: 10.1364/JOSA.38.001015.

[64] O. Montenbruck et al. "Antenna phase center calibration for precise positioning of LEO satellites". In: *GPS Solutions* (2009). DOI: 10.1007/s10291-008-0094-z.

[65] A. Jäggi et al. "Phase center modeling for LEO GPS receiver antennas and its impact on precise orbit determination". In: *Journal of Geodesy* 83 (2009), pp. 1145–1162. DOI: 10.1007/s00190-009-0333-2.

[66] LRI Project Team. *GRACE Follow-On Laser Ranging Interferometer Link Acquisition Design Description. DRR GFO-13-165*. Tech. rep. Jet Propulsion Laboratory (JPL), May 14, 2014.

[67] A. Koch et al. "Line of sight calibration for the laser ranging interferometer onboard the GRACE Follow-On mission: on-ground experimental validation". In: *Optics Express* 26.20 (2018). DOI: 10.1364/OE.26.025892.

[68] Siegman, A. E. *Lasers*. University Science Books, 1986.

[69] Saleh, B.E.A. and Teich, M.C. *Fundamentals of Photonics*. Wiley, 1991.

[70] D. M. R. Wuchenich. "Inter-Satellite Laser Interferometry". PhD thesis. Australian National University, 2014.

[71] D. Wuchenich et al. "Laser link acquisition demonstration for the GRACE Follow-On mission". In: *Opt. Exp.* 22.9 (2014), pp. 11351–66. DOI: 10.1364/OE.22.011351.

[72] Filippo Ales. "Laser Ranging Interferometry for Future Gravity Missions: Instrument Design, Link Acquisition and Data Calibration". PhD thesis. Universität Bremen, 2016.

[73] F. Ales et al. "Modeling and Simulation of a Laser Ranging Interferometer Acquisition and Guidance Algorithm". In: *Journal of Spacecraft and Rockets* 51.1 (2014), pp. 226–238. DOI: 10.2514/1.A32567.

[74] F. Ales et al. "Line of sight alignment algorithms for future gravity missions". In: *American Institute of Aeronautics and Astronautics* (2015). DOI: 10.2514/6.2015-0094.

[75] A. Görth. "Development of a Fiber-Based Intersatellite Laser Link Simulator for GRACE Follow-On". Master Thesis. Leibniz Universität Hannover, 2014.

[76] S. Rasch. "Characterisation and set-up of a FPGA-based laser beam control as a pre-examination for the GRACE-FO mission". Bachelor Thesis. Universität Bremen, 2014.

[77] J. Sanjuan et al. "Interspacecraft link simulator for the laser ranging interferometer onboard GRACE Follow-On". In: *Applied Optics* 54.22 (2015), pp. 6682–6689. DOI: 10.1364/AO.54.006682.

[78] A. Görth et al. "Test Environments for the GRACE Follow-On Laser Ranging Interferometer". In: *11th Edoardo Amaldi Conference on Gravitational Waves*. Vol. 716. J. Phys. Conf. Ser. 2016. DOI: 10.1088/1742-6596/716/1/012011.

[79] A. Koch. *Laboratory Tests of the LRI Initial Acquisiton Procedure with the Fiber OGSE*. Tech. rep. Albert Einstein Institute, 2017.

[80] Nils C. Brause. "Auxiliary function development for the LISA metrology system". PhD thesis. Leibniz Universität Hannover, 2018.

[81] G. Fernández Barranco et al. "Phase stability of photoreceivers in intersatellite laser interferometers". In: *Optics Express* 25 (7 2017), pp. 7999–8010. DOI: 10.1364/OE.25.007999.

[82] Coherent Inc. "Datasheet Mephisto 500 NE FAM, S/N HDP.1264277.110-150003". 2015.

[83] C. Mahrdt. *Laser Link Acquisition for GRACE FO*. Poster Presentation at LISA Symposium 2012. 2012.

[84] G. Heinzel, A. Rüdiger, and R. Schilling. *Spectrum and spectral density estimation by Discrete Fourier transform (DFT), including a comprehensive list of window functions and some new flat-top windows*. Tech. rep. Max-Planck-Institut für Gravitationsphysik, 2002.

[85] M. Misfeldt and V. Müller. *Far-Field Beam Intensities & TMA co-alignment estimates*. Tech. rep. Albert Einstein Institute, 2019.

[86] J. C. Lagarias, M. H. Reeds, and P. E. Wright. "Convergence Properties of the Nelder-Mead Simplex Method in Low Dimensions". In: *SIAM Journal of Optimization* 9.1 (1998). DOI: 10.1137/S1052623496303470.

[87] D. Schütze on behalf of the LRI Team. "Measuring Earth: Current status of the GRACE Follow-On Laser Ranging Interferometer". In: *11th Edoardo Amaldi Conference on Gravitational Waves*. Vol. 716. 2016. DOI: 10.1088/1742-6596/716/1/012005.

[88] Newport. *Datasheet HXP100-MECA*. 2018. URL: https://www.newport.com/medias/sys_master/images/images/h03/hcc/9134490353694/HXP100-Data-Sheet.pdf.

[89] National Instruments Corporation. *NI R Series Multifunction RIO Specifications*. 2009. URL: https://www.ni.com/pdf/manuals/372492c.pdf.

[90] Analog Devices. *Datasheet ADL5391*. 2017. URL: https://www.analog.com/media/en/technical-documentation/data-sheets/ADL5391.pdf.

[91] M. Tröbs and G. Heinzel. "Improved spectrum estimation from digitized time series on a logarithmic frequency axis". In: *Measurement* 39 (2006), pp. 120–129. DOI: 10.1016/j.measurement.2005.10.010.

[92] M. Tröbs and G. Heinzel. "Corrigendum to Improved spectrum estimation from digitized time series on a logarithmic frequency axis". In: *Measurement* 42 (1 2009), p. 170. DOI: 10.1016/j.measurement.2008.04.004.

[93] A. V. Oppenheim, A. S. Willsky, and S. H. Nawab. *Signals and Systems*. 2nd ed. Prentice Hall, 1997.

[94] J. G. Ziegler and N. B. Nichols. "Optimum settings for automatic controllers". In: *Transactions of the ASME* 64 (1942), pp. 759–768. DOI: 10.1115/1.2899060.

[95] A. Abramovici and J. Chapsky. *Feedback Control Systems. A Fast Track Guide for Scientists and Engineers*. Springer Science and Business Media, LLC, 2000. ISBN: 978-1-4613-6952-3.

[96] J. Bechhoefer. "Feedback for physicists: A tutorial essay on control". In: *Reviews of Modern Physics* 77.3 (2005).

[97] M. Chwalla et al. "Design and construction of an optical test bed for LISA imaging systems and tilt-to-length coupling". In: *Class. Quantum Grav.* 33 (2016). DOI: 10.1088/0264-9381/33/24/245015.

[98]   Maike Lieser. "LISA optical bench development - Experimental Investigation of tilt-of-length coupling for a spaceborne gravitational wave detector". PhD thesis. Leibniz Universität Hannover, 2017.

[99]   Sönke Schuster. "Tilt-to-length coupling and diffraction aspects in satellite interferometry". PhD thesis. Leibniz Universität Hannover, 2017.

[100]   ESA. *LISA Payload Design Description. Is. 2, Rev. 2.* 2018.

[101]   C. Brugge et al. "An experiment to test in-field pointing for Elisa". In: *Proceedings Volume 10563, International Conference on Space Optics ICSO 2014; 105634D* (2017). DOI: 10.1117/12.2304152.

[102]   P. G. Maghami, T. T. Hyde, and J. Kim. "An acquisition control for the laser interferometer space antenna". In: *Classical and Quantum Gravity* 22 (2005), pp. 421–428. DOI: 10.1088/0264-9381/22/10/038.

[103]   SiTek Electro Optics. *Datasheet 2L10 PSD.* 2018. URL: https://www.lasercomponents.com/de/?embedded=1&file=fileadmin/user_upload/home/Datasheets/sitek/2l10_cp6.pdf&no_cache=1.

[104]   J. T. Wallmark. "A new semiconductor photocell using lateral photo-effect". In: *Proceedings of the IRE* (1957), pp. 474–483. DOI: 10.1109/JRPROC.1957.278435.

[105]   H. J. Woltring. "Single- and dual-axis lateral photodetectors of rectangular shape". In: *IEEE Transactions on Electron Devices* (1975), pp. 581–590. DOI: 10.1109/T-ED.1975.18181.

[106]   Song Cui and Yeng Chai Soh. "Linearity Indices and Linearity Improvement of 2-D Tetralateral Position-Sensitive Detector". In: *IEEE Transactions On Electron Devices* (2010). DOI: 10.1109/TED.2010.2051862.

[107]   A. J. Mäkynen. "Position-sensitive devices and sensor systems for optical tracking and displacement sensing applications". PhD thesis. University of Oulu, 2000.

[108]   Henrik Andersson. "Position Sensitive Detectors - Device Technology and Applications in Spectroscopy". PhD thesis. Mid Sweden University, Sundsvall, Sweden, 2008.

[109]   K. K. Gunnam et al. "A Vision-Based DSP Embedded Navigation Sensor". In: *IEEE Sensors Journal* 2.5 (2002), pp. 428–442. DOI: 10.1109/JSEN.2002.806212.

[110]   S. Iqbal, M. M. S. Gualini, and K. Rashid. "Stray noises and illuminations disturbing the performance of position-sensitive devices". In: *Proceedings: Optical Modeling and Performance Predictions II* 5867 (2005). DOI: 10.1117/12.623902.

[111]   Vrushabha Raja Marlur Sunder Kumar. "Investigation of Position Sensing Detector (PSD) as possible constellation acquisition sensor for LISA". MA thesis. Technische Universität Berlin, 2019.

[112] First Sensor. *Datasheet PC50-6-TO8*. 2010. URL: https://www.mouser.com/datashe et/2/313/PC50-6-TO8-10194.pdf.

[113] Akshay Bhat. *Stabilized TIAs Key To Reliable Performance*. Ed. by Electronic Design. 2011. URL: https://www.electronicdesign.com/analog/stabilized-tias-key-reliable-performance.

[114] Gerhard Heinzel. *LISO: Program for Linear Simulation and Optimization of analog electronic circuits Version 1.7 ©G. Heinzel 1997, 1998, 1999*. URL: https://wiki.projekt.uni-hannover.de/aei-geo-q/start/software/liso.

[115] Ron Mancini. *Op Amps For Everyone. Design Reference*. Texas Instruments, 2002.

[116] D. K. Kaushik. *Analog Electronics*. 2014.

[117] Analog Devices. *Datasheet OP27*. 2015. URL: https://www.analog.com/media/en/technical-documentation/data-sheets/OP27.pdf.

[118] Raptor Photonics. *Datasheet OWL SW1.7 CL-320*. URL: https://axiomoptics.com/Brochures/OWL-SW1-7-CL-320-200912.pdf.

[119] H. Huang, L. Liu, and M. O. Ngadi. "Recent Developments in Hyperspectral Imaging for Assessment of Food Quality and Safety". In: *Sensors* 14 (2014), pp. 7248–7276. DOI: 10.3390/s140407248.

[120] S. B. Howell. *Handbook of CCD Astronomny*. Cambridge University Press, 2000.

[121] T. S. Holst G. C. ands Lomheim. *CMOS/CCD sensors*. SPIE Press, 2011.

[122] Automated Imaging Association. *Specifications of the Camera Link Interface Standard for Digital Cameras and Frame Grabbers*. Version 1.1. 2004.

[123] Alpha Data. *Datasheet ADM-XRC-7Z1*. 2019. URL: https://www.alpha-data.com/pdfs/adm-xrc-7z1_v2.2.pdf.

[124] Alpha Data. *Datasheet ADC-XMC-BREAKOUT*. 2019. URL: https://www.alpha-data.com/pdfs/adc-xmc-breakout_v1.0.pdf.

[125] Christoph Gentemann. "Calibration and implementation of an acquisition camera for a next generation geodesy mission". Bachelor thesis. Leibniz Universität Hannover, 2018.

[126] Alexander Koch. *Analysis of a template-based laser beam localization algorithm for a CAS on LISA. LISA-LCST-INST-TN-010*. Tech. rep. Albert Einstein Institute, Hannover, 2019.

[127] Newport. *Datasheet 819D-SL-3.3 Integrating Sphere*. 2015. URL: https://www.newport.com/medias/sys_master/images/images/hc3/h13/8797116858398/Integrating-Spheres-Datasheet.pdf.

[128] James R. Janesick. *Photon Transfer*. SPIE Press, 2007.

[129]   Antoni Rogalski, Krzysztof Adamiec, and Jaroslaw Rutkowski. *Narrow-Gap Semi-conductor Photodiodes*. SPIE Press, 2000.

[130]   K.-S. Kim, J. Liu, and M. F. Insana. "Beamforming using spatial matched filtering with annular arrays (L)". In: *Journal of the Acoustical Society of America* 121.4 (2009). DOI: 10.1121/1.2642214.

[131]   A. Fenster and J. C. Lacefield. *Ultrasound Imaging and Therapy*. 2015.

[132]   G. B. Airy. "On the diffraction of an object-glass with circular aperture". In: *Transactions of the Cambridge Philosophical Society* (1835).

[133]   B. Zhang, J. Zerubia, and J.-C. Olivo-Marin. "Gaussian approximations of fluorescence microscope point-spread function models". In: *Applied Optics* 46 (10 2007), pp. 1819–1829. DOI: 10.1364/AO.46.001819.

[134]   J. P. Lewis. *Fast Normalized Cross-Correlation*. Tech. rep. Industrial Light & Magic.

[135]   J. P. Lewis. "Fast Template Matching". In: *Vision Interface 95, Canadian Image Processing and Pattern Recognition Society*. Quebec City, Canada, 1995, pp. 120–123.

[136]   K. Briechle and U. D. Hanebeck. "Template matching using fast normalized cross correlation". In: *Proceedings of SPIE - The International Society for Optical Engineering* (2001). DOI: 10.1117/12.421129.

[137]   Hamamatsu. *Datasheet S3071 Si Photodiode, 5 mm*. 2014. URL: https://www.hamamatsu.com/resources/pdf/ssd/s3071_etc_kpin1044e.pdf.

[138]   R. Hartmann et al. "A high speed pnCCD detector system for optical applications". In: *Nuclear Instruments & Methods in Physics Research* (2006). DOI: 10.1016/j.nima.2006.05.229.

[139]   L. Strüder et al. "A 36 cm^2 large monolithic pn-charge coupled device x-ray detector for the European XMM satellite mission". In: *Review of Scientific Instruments* 68 (1997). DOI: 10.1063/1.1148341.

[140]   J. Arines and J. Ares. "Minimum variance centroid thresholding". In: *Optics Letters* 27.7 (2002), pp. 497–499. DOI: 10.1364/OL.27.000497.

[141]   B. L. Baker and M. M. Moallem. "Iteratively weighted centroiding for Shack-Hartmann wave-front sensors". In: *Optics Express* 15.8 (2007), pp. 5147–5159. DOI: 10.1364/OE.15.005147.

[142]   Thomas Schwarze. "Implementation and characterisation of an acquisition sensor for the LISA optical bench". Bachelor Thesis. Leibniz Universität Hannover, 2009.

[143]   Alexander Meier. "Implementierung und Charakterisierung einer InGaAs Kamera zur Satellitenausrichtung bei LISA". Bachelor Thesis. Leibniz Universität Hannover, 2012.

[144] Sebastian Schreiber. "Implementation and characterization of an acquisition sensor for LISA". Bachelor Thesis. Leibniz Universität Hannover, 2014.

[145] S. Thomas et al. "Comparison of centroid computation algorithms in a Shack-Hartmann sensor". In: *Monthly Notices of the Royal Astronomical Society* 371 (2006), pp. 323–336. DOI: 10.1111/j.1365-2966.2006.10661.x.

[146] O. Mandel et al. "Optical metrology terminal for satellite-to-satellite laser ranging". In: *Proc. International Conference on Space Optical Systems and Applications (ICSOS)* 1180 (2019). DOI: 10.1117/12.2536072.

Acknowledgments

This section is dedicated to those people, who helped, supported and accompanied me throughout my employment at the AEI. I am extremely grateful for the amazing time, that I had at this great institute. In retrospect, the timing was perfect when I began to work here as a master student in 2012: Funding for the German part of the LRI had just been granted and industry began designing and building the first engineering and then later flight models of LRI sub-units. Being able to contribute to a space mission from such an early phase, witnessing the launch from the Vandenberg Airforce Base and assisting in the instrument's in-orbit commissioning phase was extremely fulfilling. The same is true for being a member of the AEI while the first gravitational waves were detected, which led to a significant boost for the field as a whole, but also the LISA mission. It seems, all this is only possible at such a great place as the Albert Einstein Institute. I would like to thank Karsten Danzmann for shaping the AEI and for allowing me to be a part of it!

I would also like to express my deepest gratitude to Gerhard Heinzel for allowing me to pursue my PhD work in "his" Space Interferometry working group and for supervising me. We all know how much you have on your plate, however, your door is always open to us and you never shy away from sitting down with us to help us dig through our problems. Thank you for everything that I could learn from you in all these years!

I would also like to express my gratitude to Michèle Heurs, Gerhard Heinzel and Claus Braxmaier for being referees to this thesis. Likewise, I would like to thank Milutin Kovacev for chairing my thesis defense committee. Furthermore, I would like to thank Birgit Ohlendorf, from the QUEST Office, for guiding me through the rough waters that are referred to as the Promotionsordnung!

A big thank you goes to all members of the AEI Space Interferometry working group. You make the AEI an even more enjoyable place to work. It was and is a pleasure to *mensa*, travel and work with you! I am very thankful for being a member of the AEI GRACE Follow-On team. It was amazing to go on this ride together with all of you: Ben, Christina, Christoph, Daniel, Germán, Gunnar, Henry, Jens, Malte and Vitali! I would also like to thank all members of the AEI's electronic and mechanic workshop, as well as the secretaries, the administrative and the IT staff for supporting us PhD students in our undertakings!

The collaboration with our friends from the DLR Institute of Space Systems in Bremen, especially Pep and Martin, has always been fantastic. Be it the development of OGSE, our initial acquisition test campaign, testing of LRI hardware, the collaboration within our CRC and even the writing of new CRC proposals, I am deeply grateful for everything that I could learn from you guys!

The same is true for the LRI team at JPL. It was inspiring to work with such experienced scientists. Thank you for being such great hosts, when we visited you back in 2014! I am also very grateful for the uncomplicated collaboration with our colleagues from STI and Airbus D&S, who made it possible for us to spend innumerable business trips at beautiful Lake Constance.

Of course, I would like to thank all my colleagues, who proof-read this thesis. You gave great feedback and really helped to improve this thesis! In alphabetical order, I would like to thank Germán, Henry, Jonathan, Roberta, Stefan, Thomas and Vitali. It goes without saying that all remaining mistakes are my own responsibility.

Last but not least I would like to thank all my friends and my family, who have supported me throughout these 33 years of my life. I would like to express my deepest gratitude to my parents for everything that they have done for me and for enabling me to study physics. Without you, I would not be where I am today! I am absolutely certain, that my father is looking down on us right now and that he is pleased to see that his son has finally concluded his PhD work! I would like to direct the final words to you, Mona: Thank you for supporting and believing in me throughout the past ten years! I could not be more grateful for everything that we share.

Curriculum Vitae

Personal details

Full Name	Alexander Koch
Birth Name	Görth
Current Address	Bachstraße 20, 30989 Gehrden, Germany
Date of Birth	August 17th, 1986
Place of Birth	Hannover, Germany

Education and employment

1999-2006	Abitur, Matthias-Claudius-Gymnasium, Gehrden
2006-2007	Community Service, Deutsches Rotes Kreuz, Springe
2007-2010	Bachelor Studies of Physics, Leibniz Universität Hannover
2010/11	Bachelor of Science in Physics, Thesis Title "Evaluation unterschiedlicher Materialien als Gewebephantom-Teststruktur für fs-Laser in ophthalmologischen Anwendungen"
2010-2013	Master Studies of Technical Physics, Leibniz Universität Hannover
2012/07-09	Visiting Student, Massachusetts Institute of Technology, Cambridge, Massachusetts, USA
2013/11	Master of Science in Technical Physics, Thesis Title "Development of a Fiber-Based Intersatellite Laser Link Simulator for GRACE Follow-On"
Since 2013/12	Scientific Assistant and IMPRS stipend holder at the Max-Planck Institute for Gravitational Physics (Albert Einstein Institute), Hannover
2014/01	Research Visit, NASA Goddard Space Flight Center, Greenbelt, Maryland, USA
Feb. 14th, 2020	PhD Thesis Defense, Thesis Title "Link Acquisition and Optimization for Intersatellite Laser Interferometry"

Publications

Peer-reviewed publications

K. Abich et al., "In-Orbit Performance of the GRACE Follow-on Laser Ranging Interferometer", Physical Review Letters **123**, https://doi.org/10.1103/PhysRevLett.123.031101 (2019)

A. Koch, J. Sanjuan, M. Gohlke, C. Mahrdt, N. Brause, C. Braxmaier and G. Heinzel, "Line of sight calibration for the laser ranging interferometer on-board the GRACE Follow-On mission: on-ground experimental validation", Optics Express **26**, https://doi.org/10.1364/OE.26.025892 (2018)

Z. Luo, Q. Wang, C. Mahrdt, **A. Görth** and G. Heinzel, "Possible alternative acquisition scheme for the gravity recovery and climate experiment follow-on-type mission", Applied Optics **56**, https://doi.org/10.1364/AO.56.001495 (2017)

J. Sanjuan, M. Gohlke, S. Rasch, K. Abich, **A. Görth**, G. Heinzel and C. Braxmaier, "Inter-spacecraft link simulator for the laser ranging interferometer onboard GRACE Follow-On", Applied Optics **54**, http://doi.org/10.1364/AO.54.006682 (2015)

Conference proceedings

C. Dahl, A. Baatzsch, M. Dehne, F. Gilles, P. Hager, M. Herding, K. Nicklaus, K. Voss, K. Abich,C. Braxmaier, M. Gohlke, B. Guenther, J. Sanjuan, B. Zender, G. F. Barranco, **A. Görth**, C. Mahrdt, V. Müller, D. Schütze, G. Stede and G. Heinzel, "Laser ranging interferometer on Grace follow-on", SPIE Proceedings **10562**, International Conference on Space Optics — ICSO 2016, https://doi.org/10.1117/12.2297705 (2017)

A. Görth, J. Sanjuan, M. Gohlke, S. Rasch, K. Abich, C. Braxmaier and G. Heinzel, "Test environments for the GRACE follow-on laser ranging interferometer", Journal of Physics: Conference Series **716**, 012011, 11th Edoardo Amaldi Conference on Gravitational Waves, https://doi.org/10.1088/1742-6596/716/1/012011 (2016)

K. Abich, C. Bogan, C. Braxmaier, K. Danzmann, M. Dehne, M. Gohlke, **A. Görth**, G. Heinzel, M. Herding, C. Mahrdt, V. Müller, K. Nicklaus, J. Sanjuan, D. Schütze, B. S. Sheard, G. Stede, and K. Voss, "Grace follow-on laser ranging interferometer: German contribution", Journal of Physics: Conference Series **610**, 012010, 10th International LISA Symposium, https://doi.org/10.1088/1742-6596/610/1/012010 (2015)

Technical notes

A. Koch, "Analysis of a template-based laser beam localization algorithm for a CAS on LISA", LISA Consortium Technical Note, LISA-LCST-INST-TN-010 (2019)

A. Görth, "Laboratory Tests of the LRI Initial Acquisition Procedure with the Fiber OGSE", geo-Q Technical Note, GEOQ-TN-006 (2017)

Supervision

Supervision of Bachelor (six months) and Master (12 months) thesis projects:

Vrushabha Raja Marlur Sunder Kumar (2019)
Master Thesis, Technische Universität Berlin
"Investigation of Position Sensing Detector (PSD) as possible constellation acquisition sensor for LISA"

Christoph Gentemann (2018)
Bachelor Thesis, Leibniz Universität Hannover
"Calibration and implementation of an acquisition camera for a next generation geodesy mission"

Sebastian Schreiber (2017)
Master Thesis, Leibniz Universität Hannover
"Realization and validation of very low power laser beams for inter-satellite laser link experiments"